Methods for Neuroimaging with Ultra High Field MRI

By

Kingkarn Aphiwatthanasumet, M.Sc.



University of Nottingham
UK | CHINA | MALAYSIA

Thesis submitted to the University of Nottingham

for the degree of Doctor of Philosophy

November 2018

Abstract

Ultra high field MRI provides great opportunities for medical imaging. The large gain in SNR can be utilized to increase image resolution, sensitivity, and new contrast mechanisms are available to probe macromolecular changes in tissue. This work is focused on developing methods for neuroimaging *in vivo* at 7.0 T with high resolution and high contrast in a reasonable scanning time. The methods optimised here have been tested in various brain regions, in small cohorts, in both health and disease, including a consideration of the usefulness and pitfalls of high field MRI.

First, high resolution *in vivo* imaging of cochlea was demonstrated, using 3D T2W DRIVE sequence with B_1 shimming and dielectric pads is investigated at 7.0 T. The visibility of cochlea at 7.0 T was better than 3.0 T as assessed by two radiologists. There was high inter and intra-observer reliability. Some evidence of the cochlear duct could be found on the highest resolution scan at 7.0 T with isotropic voxels of 0.26 mm.

Second, *in vivo* imaging of the nucleus basalis of Meynert (NBM), using a novel 3D SW-PSIR (susceptibility and T_1 weighted PSIR image) at 7.0 T with narrow FOV and dielectric pads, produced improved contrast, and allowed subregional delineation of the NBM in healthy volunteers. Our findings confirm good repeatability between in the measurements made by two different observers.

Finally, disease evolution of multiple sclerosis was evaluated by repeated scanning in 4 MS patients using multiple contrast MRI at 7.0 T. Subtle changes in qMT, NOE and QSM could be detected prior to the first visible MS lesion on FLAIR, PSIR and T_2^* image. qMT decreased gradually and then recovered, whereas NOE was slightly decreased followed by a slow recovery, both indicating demyelination and remyelination. During the same period, susceptibility images varied considerably suggesting degradation of myelin induced extracellular iron accumulation in newly forming lesion.

Contents

Abstract i

Acknowledgements v

Abbreviations vi

1. Introduction 1

1.1 History of MR developments…….. 1

1.2 Thesis overview…… 3

2. Principles of Nuclear Magnetic Resonance (NMR) and Magnetic Resonance Imaging (MRI) 6

2.1 NMR…… 6

2.1.1 Magnetic moment and nuclear spin…… 6

2.1.2 Larmor precession…….. 8

2.1.3 Net magnetization……. 9

2.1.4 Rotating frame and resonance…… 11

2.1.5 Excitation and detection……... 12

2.1.6 Free induction decay…….. 12

2.1.7 Dephasing phenomena…… 14

2.1.8 Relaxation……..…… 16

2.1.9 Bloch equation……... 18

2.2 MRI……. 19

2.2.1 Slice selection…… 20

2.2.2 Frequency and phase encoding……... 22

2.2.3 k-space and image reconstruction……. 25

2.2.4 Field of view and spatial resolution……. 26

2.2.5 Contrast mechanisms……. 27

2.2.6 Basic pulse sequences…….. 30

2.2.7 Multislice and three-dimensional (3D) imaging……... 34

2.2.8 Multiple echoes readout……... 36

2.3 Summary…… 37

3. Ultra High Field Strength 7.0 Tesla MRI 40

3.1 Introduction…… 40

3.2 The benefits……..…….. 42

3.3 The challenges……..…… 46

3.4 Solutions…… 50

3.5 Biological effect and safety consideration……..……. 52
3.6 Instrumentation……..… 55
3.7 MR sequences commonly used for structural imaging at 7.0 T…… 60
3.8 Summary……... 66
4. High Resolution *in vivo* Imaging of Adult Cochlea 73
4.1 Introduction…… 73
4.2 Methods……. 76
4.2.1 Selecting an MR sequence for imaging the cochlea…… 78
4.2.2 Improving B_1 homogeneity……... 81
4.2.3 Measuring size of the cochlea and cochlear nerve…….. 86
4.2.4 Ultra high resolution imaging of cochlea…… 88
4.3 Results…… 88
4.3.1 MR sequence for cochlear imaging…… 88
4.3.2 Improved B_1 homogeneity…… 90
4.3.3 Normative size of the cochlea and cochlear nerve…….. 100
4.3.4 Ultra high resolution imaging of cochlea…… 104
4.4 Discussion……. 106
4.5 Conclusion……. 109
***5. In vivo* imaging of the Nucleus Basalis of Meynert (NBM) at High Field MRI 114**
5.1 Introduction……..…….. 114
5.2 Methods……. 119
5.3 Results…… 124
5.3.1 NBM characteristics…….. 124
5.3.2 Contrast-to-noise ratio from filtered MRI phase…… 130
5.3.3 NBM thickness……... 131
5.3.4 NBM volume……... 132
5.4 Discussion……. 134
5.5 Conclusion……. 136
6. Lesion Evolution of Multiple Sclerosis 141
6.1 Introduction…… 141
6.2 Methods……. 143
6.3 Results…… 148
6.3.1 Tracking new MS lesions with hyperintense rim…….. 150
6.3.2 Signal changes in new MS lesions with hyperintense rim…….. 156
6.3.3 Tracking new MS lesions with no hyperintense rim……. 158

6.3.4 Signal changes in new MS lesions with no hyperintense rim…. 164
6.3.5 Comparison between the changing of qMT and NOE……..… 165
6.3.6 Relationship between qMT and NOE……. 165
6.3.7 Intralesional veins on SWI……... 167
6.3.8 Dependence on fibre orientation…… 169
6.4 Discussion…… 172
6.5 Conclusion…… 175
7. Conclusion **181**
7.1 Summary……..…… 181
7.2 Future work……... 184

Acknowledgements

I would like to express my appreciation to all those who have touched my life to complete this thesis of total 3 years. I would like to start with a big thank you to my supervisor Penny Gowland for mentoring me throughout my PhD study. Her guidance helped me in all the time of research and writing of this thesis. I am very grateful for the cheerful and supportive environment she provided. Likewise, my co-supervisor, Paul Glover, thanks a lot for the patient advice and encouragement.

And to Richard Bowtell, Olivier Mougin, Nicolas Geades, Nikos Evangelou, and Molly Brights, thanks a lot for giving me that chance being involved in such a nice collaboration MS longitudinal study, all encouraged me to complete this work.

I thank Jim Smith (for his supports to help setting MPT motion tracking system and organize group meeting), Mobeen Ali (for his supports in the QSM works and sharing our data analysis together), Christopher Mirfin (for his support to create RF shimming GUI for multi-transmit system which I used in Chapter 5 of this work). Rosa Sanchez-Panchuelo (for her support to help optimizing MR protocols at 7.0 T).

To my thesis committee, Professor Peter Morris and Professor Adam Waldman, for their insightful comments and also the question which incented me to widen my research from various perspectives.

The past and present members of SPMIC who helped me along the way when I need volunteers for MR scan, thanks a lot for all contributed to the support, friendship and making my experience more colourful. I will remember all of them.

I thank Naresuan University, for the funding which allowed me to study abroad.

Last but definitely not the least, I thank my parents Siriroj and Kanjana Aphiwatthanasumet for their unconditional love, support and encouragement.

Abbreviations

AC	Anterior Commissure
AD	Alzheimer’s Disease
AFI	Actual Flip Angle Imaging
BET	Brain Extraction Tool
bFFE	Balanced Fast Field Echoes
CEST	Chemical Exchange Saturation Transfer
ChAT	Choline Acetyltransferase
CNR	Contrast-to-Noise Ratio
CSF	Cerebrospinal Fluid
DAT	Dopamine N-acetyltransferase
DRIVE	DRIVen Equilibrium
DTI	Diffusion Tensor Imaging
DWI	Diffusion-weighted Imaging
EM	Electromagnetic
FA	Flip Angle
FDM	Frequency Difference Mapping
FFE	Fast Field Echoes
FID	Free Induction Decay
FLAIR	Fluid-attenuated Inversion Recovery
FOV	Field of View
FRFSE	Fast Recovery Fast Spin echo
GE	Gradient Echo
GUI	Graphical User Interface
ICC	Intraclass Correlation Coefficient
IR	Inversion Recovery

LUT	Look up table
MPRAGE	Magnetisation Prepared Rapid Gradient Echo
MRI	Magnetic Resonance Imaging
MS	Multiple Sclerosis
MT	Magnetisation Transfer
MTR	Magnetisation Transfer Ratio
NAWM	Normal-appearing White Matter
NBM	Nucleus Basalis of Meynert
NOE	Nuclear Overhauser Effect
NMR	Nuclear Magnetic Resonance
PNS	Peripheral Nerve Stimulation
PSIR	Phase Sensitive Inversion Recovery
QSM	Quantitative Susceptibility Mapping
RF	Radio Frequency
ROI	Region of Interest
SAR	Specific Absorption Rate
SNR	Signal-to-Noise Ratio
SWI	Susceptibility Weight Imaging
SE	Spin Echo
TE	Echo Time
TFE	Turbo Field Echo
TI	Inversion Time
TR	Repetition Time
T/R	Transmit and Receive
UHF	Ultra High Field
WM	White Matter

Chapter 1 Introduction

1.1 History of MR Developments

The effects of magnetic fields on atomic energy levels were demonstrated in 1900s. In the 1940, nuclei were shown to be able to absorb energy in the radiofrequency (RF) range and release it at a specific frequency. This phenomenon is known as Nuclear Magnetic Resonance (NMR). NMR can be extended to produce images, this is known as magnetic resonance imaging (MRI) and is widely used in clinical imaging.

Five Nobel prizes have been awarded for MR discoveries. The Nobel Prize in Physics in 1944 was awarded to Isidor Rabi for his method of recording the magnetic properties of atomic nuclei; the 1952 Nobel prize for Physics was awarded jointly to Felix Bloch and Edward Mills Purcell for their development of method for NMR measurement; Richard Ernst was awarded the Nobel prize for Chemistry in 1991 for his contribution to develop 2D NMR spectroscopy using phase and frequency encoding and the Fourier Transform; Kurt Wuthrich was awarded the Nobel prize for Chemistry in 2002 for his application of NMR spectroscopy to determine 3D structure of biological macromolecules in solution; most recently the Nobel prize for medicine was awarded to Paul C. Lauterbur and Sir Peter Mansfield for their discoveries using NMR to create an image, also called magnetic resonance imaging in 2003. A brief historical overview is summarised in Table 1.1.

Table 1.1: Historical overview of the key discoveries and developments in MRI.

Authors, Year	Events
1937	Isidor Rabi: observed nuclear magnetic resonance (NMR) physical phenomenon. (Nobel Prize in Physics in 1944)
1946	Bloch & Purcell: developed method for NMR measurement. (Nobel Prize in 1952)
1973	Lauterbur: introduced gradients for spatial localization of the first 2D proton MR image from a water sample. (Nobel Prize in Physiology or medicine in 2003)
1975	Richard Ernst: developed 2D NMR spectroscopy. (Nobel Prize in Chemistry in 1991)
1976	The first MRI scan of a cross-section of the human finger was produced by Peter Mansfield. Then, the first MRI of the human body image was demonstrated by the Nottingham group of P. Mansfields, P.G. Morris, I.L. Pykett and R.E. Coupland.
1977	Peter Mansfield: developed Echo-planar imaging. (Nobel Prize in Physiology or medicine in 2003)
Early 80	Kurt Wuthrich: applied NMR spectroscopy to determine 3D structure of biological macromolecules in solution. (Nobel Prize in Chemistry in 2002)
1981	The first commercial MR scanner was developed using permanent magnet with field strength 0.3-0.6 Tesla.
1985	Superconductive 1.5 Tesla MRI built.
1992	Functional MRI (fMRI) in human developed.
End of 90s	3.0 Tesla MR systems in clinical use.
Today	Ultra high field MRI scanners are installed worldwide. The world's first 7.0 T MRI cleared for clinical imaging has been approved by the U.S. Food and Drug Administration (FDA) in 2017.

From their discoveries, MRI has rapidly become one of the most important medical imaging methodologies in the world. For more than 30 years, MRI has been used as a diagnostic tool in routine clinical practice. The first clinical MRI systems created in 1983 started with field strengths of 0.35 T and 0.5 T which increased to 1.0 T and 1.5 T before the end of 1980s. By the 2000s, clinical 3.0 T scanners were regularly used. Many venders offer 3.0 T whole-body systems, however, the magnet field strength of 1.5 T remains the most common choice in routine imaging. Today, more than 60 MRI scanners operating at 7.0 T or higher field strengths have been installed. The significant advantages in signal-to-noise ratio and biological information content highlight the potential of ultra high field MRI in a variety of studies.

1.2 Thesis Overview

Chapter 2 describes the background physics and theory relating to magnetic resonance, such as excitation, relaxation and detection of the NMR signal. It covers the fundamentals of nuclear magnetic resonance (NMR), magnetic moment, nuclear spin, Larmor precession, the rotating frame, resonance, relaxation, and free induction decay. Then, it proceeds to describe the formation of an MR image. The principles of magnetic resonance imaging (MRI) are presented which include the concepts of signal detection, data acquisition, slice selection, spatial encoding, dephasing phenomena, basic pulse sequences, three-dimensional imaging, accelerated imaging sequences, and contrast mechanisms.

Chapter 3 introduces the opportunities and challenges of imaging at ultra high field strength 7.0 T including; instrumentation in various phases of technology development, MR sequences for common scenarios in clinical practice, biological effects and safety concerns. It also highlights the impact of 7.0 T MRI in clinical imaging particularly with in the neuroimaging field.

Chapter 4 presents the method of neuroimaging at ultra high field MR to image the Nucleus Basalis of Meynert (NBM) which is considered to be a potential marker of neurodegenerative disorders in the human brain.

Chapter 5 focuses on high resolution *in vivo* imaging of adult cochlea at 7.0 T MRI. There are four main focuses for this study; selecting a proper MR sequence for imaging of human cochlea at both 7.0 T and 3.0 T, improving B_1 homogeneity, evaluating the normative size of the cochlea and cochlear nerve and finally improving image quality and spatial resolution of cochlear scan.

Chapter 6 demonstrates lesion evolution of multiple sclerosis (MS). The formations of new MS lesions in small cohort of 4 patients at 6 week intervals were evaluated using multi-contrast MRI at 7.0 T. The longitudinal changes in white matter (WM) tissue are also compared prior to and after lesion appearance.

Chapter 7 draws general conclusions based on the findings. Possible future work is also discussed.

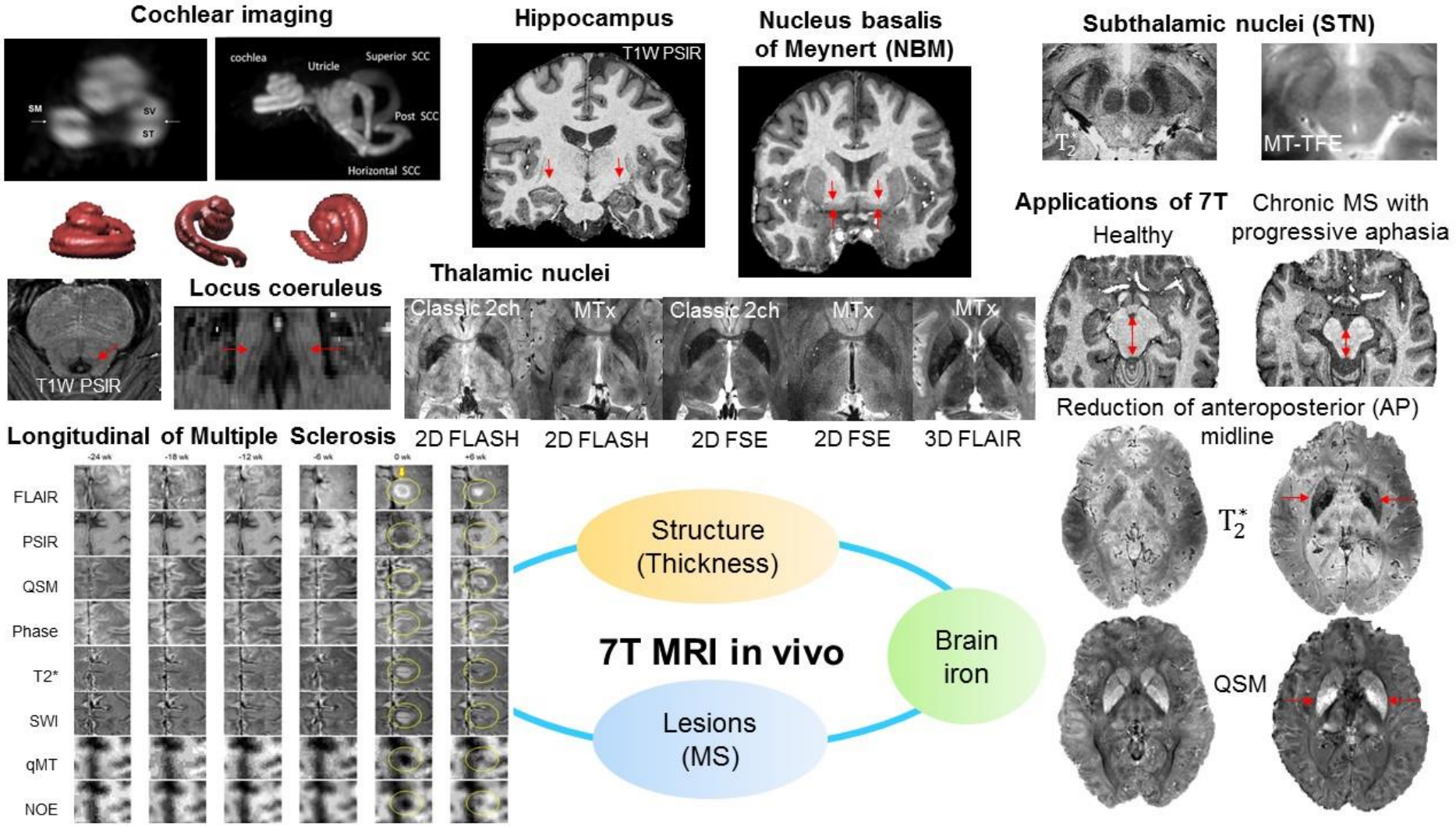


Figure 1: Structural imaging of the human parts in the brain with 7.0 T MRI was developed at Nottingham.

Chapter 2 Principles of Nuclear Magnetic Resonance and Magnetic Resonance Imaging

This chapter outlines the basic principles of nuclear magnetic resonance (NMR) and magnetic resonance imaging (MRI). NMR signals contain encoded information about physical and chemical environment of the nuclei. Section 2.1 describes the property of nuclei in a magnetic field and interactions within tissue when disturbing the dynamic equilibrium. Section 2.2 introduces how NMR signals can be used to create MR images. Techniques for spatial encoding and basic pulse sequences are described. The role of pulse sequence design to enhance or quantify contrast mechanisms is explored.

2.1 NMR

The NMR phenomenon is caused by the interaction of nuclear spin with magnetic fields.

2.1.1 Magnetic moments and nuclear spin

Among the properties of an atomic nucleus is its angular momentum (p),

$$p = \bar{h}\sqrt{I(I+1)} \qquad \text{Eq 2.1}$$

where $\bar{h}$ is Planck's constant divided by 2π and I is the nuclear spin (or quantum number). Atomic nuclei with an odd number of protons or neutrons have spin angular momentum, explained by Pauli in 1924. Nuclei with spin (Figure 2.1.1),

such as the hydrogen nucleus $I = \frac{1}{2}$, have a magnetic moment and a positive charge. The angular momentum also creates the nuclear magnetic moment

$$\vec{\mu} = \gamma I \qquad \text{Eq 2.2}$$

where γ is the gyromagnetic ratio and I is a spin quantum number. The gyromagnetic ratio is a constant for a particular nucleus and for protons is equal to 42.58 MHz/T. If we place any nucleus with no zero spin in a magnetic field, the magnetic moment can assume $2I + 1$ possible different states (Figure 2.1.2), and the direction of the external magnetic field which defines the z-axis of coordinate system $\vec{B} = (0,0,B_0)$.

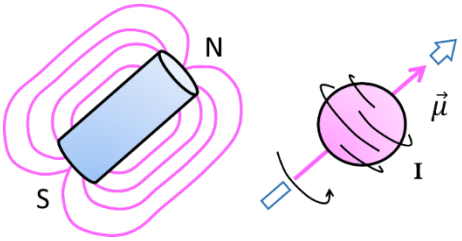


Figure 2.1.1: Nuclear magnetism of the hydrogen nucleus with net spin (I) have magnetic moment (μ) and associated magnetic field can be regarded as tiny bar magnets.

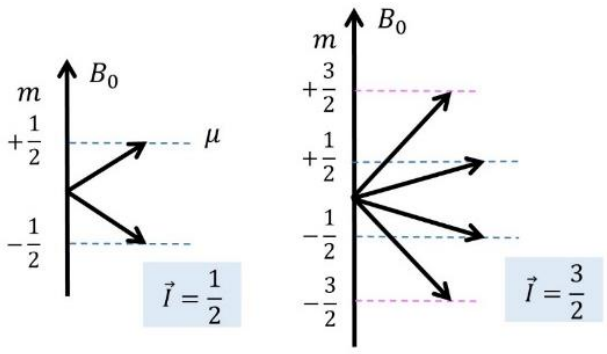


Figure 2.1.2: Nuclei in a magnetic field for spin number, I of $\frac{1}{2}$ (left) and $\frac{3}{2}$ (right).

Only nuclei with an odd number of protons or neutrons can have spin quantum numbers that may be used for NMR experiments. The most important nucleus is that of hydrogen due to its high NMR sensitivity and high abundance. NMR useful nuclei are listed in Table 2.1.1

Table 2.1.1: Nuclear spin (I), gyromagnetic factor (γ), of some relevant nuclei in biomedical MR experiments (adapted from Stark and Bradley [1]).

Nucleus	Spin (I)	Gyromagnetic ratio, $\frac{\gamma}{2\pi}$ (MHz/T)	Abundance in natural (%)	Abundance in human tissue (%)
^{1}H	1/2	42.58	99.99	63
^{19}F	1/2	40.05	100	0.0012
^{31}P	1/2	17.23	100	0.14
^{23}Na	3/2	11.26	100	0.037
^{13}C	1/2	10.71	1.11	0.13
^{17}O	5/2	5.772	0.037	0.024
^{39}K	3/2	1.99	93.1	0.031

Without an applied external magnetic field, a collection of the magnetic moments (or spins) will be randomly orientated in space, resulting in zero net magnetization $(M = 0)$. When the external magnetic field is applied, the magnetic dipoles tend to be in the low energy level state (Figure 2.1.2). However, both the low and high energy states are generally occupied at temperature above absolute zero.

2.1.2 Larmor precession

Motion of the proton magnetic moment in a magnetic field is similar to the precession of a spinning top, which possesses an angular momentum as a result of its spin (Figure 2.1.3).

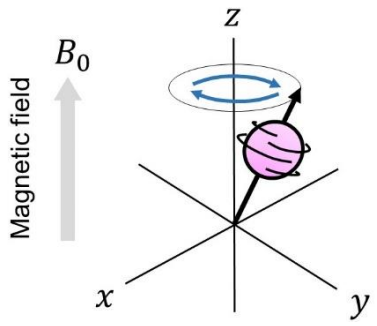


Figure 2.1.3: A spin precesses around the direction of the external magnetic field (along the z axis) at the Larmor frequency.

In the external magnetic field (B_0), the magnetic moment will experience a torque resulting in precession of the magnetic moment around B_0. This motion of the spin in a static magnetic field can be described by the Bloch equation [3], which the fundamental equation explaining the behaviour of magnetization.

$$\frac{d\vec{\mu}}{dt} = \gamma\vec{\mu} \times \vec{B} \qquad \text{Eq 2.3}$$

Therefore, the spin will precess at the Lamor frequency, which is directly proportional to the magnetic field strength.

$$\omega_0 = \gamma B_0 \qquad \text{Eq 2.4}$$

where ω_0 is the Lamor frequency (unit: MHz) and γ is the gyromagnetic ratio (unit: MHz/T).

2.1.3 Net magnetization

There is a difference in the energy level of the two states as shown in Figure 2.1.2. The ratio of the number of spins aligned parallel (N_+) to those aligned antiparallel (N_-) is given by thermodynamics and Boltzmann distribution

$$\frac{N_+}{N_-} = e^{\Delta E/kT} = e^{\bar{h}\omega_0/kT} = e^{\frac{\bar{h}\gamma B_0}{kT}} \qquad \text{Eq 2.5}$$

where ΔE is the energy difference between the two states, k is the Boltzmann constant $(k = 1.3181x10^{-23} J \cdot K^{-1})$, T is the absolute temperature (Kelvin) and ω_0 is the Lamor frequency. The difference in population of the two states is only ~ 1 in 10^6 at room temperature. However, from the equation, it can be seen that this ratio is proportional to the field strength, since the larger energy difference ΔE becomes, the larger difference in population will be (Figure 2.1.4). Resonance occurs when an electromagnetic wave of appropriate frequency stimulates the nuclei [4] to flip between states so that nuclei in lower energy state are transferred to the state of higher energy.

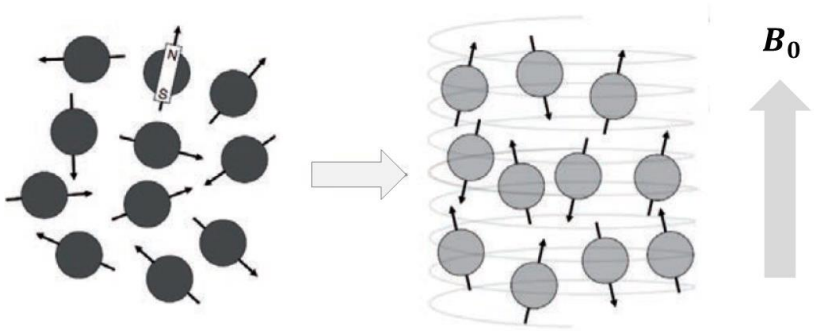


Figure 2.1.4: Comparison of spins configuration according to no applied external magnetic field (left, spins oriented randomly in space) and applied magnetic field (right, spins aligned either parallel or antiparallel to magnetic field) [2].

The individual nuclei precessing around B_0 creates a net (vector sum) of net magnetization ($\vec{M}$). The net magnetization is given by

$$\vec{M} = \sum_{i=1}^{n_s} \mu_i \qquad \text{Eq 2.6}$$

where n_s is the number of spins in the voxel and μ_i is the magnetic moment of the i^{th} state. Figure 2.1.5 shows the individual magnetic moments and the resultant of the net magnetization vector ($\vec{M}$). $\vec{M}$ is aligned along B_0. The more nuclei available for alignment, the larger the net magnetization.

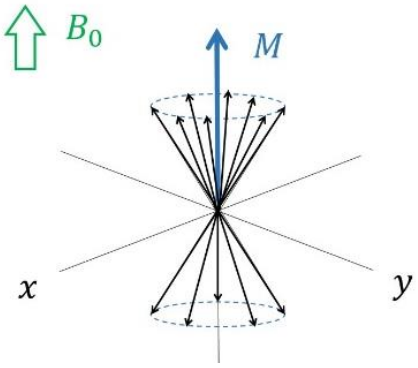


Figure 2.1.5: The net magnetization ($\vec{M}$) is proportional to the number of spins which is calculated by the sum of the nuclei precessing around the direction of external B_0 field.

At equilibrium, the value of the net magnetization is called M_0. The behaviour of the net magnetization can be treated similar to a single spin. The Bloch equation can be written to reflect the behaviour of the net magnetization as

$$\frac{d\vec{M}}{dt} = \gamma\vec{M} \times \vec{B} \qquad \text{Eq 2.7}$$

2.1.4 Rotating reference frame and resonance

In a laboratory (stationary) frame of reference, spins precess at the Larmor frequency around the direction of B_0 (Figure 2.1.6). However, we can choose another frame of reference which is rotating about the z-axis with respect the laboratory frame.

In the rotating frame, the spins precessing at the Larmor frequency (ω_0) will appear stationary whereas those that precess at different frequencies will appear to precess in the rotating frame. In this frame, the precession around B_0 field is cancelled out.

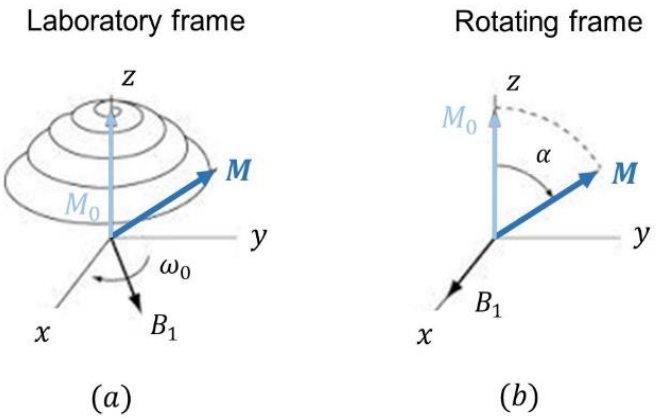


Figure 2.1.6: The magnetic moment in the laboratory frame (a) and rotating frame (b). For NMR/MRI, the frame of a choice is one rotating with respect to the laboratory frame about the z axis [5].

2.1.5 Excitation and detection

Excitation of the magnetization can be simplified by considering in the rotating frame (Figure 2.1.7-2.1.8). If an external radiofrequency (B_1) field rotating at the Lamor frequency in the transverse plane is applied to the spins in magnetic field (B_0), the magnetization will precess around the vector sum of B_0 field and the time varying B_1 field, causing special motion (Figure 2.1.7 a). In the rotating frame, the B_0 field is effectively cancelled so this corresponds to a tip around B_1 (Figure 2.1.7 b).

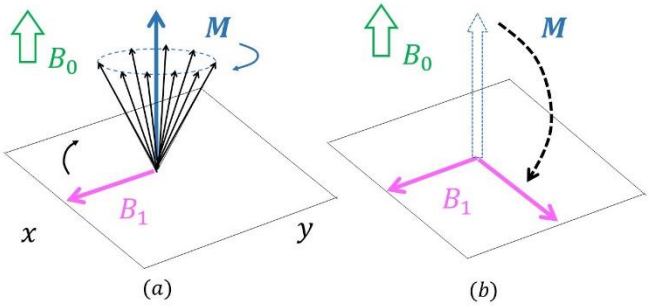


Figure 2.1.7: Tipping of longitudinal magnetization into transverse magnetization by an radiofrequency (RF) pulse. When we apply RF pulse (B_1 field), it is called forced precession because M is influenced by the B_1 field. After RF pulse ends, the magnetization is called free precession because M_{xy} precesses around B_0 field.

For optimal signal detection, once the magnetization reaches the transverse (xy) plane, the B_1 field is removed. The magnetization will continue to precess about B_0 (the z axis) at the Lamor frequency. This rotating magnetization is a changing flux and can induce a voltage in a receiver coil (according to Faraday's law of induction), that can be detected by a receiver. Details of the RF coils and other imaging hardware at 7.0 T are discussed in Chapter 3.

2.1.6 Free induction decay (FID)

Once the excitation pulse is switched off, the spins gradually return to their equilibrium state (relaxation) through T_1 relaxation, while the magnetization in the

transverse plane decays exponentially with a T_2 time constant and largely independent of B_0. The free induction decays described by a rate constant at a rate T_2^*. The MR rotating signal that is received from the RF coil is called “free induction decay (FID)” [6].

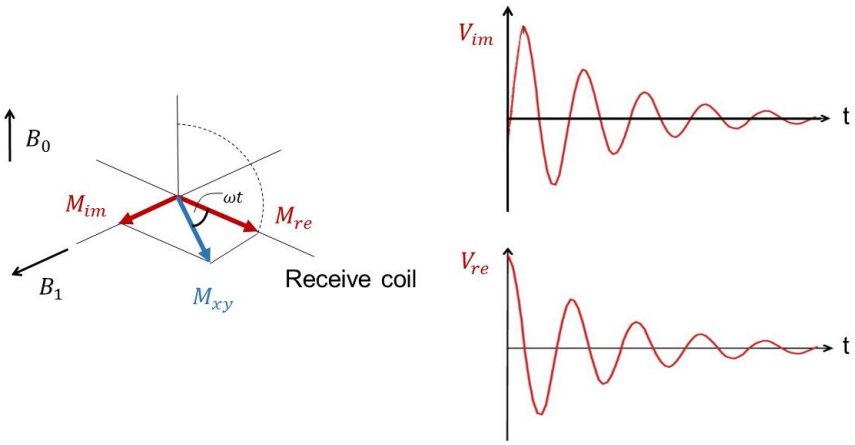


Figure 2.1.8: Transverse magnetization and signal detection. Transverse magnetization is detected by the voltage induced in a pickup coil. The transverse magnetization (M_{xy}) is regarded as a complex number (real part ; M_{re} and imaginary part; M_{im}). The real component of transverse magnetization is 90° out of phase relative to the B_1 field, while the imaginary component is in phase with B_1 field. The signal can be represented as a vector with real v_{re} and imaginary v_{im} components recorded from RF coil.

The oscillations observed in the FID in Figure 2.1.8 depend on the difference between the receiver frequency and the actual spin resonance. To increase SNR, two RF coils in quadrature may be used for detection, which can detect signal as

$$S_x(t) = Ae^{-\frac{t}{T_2}}\cos(-\omega_0 t) \qquad \text{Eq 2.8}$$

$$S_y(t) = Ae^{-\frac{t}{T_2}}\sin(-\omega_0 t) \qquad \text{Eq 2.9}$$

where A is a constant corresponding to the number of excited spins. The complex signal in the stationary reference frame is

$$S(t) = S_x(t) + S_y(t) = Ae^{-\frac{t}{T_2}}e^{-i\omega_0 t} \qquad \text{Eq 2.10}$$

and the signal in the rotating frame becomes

$$S(t) = Ae^{-\frac{t}{T_2}} \qquad \text{Eq 2.11}$$

The acquired signal has no positional information. It shows how many spins are present in the selected volume. The explanation of how positional information can be encoded in the signal in order to produce images of spin will be presented in section 2.2.1.

As shown in Figure 2.1.9, the frequency spectrum of the FID can be obtained simply by taking the Fourier transform (FT), the result is a function whose real component can be expressed by a Lorentzian. The peak of the Lorentzian curve will be centred at the Larmor frequency (ω_0), and the full width at half maximum (FWHM), will be equal to $\frac{1}{\pi T_2}$.



Figure 2.1.9: FID following RF excitation, the transverse (xy) magnetization can be detected showing the signal oscillation decay as a function of time. The FT of the FID is a Lorentzian function centred at the Larmor frequency.

2.1.7 Dephasing phenomena

The magnetization vector is the sum of a large number of individual magnetic moments. Different spin vectors can experience a different magnetic field and thus precess with a different Larmor frequency. This results in dephasing, loss of phase coherence and reduction in the net (transverse) magnetization. There are three type of dephasing which can be differentiated;

- Dephasing by **spin-spin interaction**. It is irreversible process described by the time constant T_2.
- Dephasing by **magnetic field $(\boldsymbol{B_0})$ inhomogeneity**. This is reversible process described by the time constant $T_2^* < T_2$. The inhomogeneities are

due to a non-uniform B_0 field generally caused by differences in the magnetic susceptibility of tissues. The higher magnetic susceptibility value, the more a substance is able to disturb the homogeneity of the local magnetic field. Iron and air are well-known examples.

- Dephasing by the **magnetic field gradient** required for imaging.

To restore the dephasing effect of B_0 inhomogeneities, a 180° pulse is applied. If the RF pulse is applied at $t = TE/2$, the so-called "spin echo" is created at $2t = TE$. As shown in Figure 2.2.10, the signal initially generated by a 90° RF excitation is restored by the 180° pulse. The delay between the 90° pulse and the spin echo signal is twice the time period between the 90° and 180° pulse. However, the effect of any irreversible processes persist and so the spin echo is lower than the maximum at $t = 0$.

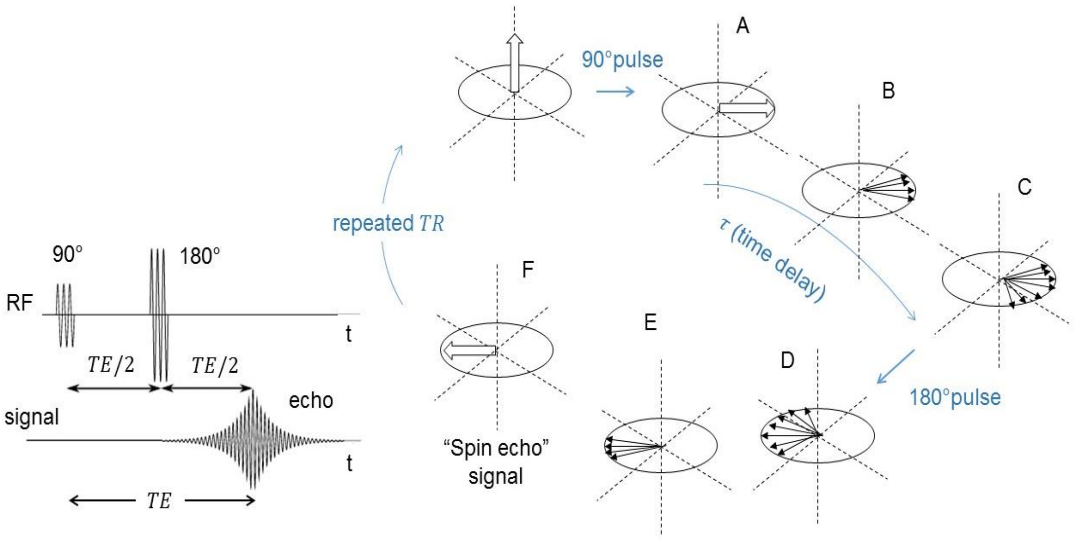


Figure 2.2.10: Following a 90° excitation (A), protons begin to dephase (B-C) and signal amplitude decreases. The signal is restored (D-E) by the application of a 180° pulse. At time TE, the protons regain phase resulting in a strong net transversal magnetization. The signal obtained is given the name "spin echo".

In the dephasing by magnetic field gradients (Figure 2.2.11), an RF pulse causes transverse magnetization and initiation of an FID signal, then the signal is dephased by a spatial gradient of magnetic field. After that, another gradient with opposite

polarity in the same duration is applied to restore the dephasing effect. This creates a “gradient echo” and the resulting signal will be attenuated by any B_0 field inhomogeneities, and therefore is weighted by T_2^*.

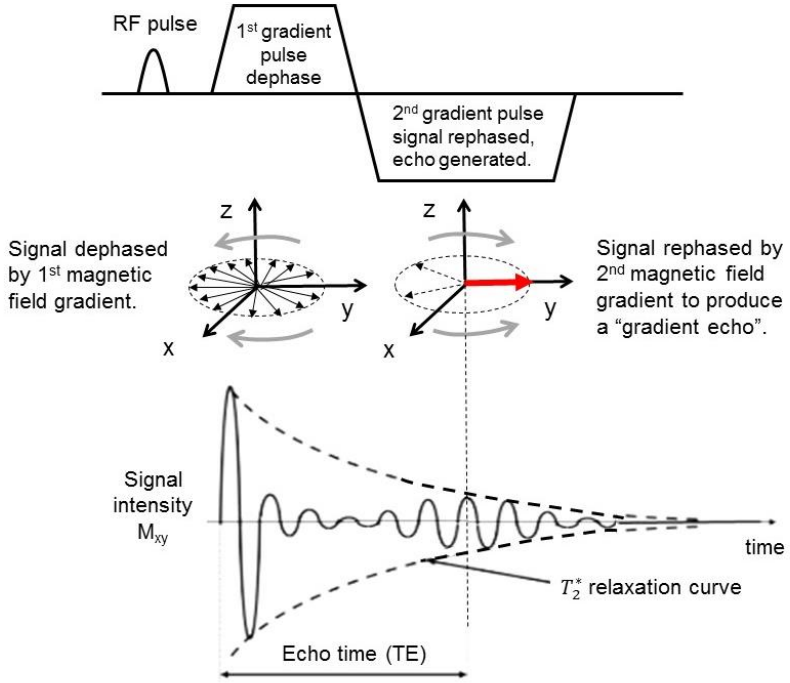


Figure 2.2.11: Gradient dephasing can be restored by applied another gradient with the same amplitude but opposite polarity. This called “gradient echo”.

2.1.8 Relaxation

Relaxation times are fundamental MR parameters reflecting the local tissue environment via proton binding of the water molecule and its mobility within tissues. After disturbing magnetization by RF excitation, the magnetization will continue to precess in the transverse (x, y) plane but the system will start to return to the original configuration (equilibrium state) described by two main time constants T_1 and T_2 [6, 7]. The energy absorbed by the spin from the applied RF is lost to its surroundings (or its lattice) which is called spin-lattice (or longitudinal relaxation) and time constant for this phenomenon is described by T_1. T_1 relaxation depends on the mobility of the lattice via dipole-dipole interactions, and the rate of energy transfer from excited spins to its lattice. Following a 90° pulse, the longitudinal magnetization (M_z) returns to its equilibrium state, M_0 according to

$$M_z(t) = M_0 \cdot \left(1 - e^{-\frac{t}{T_1}}\right) \qquad \text{Eq 2.12}$$

where M_0 is the initial longitudinal magnetization following RF excitation (Figure 2.1.12). T_1 values lengthen with increasing of B_0 field and T_1 contrast provides a good differentiation of anatomical structures on an MR image.

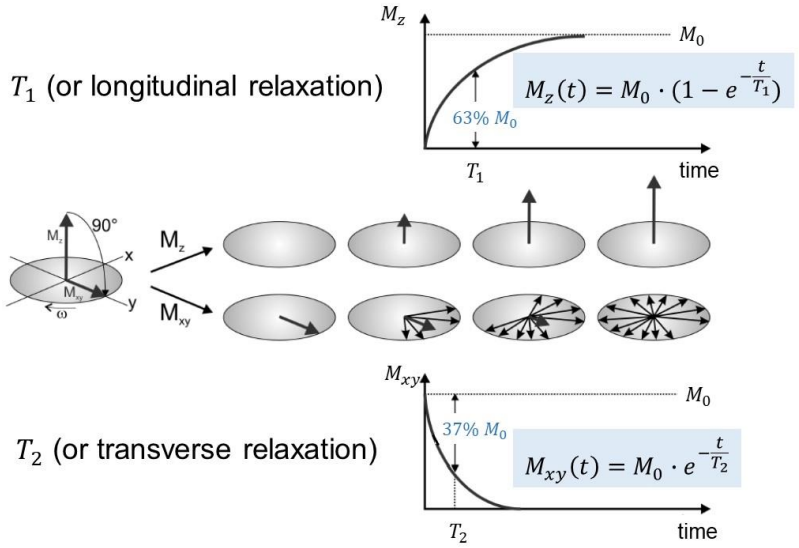


Figure 2.1.12: The behaviour of the longitudinal (M_z) and transverse (M_{xy}) magnetization after a 90° excitation RF pulse where the relaxation time of M_z is described by the time constant T_1 and the decay of M_{xy} by T_2.

In addition to interactions with the lattice, the spins also interact with each other, leading to spin-spin relaxation. Each spin produces its own magnetic field dipole, which is slightly different to its surroundings. Any spin that is close to another will experience this additional field, slightly altering its precession frequency. As the spins are in constant motion, the precessional frequency of each spin is in constant flux, lending to loss of phase coherence due to interaction between nearby dipoles. This loss results in an exponential decay of signal in the transverse plane (xy) with a time constant of T_2. The magnitude of the transverse component decays as

$$M_{xy}(t) = M_0 \cdot e^{-\frac{t}{T_2}} \qquad \text{Eq 2.13}$$

where the equilibrium magnetization (M_0) creates the initial transverse magnetization following a 90° RF excitation. Strictly T_2 is the spin-spin time constant

(or transverse relaxation time) in a homogeneous static magnetic field. T_2 is time taken for signal to decay to 37% of its initial value and also largely independent of B_0 field. The changes of T_2 value is found in pathological regions. However, the transverse decay of an FID is also affected B_0 field inhomogeneity. The net decay rate is called T_2^*. T_2^* is shorter than T_2 and their relationship can be illustrated by

$$\frac{1}{T_2^*} = \frac{1}{T_2} + \frac{1}{T_2'} \qquad \text{Eq 2.14}$$

where $\frac{1}{T_2'} \approx \gamma \Delta B_{inhomo}$, and γ is the gyromagnetic ratio. ΔB_{inhomo} is a non-uniform magnetic field. T_2^* in an inhomogeneous field may not be exponential. T_2^* is measure of the time taken for precessing spins to lose phase coherence (Figure 2.2.11).

In practice, the process of excitation and signal detection is often repeated many times until sufficient data have been acquired for image reconstruction. The time between subsequent RF excitation applied to the same region of the sample is the repetition time (TR). TR determines to what extent tissues with different T_1 values have returned toward their fully relaxed equilibrium between excitation.

2.1.9 Bloch equations

The Bloch equations provide a complete classical description of the behaviour of magnetisation under influence of an applied field, and the evolution of the MR signal [3]. The precession of Magnetization $(\vec{M})$ around B_0 field is explained by

$$\frac{d\vec{M}}{dt} = \gamma \vec{M} \times \vec{B} \qquad \text{Eq 2.15}$$

which can be expanded into

$$\frac{dM_x}{dt} = \gamma (M_y B_z - M_z B_y) \qquad \text{Eq 2.16}$$

$$\frac{dM_y}{dt} = \gamma (M_z B_x - M_x B_z) \qquad \text{Eq 2.17}$$

$$\frac{dM_z}{dt} = \gamma (M_x B_y - M_y B_x) \qquad \text{Eq 2.18}$$

Moreover, relaxation is dealt by additional phenomenological terms as

$$\frac{dM_x}{dt} = \gamma\left(M_y B_z - M_z B_y\right) - \frac{M_x}{T_2} \qquad \text{Eq 2.19}$$

$$\frac{dM_y}{dt} = \gamma(M_z B_x - M_x B_z) - \frac{M_y}{T_2} \qquad \text{Eq 2.20}$$

$$\frac{dM_z}{dt} = \gamma\left(M_x B_y - M_y B_x\right) + \frac{M_0 - M_z}{T_1} \qquad \text{Eq 2.21}$$

In the absence of an RF field, so the only magnetic field is along the z-axis ($B_0 = B_z, B_x = B_y$), the equations simplify to

$$\frac{dM_x}{dt} = \gamma M_y B_0 - \frac{M_x}{T_2} \qquad \text{Eq 2.22}$$

$$\frac{dM_y}{dt} = -\gamma M_x B_0 - \frac{M_y}{T_2} \qquad \text{Eq 2.23}$$

$$\frac{dM_z}{dt} = -\frac{(M_z - M_0)}{T_1} \qquad \text{Eq 2.24}$$

Finally, these can be combined to give

$$\frac{d}{dt}\vec{M} = \underbrace{\vec{M} \times \gamma\vec{B}}_{\text{(precession)}} - \underbrace{\frac{M_x\vec{\imath} + M_y\vec{\jmath}}{T_2}}_{\text{(relaxation)}} - \underbrace{\frac{(M_0 - M_z)\vec{k}}{T1}}_{\text{(to equilibrium)}} \qquad \text{Eq 2.25}$$

2.2 MRI

This section describes how spatial information can be encoded in the NMR signal by making the magnetic field spatially dependent. This is achieved by applying a series of linear magnetic field gradients in the x, y, and z directions across the object. The aim of applied gradients is for slice volume selection and position encoding within the selected slice (or volume). Once the spatial information is encoded in the phase of the signal, MR images are obtained by simply taking the Fourier transform. This was the key innovation which moved the science of NMR towards MRI [10]. The formation of MR images involves the following steps; excitation of selected spins, spatial encoding of signal, signal detection, and reconstruction which are discussed in detail below.

2.2.1 Slice selection

Localization of spins with magnetic field gradients

Previously, we said that if we applied only a perfectly uniform B_0 field, all spins will oscillate at the same frequency. For localization field gradients are used, which cause the resonant frequency to vary with position.

The field is still oriented along the z direction but now the field strength depends on location (Figure 2.2.1). With the slice selection gradient applied, the Larmor frequency now becomes

$$\omega(z) = \gamma(B_0 + G_z z) \qquad \text{Eq 2.26}$$

A slice with thickness Δz contains a well-defined range of precession frequencies

$$\Delta\omega = \gamma G_z \Delta z \qquad \text{Eq 2.27}$$

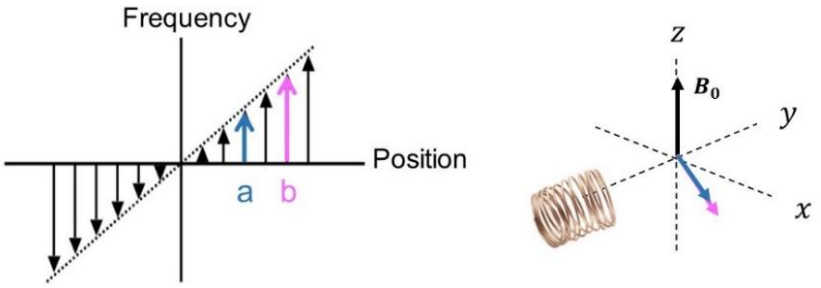


Figure 2.2.1: Gradient causes resonant frequency to vary with position. Protons at “z=a” will precess at different frequency than those at “z=b”.

Let the required slice be at position z_0 with thickness Δz. An RF pulse with nonzero bandwidth $BW = \Delta\omega$ and centred around the frequency $\gamma(B_0 + G_z z_0)$ with $\Delta\omega = \gamma G_z \Delta z)$ is needed to excite the spins. Application of weaker gradient yields a thicker slice (Figure 2.2.2).

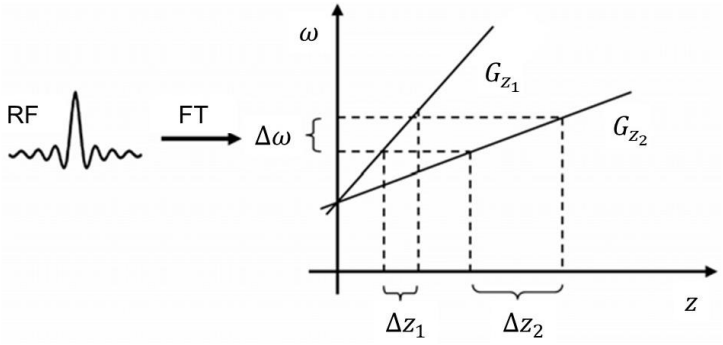


Figure 2.2.2: Principle of slice selection. The RF pulse with a given bandwidth $(\Delta\omega)$is applied for slice selection gradient (G_z). Only spins within $z + \Delta z$ meet the resonance condition and are exited. According to the weaker gradient, slice G_{z_2} is thicker than slice G_{z_1}.

The Fourier transform may use to determine the approximate required pulse shape. However, the Fourier approximation is only accurate for small flip angles (FA<30°). It can be used for a 90° excitation, but the slice profile will slightly deviate from the predicted shape at this flip angle. Furthermore, for a rectangular profile, the sinc function has an infinite extent, so in resulting slice profile cannot be a perfect rectangle in frequency domain as shown in Figure 2.2.3. Although the sinc pulse is the most commonly used, other RF pulse shapes, such as Gaussian, can be utilized. The thickness of the selected slice (Δz) is a function of the bandwidth (BW) of the sinc pulse and the amplitude of slice selection gradient (G_z) where

$$\Delta z = \frac{BW}{\gamma G_z} \qquad \text{Eq 2.28}$$

In MRI, there are three sets of linear gradient coils using for spatial encoding (G_x, G_y, G_z) which provide linear gradients along the x, y, and z axes, respectively. The excited plane will be perpendicular to the direction of the net gradient applied along the RF pulse.

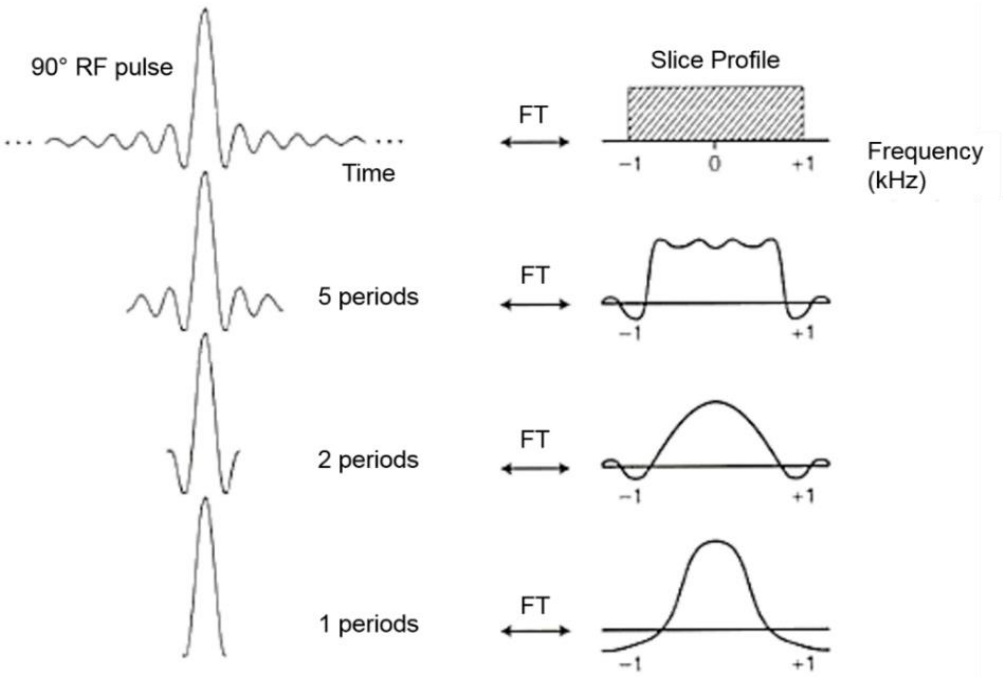


Figure 2.2.3: Truncation of a sinc RF pulse and imperfect slice profile.

2.2.2 Frequency and phase encoding

After exciting the slice, spatial encoding within the plane of the selected slice is applied. This is achieved by utilizing linear gradients along the two perpendicular in-plane directions (assumed to be G_x and G_y following excitation of the axial slice along the G_z gradient). If a gradient applied in the x direction, spins at different positions along the x direction will precess at different frequencies

$$\omega_x = \gamma G_x x \qquad \text{Eq 2.29}$$

where G_x is the applied magnetic field gradient along the x axis and ω_x is the resonance frequency of the spins at position x. Data is acquired while this readout gradient is applied and encoding spatial information in this manner is referred to as “frequency encoding”. This gradient generates following magnetization from an isochromat at position x.

$$M_{tr}(x, y, t) = M_{tr}(x, y, 0)e^{-i\gamma G_x x t} \qquad \text{Eq 2.30}$$

The term in the exponent is a phase term and represents the relative phase accumulated in the rotating frame due to the frequency encoding gradient. Typically, time varying gradients are used, and in this case, the accumulated phase term in the above equation needs to be replaced by a time integral of the readout gradient (G_x) by

$$k_x = \gamma \int_{-\infty}^{\infty} G_x(t)dt \qquad \text{Eq 2.31}$$

The position variable x and the spatial frequency variable k_x or, equivalently, image space and k-space are a Fourier pair. This is indicated in Figure 2.2.4.

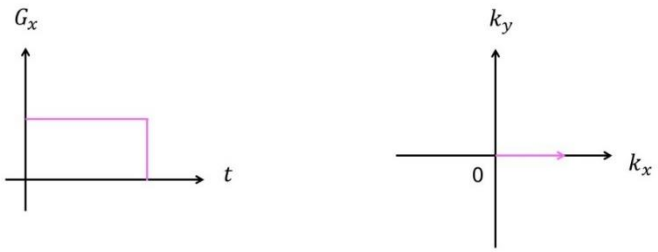


Figure 2.2.4: The application of a positive gradient in x direction is applied and the spatial frequency (k_x) increases.

The signal $S(t)$ is created by the sum of all the magnetization from all the isochromats in the imaging volume, each resonating at a frequency corresponding to its position along the readout gradient (G_x) direction, so that the signal is given by

$$S(t) = \int_{-\infty}^{\infty} \rho\,(x)e^{-i\omega_x t}dx = \int_{-\infty}^{\infty} \rho\,(x)e^{-i\gamma G_x x t}dx = \int_{-\infty}^{\infty} \rho(x)e^{-ik_x x}dx \qquad \text{Eq 2.32}$$

where $\rho(x)$ is the spin density and T_1 and T_2 dependence have been ignored for simplicity. If we define $k_x = \frac{\gamma}{2\pi} G_x t$ and $k_y = \frac{\gamma}{2\pi} G_y t$, we can write the detected signal as

$$S(t) = \int_{-\infty}^{\infty}\int_{-\infty}^{\infty} \rho(x,y)e^{-i2\pi(k_x x + k_y y)}dxdy \qquad \text{Eq 2.33}$$

which can be reformulated as

$$S(k_x, k_y) = \mathcal{F}\{S(x,y)\} \triangleq \int_{-\infty}^{\infty}\int_{-\infty}^{\infty} S(x,y)e^{-i2\pi(k_x x + k_y y)}dxdy \qquad \text{Eq 2.34}$$

The measured signal for a single excursion along k_x is given by

$$S(t) = S(k_x, 0) = \mathcal{F}\{\rho(x,y)\}_{(k_x,0)} \qquad \text{Eq 2.35}$$

The desired k-space data $S(k_x, k_y)$ can be acquired by navigating through k-space with the G_x and G_y gradients, and this can be extended into 3D. To sample the other parts of k-space (or Fourier transform of the object of interest), we apply a pre-determined gradient in the perpendicular y direction before the readout gradient G_x for the process known as phase encoding (Figure 2.2.5).

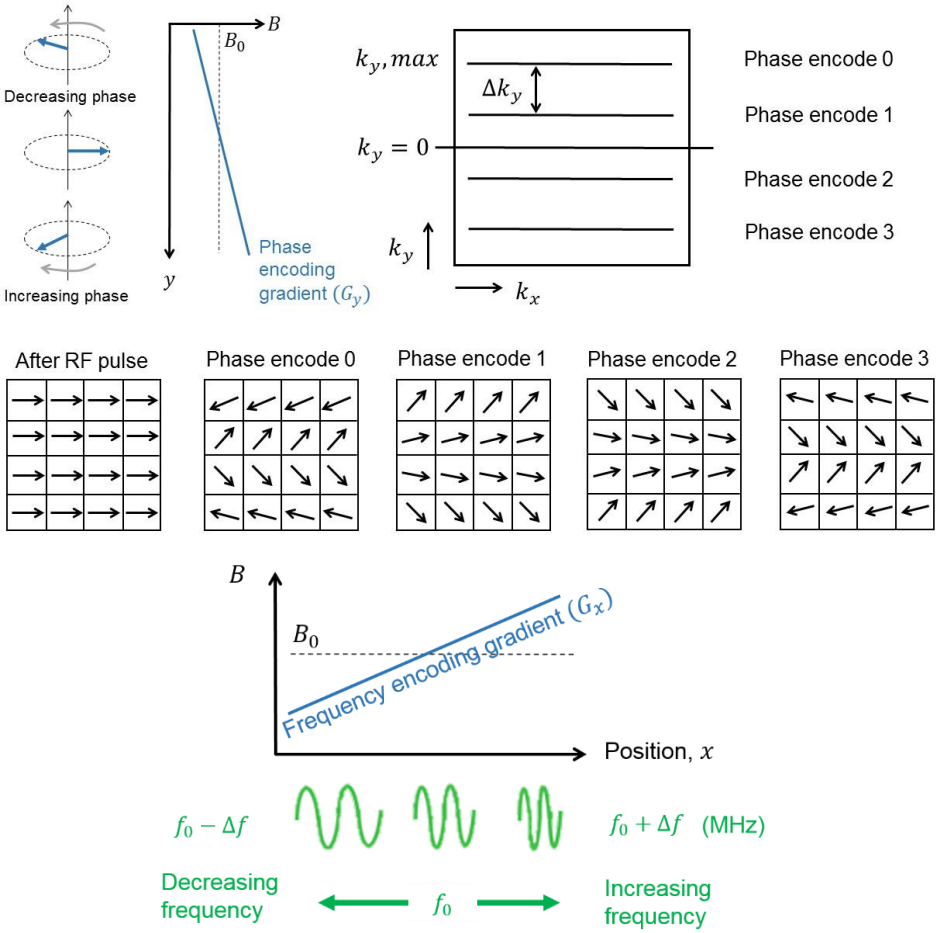


Figure 2.2.5: Illustration of phase and frequency encoding gradient.

Generating the magnetization density $\rho(x,y)$ and the position vector $\vec{r} = (x,y,z)$ as 3D functions, the angular frequency is given by

$$\omega(\vec{r}, t) = \gamma \vec{G}(t) \cdot \vec{r}(t) \qquad \text{Eq 2.36}$$

So that the measured signal now becomes

$$S(t) = \int_{-\infty}^{\infty}\int_{-\infty}^{\infty}\int_{-\infty}^{\infty}\rho(x,y,z)e^{-i\gamma\int_0^t \vec{G}(\tau)\cdot\vec{r}(\tau)d\tau}dxdydz \qquad \text{Eq 2.37}$$

Spin density needs to be weighted to take account of relaxation effects. If $g(t,T_1)$ describes the recovery of longitudinal component and $h(t,T_2)$ describes the decay of transverse component. The measured signal is

$$S(t) = \int_{-\infty}^{\infty}\int_{-\infty}^{\infty}\int_{-\infty}^{\infty}g(t,T_1)h(t,T_2)\rho(x,y,z)e^{-i\gamma\int_0^t \vec{G}(\tau)\cdot\vec{r}(\tau)d\tau}dxdydz \qquad \text{Eq 2.38}$$

2.2.3 k-space and image reconstruction

Images can be decomposed by Fourier transformation into sine and cosine waves (real and imaginary data) of different frequency and orientation [8, 9]. k-space holds the weighting factor for each of these components as shown in figure 2.2.6-2.2.7. Each k-space point contributes across whole MR image. Small values of k_x and k_y, called “low spatial frequencies”, in the centre of k-space, which encodes coarse features in an image. The edge of k-space contains high spatial frequencies, which encodes finer details. Complex k-space data is passed to inverse 2D FT as shown in Figure 2.2.8 and the output is a matrix of complex numbers split into real (R) and imaginary components of the complex image (I). The amplitude and phase extracted from the real and imaginary images and presented in magnitude (M) and phase image (ϕ), respectively.

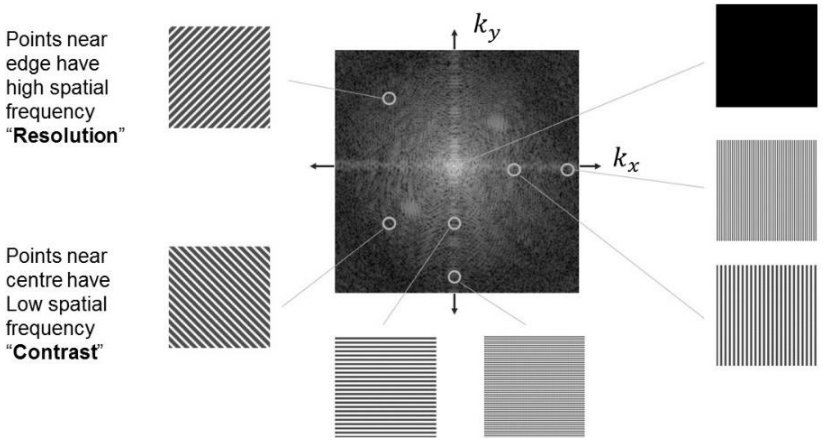


Figure 2.2.6: k-space represents the weighting factor for each of sine waves. These waves have different frequency and orientation.

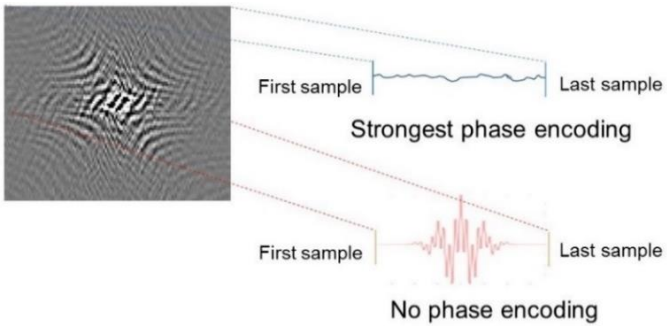


Figure 2.2.7: The k-space with different phase encoding. Each row stores the sample from one echo. The first row contains the echo following the strongest phase encoding gradient.

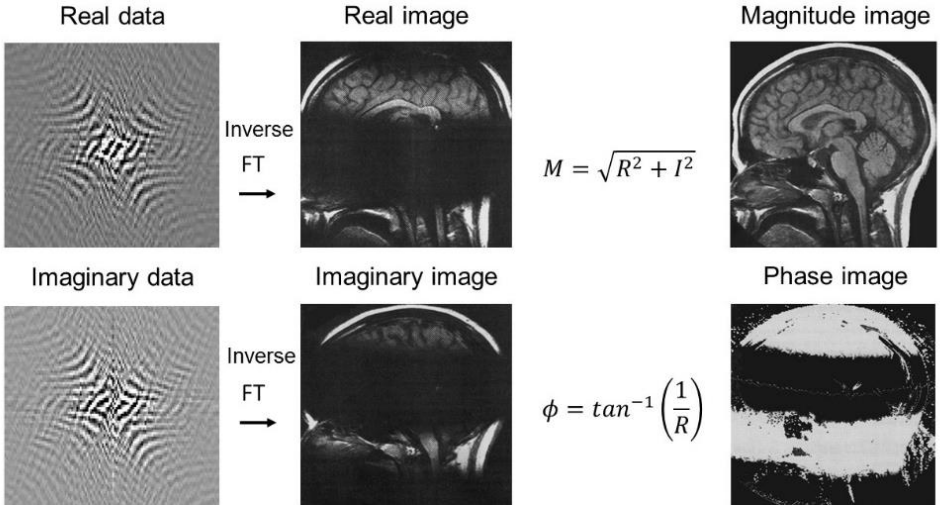


Figure 2.2.8: Reconstruction of 2D k-space into 2D MR image via inverse FT.

2.2.4 Field of view and spatial resolution

The field of view (FOV) and spatial resolution of an image are determined by the manner in which the k-space is sampled, as the image space (units of distance) and k-space (units of 1/distance) corresponding to spatial location and spatial frequency, have an inverse relationship via the Fourier transform. A larger FOV requires finer k-space sampling.

$$FOV_x = \frac{1}{\Delta k_x} \qquad \text{Eq 2.39}$$

$$FOV_y = \frac{1}{\Delta k_y} \qquad \text{Eq 2.40}$$

where Δk_x and Δk_y are the spacing between k-space point along k_x and k_y.

On the other hand, the spatial resolution (or the pixel widths Δx and Δy, is determined by the range of the sampled k-space region

$$\Delta x = \frac{1}{2k_{x,max}} \qquad \text{Eq 2.41}$$

$$\Delta y = \frac{1}{2k_{y,max}} \qquad \text{Eq 2.42}$$

where $k_{x,max}$ and $k_{y,max}$ are the maximum positions along $k_x$and k_y that are sampled, so a smaller pixel size (or higher spatial resolution) requires that a larger region of k-space be sampled.

2.2.5 Contrast mechanisms

Spin density (ρ), spin-lattice relaxation time (T_1), and spin-spin relaxation time (T_2) are essential tissue parameters that influence image contrast in MRI [5, 7]. Table 2.2.1 lists typical T_1 and T_2 values in human brain tissues which differ by approximately a factor of ~10 and depend on field strength.

Table 2.2.1: Relaxation times by tissue types at 1.5 T, 3.0 T and 7.0 T (adapted from [9]) Typical T_1 values range from approximately 500-4500 ms while T_2 range from approximately 35-300 ms.

Tissue	1.5 T		3.0 T		7.0 T	
	T_1(ms)	T_2(ms)	T_1(ms)	T_2(ms)	T_1(ms)	T_2(ms)
White matter	510	87	1080	68	1220	38
Grey matter	760	119	1820	100	2132	49
CSF	2650	280	3817	207	4425	125

2.2.5.1 T_1-weighted imaging

The difference in T_1 relaxation times of tissues can be used to produce contrast in T_1 weighted image. To achieve this, a TR is selected which is short enough to ensure that the magnetization in neither water nor fat has had time to return back to equilibrium prior to the next excitation RF pulse. If the TR is too long, the magnetization in both water and fat recovers, tissues cannot be distinguished.

To maximize signal differences between tissues with different T_1 relaxation times, the TR must be short. To diminish the effects from T_2, the TE must be short. In practice, a T_1 weighted image is used to demonstrate the anatomy and is useful for segmentation particularly in the brain.

2.2.5.2 T_2-weighted imaging

In T_2 weighted image, the differences in the T_2 relaxation times depends on a correct choice of TE in a spin echo sequence. For T_2 weighting, the TE must be long to maximize the difference in T_2 decay times. Similarly, the TR must be long to diminish the effects from T_1. T_2 weighted imaging is used to demonstrate pathology as most pathology has an increased water content, resulting in hyperintensity on T_2 weighted images.

2.2.5.3 T_2^*-weighted imaging

T_2^* weighted imaging is useful when local magnetic field susceptibility differences between tissues are present. T_2^* relaxation indicates the decay of transverse magnetization seen in gradient echo sequence. The TE must be long to provide maximum dephasing in the measured signal. The flip angle must be small, and the TR must be long enough to limit saturation and T_1 weighting. The relaxation rate of T_2^* can be calculated by varying the echo time which has been found useful in the quantification of tissue iron content, since T_2^* contrast provides paramagnetic information with a sensitivity superior to T_1 and T_2, especially at high field MRI [18]. The GE sequence with T_2^* based contrast is used to detect haemorrhage, microbleeds, calcification, and iron deposition in tissues via susceptibility weighted imaging (SWI) or blood oxygenation level dependent (BOLD) in functional MRI.

2.2.5.4 Spin density (PD) weighted imaging

The difference in the proton density (a number of ^{1}H proton in tissue) determines the maximum level of magnetization that can be used to produce

contrast in PD weighted image. Tissue with low proton density appears dark (low signal) because the low number of protons result in a small component of transverse magnetization. Tissue with a high proton density appears bright (high signal) because the high number of protons result in a large component of transverse magnetization. For PD weighting, TR must be long to minimize saturation and T_1 effects, the TE must be short to minimize the T_2/T_2^* effects, and the flip angle must be *small* to produce minimum T_1 effects. PD was widely used for brain imaging to evaluate grey matter (GM) or white matter (WM) pathology (GM has a higher proton density than WM), however it has been replaced by Fluid-attenuated inversion recovery (FLAIR). In addition to brain pathology, PD provides excellent signal distinction between fluid, hyaline cartilage and fibrocartilage, which makes this sequence ideal for assessing of infectious and inflammatory joint diseases.

2.2.5.5 Magnetization transfer (MT)

Magnetization transfer imaging relies on interactions between bulk water protons and macromolecular protons. Water protons close to macromolecules are described as “bound”. They have a short T_2 corresponding to a broad resonance spectrum that dephases the MR signal. Applying a saturation pulse below the Lamor frequency, some of the protons in macromolecular pool can be supressed with little direct effect on the protons in the “free” water. Certain mechanisms such as chemical exchange and cross relaxation can transfer this saturation to the visible free water pool. Exchange between free water and bound water provides a unique contrast mechanism [19]. The magnitude of MT can be quantified by two sets of images (one with an MT pulse and no MT pulse) and then calculation of the magnetization transfer ratio (MTR)

$$MTR = \frac{M_0 - M_{sat}}{M_0} \qquad \text{Eq 2.43}$$

where M_0 is the magnitude of tissue signal prior to MT pulse and M_{sat} is the signal obtained following the saturation MT pulse. MT is used in MR angiography to attenuate the MR signal from brain parenchyma while enhancing signal from blood. Moreover, MT can be used to study of white-matter diseases such as multiple sclerosis (MS), breast imaging, knee or cartilage imaging [20].

2.2.5.6 Magnetic susceptibility

Magnetic susceptibility provides image contrast based on tissue magnetic properties. The magnetic susceptibility of a material (χ) is equivalent to the ratio of the magnetization within material to the applied magnetic field strength (B_0)

$$\chi = \frac{M}{B_0} \qquad \text{Eq 2.44}$$

Magnetic susceptibility can be classified as diamagnetic, paramagnetic and ferromagnetic depending on susceptibilities of a material. Biological tissues can be both diamagnetic or paramagnetic depending on their molecular contents. Magnetic susceptibility can be measured simultaneously with T_2^* using a multi-gradient echo sequence, and is strongly correlated with iron concentration in tissue [10-12]. There are numerous applications in quantifying iron content especially in deep brain nuclei, intracerebral haemorrhage and liver. Furthermore, quantitative susceptibility mapping has become a useful technique for the assessment of demyelinating disease such as multiple sclerosis [24].

2.2.6 Basic pulse sequences

In this section, basic MRI sequences are described.

2.2.6.1 Gradient Echo (GE)

Gradient echo imaging can be used for fast data acquisition by employing a short TR and small angle excitation due to the rapid reduction of magnetization [15]. There is no 180° RF pulse, rephasing is achieved by gradient reversal alone (Figure 2.2.9), which implies that the characteristics of signal are influenced by T_2^*

(not T_2). The GE sequences are primarily used for fast 2D and 3D acquisition of T_1 weighted images.

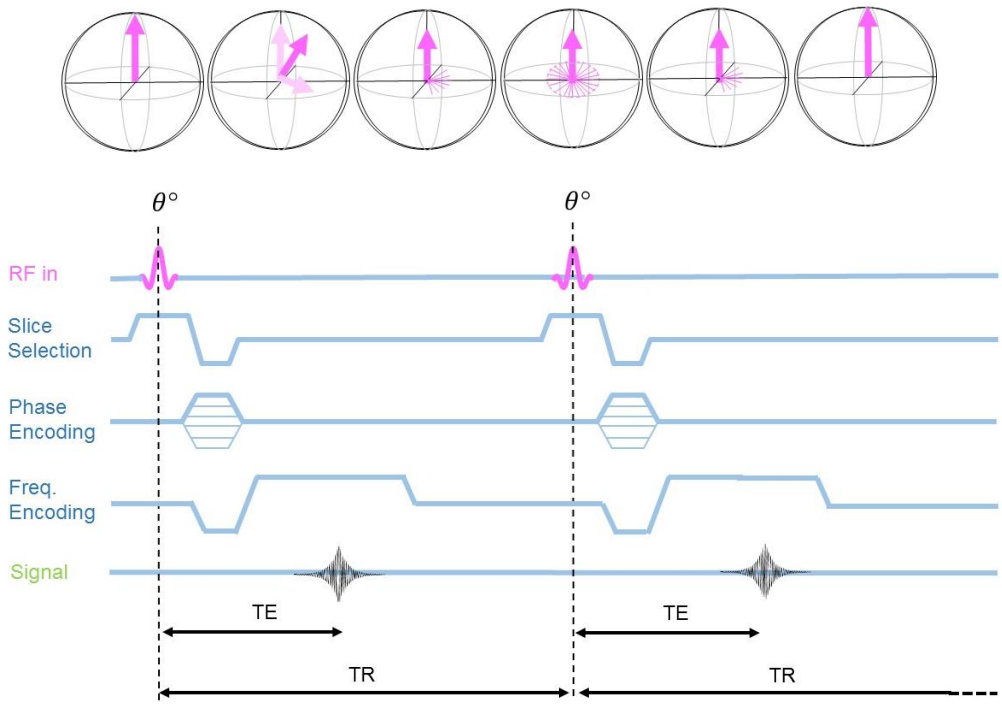


Figure 2.2.9: Schematic of a 2D GE pulse sequence, as there is no 180° pulse.

2.2.6.2 Spin Echo (SE)

Two-dimensional Fourier transform spin echo imaging is the mainstay of clinical MRI because SE pulse sequences are very robust, flexible, and allow the user to acquire images in which either T_1 or T_2 influences the grey values displayed in the MR images (T_1 or T_2 weighting) [13, 14]. Figure 2.2.10 shows the 2D SE pulse sequence which contains the following components:

Slice selection gradient (G_z) (lobes A and B) are applied together with both the 90° and 180° RF pulse. To restore dephasing of the 90° slice selection gradient (lobe A), the polarity of this gradient could be reversed immediately after its application. However, it is easier to extend the second gradient a little longer (lobe B), since a positive gradient after 180° pulse has the same effect as a negative gradient before the 180° pulse.

The phase encoding gradient ($\boldsymbol{G_y}$) (lobe C) applied before the measurement

$$\phi(y) = \gamma G_y y T_{ph} \qquad \text{Eq 2.45}$$

where T_{ph} is a constant time interval, representing the on-time of the phase encoding gradient (G_y), In practice, G_y has a variable amplitude

$$G_y = m g_y \qquad \text{Eq 2.46}$$

where m is an integer and g_y is constant step size.

$$k_y = \frac{\gamma}{2\pi} m g_y T_{ph} \qquad \text{Eq 2.47}$$

Each line of the phase encoding gradient (G_y) prepares the measurement of the different trajectories in the k-space.

The frequency encoding gradient ($\boldsymbol{G_x}$) (lobe E), during which the signal $S(t)$ is measured. To ensure an echo is acquired, a compensating gradient (lobe D) is applied before measurement, typically before 180°. So, a horizontal line centred around $k_x = 0$ is measured, as echo is acquired rather than FID to avoid phase artefacts.

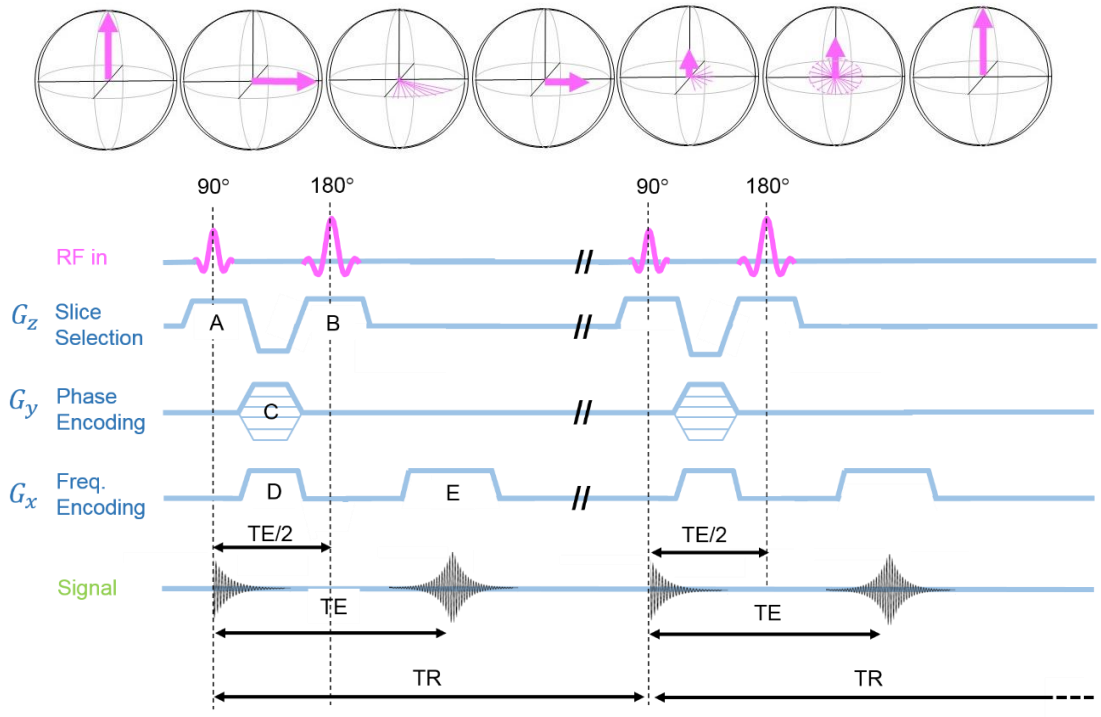


Figure 2.2.10: Schematic of a 2D spin echo pulse sequence

In the preceding 2D SE imaging sequence, typically 256 rows of k-space are measured by applying 256 phase encoding gradients and 256 samples per row are taken during one measurement. However, the spin density is a real function, the FT of the real function is Hermitian. Hence, it is in principle sufficient to measure half of the k-space, for example, for $k_y \in [-128,0]$. This is called half Fourier imaging. Although half Fourier imaging halves the acquisition time, this can cause artefacts in the reconstructed images particular where phase is changing rapidly.

2.2.6.3 Inversion recovery (IR)

After applying the 180° inversion pulse, the magnetization of tissue is flipped into $-z$ axis (opposite to B_0). During the inversion time (TI), delay before the application of the excitation pulses, the inverted magnetization recovers under T_1 relaxation toward $+z$ axis. Certain TI values result in selective signal suppression as the magnetization poses through M_Z = 0. Additional contrast effects are obtained by controlling TR and TE (Figure 2.2.11).

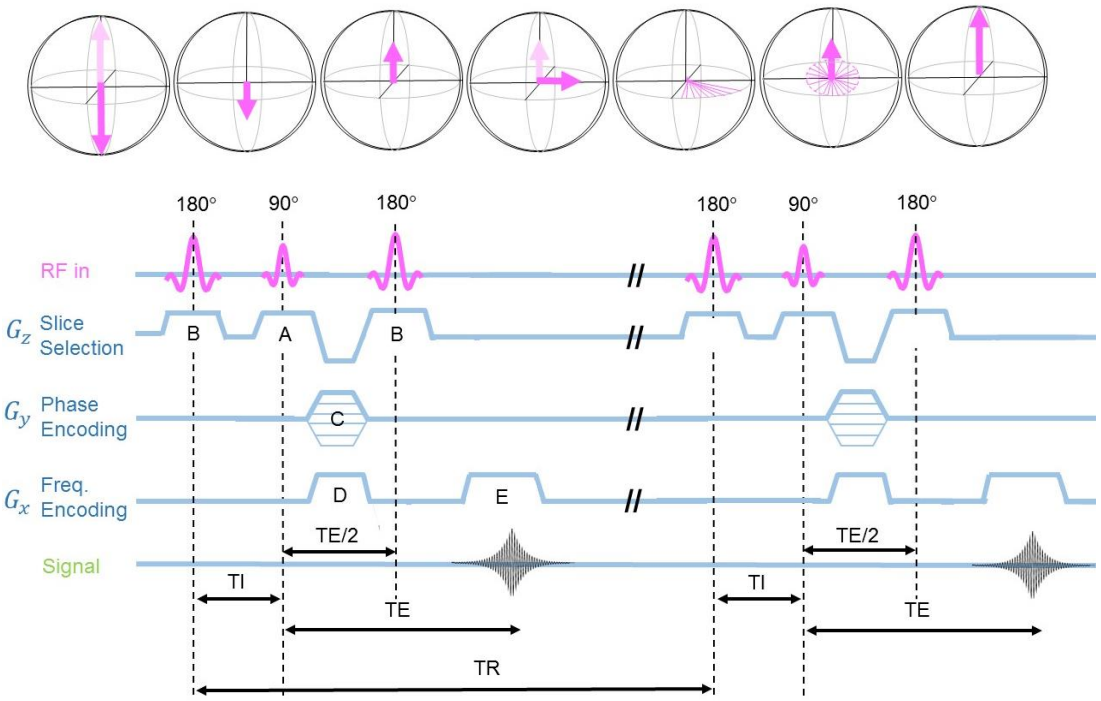


Figure 2.2.11: Schematic of inversion recovery (IR) pulse sequence.

The application of IR sequence can be used to suppress the signal from fat by selecting image readout at a time when the longitudinal recovery of fat is passing the null point. It is called short time inversion recovery (STIR). Another application is used to null the signal from cerebrospinal fluid (CSF) or fluids elsewhere in human body, called fluid attenuated inversion recovery (FLAIR). This can facilitate the visualization of tissues with no signal or flow artefacts from adjacent fluids. Further variants of IR sequence allow double inversion, so that signal from two types of tissue can be nulled [16].

2.2.7 Multislice and three-dimensional (3D) imaging

In MRI, there are two ways to acquire 3D data. The first method repeatedly acquires single slices with shifted slice position, by modulating the frequency of the RF excitation. All gradient waveforms remain unchanged. The centre of excited slice is determined by

$$Z_{slice} = \frac{\Delta f}{\gamma G_{ss}} \qquad \text{Eq 2.48}$$

where Δf is the offset frequency of the RF pulse relative to the resonance frequency at the isocentre. G_{ss} is the amplitude of slice selection gradient. The acquisition of multiple 2Dslices is commonly carried out an interleaved acquisition (Figure 2.2.12).

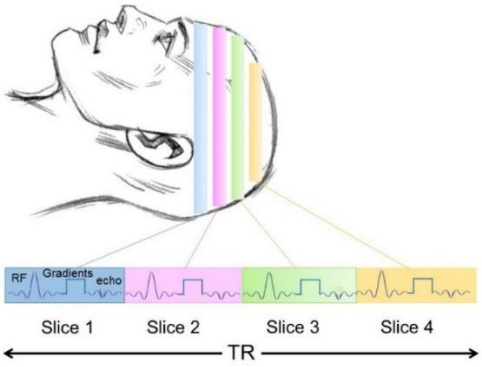


Figure 2.2.12: Interleaved acquisition of multiple 2D slices [1].

A different slice is excited, and data acquired during the deadtime between the end of data acquisition and the next excitation pulse for the previous slice. However, if a

short TR is required only a subset of echoes can be interleaved. In this way, after data acquisition, images are reconstructed by applying a separate 2D FT for each slice.

In 3D imaging, a volume is selected instead of a single slice. The z position is encoded by a second phase encoding gradient (ng_z)

$$\phi(y,z) = \gamma(mg_z yT_{ph} + ng_z zT_{ss}) \qquad \text{Eq 2.49}$$

where T_{ss} is the on-time of phase encoding gradient in the slice selection direction. The number of n corresponds to the different planes in the k-space. Thus, phase encoding is applied along both in-plane and slice (or through plane) directions (Figure 2.2.13), and image reconstruction is done by means of a 3D inverse FT. The SNR in 3D imaging is better than 2D imaging because each excitation acquires all spins in whole volume instead of a single slice. However, 2D imaging is better of a long TR is required.

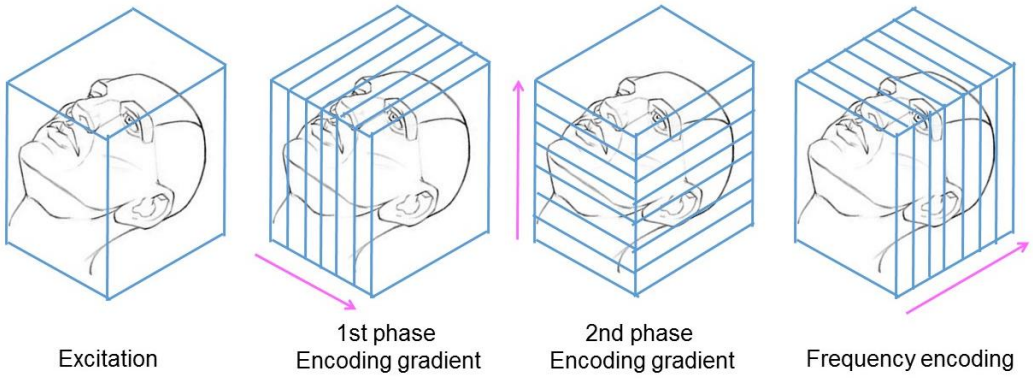


Figure 2.2.13: The procedure for creating a 3D image. An RF pulse excites the magnetization within a slab covering the middle of the head. Two directions are phase encoding separately. The first phase encoding procedure partitions the slab into slices, which are in the sagittal orientation. Each slice is resolved by a second phase encoding procedure and frequency encoding, similar to 2D Fourier imaging.

However, the drawback of 3D imaging is a long acquisition time causes sensitivity to motion. The acquisition time (T_{scan}) is equal to the number of excitations times.

- For 2D pulse sequence

$$T_{scan\ 2D} = N_{phase} \cdot N_{ac} \cdot TR \qquad \text{Eq 2.50}$$

- For 3D pulse sequence

$$T_{scan\ 3D} = N_{phase} \cdot N_{slice} \cdot N_{ac} \cdot TR \qquad \text{Eq 2.51}$$

where N_{phase} is the number of in-plane phase encoding. N_{phase} is the number of phases encoding within the slab selection. N_{ac} is the number of acquisitions.

2.2.8 Multiple echoes readout

Fast imaging sequences have been developed for multislice imaging and have in common that multiple lines of data are acquired following a single excitation pulse. This reduces the acquisition time. Typically 16 or 32 or more lines of data are acquired within each TR, but single shot acquisitions collected all lines are possible.

$$T_{scan\ 2D} = \frac{N_{phase} \cdot N_{ac} \cdot TR}{ETL} \qquad \text{Eq 2.52}$$

where ETL is echo train length (or the number of echoes per excitation). It can be seen from equation that the acquisition time can be decreased by decreasing TR, decreasing N_{phase} and increasing ETL.

A fast or turbo SE technique is a SE sequence in which multiple spin echoes are generated within the same excitation. After the first echo, a new phase encoding gradient is applied to select a different line in the k-space, a new echo is created. The k-space is divided into distinct segments. Within a single excitation, one line of each segment is sampled. Turbo SE technique is used to obtain T_2 weighted image of brain. For example, a 256x256 T_2 weighted image acquired with TR = 2500 ms and four segments, the acquisition time (T_{scan}) is 160 seconds (less than 3 minutes).

2.3 Summary

This chapter has outlined the knowledge of the physical principles of NMR that underly the MR imaging. The key concepts including physics overview, excitation, image formation and MR sequences have been described. The Bloch and image reconstruction mathematics are demonstrated. Finally, a review of imaging technique and how they influence image contrast and acquisition time is presented.

Bibliography

[1] D. D. Stark and W. G. Bradley, “Magnetic Resonance Imaging,” *Radiol. Technol.*, 2007.

[2] I. M. D. Dance, S. Christofides, M. Maidment, “Diagnostic Radiology Physics: A handbook for teachers and students,” *IAEA*, 2014.

[3] F. Bloch, W. W. Hansen, and M. Packard, “The nuclear induction experiment,” *Phys. Rev.*, 1946.

[4] E. Purcell, H. Torrey, and R. Pound, “Resonance Absorption by Nuclear Magnetic Moments in a Solid,” *Phys. Rev.*, 1946.

[5] I. I. Rabi, N. F. Ramsey, and J. Schwinger, “Use of rotating coordinates in magnetic resonance problems,” *Rev. Mod. Phys.*, 1954.

[6] E. M. Haacke, R. W. Brown, M. R. Thompson, and R. Venkatesan, *Magnetic Resonance Imaging: Physical Principles and Sequence Design*, vol. 1st. 1999.

[7] A. G. Redfield, “The Theory of Relaxation Processes,” *Adv. Magn. Opt. Reson.*, 1965.

[8] K. N. Shrivastava, “Theory of Spin–Lattice Relaxation,” *physica status solidi (b)*. 1983.

[9] B. J. MacIntosh and S. J. Graham, “Magnetic resonance imaging to visualize stroke and characterize stroke recovery: A review,” *Front. Neurol.*, 2013.

[10] P. C. Lauterbur, “Image formation by induced local interactions: Examples employing nuclear magnetic resonance,” *Nature*, 1973.

[11] R. Mezrich, “A perspective on K-space.,” *Radiology*, 1995.

[12] Y. Zhang, H. P. Hetherington, E. M. Stokely, G. F. Mason, and D. B. Twieg, “A novel k-space trajectory measurement technique,” *Magn. Reson. Med.*, 1998.

[13] E. L. Hahn, “Spin Echoes,” *Phys. Rev.*, 1950.

[14] M. A. Bernstein, K. F. King, and X. J. Zhou, *Handbook of MRI Pulse Sequences*. 2004.

[15] A. D. Elster, “Gradient-echo MR imaging: techniques and acronyms.,” *Radiology*, 1993.

[16] G. M. Bydder and I. R. Young, “Mr imaging: Clinical use of the inversion recovery sequence,” *J. Comput. Assist. Tomogr.*, 1985.

[17] W. R. Nitz and P. Reimer, “Contrast mechanisms in MR imaging,” *European Radiology*. 1999.

[18] G. B. Chavhan, P. S. Babyn, B. Thomas, M. M. Shroff, and E. M. Haacke, “Principles, techniques, and applications of T2*-based MR imaging and its special applications.,” *Radiographics*, 2009.

[19] D. F. NORDENBERG, J. M. PRAGER, J. D. ROSENBLUM, and M. M. TOMIAK, “MAGNETIZATION TRANSFER CONTRAST,” *Invest. Radiol.*, 1992.

[20] R. M. Henkelman, G. J. Stanisz, and S. J. Graham, “Magnetization transfer in MRI: A review,” *NMR in Biomedicine*. 2001.

[21] A. Deistung, F. Schweser, and J. R. Reichenbach, “Overview of quantitative susceptibility mapping,” *NMR in Biomedicine*. 2017.

[22] E. M. Haacke, S. Mittal, Z. Wu, J. Neelavalli, and Y. C. N. Cheng, “Susceptibility-weighted imaging: Technical aspects and clinical applications, part 1,” *American Journal of Neuroradiology*. 2009.

[23] S. Mittal, Z. Wu, J. Neelavalli, and E. M. Haacke, “Susceptibility-weighted imaging: Technical aspects and clinical applications, part 2,” *American Journal of Neuroradiology*. 2009.

[24] J. Duyn, “MR susceptibility imaging,” *J. Magn. Reson.*, 2013.

Chapter 3 Ultra High Field Strength 7.0 Tesla MRI

3.1 Introduction

The move to 7.0 T is driven by the significant improvements available in signal-to-noise ratio (SNR), contrast-to-noise ratio (CNR), spatial resolution and susceptibility contrast which have the potential to provide increased details of pathological conditions to personalise disease management. But transition to 7.0 T comes with substantial technical challenges including inhomogeneity of B_0 and B_1 fields, radiofrequency (RF) coil design, tissue heating, and adverse effects resulting from the static field exposure. Table 3.1 outlines the promises and challenges when moving B_0 field strengths from 3.0 T to 7.0 T. and the following sections will explain these issues in more details.

7.0 T MRI is currently used for research purposes although the U.S. Food and Drug Administration (FDA) cleared in Siemens scanner for clinical use in 2017. One of the great challenges is to encourage physicians to investigate the potential for this complex technology in clinical practice. I reviewed the studies published between January 2014 to September 2018 with three different databases including Pubmed, Embase, and Ovid. The key words “7.0 T MRI” and “neuroimaging” were used. I excluded studies not written in English and considered scientific papers only. It is apparent from Figure 3.1.1 that the number of publications has increased every year.

Table 3.1: The pros and cons of increasing field strength from 3.0 T to 7.0 T although the consequences may depend on technical and anatomical details [1].

Trend as increased (B_0)		Pros	Cons
Static field	↑ MR signal	Higher SNR Higher resolution Shorter scan time	
Susceptibility	Shorter ↑ SWI ↑ BOLD signal	New contrast in phase images and SWI	Geometric distortion Intravoxel dephasing
Relaxation	Longer T_1 (Stronger suppression background tissue)	ASL, TOF, cardiac	Longer scan time
	Shorter T_2	Increased spectral linewidths in ^1H MRS	DWI, DTI
	Shorter T_2^* (required shorter TE to compensate the signal loss)	SWI, BOLD	
RF homogeneity	↓ RF (unwanted spatially varying contrast)	Parallel reception, Parallel transmission	Position-dependent flip angle (FA), poor inversion, unexpected contrast
Others	↑ Chemical shift (Improved spectral quantification)	Fat saturation, CEST, MRS	Fat/water and metabolite misregistration
	Adverse physiological effects		Dizziness, nausea, vertigo
	SAR (increased RF power deposition)		Fewer slices, smaller FA, Longer TR, breath hold

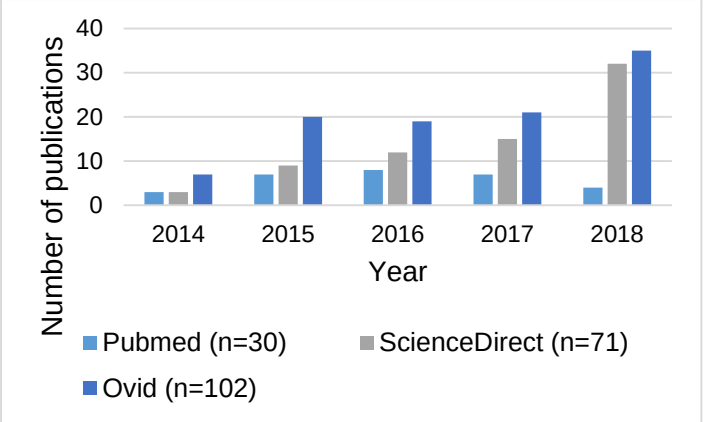


Figure 3.1.1: The studies of 7.0 T MRI in neuroimaging published between 2014 and September 2018 from three databases.

3.2 The benefits

As indicated previously, the move to 7.0 T is driven by the scaling of some fundamental physical properties with increased field strength.

3.2.1 Signal to noise ratio (SNR)

This ratio compares a level of signal amplitude relative to noise amplitude and determines the ultimate sensitivity of the images. Figure 3.1.2 demonstrates the improved SNR at higher field strength. The SNR is approximately proportional to main magnetic field (B_0) as

$$SNR \propto B_0 \qquad \text{Eq 3.1}$$

The thermal equilibrium spin polarization for nuclei is defined as

$$\rho_0 \frac{\gamma^2 \vec{h}^2 I(I+1)}{3kT} B_0 \qquad \text{Eq 3.2}$$

where ρ_0 is the spin density, γ is the gyromagnetic ratio, $\vec{h}$ is the Plank constant divided by 2π, k is the Boltzmsnn's constant, T is the absolute temperature and I is the spin nuclear number. The thermal equilibrium spin polarization depends directly on the static magnetic field strength. In practice, other factors such as coil design will affect variation in SNR and B_0. The increased SNR can be used to increase spatial resolution since $SNR \sim voxel\ volume$. The improved SNR can alternately be used to reduce acquisition time, since $SNR \sim (t_{scan})^{1/2}$.

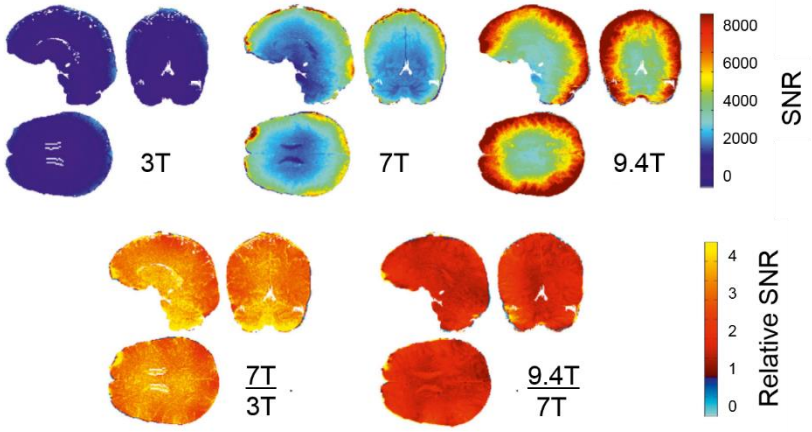


Figure 3.1.2: SNR distributions and relative SNR differences between magnetic field measured over three slices in the same subject at 3.0 T, 7.0 T and 9.4T, respectively [2].

3.2.2 Susceptibility effect

Local variations in magnetic properties produces susceptibility contrast within human tissue for characterizing pathological changes between normal appearing brain tissue and disease. This is manifest as a phase shift in the NMR signal. However, local field B_0 variations produced at tissue boundaries such as soft tissue-air and soft tissue-bone also lead to reduced T_2^*. The susceptibility variation (χ) measured in ppm is independent of B_0 field strength, but the field shift depends on B_0 field. Thus, the frequency shift is

$$\Delta f = \frac{\gamma}{2\pi} \Delta B = \frac{\gamma}{2\pi} \chi B_0 \qquad \text{Eq 3.3}$$

Susceptibility weighted imaging has been used in the human brain in microvascular disease, multiple sclerosis, epilepsy, dementia, Alzheimer's disease, Parkinson's disease and other neurodegenerative diseases because of the sensitivity to deoxygenated blood, myelination and the chemical changes. Moreover, some groups applied susceptibility imaging to other organs such as the heart and liver for additional tissue characterization and quantification of blood oxygenation [3].

3.2.3 Chemical shift

The chemical shift measured in hertz (Hz) is proportional to B_0 field strength which can be calculated as

$$\vec{B}_i = B_0(1 - \sigma_i) \qquad \text{Eq 3.4}$$

where σ_i is shielding constant, which depends on the chemical environment of the proton. Chemical shift is the basis of MR spectroscopy. Thus, the resonance is

$$\omega = \frac{\gamma}{2\pi} B_0(1 - \sigma) \qquad \text{Eq 3.5}$$

Chemical shift measurements are described in parts per million (ppm) to make them independent of B_0 field strength

$$\delta_i = (\omega_i - \omega_{ref})/\omega_{ref} \qquad \text{Eq 3.6}$$

where ω_i is the NMR frequency of a particular proton and ω_{ref} is the NMR frequency of a reference compound. The frequency difference $(\omega_i - \omega_{ref})$ is generating around a few hundred to a few thousand hertz (Hz), while the reference frequency (ω_{ref}) is measured in MHz.

The water fat-shift is much more significant at higher field strengths. At the Larmor frequency, water and fat protons resonate at different frequencies that cause different chemical shifts. The average chemical shift difference between water and fat is about 3.3-3.5 ppm. This is equivalent to 140-150 Hz per Tesla. Therefore, at 3.0 T water resonates at the Larmor frequency approximately 420-440 Hz higher than fat. Figure 3.1.3 show the impact of field strength on chemical shift in the ^{1}H spectrum in human brain [4], where 7.0 T provides better separation of the peaks and increased metabolite quantification at higher magnetic field.

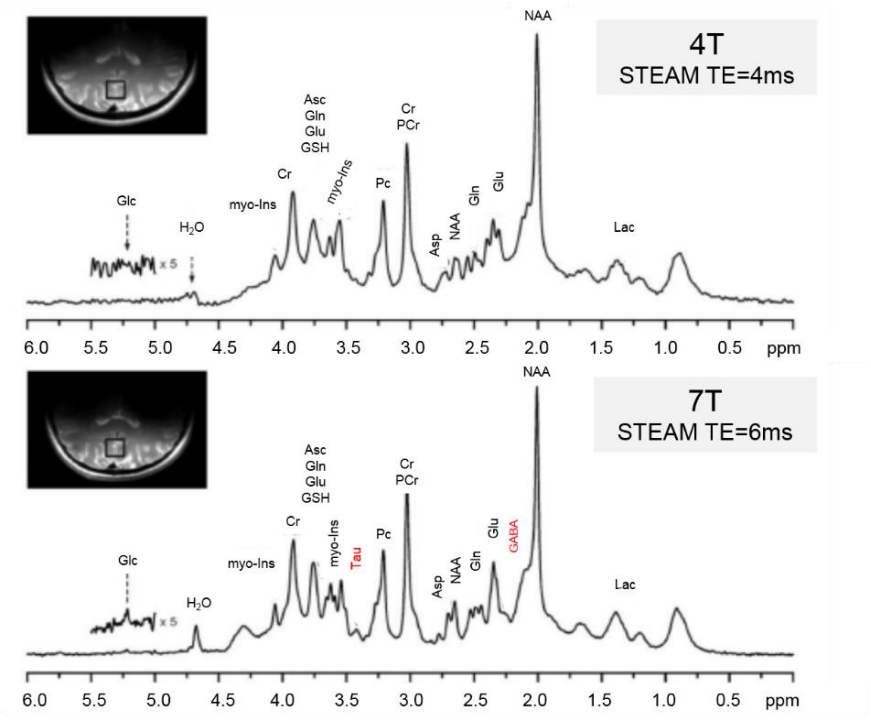


Figure 3.1.3: The ^{1}H NMR spectrum *in vivo* from occipital lobe at 4T and 7.0 T.

3.2.4 Longitudinal relaxation time (T_1)

With increasing B_0 field, T_1 relaxation time increases in tissues such as brain parenchyma and CSF. Longer T_1 relaxation time enhances signal from inflowing blood and background suppression in time-of-flight (TOF) angiography. Moreover, increases in T_1 relaxation time also improve arterial spin labelling (ASL) perfusion technique. Protons in blood are magnetically labelled and imaged as intrinsic tracer. Longer T_1 of blood results in magnetic labelling lasts for longer period of time and increased SNR at 7.0 T. Improved background suppression in contrast enhanced angiography also leads to improve visibility of blood vessels at 7.0 T. As result, the amount of contrast media administration is significantly reduced in some cases.

3.2.5 Parallel imaging

Parallel imaging is the major interest at ultrahigh field MRI where more local coil profiles and high intrinsic signal-to-noise ratio allows the chance to reduce scan time. The technique provides improved temporal resolution in dynamic imaging and

shorter echo times leading to reduced distortion in multiecho imaging at high field The Philips MR scanner at Nottingham equipped with SENSitivity Encoding "SENSE" (see chapter 4 and 5).

3.3 The challenges

3.3.1 Radiofrequency field (B_1) and electric field (E)

The Larmor frequency is given by γ_ω so the wavelength of the RF field used in MRI is given by

$$\lambda = \frac{c}{2\pi\omega} = \frac{c}{2\pi\gamma B_0} \qquad \text{Eq 3.7}$$

where the speed of light in tissue is given by $\frac{C_0}{\sqrt{\varepsilon\mu}}$ and C_0 is speed of light in a vacuum. Therefore

$$\lambda \propto \frac{1}{\sqrt{\varepsilon} B_0} \qquad \text{Eq 3.8}$$

Since the electric permeability (ε) slightly decreases with increasing frequency, wavelength in tissues is reduced (Figure 3.1.4).

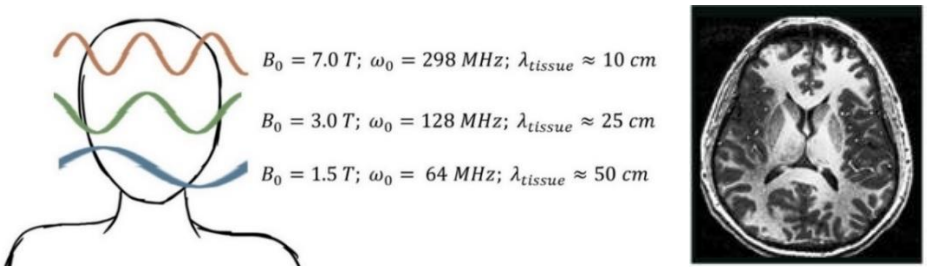


Figure 3.1.4: Comparison RF wavelength in tissues at different frequency of protons for static magnetic field of 1.5 T, 3.0 T and 7.0 T, respectively (left). A typical dielectric effect appears as a brightening in human head at 7.0 T (right).

Spatial variation in the magnitude and phase of the B_1 and E field components of the transmitter RF field are caused by reduced RF wavelength at 7.0 T. Spatial variations in field B_1 influence the MR signal and image contrast. The variation in E field affects power deposition and heating of tissue. B_1 fields can be mapped but E fields can only be estimated by modelling (see section 3.3.2). A technique attempts to minimize variations in field B_1 is explained further in the next section.

3.3.2 RF power deposition

The B_1 field used in MRI creates an electromagnetic field in the human body which causes power deposition. The RF power deposition is measured by the specific absorption rate (SAR) in Watts per kilogram (W/kg). At ultrahigh field MRI, the SAR value approximately scales as

$$SAR \sim B_0^2 \alpha^2 \sim \omega_0^2 B_1^2 \qquad \text{Eq 3.9}$$

where B_0 is the magnetic field, α is the flip angle, and ω_0 is the NMR frequency. The calculation of SAR is as follows

$$SAR = \int \frac{\sigma(r)|E(r)|^2}{\rho(r)} dr \qquad \text{Eq 3.10}$$

where E is the electric field, σ is the electric conductivity, and ρ is the density of tissue. In a simple model (quadrature coil), the RF power deposited in the tissue increases at higher field strength. A high value is found at the centre of brain and significantly lower along the periphery of the brain. SAR is useful for pulse sequence design because high flip angles or short TR causes increase in body temperature. SAR is limited both globally and locally (10-g averaged) according to the International Electrotechnical Commission (IEC) guidelines. However, local SAR cannot be assessed *in vivo* with sufficient accuracy. The electromagnetic simulations must be conducted to compute local SAR distribution and assess patient safety. Model of human head in a quadrature head coil with birdcage design was used for SAR calculation. The simulation results of B_1field maps and SAR distribution between 1.5 T and 7.0 T are also presented in Figure 3.1.5.

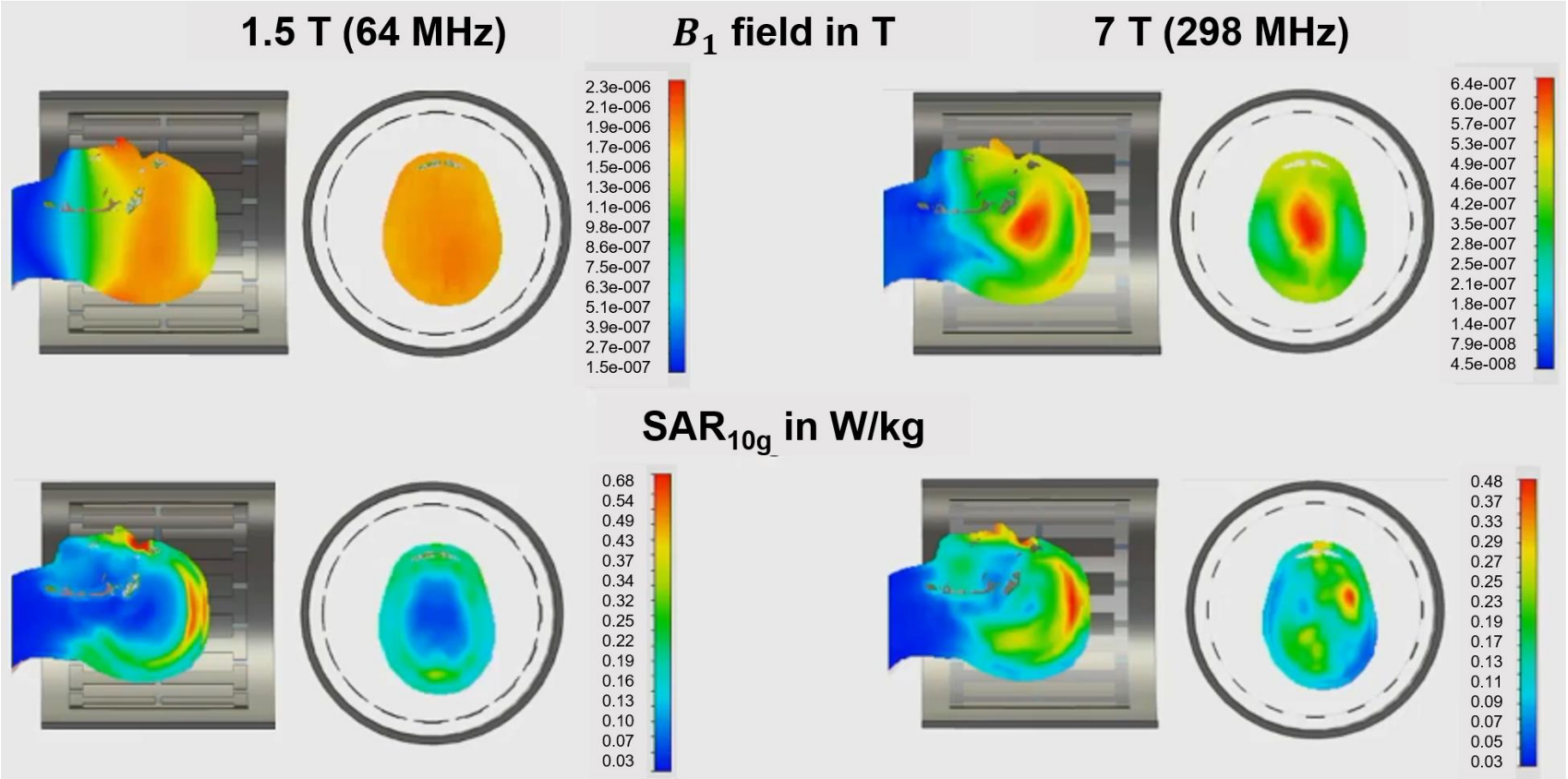


Figure 3.1.5: B_1 field maps and SAR results from EM simulation showing RF power deposited in the tissue increases at higher field strength 7.0 T compared with 1.5 T [5].

The 7.0 T MRI used the same SAR regulation as at lower field strength. With respect to RF exposure, the limits for significant risk are shown in Table 3.2.

Table 3.2: Limits for global and local SAR as recommended by the FDA and IEC.

Significant risk criteria from FDA			
Global SAR	Maximum SAR value (W/kg)		
• Whole body (averaged over 15 minutes)	4		
• Head (averaged over 10 minutes)	3		
Significant risk criteria from IEC			
IEC has three level with values of a 6-minute average	Operating mode		
	Level 0 (normal)	Level I (controlled)	Level II (controlled)
Global SAR	Maximum SAR value (W/kg)		
• Whole body	2	4	> 4
• Partial body	2-10	4-10	> 4-10
• Head	3.2	3.2	> 3.2
Local SAR	Maximum SAR value (W/kg)		
• Head	10	20	> 20
• Extremities	20	40	> 40

3.3.3 Subject acceptability

The biological effects produced by a strong magnetic field include vertigo, metallic taste, nausea, light flashes, nerve stimulation, acoustic noise level, and discomfort. These phenomena depend variously on field strength, gradient of field, and movement of the field, but the effects differ between subjects. Magnetic-field associated nausea and vertigo are caused by interactions with the vestibular system [7, 8]. Details of the health effects associated with MRI exposure will present in the section 3.5.

3.4 Solutions

Addressing the B_1 field inhomogeneity at 7.0 T

3.4.1 B_1^+ shimming

The B_1 field inhomogeneity has historically been reduced by using adiabatic RF pulses. Effects of these pulses depend primarily on the phase rather than amplitude variation of the pulse but required a high RF power. Recently, parallel transmission with different RF pulse on multichannel transmission (Multix) has been proposed and made available. The idea of Multix is to use a transmit array with independent magnitudes and phases on each channel that can be manipulated to control and improve the homogeneity of RF excitation. A gradient echo sequence was used to produce a B_1 sensitivity map per channel (Figure 3.1.6).

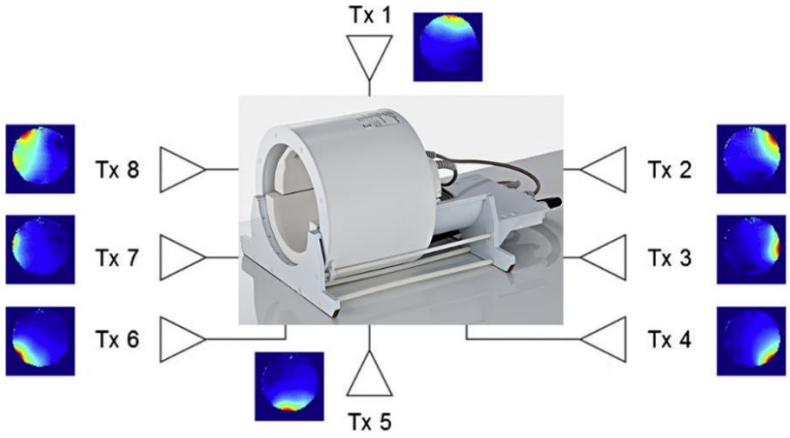


Figure 3.1.6: The 8-channel RF transmission head coil showing B1 maps from each channel.

In Figure 3.1.6, the power on each transmit element can be tailored to achieve uniform RF excitation. The net B_1 field is the summation of subfields produced by each element where N_T is number of channels

$$B_1^+(r,t) = \sum_{i=1}^{N_T} B_{1,j}^+(r,t) \qquad \text{Eq 3.11}$$

However, the component of $B_{1,i}^+$ can be separated as

$$B_1^+(r,t) = \sum_{i=1}^{N_T} p_i(t)\, s_i(r) \qquad \text{Eq 3.12}$$

where $s_i(r)$ is the transmit sensitivity map of channel and $p_i(t)$ is the RF pulse applied through the i^{th} transmitter. For the same RF pulse waveform on each channel, the channel-specific weights can be used

$$B_1^+(r,t) = p_i(t) \sum_{i=1}^{N_T} w_i \, s_i(r) \qquad \text{Eq 3.13}$$

where $p_i(t)$ is the common pulse slope transmitted on each channel and w_i is weighting factor for each channel i. An example problem formulation for RF shimming is

$$min_w \|Sw - b\|^2 \qquad \text{Eq 3.14}$$

where w is a map of complex weights, S is the sensitivity matrix which is created from the B_1^+ field of all channels in a user-defined ROIs, and b is a map of the target transmit field distribution. On the 7.0 T MR Philips scanner at Nottingham both dual channel and Multix (8-channel) RF transmission systems are available.

This method is beneficial for localized excitation in small target volumes such as prostate [8] whereas in larger target volume such as heart, liver, kidneys, or whole brain, it does not generally yield significanty improvement. On the other hand, Schmitter et al. [9] found that using multi-channel transmit B_1 shimming improved image quality and reduced RF pulse energy in cardiac imaging at 7.0 T. Time-interleaved acquisition of modes (TIAMO) [10, 11] can also be used to improve a nonuniform transmit B_1 field. This method acquires two identical scans with two complementary shim solutions (different B_1 weights). The two images are combined using Open-GRAPPA reconstruction to generate a single image with less B_1 variation, less signal dropout, and better image contrast. This yields sufficient signal homogeneity at 7.0 T even in large targets such as abdominal imaging [12], extremity imaging [13], or brain imaging at 9.4 T [14]. In addition, using spoke RF pulses for the slice selective case [15] or kt-pulses for the non-slice selective case [16] are very favourable trade-off for the B_1 mitigation. Both pulses contain B_1 shim sub-pulses and gradient blips in between sub-pulses. Combined B_1 shimming and

gradient blips provide improved uniformity within the target volume compared to B_1 shimming alone. Most applications target the brain [14-18] but body imaging has also been investigated [3, 19].

3.4.2 Dielectric pads

These provide a simpler approach to mitigate B_1 inhomogeneity. Dielectric pads are made from suspensions of high permittivity material such as calcium titanate ($CaTio_3$) powder in deuterated water (Figure 3.1.7), materials which are widely available at low cost. The pads can be used to tailor the B_1 distribution and increase the homogeneity of the magnetic component of RF transmit field [20-22]. When the dielectric pads are placed beside the head, there is the significant increase in transmit field (B_1) in the temporal lobes, where signal dropout is typically observed. The properties of these suspensions are; (i) a high permittivity between 100 and 120 for the calcium titanate, (ii) a low background signal from short T_2 and T_2^*, (iii) a fully eliminated background signal from deuterated water, (iv) stable suspension. The T_1 value of the dielectric pads is 110 ms, T_2 value is 12 ms and T_2^* value is less than 2 ms [23].



Figure 3.1.7: Dielectric pads consisting of a suspension of $CaTio_3$, used at 7.0 T.

3.5 Biological effect and safety consideration

A number of the side effects associated with MRI are given in Table 3.3. Possible hazards can be categorized as acute and subacute and details of adverse effects associated with MRIs are given in the following section.

Table 3.3: An overview of MRI-related harm, hazards and causes.

	Physical cause	Consequence	Potential harm
Magnet	- Superconductivity loss - Influence of static magnetic on metal objects - Exposure to magnetic field	- Quench, Helium release - Projectile effect - Vertigo, Dizziness, Nausea	- Damage the magnet coils - (Severe) injury - Discomfort
Gradient	- Rapid changes of current with the gradient coils - Currents generated in the body by a function of the gradient strength and rise time	- Lorenz forces are generated - Peripheral nerve or muscle stimulation	- Acoustic noise - Unpleasant or painful at higher levels
RF	- RF induced currents	- Thermal effects of RF for the body	- Tissue heating and burns

3.5.1 Static magnetic field (B_0)

The currents generate oscillatory Lorentz forces when a static magnetic is present. Increased electromechanical forces and torques are described by the cross product of the main magnetic field vector (B_0) and the current vector (I)

$$dF = dl \cdot (B_0 \times I) \qquad \text{Eq 3.15}$$

When currents are flowing in a conductor that is oriented in any direction except for parallel to B_0 field, Lorentz forces are generated perpendicular to B_0 and on the conductor direction [35].

The main safety issue related to the main field is the magnetic force which can make projectiles from equipment and objects containing ferromagnetic materials and have effects on implants. The projectile force is high near the bore and is much stronger at higher field MRI. It is important to note that all equipment and objects to be used near the strong magnet need to be tested, and controlled zones should be defined within the MRI facility for site access restriction. The 5

Gauss line defines the border of an area in which the magnetic field could affect implanted devices such as pacemakers, and it is sometimes outside the RF-shield room. There is a publication [24] and useful website maintained by F. Shellock [25] which describes the MR safety check for implantable devices before exposing a patient with an implant to an MRI scan.

As mentioned earlier, the interaction of a static magnetic field with the human body can cause various biological effects. However, no clinically significant changes in blood pressure, cardiac output, heart rate and vital signs are presented in subjects exposed to MRI up 8.0 T [26, 27]. A study by Rauschenberg et al. [6] found that only 1% of participants reported unwillingness to undergo a further MRI examination at ultrahigh field. The most regular complaints include scan duration, acoustic noise and need to stay still during MRI scan. All sensory effects are usually avoided by moving slowly in the magnetic field. Another well-known effect at ultrahigh field MRI is distortion of detected an electrocardiogram (EKG), but this is an artefact. It does not represent a change in cardiac elevated behaviour. As shown in Figure 3.1.8, the magnetohydrodynamic effect can be induced an elevated T-wave in the EKG signal leading to false detection of the R-peak and difficult to image correctly [28].

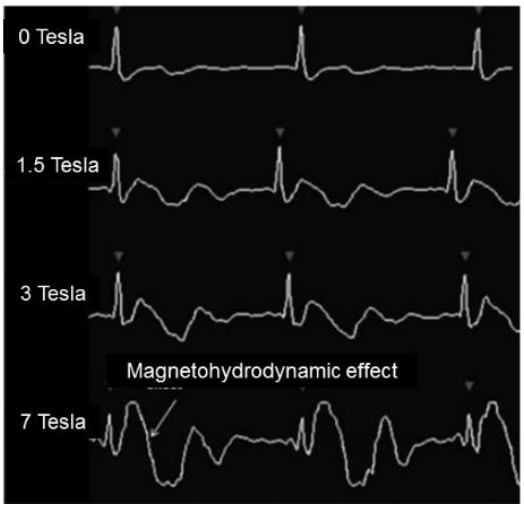


Figure 3.1.8: Example of electrocardiogram (EKG) signal from 0 T to 7.0 T MRI.

3.5.2 Time-varying magnetic field gradient (dB/dt)

Gradient field considerations involve peripheral nerve stimulation (PNS) and sound pressure level. PNS is major limitation factor in gradient performance. PNS arises from rapid switching of strong gradients. This effect is greatest when high resolution imaging at 7.0 T with large bandwidth over FOV is acquired. The switched gradient fields induced currents in the body which can cause involuntary nerve stimulation. These include muscle twitching and causing pain at high levels of stimulation. A degree of nerve stimulation depends on the design of gradient system, switching rates of the gradient, and gradient waveform. The design of gradient coils size and the position in the magnet bore determine PNS thresholds [29]. High PNS effect is found when decreasing linear region length, decreasing gradient coils size, or both. As a result, dedicated gradient coils for human imaging has been developed to try to limit this effect. The gradient coil design at 7.0 T is similar to 3.0 T so the effect should be similar except that there is a temptation to scan faster at 7.0 T, reducing bandwidth can increase PNS.

The vibrations of gradient coils produce loud acoustic noise requiring hearing protection for an MRI scan. In conventional clinical MRI system, sound pressure levels (SPL) is limited below 100 dB, but certain pulse sequences may produce noise levels exceed the limit value which needs to be aware. The forces increase with field strength although the acoustic noise may not solve in a simple way since the magnetic design is so different.

3.6 Instrumentation

MR systems have three main components. A static magnet, time vary gradient field, and RF transmit/receive system (Figure 3.1.9) all controlled by a spectrometer. The static magnet generates a strong and highly homogeneous magnetic field as $B_z = B_0$ via superconducting material. The gradient coils generate

a magnetic field gradient $(G_x, G_y, G_z) = \left(\frac{dB_z}{dx}, \frac{dB_z}{dy}, \frac{dB_z}{dz}\right)$. The RF coils tuned to the NMR frequency generate a linearly or circularly polarised RF field orthogonal to B_0. Although the transmit coil ideally generates a uniform field in the body, a local coil needs to be used due to inhomogeneity of transmit field presents at 7.0 T. Receive coils generally produce a more localised fields and provide higher sensitivity. The basic hardware components including their interaction and function will be explained briefly in the following section.

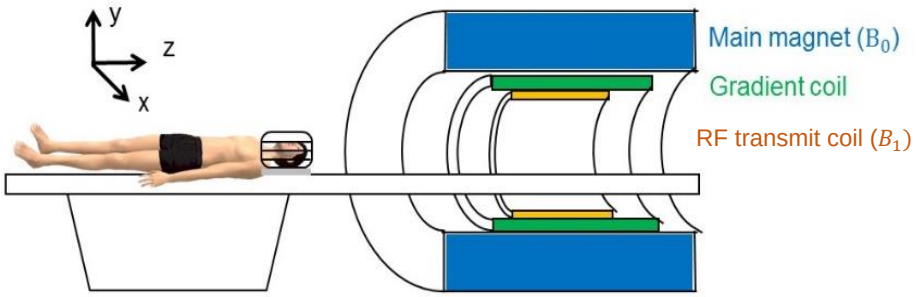


Figure 3.1.9: MR system components showing the relative locations of the main magnet in the z-direction, gradient coils used to produce linear field gradients along x, y and z direction, integral RF transmitter (body) coil and head coil used for RF excitation and detection MR signal.

3.6.1 Main magnet

Most MRI magnets have superconducting coils which includes a pair of solenoid Helmholtz coils to create a strong and homogeneous magnetic field. MR scanners are mainly classified into two types; open-bore and closed-bore system (Figure 3.1.10). Most scanners worldwide used the closed-bore cylindrical design to generate the field by passing current through a solenoid Helmholtz coils at superconducting temperature.



Figure 3.1.10: Two types of MRI scanners: open bore (left) and closed bore (right).

A modern 7.0 T magnet uses actively shielded superconducting (niobium titanium: NbTi) with a total footprint approximately 5 m radially and 8 m axially. Magnet bore is approximately 55-60 cm and bore length is about 2.7-3.0 m (Figure 3.1.11). The weight has reduced compared to the first generation passively shielded 7.0 T magnets was used at Nottingham. In the future, we may see these magnets equipped with zero helium boil-off technology lead to reducing helium consumption.



Figure 3.1.11: The 7.0 T MRI from the three major commercial MRI vendors.

The coils are placed in liquid helium to enable superconducting operation which ensures high temperature stability. This design maintains a uniform field along the z-axis (B_0 direction), minimizes fringe fields at the end of MR scanner, and improves field homogeneity. However, there remains small fluctuations in field strength. By increasing their capabilities, main magnets were delivered with shim coils where correctional fields of known geometry were made for inherent inhomogeneity of the magnet. Shimming methods can be broadly classified into passive (using magnetic material placed in a magnet at the time of installation to

create the B_0 field as uniform as possible) and active (using currents controlled by specialized circuity to produce corrective magnetic field).

A common design for passive shimming uses of multiple trays with metallic shims arranged symmetrically around the circumference of the magnet. The advantage of passive shimming is that high order spherical harmonics can be used. On the other hand, passive shimming has disadvantages such as temperature sensitive, field shifts when the bore heats, requiring replacement and/or reposition. Although most vendors use passive shims to create a more uniform B_0, active shim coils are commonly used to provide individual correction from subject to subject [30]. Magnetic field distortion induced by the subject during a scan, can be controlled by active shimming technology.

Active shimming is driven by resistive shim coils located between primary and secondary gradient coils which can be controlled actively. The theory of active shimming is based on spherical harmonics function. To investigate distortion, B_0 field maps are acquired using dual or multi gradient echo sequences with low resolution over region of interest. Then, an optimal shim field is computed from the shim coils presented. Most MR scanners have standard configuration of static first and second order spherical harmonic shims to mitigate B_0 fluctuations. Simulations and experimental results by Stockman and Wald [31] show great benefit to compensating for B_0 inhomogeneity by increasing the spatial order of shim fields and dynamic shimming beyond global static shimming.

3.6.2 Field gradients

The maximum gradient available on a Philips 7.0 T Achieva system at University of Nottingham is 40 mT/m with a maximum slew rate of 200 T/m/s. This is significantly lower than maximum gradient strength of the gradient systems of modern 3.0 T systems. The maximum gradient strength used in the Human Connectome Project is about 100-300 mT/m [32, 33]. However, new 7.0 T gradient

coils with strengths above 100 T/m may be possible in the future [34]. Alternatively, head insert gradient coils might be attractive for brain applications due to smaller exposed area, lower electric fields and therefore lower PNS levels.

The main reason for the lower gradient strength at 7.0 T is that Lorentz forces on the current carrying conductor in the gradient coils are larger at 7.0 T. These forces cause gradient coil vibrations which create displacement of gradient coil surface. This vibration may induce motion artefact on images and generate higher acoustic noise level well exceeding 100 dB. The example of gradient systems at 7.0 T is shown in Figure 3.1.12

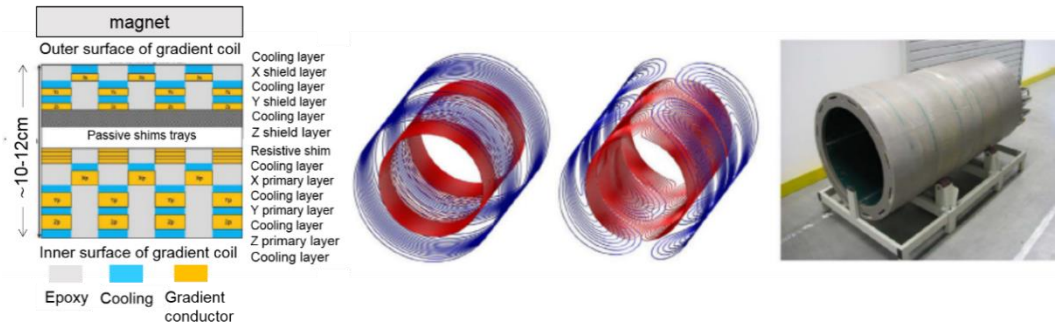


Figure 3.1.12: Gradient systems with a typical gradient plate layout; cross-section of gradient coil (left), typical wire path for z gradient consists of inner primary layer in red and outer shield layer in blue (middle left), typical wire path for transverse xy gradient consists of inner primary layer in red and outer shield layer in blue (middle right), and gradient coil cylinder potted in epoxy (right), respectively [36].

3.6.3 Radiofrequency (RF) system

As discussed above, the 7.0 T system benefits from access to two multichannel transmit systems in which individual transmit channels are separately controlled by a custom RF shimming set up including SAR supervision (section 3.4.1). In fact, it can operate in quad, 2 channel, or 8 channel transmit modes, always with a 32 channel receive coil. For multichannel transmit, independent variable amplitude and phase are then estimated to mitigate B_1 inhomogeneity. The example of commercial 7.0 T head coils are shown in Figure 3.1.13. The work in

this thesis used 2Tx/32 Rx channel head coil (Nova Medical) and prototype transmit volume coil of NOVA 8Tx/32 Rx channel head coil via operator's room switch (Figure 3.1.14).

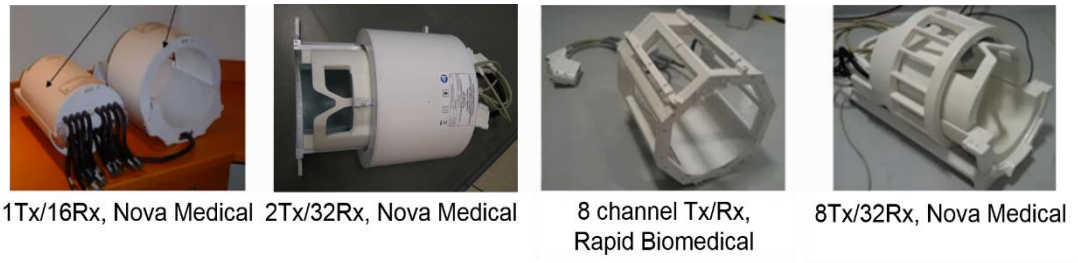


Figure 3.1.13: Example of commercial head coils available for a 7.0 T MRI scan.

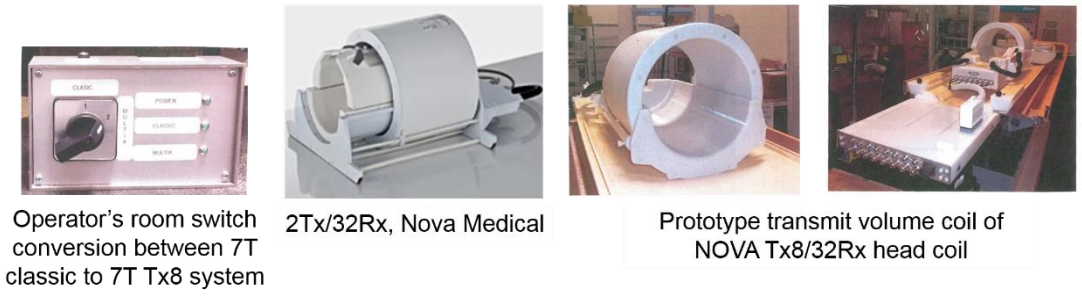


Figure 3.1.14: Two head coils were used in this study for brain imaging at 7.0 T.

3.7 MR sequences commonly used for structural imaging at 7.0 T

Structural MR imaging has become a more widely used in routine clinical scan which the anatomical details such as size, shape and the integrity of grey and white matter in the human brain are required. Additional advantages include its ability to provide both qualitative and quantitative information of biological macromolecules. The available conventional and advanced MR sequences for brain imaging are briefly presented in the following sections.

3.7.1 T_1-weighted imaging

Similar to lower field MRI, T_1 weighted imaging is widely used as anatomical reference. To achieve optimum T_1 contrast, increasing the flip angle of

the gradient echo sequence above the Ernst angle of tissue is required. The use of magnetization prepared rapid gradient recalled echo sequences (MPRAGE) [37] allows preservation of bulk T_1 contrast through space by an adiabatic inversion RF pulse. MPRAGE sequence is designed for a rapid acquisition with T_1-weighted dominance, with a short TR ~ 6-10 ms at ~ Ernst angle, $\alpha_E = \arccos\left(e^{-TR/T_1}\right)$. The T_1-MPRAGE images are mainly used in brain tissue segmentation due to greater tissue contrast between grey and white matter. With an extension of the MPRAGE sequence, MP2RAGE (two inversion-contrast magnetization-prepared rapid gradient echo sequence) has been developed to generate T_1-weighted image with increased SNR [38] and automated image flattening (bias field correction). Likewise, T_1-weighted phase sensitive inversion recovery (PSIR) sequence is very similar with image reconstruction [39] (see chapter 5).

3.7.2 T_2-weighted imaging

Fast T_2 weighted imaging sequences such as turbo spin echo (TSE) is the standard for T_2 imaging, with 180° RF pulses are applied to generate T_2 weighted information with rapid k-space coverage. However, the interplay between excitation and refocusing pulse are important. Typically at Nottingham, we use reduced flip angle refocusing pulse to reduce SAR, increased speed and contrast-to-noise ratio. Different strategies have been realized to optimize the signal for such sequences [40-43].

3.7.3 T_2^*-weighted imaging

T_2^* contrast provides unique information on tissue magnetic susceptibility which is produced by a gradient echo sequence. Magnetic field inhomogeneities from susceptibility differences between tissues induce faster relaxation leading to signal detection or contrast on gradient echo images. T_2^*-based contrast is widely used at 7.0 T. The FLASH gradient echo sequence [44] is usually used for T_2^* weighting. To increase the T_2^* sensitivity in the gradient echo sequence, for a given

TR, a smaller flip angle than the Ernst angle (α_E) and relatively long echo time is required. Low flip angle excitation ensures that the longitudinal magnetization remains close to the fully relaxed state which reduces the influence of T_1 so that T_2^* weighting becomes more dominant. Thus, it is possible to achieve short TR, a low flip angle and faster 3D volume coverage with high FLASH T_2^* contrast, low SAR and low sensitivity to B_1 variation. T_2^* weighted imaging has been found to be useful in neuroimaging in venography, detection of haemorrhage, blood products, and changes in iron content. The gradient echo sequence can be further exploited for producing R_2^* maps as well as SWI and QSM data.

R_2^* mapping

R_2^* maps are produced by multi-gradient echo sequences with selected flip angles around the Ernst angle of tissues. R_2^* is an inverse rate of transverse relaxation time, $R_2^* = (\frac{1}{T_2^*})$ and shows high correlation with paramagnetic iron in tissue [45]. The rate of relaxation depends on variation in magnetic properties (between paramagnetic iron and diamagnetic myelin) and also the orientation of the axons relative to the main magnetic field in white matter [46, 47]. The key considerations in R_2^* measurement include the range of values to be mapped, and the effect of macroscopic field variation due to poor shimming.

Susceptibility weighted imaging (SWI)

The phase data contains information about the average susceptibility of tissues (χ) in the voxel whereas T_2^* is sensitive to the heterogeneity of susceptibility within and around the voxel. The magnitude and phase information can be combined to produce a unique physical contrast which can be greater than T_2^* weighting in some cases. Furthermore, magnitude and phase data after high pass filtering are combined to produce a SWI image [48], in which information from phase data enhances the contrast of paramagnetic perturbations rose due to blood deoxyhaemoglobin and hemosiderin in SWI data (Figure 3.1.15).

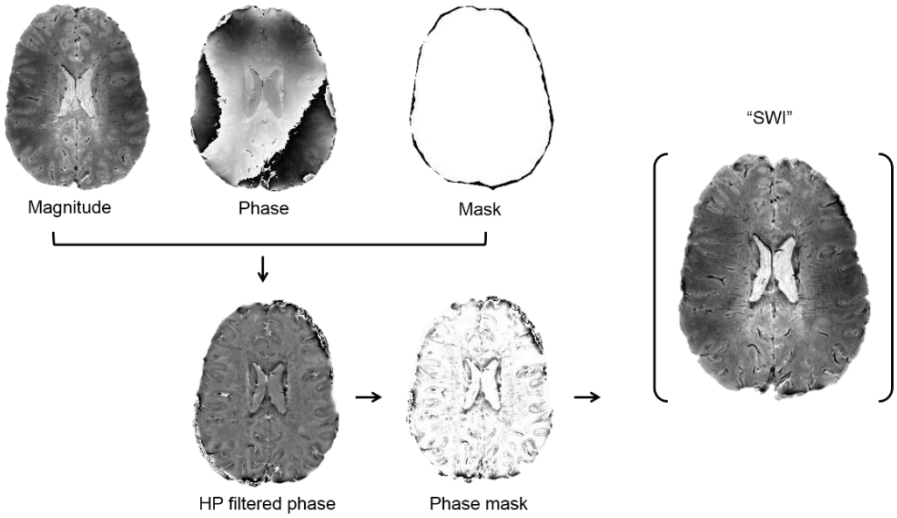


Figure 3.1.15: Schematic of SWI from a volunteer at 7.0 T.

Quantitative susceptibility mapping (QSM)

Tissues are generally diamagnetic with a susceptibility similar to water (about -9.05 ppm). The presence of iron makes tissue susceptibility less negative. Quantitative susceptibility maps present a local anatomical contrast of tissue from the complex gradient echo signals, for instance depicting variations in brain iron and myelin content. Magnitude data is sensitive to dephasing due to susceptibility variation. Maps of field (or phase variation) show effects of susceptibility more directly, however the signal is not localized to the source of susceptibility perturbation. We therefore need to solve the inverse problem to relate the magnetic field to susceptibility maps.

Figure 3.1.16 shows the steps involved in creating a susceptibility map from phase data with separation of background of field perturbation and tissue field perturbation. First, phase wrapping occurs, so angle outside the range from π to $-\pi$ can be folded back, but this effect will be removed by a high-pass filter (Laplacian-based phase unwrapping) [49]. Second, the sophisticated harmonic artefact reduction for phase data (SHARP) method is used to filter out fields that are generated by sources outside [50]. The SHARP is reliable and rapid processing since convolution and deconvolution can be carried out in the Fourier domain.

Finally, the improved sparse linear equation and least-square (iLSQR) algorithm is used to calculate susceptibility from the filtered field map [51]. In QSM maps, a bright pixel represents paramagnetic susceptibility and a dark pixel represents diamagnetic susceptibility. Nevertheless, there is an exception in visualising susceptibility in anisotropic white matter. In this thesis, the STI Suite V2.2 was used for QSM reconstruction which can be downloaded at https://people.eecs.berkeley.edu/~chunlei.liu/software.html/. Processing details for QSM from the STI Suite toolbox are described in [49].

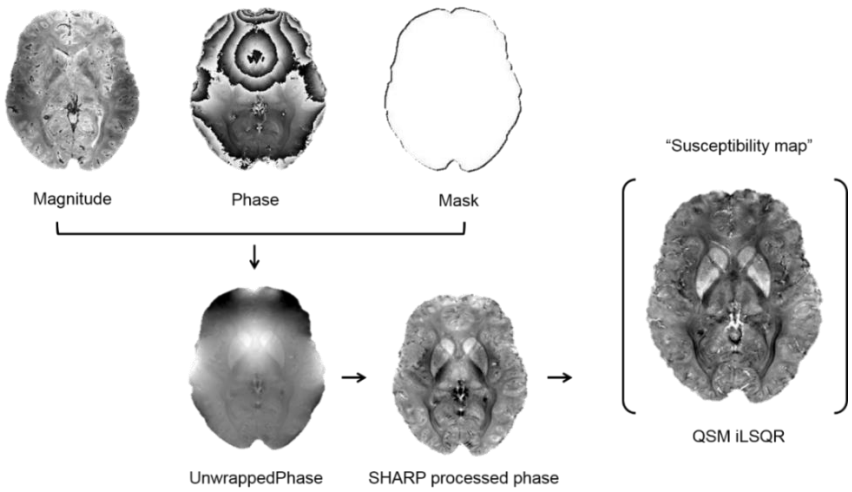


Figure 3.1.16: Schematic of QSM framework from a healthy volunteer at 7.0 T.

3.7.4 Clinical applications

For human brain imaging, the submillimetre spatial resolution available at 7.0 T MRI has been widely used in various applications (Table 3.4). It has proven useful in characterising neurodegenerative diseases such as Alzheimer's disease, Parkinson disease, cerebrovascular small-vessel disease, cerebral autosomal dominant arteriopathy with subcortical infarcts and leukoencephalopathy (CADASIL), Multiple Sclerosis (MS), cerebral amyloid angiopathy (CAA) and staging tumour cell in low-grade and high-grade [52-55].

Table 3.4: MR techniques at 7.0 T and applications in the human brain.

Method	Techniques	Information
Structural	T1W, T2W, IR, MT	Morphometry
Functional	Blood-oxygen-level dependent (BOLD) fMRI	Functional connectivity in the brain (oxygenated and deoxygenated blood) between resting/active stage
MR spectroscopy	^{1}H MRS	Metabolites such as NAA, Cho, Lac, GABA
Magnetization transfer	Images with (M_T) and without MT pulse (M_0)	Myelination and axonal density
Relaxometry	T_2 or T_2^* measurement	Brain iron
Susceptibility weighted	Phase data	Brain iron
Diffusion	Diffusion tensor imaging (DTI)	Diffusion of water in tissue
Tractography	Diffusion tensor imaging (DTI)	Fractional anisotropy (FA) changes and fibre tract-specific reconstruction
Perfusion	Arterial spin labelling (ASL) use magnetic field to invert existing water spins to trace blood flow	Cerebral blood flow (CBF),
MR angiography	PCA velocity of spins, TOF thin slabs oriented perpendicular to the flow	Volume flow rate, morphometry of the vessel

3.8 Summary

This chapter has described the physical changes occurring when moving to 7.0 T MRI. From development in MR instrumentation, a lot of clinical benefits from 7.0 T MRI have highlighted areas where subtle anatomic changes associated with disease can be detected. Optimised sequences and MR parameters have resulted in improving both image contrast and SNR. However, technical limitations (such as B_0, B_1 field inhomogeneity, increased RF power deposition, and errors in chemical shift localization) remain a substantial challenge for *in vivo* imaging that needs to be overcome.

Bibliography

[1] M. E. Ladd *et al.*, “Pros and cons of ultra-high-field MRI/MRS for human application,” *Progress in Nuclear Magnetic Resonance Spectroscopy*. 2018.

[2] R. Pohmann, O. Speck, and K. Scheffler, “Signal-to-noise ratio and MR tissue parameters in human brain imaging at 3, 7, and 9.4 tesla using current receive coil arrays,” *Magn. Reson. Med.*, 2016.

[3] S. Schmitter *et al.*, “Cardiac imaging at 7 tesla: Single- and two-spoke radiofrequency pulse design with 16-channel parallel excitation,” *Magn. Reson. Med.*, 2013.

[4] I. Tkáč, G. Öz, G. Adriany, K. Uğurbil, and R. Gruetter, “In vivo 1H NMR spectroscopy of the human brain at high magnetic fields: Metabolite quantification at 4T vs. 7T,” *Magn. Reson. Med.*, 2009.

[5] T. M. Fiedler, M. E. Ladd, and A. K. Bitz, “SAR Simulations & Safety,” *Neuroimage*, 2018.

[6] J. Rauschenberg *et al.*, “Multicenter study of subjective acceptance during magnetic resonance imaging at 7 and 9.4 T,” *Invest. Radiol.*, 2014.

[7] J. M. Theysohn, S. Maderwald, O. Kraff, C. Moenninghoff, M. E. Ladd, and S. C. Ladd, “Subjective acceptance of 7 Tesla MRI for human imaging,” *Magn. Reson. Mater. Physics, Biol. Med.*, 2008.

[8] G. J. Metzger, C. Snyder, C. Akgun, T. Vaughan, K. Ugurbil, and P. F. Van De Moortele, “Local B1+ shimming for prostate imaging with transceiver arrays at 7T based on subject-dependent transmit phase measurements,” *Magn. Reson. Med.*, 2008.

[9] X. Zhang, P. F. Van De Moortele, S. Schmitter, and B. He, “Complex B1 mapping and electrical properties imaging of the human brain using a 16-channel transceiver coil at 7T,” *Magn. Reson. Med.*, vol. 69, no. 5, pp. 1285–

1296, 2013.

[10] S. Orzada, S. Maderwald, B. A. Poser, A. K. Bitz, H. H. Quick, and M. E. Ladd, “RF excitation using Time Interleaved Acquisition of Modes (TIAMO) to address B1 inhomogeneity in high-field MRI,” *Magn. Reson. Med.*, 2010.

[11] S. Orzada, S. Johst, S. Maderwald, A. K. Bitz, K. Solbach, and M. E. Ladd, “Mitigation of B1+ inhomogeneity on single-channel transmit systems with TIAMO,” *Magn. Reson. Med.*, 2013.

[12] M. L. Hahnemann *et al.*, “Non-enhanced magnetic resonance imaging of the small bowel at 7 Tesla in comparison to 1.5 Tesla: First steps towards clinical application,” *Magn. Reson. Imaging*, 2016.

[13] S. Johst, S. Maderwald, A. Fischer, H. H. Quick, M. E. Ladd, and S. Orzada, “Investigation of the Saturation Pulse Artifact in Non-Enhanced MR Angiography of the Lower Extremity Arteries at 7 Tesla,” *PLoS One*, vol. 10, no. 3, p. e0119845, Mar. 2015.

[14] J. Hoffmann, C. Mirkes, G. Shajan, K. Scheffler, and R. Pohmann, “Combination of a multimode antenna and TIAMO for traveling-wave imaging at 9.4 Tesla,” *Magn. Reson. Med.*, 2016.

[15] K. Setsompop *et al.*, “Slice-selective RF pulses for in vivo B1+inhomogeneity mitigation at 7 Tesla using parallel RF excitation with a 16-element coil,” *Magn. Reson. Med.*, 2008.

[16] M. A. Cloos *et al.*, “KT-points: Short three-dimensional tailored RF pulses for flip-angle homogenization over an extended volume,” *Magn. Reson. Med.*, 2012.

[17] X. Wu, G. Adriany, K. Ugurbil, and P. F. Van de Moortele, “Correcting for Strong Eddy Current Induced B0 Modulation Enables Two-Spoke RF Pulse Design with Parallel Transmission: Demonstration at 9.4T in the Human Brain,” *PLoS One*, 2013.

[18] V. Gras *et al.*, “Design of universal parallel-transmit refocusing kT-point

pulses and application to 3D T2-weighted imaging at 7T," *Magn. Reson. Med.*, 2018.

[19] X. Wu, S. Schmitter, E. J. Auerbach, K. Uğurbil, and P.-F. Van de Moortele, "Mitigating transmit B 1 inhomogeneity in the liver at 7T using multi-spoke parallel transmit RF pulse design.," *Quant. Imaging Med. Surg.*, 2014.

[20] W. M. Teeuwisse, W. M. Brink, K. N. Haines, and A. G. Webb, "Simulations of high permittivity materials for 7 T neuroimaging and evaluation of a new barium titanate-based dielectric," *Magn. Reson. Med.*, vol. 67, no. 4, pp. 912–918, 2012.

[21] R. Schmidt and A. Webb, "Improvements in RF shimming in high field MRI using high permittivity materials with low order pre-fractal geometries," *IEEE Trans. Med. Imaging*, vol. 35, no. 8, pp. 1837–1844, 2016.

[22] W. M. Brink, A. M. A. van der Jagt, M. J. Versluis, B. M. Verbist, and A. G. Webb, "High Permittivity Dielectric Pads Improve High Spatial Resolution Magnetic Resonance Imaging of the Inner Ear at 7 T.," *Invest. Radiol.*, vol. 49, no. 5, pp. 271–277, 2014.

[23] A. G. Webb, "Dielectric Materials in Magnetic Resonance," *Concepts Magn. Reson. Part A*, vol. 38(a), no. 4, pp. 148–184, 2011.

[24] A. N. Dula, J. Virostko, and F. G. Shellock, "Assessment of MRI issues at 7 T for 28 implants and other objects," *Am. J. Roentgenol.*, 2014.

[25] F. G. Shellock, "No Title." [Online]. Available: http://mrisafety.com/.

[26] D. W. Chakeres, A. Kangarlu, H. Boudoulas, and D. C. Young, "Effect of static magnetic field exposure of up to 8 Tesla on sequential human vital sign measurements," *J. Magn. Reson. Imaging*, 2003.

[27] A. Kangarlu *et al.*, "Cognitive, cardiac, and physiological safety studies in ultra high field magnetic resonance imaging," *Magn. Reson. Imaging*, 1999.

[28] J. J. Suttie *et al.*, "7 Tesla (T) human cardiovascular magnetic resonance imaging using FLASH and SSFP to assess cardiac function: validation

against 1.5 T and 3 T.," *NMR Biomed.*, 2012.

[29] B. Zhang, Y. F. Yen, B. A. Chronik, G. C. McKinnon, D. J. Schaefer, and B. K. Rutt, "Peripheral nerve stimulation properties of head and body gradient coils of various sizes," *Magn. Reson. Med.*, 2003.

[30] P. Jezzard, "Shim Coil Design, Limitations and Implications," *Abstr. from Int. Soc. Magn. Reson. Med. Annu. Meet.*, 2006.

[31] J. P. Stockmann and L. L. Wald, "In vivo B0field shimming methods for MRI at 7 T," *Neuroimage*, 2018.

[32] J. A. McNab *et al.*, "The Human Connectome Project and beyond: Initial applications of 300mT/m gradients," *Neuroimage*, 2013.

[33] K. Setsompop *et al.*, "Pushing the limits of in vivo diffusion MRI for the Human Connectome Project," *Neuroimage*, 2013.

[34] A. G. Webb and P. F. Van de Moortele, "The technological future of 7 T MRI hardware," *NMR in Biomedicine*. 2016.

[35] P. Mansfield and B. Chapman, "Active magnetic screening of coils for static and time-dependent magnetic field generation in NMR imaging," *J. Phys. E.*, 1986.

[36] S. A. Winkler *et al.*, "Gradient and shim technologies for ultra high field MRI," *Neuroimage*, 2018.

[37] J. P. Mugler and J. R. Brookeman, "Three-dimensional magnetization-prepared rapid gradient-echo imaging (3D MP RAGE)," *Magn. Reson. Med.*, vol. 15, no. 1, pp. 152–157, 1990.

[38] J. P. Marques, T. Kober, G. Krueger, W. van der Zwaag, P. F. Van de Moortele, and R. Gruetter, "MP2RAGE, a self bias-field corrected sequence for improved segmentation and T1-mapping at high field," *Neuroimage*, vol. 49, no. 2, pp. 1271–1281, 2010.

[39] O. Mougin, R. Abdel-Fahim, R. Dineen, A. Pitiot, N. Evangelou, and P. Gowland, "Imaging gray matter with concomitant null point imaging from the

phase sensitive inversion recovery sequence," *Magn. Reson. Med.*, vol. 76, no. 5, pp. 1512–1516, 2016.

[40] F. Eggenschwiler, K. R. O'Brien, R. Gruetter, and J. P. Marques, "Improving T2-weighted imaging at high field through the use of kT-points," *Magn. Reson. Med.*, 2014.

[41] S. J. Malik, A. Beqiri, F. Padormo, and J. V. Hajnal, "Direct Signal Control of the steady-state response of 3D-FSE sequences," *Magn. Reson. Med.*, 2015.

[42] A. Massire, A. Vignaud, B. Robert, D. Le Bihan, N. Boulant, and A. Amadon, "Parallel-transmission-enabled three-dimensional T2 -weighted imaging of the human brain at 7 Tesla.," *Magn. Reson. Med.*, 2014.

[43] A. Sbrizzi, H. Hoogduin, J. V. Hajnal, C. A. T. van den Berg, P. R. Luijten, and S. J. Malik, "Optimal control design of turbo spin-echo sequences with applications to parallel-transmit systems," *Magn. Reson. Med.*, 2017.

[44] A. Haase, J. Frahm, D. Matthaei, W. Hanicke, and K. D. Merboldt, "FLASH imaging. Rapid NMR imaging using low flip-angle pulses," *J. Magn. Reson.*, 1986.

[45] A. Deistung, A. Schäfer, F. Schweser, U. Biedermann, R. Turner, and J. R. Reichenbach, "Toward in vivo histology: A comparison of quantitative susceptibility mapping (QSM) with magnitude-, phase-, and R2*-imaging at ultra-high magnetic field strength," *Neuroimage*, 2013.

[46] S. Wharton and R. Bowtell, "Fiber orientation-dependent white matter contrast in gradient echo MRI," *Proc. Natl. Acad. Sci.*, vol. 109, no. 45, pp. 18559–18564, 2012.

[47] J. Cohen-Adad, "What can we learn from T2* maps of the cortex?," *NeuroImage*. 2014.

[48] E. M. Haacke, Y. Xu, Y.-C. N. Cheng, and J. R. Reichenbach, "Susceptibility weighted imaging (SWI).," *Magn. Reson. Med.*, vol. 52, no. 3, pp. 612–618, 2004.

[49] W. Li, A. V. Avram, B. Wu, X. Xiao, and C. Liu, “Integrated Laplacian-based phase unwrapping and background phase removal for quantitative susceptibility mapping,” *NMR Biomed.*, vol. 27, no. 2, pp. 219–227, 2014.

[50] F. Schweser, A. Deistung, B. W. Lehr, and J. R. Reichenbach, “Quantitative imaging of intrinsic magnetic tissue properties using MRI signal phase: An approach to in vivo brain iron metabolism?,” *Neuroimage*, 2011.

[51] A. Deistung, F. Schweser, and J. R. Reichenbach, “Overview of quantitative susceptibility mapping,” *NMR in Biomedicine*. 2017.

[52] S. Trattnig *et al.*, “Key clinical benefits of neuroimaging at 7 T,” *Neuroimage*, 2018.

[53] C. Grochowski and G. Staśkiewicz, “Ultra high field TOF-MRA: A method to visualize small cerebral vessels. 7 T TOF-MRA sequence parameters on different MRI scanners – Literature review,” *Neurologia i Neurochirurgia Polska*. 2017.

[54] E. R. Gizewski, C. Mönninghoff, and M. Forsting, “Perspectives of Ultra-High-Field MRI in Neuroradiology,” *Clin. Neuroradiol.*, vol. 25, pp. 267–273, 2015.

[55] S. T. Schwarz *et al.*, “Parkinson’s disease related signal change in the nigrosomes 1–5 and the substantia nigra using T2* weighted 7T MRI,” *NeuroImage Clin.*, 2018.

Chapter 4 High Resolution *in vivo* Imaging of Adult Cochlea

4.1 Introduction

In 2015, there were almost 10 million people with hearing problems in the UK. Approximately 6.5 million were elderly over 60 years-old but 3.7 million were working-age adults [1]. By 2035, an estimated 15.6 million people across the UK will suffer from hearing loss. A report from the Royal National Institute for deaf people (RNID) showed around 50,000 deaf children in the UK with around half born with hearing loss while other half lost their hearing during childhood. Profound hearing loss is increasingly treated by cochlear implantation. In some cases, problems are caused by abnormalities of the cochlea (Figure 4.1) and associated nerve. Detection of an abnormality in the cochlear nerve is beneficial in the selection of patients for cochlear implantation.

The inner ear is a complex structure that includes the cochlea (the organ of hearing) which is located in the temporal bone. It is composed of four main parts which are the bony labyrinth, the membranous labyrinth, endolymph and perilymph. The bony labyrinth is a cavity in the temporal bone which contains the vestibule, three semi-circular canals and cochlea. The membranous labyrinth is a collection of membranous sacs, forming a space filled with fluid (endolymph), surrounded by perilymph. There are different compositions of fluids inside the cochlear duct. Endolymph has a smaller value of ionic concentration with relativity high potassium (K^+) not normally found in body fluids (a dashed line in Figure 4.2).

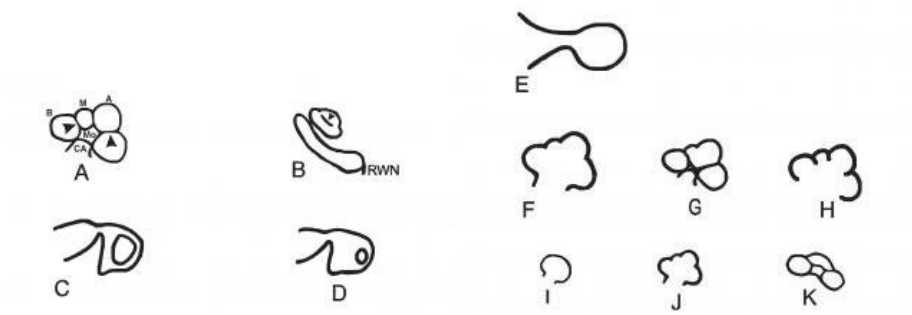


Figure 4.1: Schematic of the normal cochlea and cochlear malformations. A: normal cochlea, mid-modiolar section; Mo = modiolus, CA = cochlear aperture, B = basal turn, M = middle turn, A = apical turn, arrowheads = interscalar septa. B: Normal cochlea, inferior section passing through the round window niche (RWN); arrowhead = interscalar septum between middle and apical turns. C: Cochlear aplasia with normal vestibule. D: Cochlear aplasia with enlarged vestibule. E: Common cavity. F: Incomplete partition type I. G: Incomplete partition type II. H: Incomplete partition type III. I: Cochlear hypoplasia, bud type (type I). J: Cochlear hypoplasia, cystic cochlea type (type II). K: Cochlear hypoplasia, with less than 2 turns (type III). (Data From https://emedicine.medscape.com/article/2037435-overview#a5).

The human cochlea is shaped like a snail shell with 2.50 to 2.75 turns. A post mortem study on temporal bones showed that the bony cochlear tube is approximately 35 mm long [2] and vestibular cochlear nerve diameter is around 2 mm [3]. Within the cochlea, as shown in Figure 4.2, the space is separated into three canals; scala tympani, scala vestibuli and scala media (or cochlear duct). The receptor cell for hearing called the organ of corti is positioned between the scala tympani and scala vestibuli. Abnormalities include enlarged, narrowed and deformed shapes of the inner ear which may affect both the auditory and vestibular system. This nerve runs straight in the anterior compartment of the canal and makes a sharp turn at the base of modiolus. Lack of a cochlear nerve or cochlear nerve agenesia is now the contraindication for surgery.

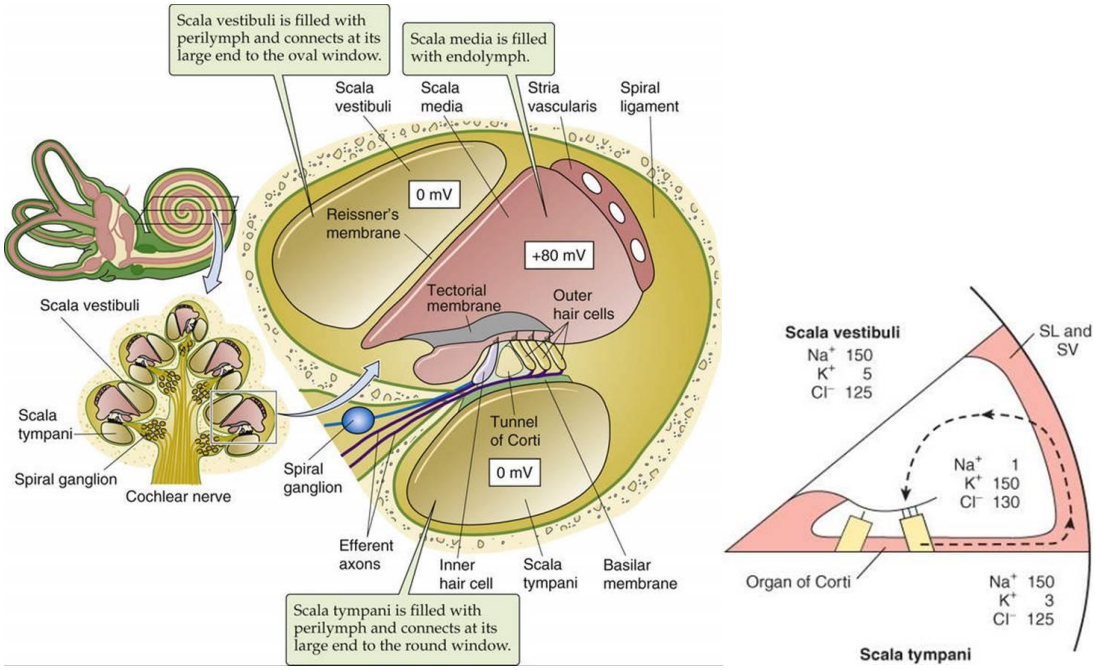


Figure 4.2: The cochlea consists of one endolymphatic lumen (cochlear duct) and two perilymphatic lumina; the scala vestibule, which transmits the acoustic fluid wave from the vestibule, and the scala tympani, which allows the fluid wave to decompress at the round window membrane. (Data from Philine Wangemann, Kansas State University).

Recently, modern surgery has raised interest to design and develop a new cochlear implant for reducing intracochlear damage. Modern designs or placement of electrode arrays can make the electrode smaller and closer to the target [4, 5]. However, there is an uncertainty in the optimum position and depth of guided insertion for the electrode array on an individual basis [6]. The inherent MRI signal in the bony and membranous labyrinths will be greater at 7.0 T than lower field due to the stronger static field and resulting proton magnetization. However, large susceptibility differences between tissue, air, and bone interfaces near the temporal lobes can lead to an increase of static field inhomogeneity which produces distortion artefacts in the images. Furthermore, the radio-frequency (B_1) magnetic field can be very inhomogeneous in this region. As discussed in chapter 3, the wavelength of RF becomes similar to the size of the head at 7.0 T interference effects occur which cause shading artefacts degrading image quality. When using volume head coil for

brain imaging, typically the intensity is higher at the centre of the brain and darker in the periphery (section 3.3.1 in Chapter 3).

This can either be addressed by using multichannel RF shimming solution. Passive B_1 shimming can be achieved by using dielectric material (dielectric pads) placed between the subject's ears and receiver coil, to modify the local the B_1 field. High permittivity materials can reduce the B_1 field variations by changing RF waveform within the brain (section 3.4.2 in Chapter 3).

The goals of this study were: (i) to present MR protocols which optimize contrast, resolution and scan time for 3D *in vivo* imaging of adult cochlea and auditory nerves at 7.0 T, and to compare these at 3.0 T MRI and (ii) to evaluate anatomical variability of the bony cochlea and cochlear nerve which would be useful to avoid intracochlear damage during implantation.

4.2 Methods

The outline of this section and general methods will be described. First of all, a series of experiments were performed in order to optimize imaging of the cochlea at 7.0 T MRI. Section 4.2.1 describes work aimed at selecting the optimum sequence for imaging of human cochlea by comparing the 3D TSE, 3D bFFE and 3D T2W DRIVE MR sequences at 7.0 T in nine healthy volunteers. These sequences have previously been shown to be useful for imaging the cochlear at 3.0 T. Next in section 4.2.2, the DRIVE sequence (which had been shown to provide the best bone-nerve contrast) was compared for different B_1 conditions. For this work it was essential to map B_1, and details of how this was done are described. We then evaluated any improvements in B_1 homogeneity by comparing B_1 maps produced using dielectric pads or B_1 shimming with two or eight channels transmit system in twelve healthy subjects. In section 4.2.3, measurements of adult cochlea and the cochlear nerve were performed at 7.0 T MRI. Maximum intensity Projections (MIPs)

were created to visualize cochlear structure and observed cochlear geometry (e.g. size, width, length and volume) were then evaluated. Measurements of the diameter of cochlear nerve were determined as short diameter (mm); long diameter (mm) and cross-sectional area (mm^2). Two radiologists accessed the image quality and two additional observers made the measurements. On each assessment, the interobserver and intra-observer reliability were evaluated. Finally, section 4.2.4 presents the first attempt at *in vivo* imaging at 7.0 T with the smallest isotropic voxel size of 0.26 mm to visualize all three chambers of the cochlea including the scala media, the scala tympani and the scala vestibuli.

This study was approved by the Institutional Ethic Committees and Review Boards at the University of Nottingham (H14082014/22), healthy volunteers aged between 25 and 55 years with normal hearing were included in the study. All subjects were screened with MR safety questionnaires and written informed consent was obtained from all participants before each scan. Three healthy subjects were imaged at both 3.0 T and 7.0 T MRI. For high resolution imaging (maximum isotropic voxel of 0.34 mm^3) of the cochlea at 7.0 T, nine subjects were scanned with the final protocol which used 2-channel RF shimming and dielectric pads over subject's ears. Three subjects were tested with 8-channel transmit system head coil. In this study RF shimming was not used to reduce the scan time.

Experiments at 7.0 T were performed using Philips MR scanner (Achieva) equipped with both a 2-channel and an 8-channel transmit system head coil (Nova Medical Inc., USA). The 2-channel system was used for most of this work. Experiments at 3.0 T were performed using Philips MR scanner (Achieva) with a 32-channel head coil. Each subject was scanned with a comparable imaging parameters to 7.0 T MRI. Figure 4.3 shows slice positioning where the positioning was checked on all views to ensure slices covered the whole cochlea and three semi-circular canals. Then, volumetric data was acquired in axial planes planned on the sagittal view with the block aligned parallel to the genu and

splenium of the corpus callosum, but it could be reconstructed in any direction. After acquisition, the normal size and diameter of these structures were evaluated.

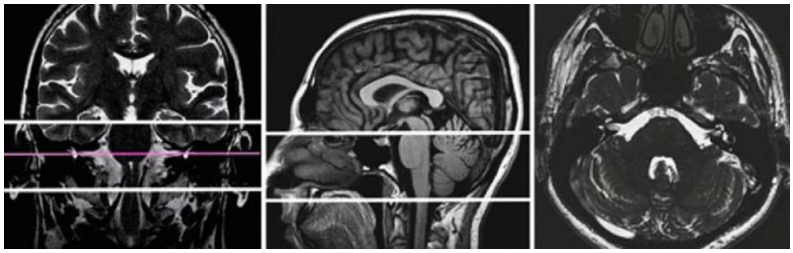


Figure 4.3: Example of slice positioning *in vivo* imaging of cochlea.

4.2.1 Selecting an MR Sequence for imaging the cochlea

Three-Dimensional (3D) imaging is helpful in clinical evaluation of normal and pathological anatomy of the auditory canal. The 3D acquisition techniques are based on the excitation of a 3D volume and phase encoding applied across the slab to create datasets without gaps between image slices, thereby facilitating complete coverage of the entire volume of interest. 3D imaging with isotropic or nearly isotropic resolution enables better visualization of the complex 3D anatomy by allowing the production of maximum intensity projections (MIPs). MIPs provide improved visualization for complex structures. 3D imaging also offers improved signal-to-noise ratio (SNR) compared with two-dimensional (2D) multislice imaging due to the inherent averaging in the Fourier Transform. The sequences considered were initially selected from current non-contrast enhanced clinical protocols used to study the cochlear [8–11] and are described below in sections 4.2.1.1.

4.2.1.1 Pulse sequences considered

Turbo (Fast) Spin Echo

In spin echo imaging, a 90° RF pulse is followed by a single 180° refocusing pulse, and hence spin echo (SE) sequences are less sensitive to susceptibility artefacts around bone than gradient echo (GE) sequences. For turbo (fast) spin echo imaging, multiple 180° refocusing pulses are used to produce

multiple spin-echoes, as originally explained by Hennig et al [12]. This can be given in shorthand notation as

SE: 90° - 180° - echo ... // 90° - 180° - echo

TSE: 90° - 180° - echo - 180° - echo - 180° ... // 90° - 180° - echo - 180° - echo

where // is the repetition time (TR).

A different phase encoding value is applied to each echo and hence each fills a different line of k-space, so that as the number of echoes acquired after a 90° degree excitation increases, the scan time decreases. This potentially allows increased T_1 recovery and hence increased SNR particularly for cochlea which has a long T_1 and T_2 [13]. These features can be used to increase spatial resolution, although all SE sequences are sensitive to RF inhomogeneity at 7.0 T. Because the head is inhomogeneous leads to signal dropout in area near air cavities and tissue/bone interface.

Balanced Fast Field Echo Sequence (bFFE)

This is a steady-state free precession MR technique for fast imaging with high SNR [14, 15]. Balanced gradients are applied to refocus dephasing between excitation pulses ensuring that the initial signal (FID) from each pulse overlaps with residual transverse magnetization, so that both contribute to the steady state (equilibrium magnetization). This makes the sequence relatively insensitive to motion and means that it offers the highest SNR per unit time of all MR sequences. The contrast depends on the ratio T_2/T_1 giving high signal of fluid and fat and low signal of soft tissue. B_0 field inhomogeneity will cause banding artefacts, which can be reduced by alternating the phase of the RF pulse by 180° in subsequent TR periods (keeping TR as short as possible) or using better shimming. Clinical applications of bFFE in neuroradiology include MR myelography, Brachial plexus

injury, detection of CSF leakage or CSF-flow obstruction, delineation of CSF space lesion and imaging of cranial nerve or intradural cervical nerve roots.

DRIVen Equilibrium (DRIVE)

The DRIVE sequence is based on TSE technique but has shorter scan time due to a shorter TR. A (-90°) flip-back pulse is used to accelerate the longitudinal recovery by tipping residual transverse magnetization back to longitudinal magnetization. Materials with long T_1 (such as CSF) may not fully recover by the end of each TR in a conventional spin echo sequence. However, since they also have a long T_2 the recovery can effectively be accelerated by tipping the longitudinal magnetization back along z prior to the start of the next sequence [16]. This sequence can be summarised as

DRIVE: 90° - 180° - echo - 180° - echo - 180° - echo - (-90°) ... // 90° - 180° - echo

where // is the repetition time (TR).

On different MR scanners, there are different trade names; For this sequence, Siemens uses "RESTORE", GE uses "Fast recovery fast spin echo (FRFSE)", Philips uses "DRIVE", Hitachi uses "Driven equilibrium FSE", and Toshiba "T_2 plus FSE". This heavily T_2 weighted sequence can visualize the anatomy of the fluid filled bony structures (the cochlea) and details of auditory nerve very clearly [17].

4.2.1.2 Experiments to compare these pulse sequences

Preliminary comparison of the sequences described in section 4.2.1.1 was performed in nine healthy volunteers (5 male, 4 female) to determine which sequence would best depict the cochlear duct and branches of cranial nerves. The scanning parameters for these three sequences are shown in Table 4.1. Only the best T_2 weighted sequence identified at 7.0 T was applied to 3.0 T.

Table 4.1: Comparing 3D MR sequences for high resolution cochlear imaging at 7.0 T. For the DRIVE sequence the range of values investigated is given (final optimized values selected indicated in bold).

Parameters	7.0 T MRI			3.0 T MRI
MR sequence	TSE	bFFE	DRIVE	DRIVE
Subjects	n=3	n=3	n=8 (using high resolution in 4 subjects)	n=3
Scan mode	3D	3D	3D	3D
Voxel size (mm)	0.4x0.4x0.8	0.4x0.4x0.8	0.4x0.4x0.8 - **0.26x0.26x0.26**	0.5x0.4x1.0
Resolution (x,y)	412x412	384x356	388x362 -**860x860**	440x392
Slices	30	100	45 **- 76**	60
FOV (mm) (AP, FH, RL)	139x30x165	140x40x164	166x18x160 **- 224x20x164**	220x30x180
SENSE	2	2	2	2
TSE factor	50	-	50	56
Flip angle (°)	90	40	90-**100**	90
TR (ms)	2500	11	4200 -**3300**	2000
TE (ms)	395	5.6	220 -**282**	193-197
Scan duration(min)	6:42	3:45	6:49 -**14:47**	4:00

4.2.2 Improving B_1 homogeneity

As explained in the introduction it is challenging to create a uniform B_1 field within tissue at higher field due to the short electromagnetic wavelength of the transmitted RF field in tissue. Several approaches are available to attempt to overcome this but to implement and test them, we needed to map the B_1 transmit field and this is described in section 4.2.2.1. We then compared the changes in B_1

field when using dielectric pads, and B_1 shimming method on both a two and eight channel transmit system (section 4.2.2.2-4.2.2.6).

4.2.2.1 B_1 mapping with the Actual Flip-Angle Imaging (AFI) Method

Several B_1 mapping techniques have been proposed to estimate B_1 field inhomogeneity but here we used the actual flip-angle imaging (AFI) method because it provides robust B_1 maps in the brain, AFI was initially developed for rapid measurement of the B_1 field by Yarnykh [18]. In theory, two identical RF pulses of the flip angle (θ) are applied at two different interleaved repetition times, TR_1 and TR_2 with the corresponding signals (S_1 and S_2) being detected as gradient echos. This method measures the actual flip angle from the ratio of two signals, $r = S_2/S_1$ where S_1 is the signal from TR_1 and S_2 is the signal from TR_2 (assuming that the second TR (TR_2) is longer than the first TR (TR_1)). In the pulsed steady state, the Bloch equations for longitudinal magnetization before each excitation pulse can be expressed as

$$M_{z1} = M_0 \frac{1-E_2+(1-E_1)E_2 cos\alpha}{1-E_1E_2cos^2\alpha} \quad \text{Eq 4.1}$$

$$M_{z2} = M_0 \frac{1-E_1+(1-E_2)E_1 cos\alpha}{1-E_1E_2cos^2\alpha} \quad \text{Eq 4.2}$$

where $E_{12} = e^{-\frac{TR_{12}}{T_1}}$ and M_0 is the equilibrium magnetization. So, the observed signals S_1 and S_2 are

$$S_{(1,2)} = M_{z1,2}(\sin\alpha)\, e^{\left(\frac{-TE}{T_2^*}\right)} \quad \text{Eq 4.3}$$

Then the ratio of the steady-state signals can be expressed as

$$r = \frac{S_2}{s_1} = \frac{1-E_2+(1-E_1)E_2 cos\alpha}{1-E_1+(1-E_2)E_1 cos\alpha} \quad \text{Eq 4.4}$$

Taking the first-order approximation for the exponential terms with short TR_1, TR_2 this simplifies to

$$r = \frac{1+n\cos\alpha}{n+\cos\alpha} \qquad \text{Eq 4.5}$$

where $n = TR_1/TR_2$ Thus, actual flip angle map is given by

$$FAmap = arccos\frac{rn-1}{n-r} \qquad \text{Eq 4.6}$$

and the percentage (%) of the expected flip angle is expressed as

$$\%FAmap = 100\left|\frac{FAmap}{flip_angle}\right| \qquad \text{Eq 4.7}$$

4.2.2.2 B_1 shimming using the 2-channel transmit system head coil

The 2-channel B_1 shimming was first investigated to improve transmit efficiency and uniformity in the cochlea. Axial B_1 maps were acquired with different B_1 shim settings, fixed and volume B_1 shimming (using the Philips B_1 shim programme) in two healthy volunteers (1 male and 1 female). Scanning parameters are summarized in Table 4.2. The parameters varied as several parameters (e.g. required SNR and field homogeneity) were sometimes being optimized together. After mapping the B_1 field, high resolution cochlear imaging was also performed using the 3D T2W DRIVE sequence (Table 4.1, bold values).

4.2.2.3 B_1 shimming using the 8-channel transmit system head coil

Multi-transmit RF technology was also investigated to attempt to improve flip angle uniformity in the auditory cannel. Multiple transmit channels provide different B_1 fields from each channel to enable B_1 shimming to compensate B_1 field non-uniformity across the entire brain (section 3.4.1 in Chapter 3). A Nova 8-channel transmit/32-channel receive head coil was used with an 8 channel transmit system, and an RF shimming algorithm developed by Christopher Mirfin (University of Nottingham, UK). The programme computed the relative phase and amplitude needed on each coil to produce a homogeneous transmit field in a selected region of interest. It used magnitude least squares (LS) optimization, with Tikhonov regularisation to calculate the weights needed on the eight channels to yield the

required B_1 field close to the desired field [19]. The GUI used to select the target ROI is shown in Figure 4.4. We tested the impact of shimming in six healthy volunteers (2 males, 4 females) selecting a target ROI in the temporal lobes. B_1 maps were acquired as described in Table 4.2, followed by cochlear imaging used the optimized parameters shown in Table 4.1.

Table 4.2: Comparing different B_1 shimming conditions in cochlear imaging at 7.0 T.

Parameters	2-channel Tx		8-channel Tx	Dielectric pads	Combined 2-channel Tx and the pads
	Fixed shim	Volume shim	RF shim GUI	Fixed shim	Fixed shim
Subjects(n)	2	2	3	2	3
Scan mode	3D	3D	3D	3D	3D
Technique	T_1FFE	T_1FFE	T_1FFE	T_1FFE	T_1FFE
Voxel size (mm)	4x4x4.5	4x4x4.5	3x3x7-4x4x5	4x4x5	4x4x5
Resolution	64x57	64x57	64x64	64x51	64x51
Slices	12	12	18	31	14
FOV (mm) (AP,FH,RL)	256x54x256	256x54x256	192x162x192	256x155x256	256x70x256
Flip angle (°)	60	60	40, 60	60	60
TR (ms)	20, 100	20, 100	40, 200 30, 150	20, 100	20, 100
TE (ms)	2.21	2.49	2.08-2.72	2.16	2.16-2.19
Scan duration (min)	2.42	2.42 (B_1 calibration 3 minute)	2.42-3.28	3.13	2.80

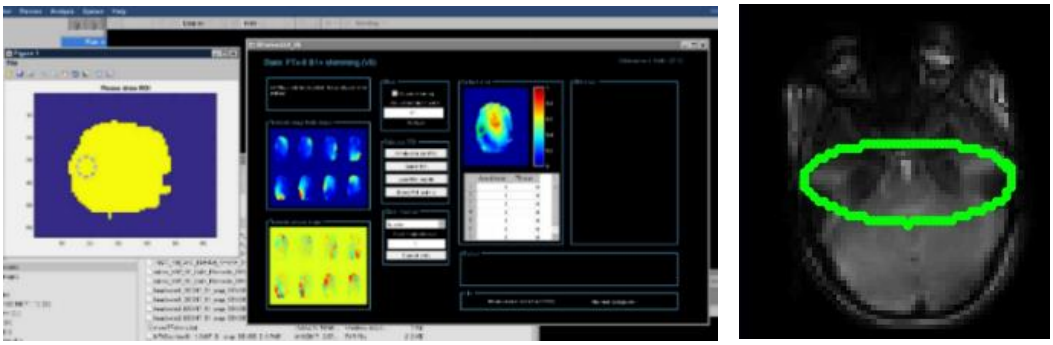


Figure 4.4: RF shimming GUI for multi-transmit which was tested in cochlear imaging at 7.0 T (left) and ROI selection in the temporal lobes (right).

4.2.2.4 Dielectric pads

Flexible dielectric pads of size 18x18x0.8 cm^3 similar to previous work in [20– 22] were also investigated as a way to shape the B_1 field in head. As discussed in chapter 3, they contained a suspension of calcium titanate with weights in the ratio 2.8:1 and deuterated water which had a high-dielectric constant (permittivity~110) producing lighter, thinner and more comfortable pads. The pads were designed to be placed over the subject's ear (Figure 4.5).

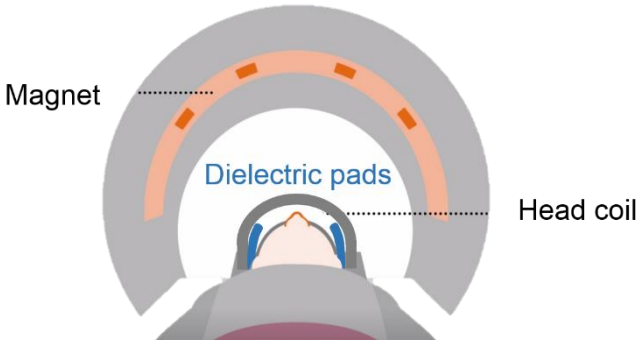


Figure 4.5: Dielectric pads contained a 2.8:1 ratio of calcium titanate and deuterated water (blue) and the position of the pads over the subject's ears and receiver coil in cochlear imaging at 7.0 T (right).

However, there was concern that pads would modify the electric field to increase local SAR. One of our team, Xiao Liang, performed electromagnetic (EM) simulation using a head model (adult head "Hugo") of size 14 cm (right to left), 20 cm (superior to inferior) and 18 cm (anterior and posterior) to investigate the effect

of dielectric pads on the transmit B_1 fields and EM field. Specific absorption rates (SAR) refers to an amount of energy absorbed in tissue when placed in a magnetic field, as power per tissue mass (W/kg) is given by

$$SAR = \frac{\sigma E^2}{\rho} \qquad \text{Eq 4.8}$$

where σ is the electric conductivity of the tissue, E is the electric field strength and ρ is the density of tissue. SAR generally increases and becomes more inhomogeneous with field strength, so that SAR should be determined both globally across the whole body and locally within tissue. The local SAR averaged over 10g of tissue (SAR_{10g}) must also be estimated as there are limits on both local and global SAR. All field computations were performed with the commercially available software REMCOM with post-processing of the EM field maps in MATLAB (Mathwork, MA, USA).

Subsequently the dielectric pads were tested in two healthy volunteers (1 male, 1 female). Two set of scans were collected: B_1 maps with and without the pads. The parameters for each scan are shown in Table 4.2. Then, high-resolution anatomical imaging using a 3D T2W DRIVE sequence was repeated (Table 4.1).

4.2.2.5 Combined 2-channel transmit head coil and dielectric pads

Finally, we investigated the benefits of combining the 2-channel B_1 shimming and dielectric pads. Axial B_1 maps were acquired by scanning three healthy volunteers with the scan parameters shown in Table 4.2. Once the B_1 maps data were collected, high-resolution anatomical scanning with the DRIVE sequence was performed (Table 4.1). Combined 8-channel transmit head coil and dielectric pads are not presented in this study.

4.2.3 Measuring size of the cochlea and cochlear nerve

As previously mentioned, cochlear diameter is significant for cochlear implantation. Quantitative measurements were made on maximum intensity

projections (MIPs) image. The following parameters for size measurement of human cochlea were measured (i) BTLD; basal turn of cochlea lumen diameter (ii) cochlear height (iii) cochlear width (vi) cochlear length (v) cochlear volume as introduced by Sobrinho et al. [23] and Pelliccia et al. [24]. Results from all measurements in both ears were presented as mean ± standard deviation (SD) to determine the normal variation of observed cochlear geometry in both ears. Every measurement was made at least twice by one observer. Then, intraclass correlation coefficient (ICC) was used to measure intraobserver variability.

To evaluate a normal value of cochlear nerve diameters on 3D DRIVE at 7.0 T MRI in normal hearing subjects, we identified anatomy of the facial-vestibulocochlear nerves (CN VII, VIII) passing through auditory canal as shown in Figure 4.6. The visibility of the auditory nerves was determined in oblique sagittal sections perpendicular to long axis of IAC. The cochlear nerve (green) is generally larger than the facial nerve (yellow) and if smaller, hypoplasia or agenesia is suspected. This is an absolute contra-indication of the cochlear implantation. Subjects with cochlear nerve deficiency are not suitable for cochlear implants.

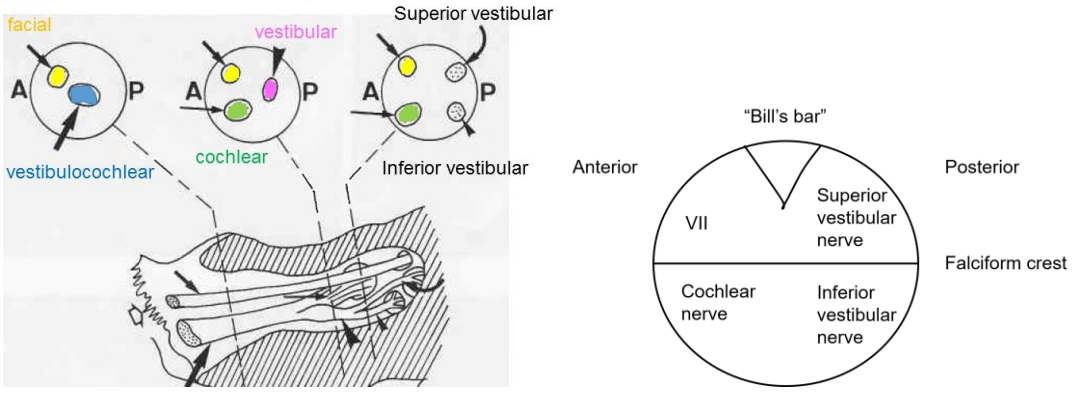


Figure 4.6: Schematic of cranial nerves VII, VIII in the internal acoustic canal from anterior (A) to posterior (P).

The dimensions of the thickness of the cochlear nerve were measured (Figure 4.7) by defining the long diameter "LD" (mm); short diameter "SD" (mm) and calculated cross-sectional area "CSA" (mm^2) is given by

$$CSA = \pi \left(\frac{LD}{2}\right)\left(\frac{SD}{2}\right) \qquad \text{Eq 4.9}$$

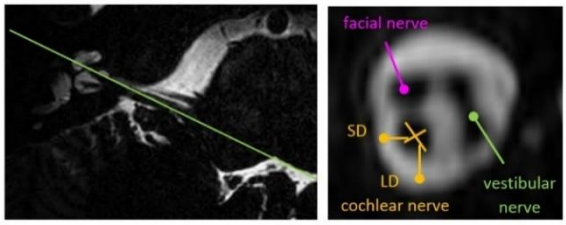


Figure 4.7: Cochlear nerve diameter LD, SD and CSA.

All sizes were measured in the mid modiolar projections by drawing a line passing through the vestibulocochlear nerve and fourth ventricle (green line in Figure 4.9). On each measurement, the mean values made by two observers were calculated. Then, intra- and inter-observer agreement were evaluated using the Pearson correlation coefficient. P<0.05 was considered statistically significant.

4.2.4 Ultra high resolution imaging of cochlea

This is the first attempt to produce a very high resolution imaging of the cochlea *in vivo* at 7.0 T. The optimization was performed on 7.0 T MR scanner using 2-channel B_1 shim setting and dielectric pads to achieve the best picture of human cochlea *in vivo*. Visualization of separate membranous compartments of the cochlea was a goal for this experiment. A smaller isotropic voxel from 0.30 mm to 0.26 mm, with varying flip angle = 80°, 90° and 100° and refocusing pulse = 90°, 100° and 120° were used. Other scan parameters were not changed and can be seen in Table 4.1.

4.3 Results

4.3.1 MR sequence for cochlear imaging

The axial 3D TSE and 3D T2W DRIVE showed well-defined structures of the inner ear auditory canal. 3D DRIVE was superior to TSE at enhancing both bony structures (internal chamber of cochlea) and cranial nerves in auditory canal,

whereas bFFE showed high contrast in these regions but gave banding artefact (as shown in Figure 4.8).

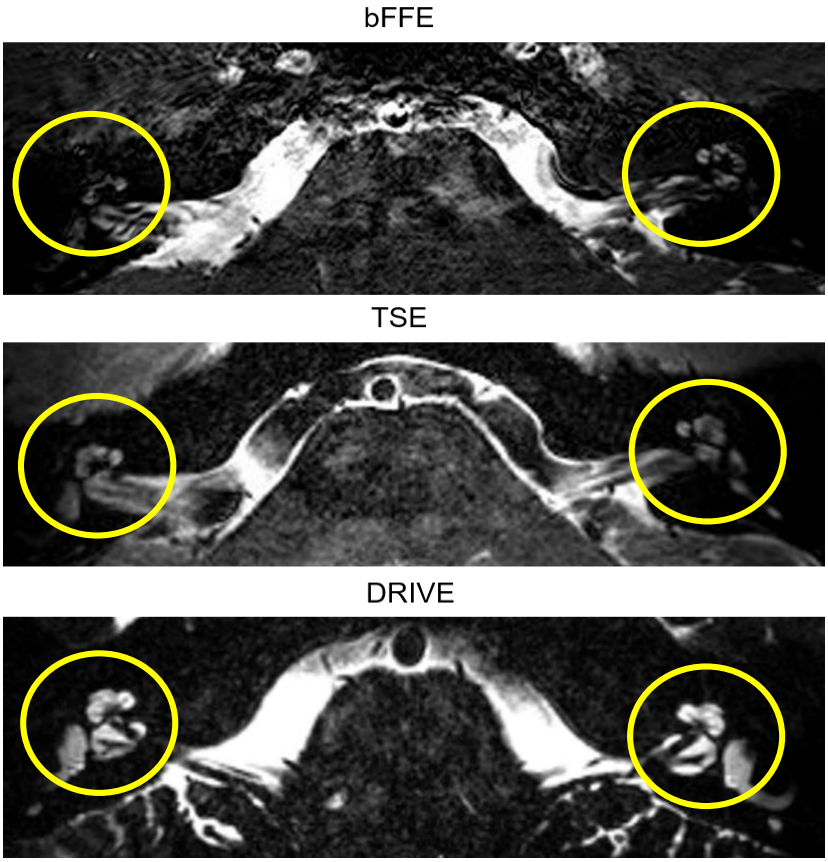


Figure 4.8: Comparison of three MR sequences in cochlear imaging at 7.0 T.

Figure 4.9 shows that subject's cochlea was visible and clearly defined with 3D DRIVE sequence at both 3.0 T and 7.0 T (n=3), but the 7.0 T images showed much better definition than routinely scanned at 3.0 T MRI. All four cranial nerves; VIII vestibular superior and inferior, cochlear and facial nerve are clearly visible. The intermediate part of cochlea (interscalar septum) was not sharply seen at 3.0 T but was demonstrated well at 7.0 T MRI. Likewise, the visibility of utricular macular, modiolus and scala media at 7.0 T were better than at 3.0 T MRI. However, Reissners membrane could not be imaged at either field *in vivo*. The comparisons of MIPs cochlear structures are shown in Figure 4.10. The increased SNR at 7.0 T provides a great opportunity for the illustration of detailed structures but improved contrast homogeneity is major challenges.

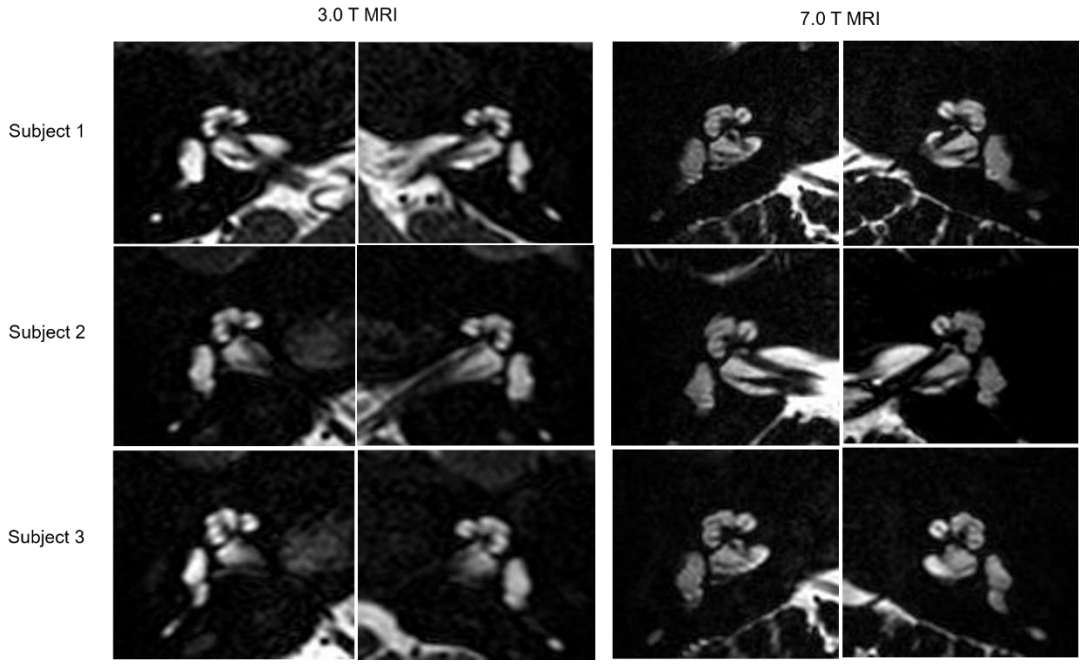


Figure 4.9: The normal anatomy of the cochlea in axial view from three subjects with 3D T2W DRIVE sequence at 3.0 T and 7.0 T.

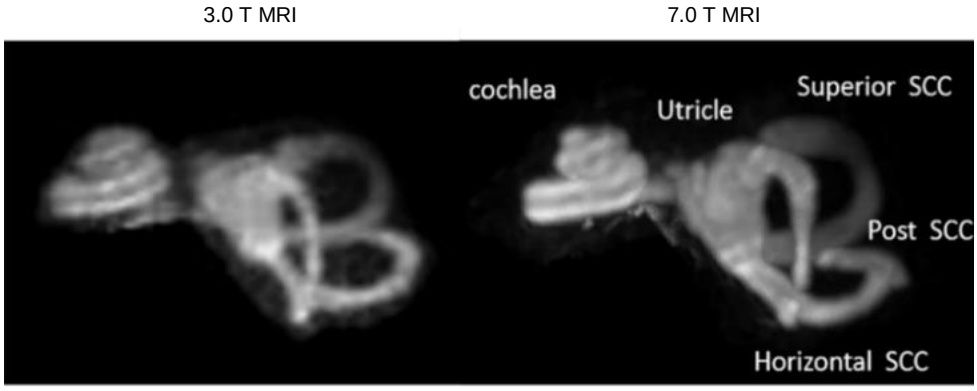


Figure 4.10: MIPs images of inner ear (from subject 1) where the semi-circular canals connect to the cochlea at both 3.0 T and 7.0 T.

4.3.2 Improved B_1 homogeneity

4.3.2.1 B_1 homogeneity with 2-channel transmit system

We carried out an experiment under the same conditions in different volunteers. Figure 4.11 shows an example of anatomical image from 3D T2W DRIVE sequence with applied 2-channel B_1 shimming at 7.0 T. The cochlear structures were markedly hyperintense and the modiolus of the the fluid-filled cochlea are also clearly seen bilaterally (yellow circle) whereas cranial nerves

appeared as hypointense signal on T_2 weighted imaging. Heavy T_2 weighting from the 3D T2W DRIVE sequence allowed the internal compartments of the cochlea to be seen clearly.

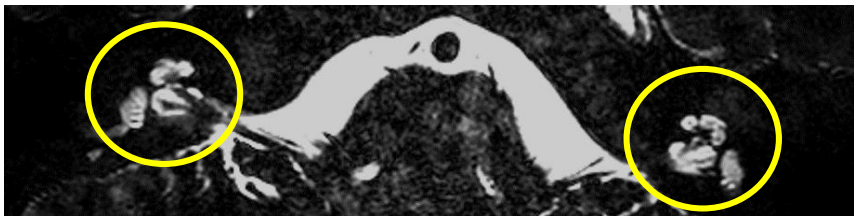


Figure 4.11: Anatomical image of the cochlea using 3D T2W DRIVE sequence and 2-channel transmit system with B_1 shimming at 7.0 T.

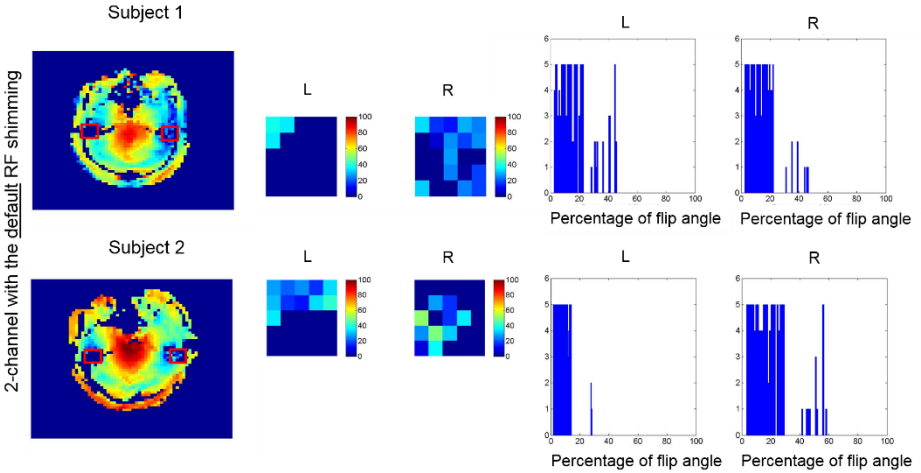
Figure 4.12 shows the improvement in the B_1 amplitude and homogeneity created by 2-channel and 8-channel B_1 shimming. On the 2-channel system, results showed a low percentage of achieved flip angle was found in both ears with the default B_1 shimming (A). Using fixed (B) and volume shimming (C) showed an increase of achieved flip angle in the subject's ear compared to A. Shim results in selected ROI on 8-channel with RF shimming GUI showed that the effect of B_1 field variation reduced. Different subjects have increased flip angle (D), differences arise from coil tuning and variable anatomy. Corresponding flip angle in the subject's ear was improved compared to standard 2-channel shimming, but not better than fixed and volume shimming with 2-channel system.

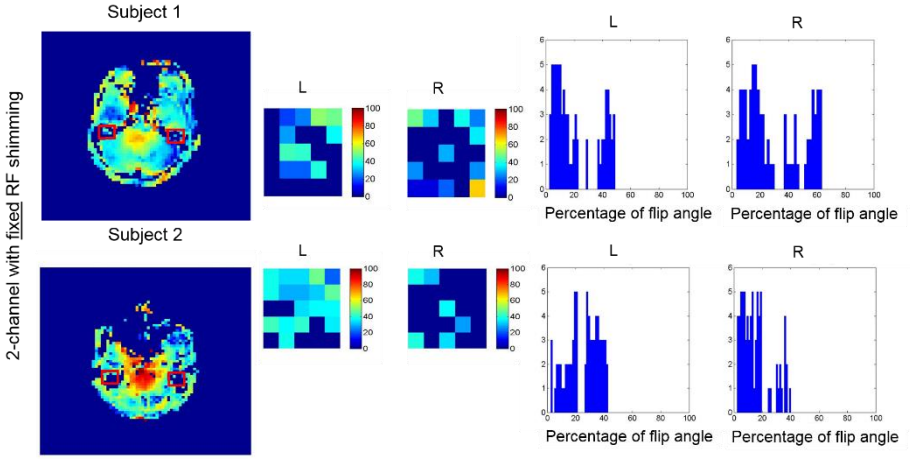
4.3.2.2 B_1 homogeneity with 8-channel transmit system

Figure 4.13 shows the normal anatomy of the cochlea on 8-channel transmit system with RF shimming GUI at 7.0 T. The detailed anatomy of cochlea and auditory nerves are not clearly visible. Some artefacts (stripe-like) with reduced bone-nerve contrast in the target area were found on the image. Moreover, the MR scanner stopped scanning with some restrictions about power regularisation that prevented the scan from finishing. This is caused by differences in power calculation between systems at 7.0 T MRI.

(A) B_1 maps *in vivo* on 2-channel with the default B_1 shimming in two subjects.

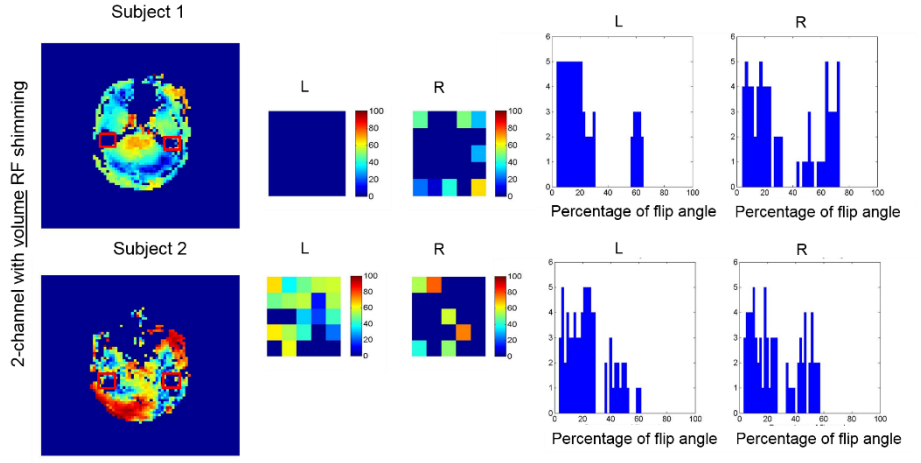
(B) B_1 maps *in vivo* on 2-channel with fixed B_1 shimming in two subjects.





(C) B_1 maps *in vivo* on 2-channel with volume B_1 shimming in two subjects.

(D) B_1 maps *in vivo* on 8-channel with RF shimming GUI in three subjects.



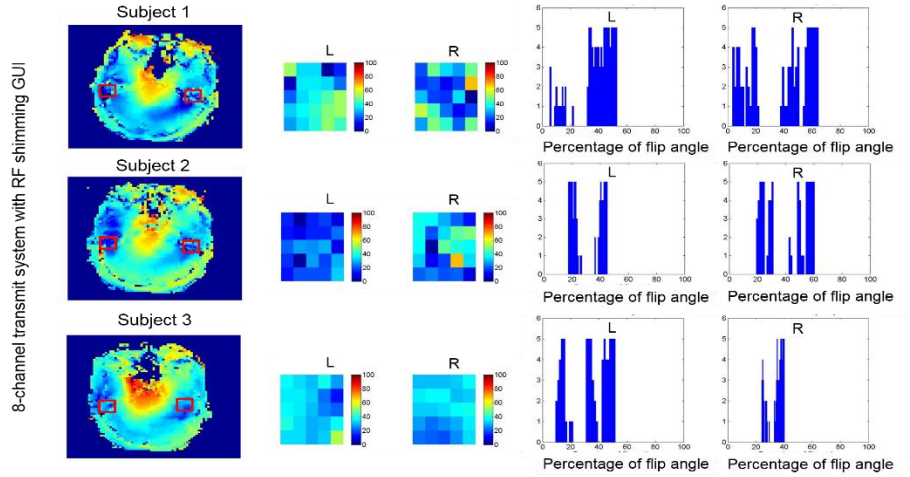


Figure 4.12: B_1 maps *in vivo* on 2-channel and 8-channel system. The percentage of achieved flip angle in the subject's ears is presented as a histogram.



Figure 4.13: Anatomical image of the cochlea from 3D T2W DRIVE sequence on 8-channel transmit system with B_1 shimming at 7.0 T.

4.3.2.3 B_1 maps with dielectric pads

The EM simulation designed to check for any changes in local or global SAR with dielectric pads showed that the centre frequency of the resonance peak shifted within 2.5 MHz and the half-width exceeded 6 MHz. The difference of selected exciting frequency was 1 MHz. The incident power was 0.0025 W. Comparing the use of pads and no pads, input power was about 0.00248 W and 0.00239 W, respectively. The maximum SAR_{10g} of the whole head was 1.775 W/kg (without pads) and 1.236 W/kg (pads), indicating that there was little effect on the distribution of electric field in the human head caused by dielectric pads (Figure 4.14-4.16).

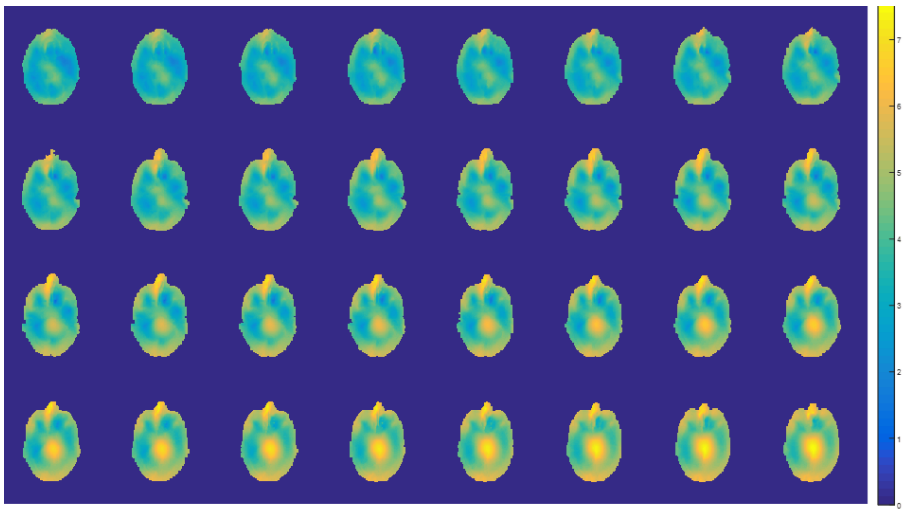


Figure 4.14: EM simulation on 2-channel transmit system in the head with no pads.

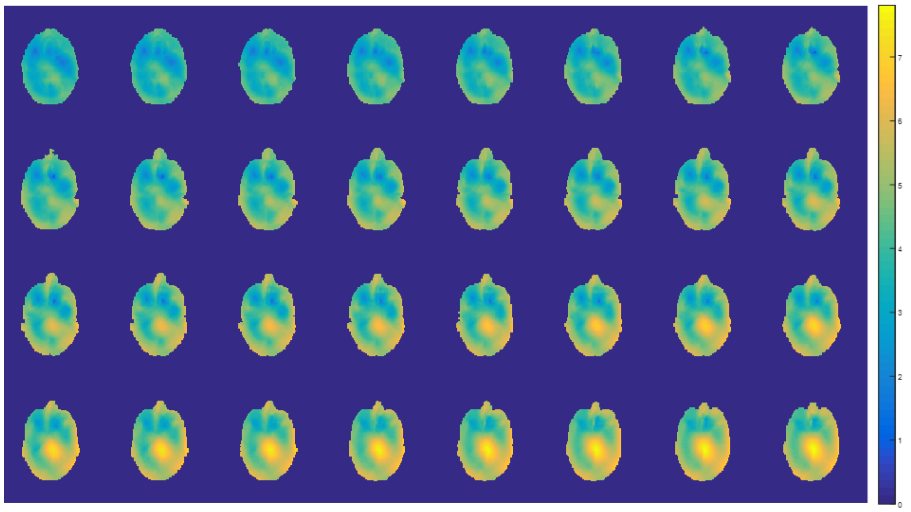


Figure 4.15: EM simulation on 2-channel transmit system in the head with the pads.

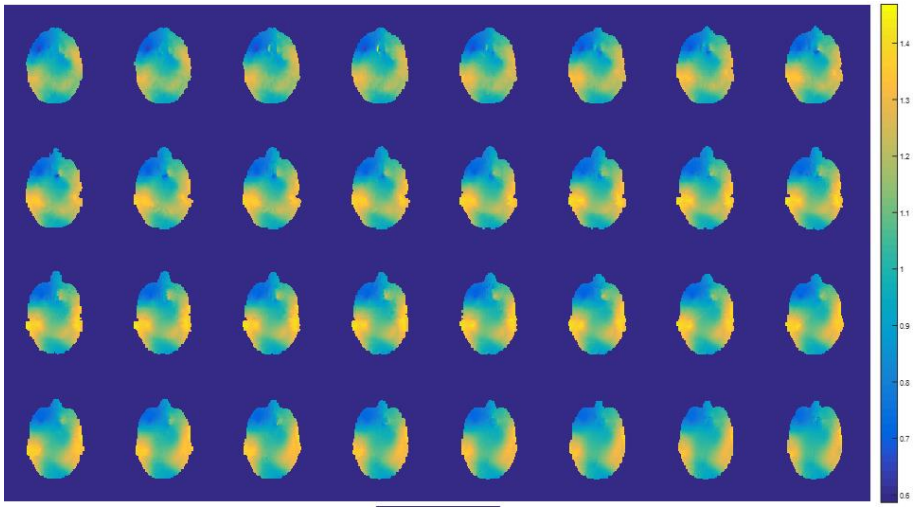


Figure 4.16: Calculation the ratio (Ratio = using pads / no pads).

The impact of using dielectric pads in cochlear imaging at 7.0 T MRI is shown in Figure 4.17. Dielectric pads improved B_1 delivery in the ears where the detailed structures of cochlea and the nerves were clearly visible on the 3D T2W DRIVE sequence.

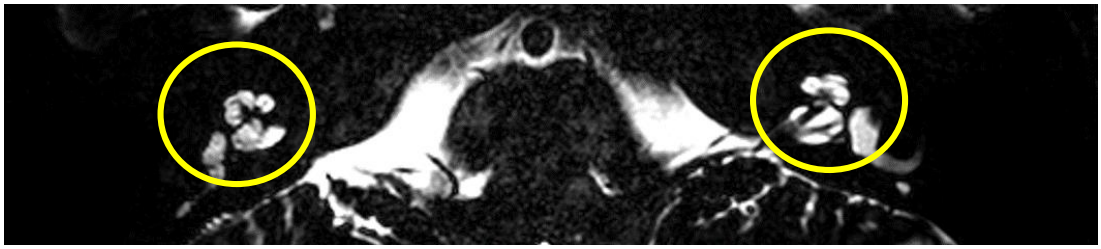
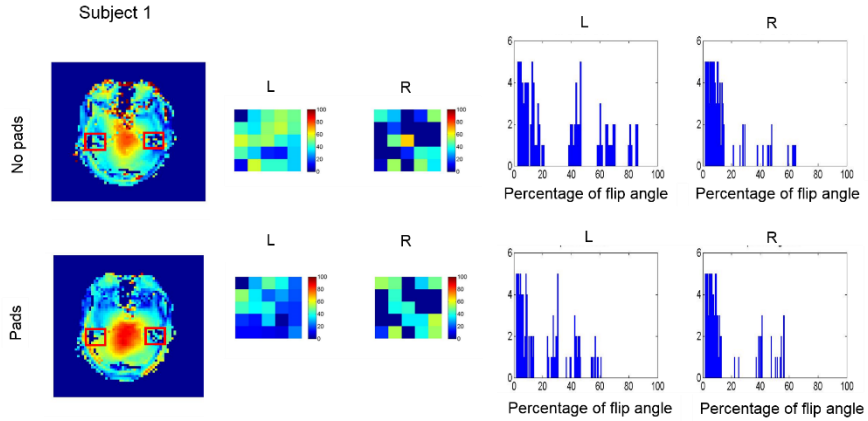
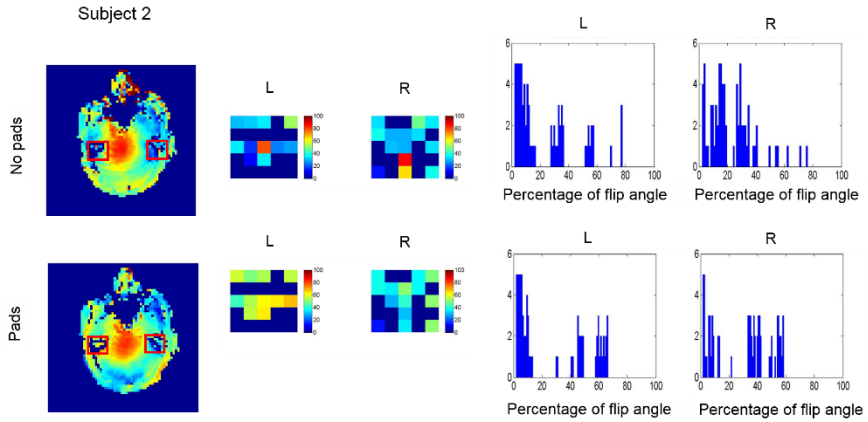


Figure 4.17: Anatomical image from 3D T2W DRIVE sequence on 2-channel with dielectric pads at 7.0 T MRI.

(E) B_1 maps *in vivo* on 2-channel with pads and no pads in subject 1.



(F) B_1 maps *in vivo* on 2-channel with pads and no pads in subject 2.



(G) B_1 field maps *in vivo* on 2-channel with combined B_1 shimming and the pads in three subjects.

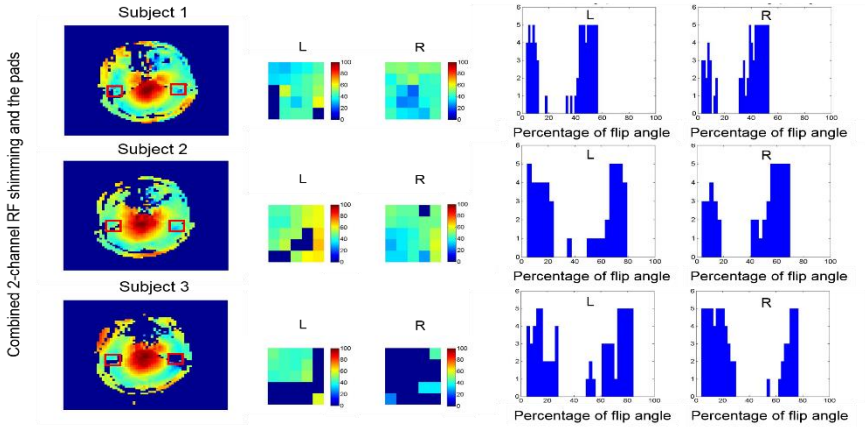


Figure 4.18: B_1maps on 2-channel with B_1 shimming and the pads. The percentage of achieved flip angle in the ears is presented as a histogram

Figure 4.18 shows the improvement of B_1 homogeneity *in vivo* cochlear imaging on 2-channel transmit system with the pads. Results showed the percentage of achieved flip angle was markedly increased in the temporal lobe. Repeated experiment in two subjects showed the higher percentage of expected flip angle in the region of low B_1 (E and F). Using combined B_1 shimming and the pads showed a further improve of B_1 homogeneity. The percentage of achieved flip angle in the subject's ears were increased considerably (G) compared to previous results.

4.3.2.4 Combined 2-channel B_1 shimming and dielectric pads

As expected, the combined use of 2-channel B_1 shimming and the dielectric pads is beneficial in increasing signal intensity in the auditory canal and presenting anatomy of cochlea in good detail (Figure 4.19). Comparison these results with histological findings confirms that 7.0 T MRI does not adequately resolve the Reissner's membrane and additional features of the basilar membrane, such as the organ of corti (Figure 4.20).

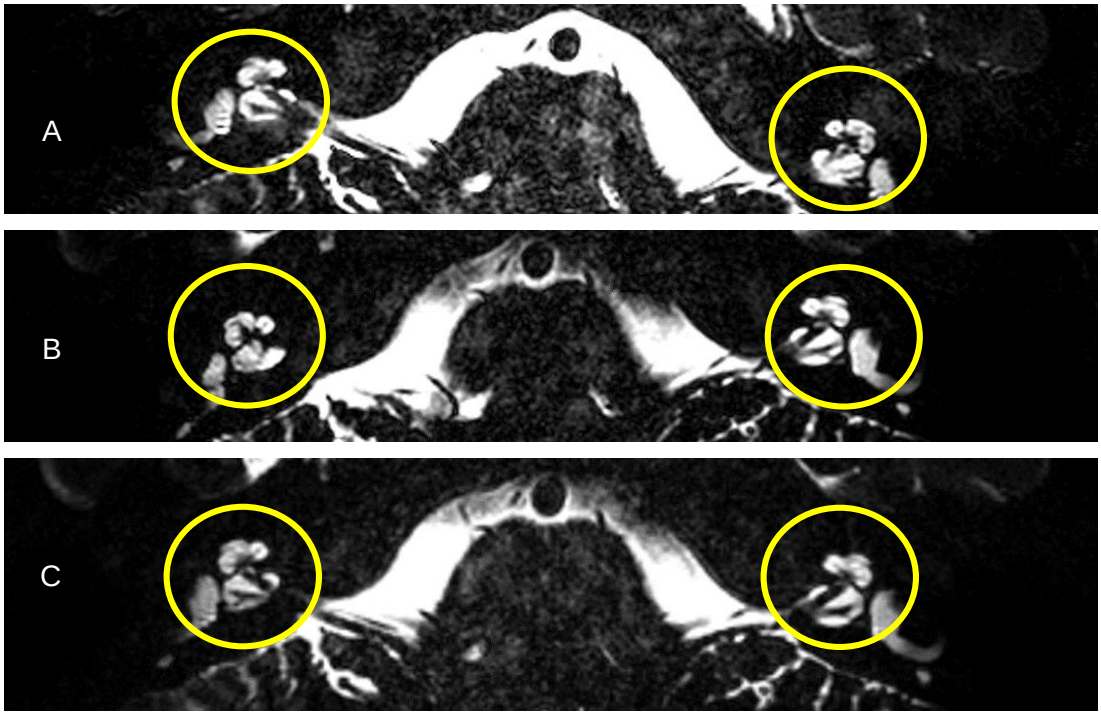


Figure 4.19: Comparing anatomical image from 3D T2W DRIVE sequence on 2-channel with default shimming (A), fixed B_1 shimming (B) and combined fixed B_1 shimming and the pads (C) at 7.0 T MRI.

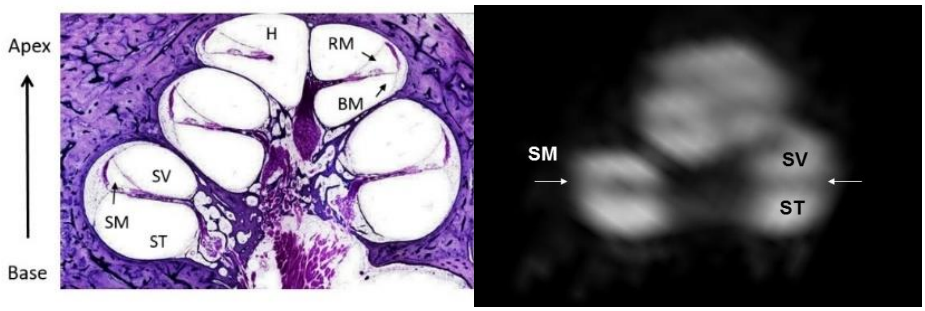


Figure 4.20: Histologic section in a spiral shape and high resolution MRI (maximum 0.26 mm isotropic resolution) from 3D DRIVE using combined 2-channel B_1 shimming with dielectric pads, M: modiolus. BM: basilar membrane; RM: Reissner's membrane, ST: scala tympani; SM: scala media; SV: scala vestibuli and H: Helicotrema (from http://clinicalgate.com/physiology-ofthe-auditory-system).

The next section of the result was concerned with SNR measurements taken from middle slice of cochlear modiolus. Figure 4.21 shows the change in SNR of both sides of cochlea comparing the pads, no pads and using both B_1 shimming and the pads. On the 2-channel transmit head coil, the highest SNR in the cochlea was found when using both B_1 shimming and the pads.

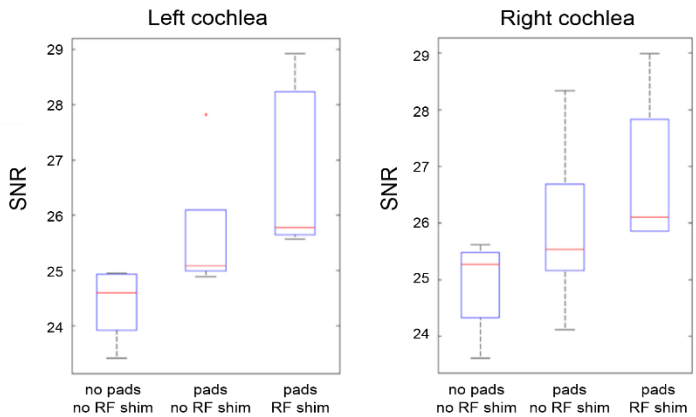


Figure 4.21: Comparing SNR in both sides of cochlea, with pads, no pads and combined B_1 shimming and the pads, respectively.

Finally, Figure 4.22 compares the imaging results for difference options. Using 2-channel B_1 shimming and the pads were well-defined intra-cochlear structures whereas shim results from 8-channel transmit system in the current configuration do not yield an image quality improvement sufficient to use *in vivo*

cochlear imaging. Low SNR and stripe-like artefacts were found in the temporal lobes, suggesting that further work is needed to improve B_1 shimming and RF power available at 7.0 T Multix system including applied dielectric pads on subject's ears during the scan.

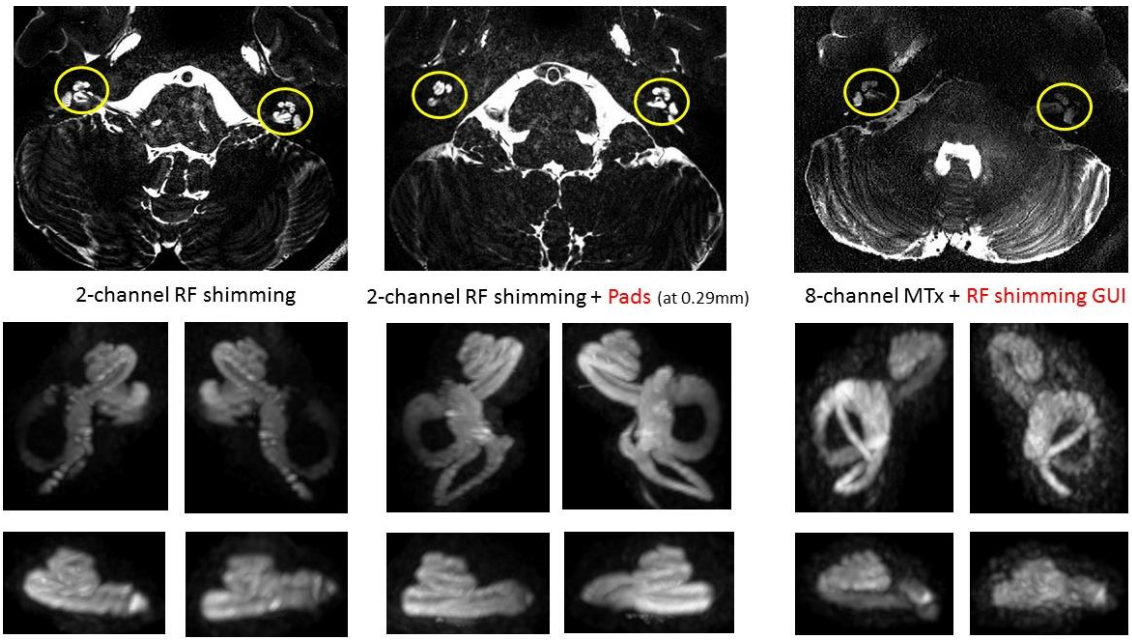


Figure 4.22: Comparing the normal cochlea anatomy at 7.0 T using 2-channel B_1 shimming (left), combined 2-channel B_1 shimming with dielectric pads at high resolution imaging (middle) and 8-channel transmit system with B_1 shimming GUI (right).

To assess image quality, the overall grading scores by two radiologists in three healthy subjects who were scanned at both 7.0 T and 3.0 T MRI are presented in Figure 4.23. From axial view in the original image, the visibility of utricular macular, interscalar septum and scala media at 7.0 T is better than 3.0 T MRI but Reissners membrane could not be imaged at either field. The intra- and inter-observer ICC values (95% confidence interval) for these results are shown in Table 4.3. The intra-observer ICC value varied from high to excellent (ICC = 0.882-0.903) for 7.0 T MRI, and it remained high (ICC = 0.941) for 3.0 T MRI, but the overall ICC inter-observer value for two observers was excellent (ICC = 0.955-0.980).

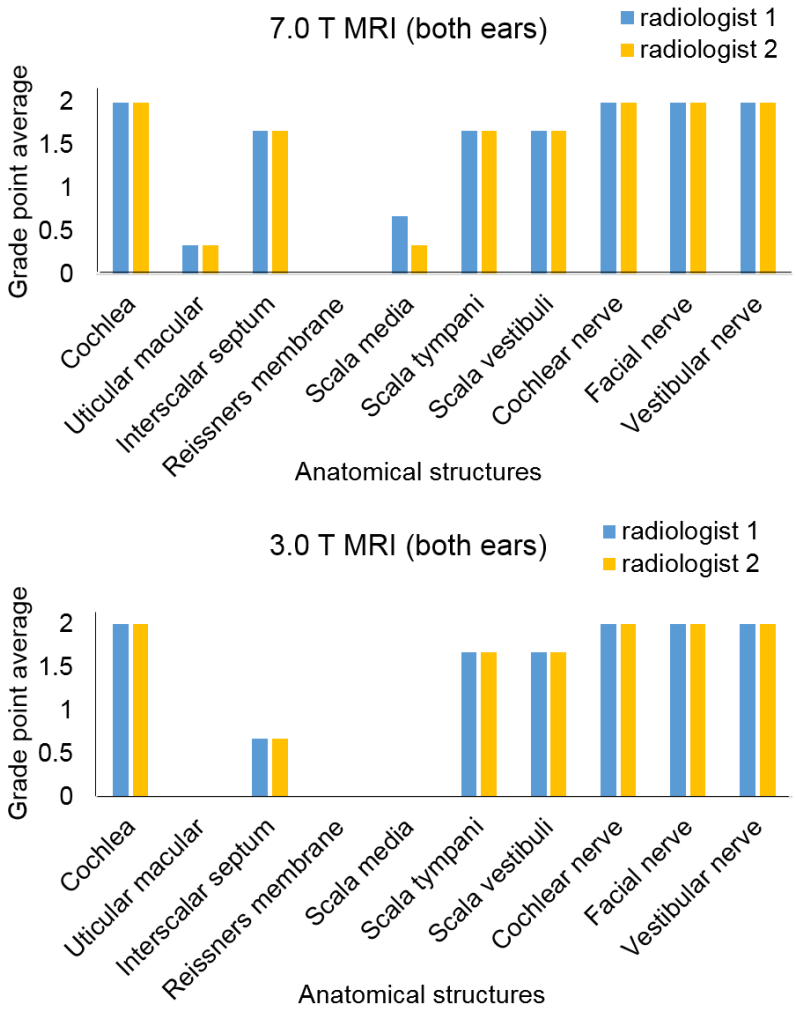


Figure 4.23: Image quality assessment by two radiologists in three healthy volunteers who were scanned at 7.0 T and 3.0 T MRI. On average, three-point grading scale ranged from 0 to 2 (0, not visible; 1, partially visible; 2, completely visible).

Table 4.3: Intra-class correlation coefficient (ICC) showing inter and intra-observer reliability

Bony cochlea and nerves		Inter-observer ICC	Intra-observer ICC	
			Observer 1	Observer 2
7.0 T MRI	L	0.955 (0.871-0.991)	0.903 (0.637-0.982)	0.882 (0.559-0.978)
	R	0.955 (0.871-0.991)	0.903 (0.637-0.982)	0.882 (0.559-0.978)
3.0 T MRI	L	0.976 (0.933-0.995)	0.941 (0.781-0.989)	0.941 (0.781-0.989)
	R	0.980 (0.944-0.996)	0.961 (0.854-0.993)	0.941 (0.781-0.989)

Note: 95% confident interval (lower bound-upper bound)

4.3.3 Normative size of the cochlea and cochlear nerve

4.3.3.1 Bony cochlea

Figure 4.24-4.25 shows the 3D rendering images and measurements of cochlear geometry for both ears in eight subjects scanned at 7.0 T. The result obtained from these measurements are shown in Figure 4.26 which indicated that spiral curled tube of cochlea had 2.5 turns around its axis. The average length of left cochlea was about 14.6±0.4 mm, width 4.4±0.2 mm, height 4.9±0.1 mm, basal lumen diameter 2.6±0.05 mm and volume 0.16±0.02 mm^3. The average length of right cochlea was about 14.2±0.4 mm, width 4.5±0.3 mm, height 4.9±0.1 mm, basal lumen diameter 2.6±0.04 mm and volume 0.16±0.02 mm^3. There was no significant difference between the results for both ears for any measurement ($p>0.05$). Measurements of cochlear geometry had a high intra-observer reliability. The ICC was 0.88 (95% CI= 0.78-0.95).



Figure 4.24: The rendering 3D view from orthogonal MIP images at 7.0 T MRI.

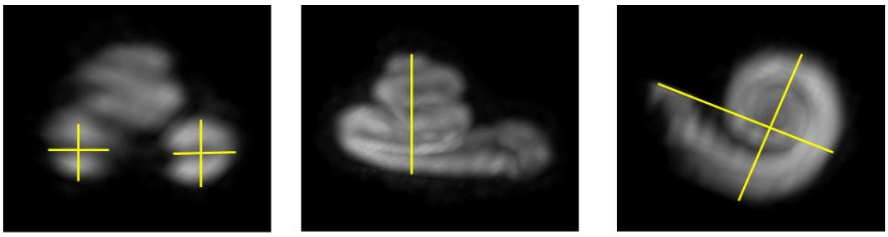


Figure 4.25: The measurement of cochlear dimension. BTLD (left), height (middle), width and length (right).

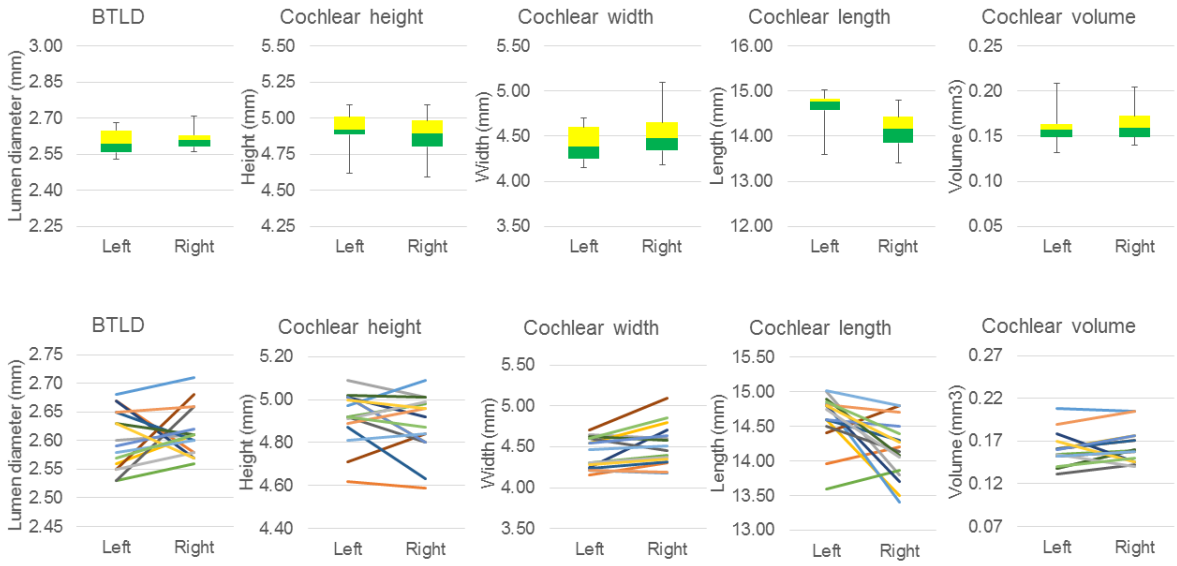


Figure 4.26: Parameters characterizing cochlea geometry across all 8 subjects.

5.3.3.2 Cochlear nerve

Figure 4.27 shows that the vestibulocochlear nerve is posterior to the facial nerve and runs laterally in the auditory canal. It was generally identified easily at 7.0 T MRI in all subjects and well-defined the facial-vestibulocochlear nerve as seen in four-chamber structure better than 3.0 T (Figure 4.28). In the cochlear nerve of 8 subjects, the mean of long diameter (LD), short diameter (SD), cross-sectional area (CSA) in the left ear were 1.31±0.07 mm, 1.06±0.08 mm, 1.1±0.1 mm^2 and those in right ear were 1.3±0.1 mm, 1.1±0.1 mm, 1.1±0.2 mm^2, respectively. The mean and standard deviation of LD, SD and CSA of cochlear nerve of both ears are shown in Figure 4.29. The measurement values of each observer and the mean of two observers are shown in Table 4.4. The ICC of intra-observer reliability tended to be higher than inter-observer reliability. The inter-observer ICC varied from moderate to high (ICC = 0.547-0.811), but the intra-observer was high. The intra-observer ICC ranged from 0.836 to 0.938 for observer 1, and observer 2 ranged from 0.768 to 0.866 (Table 4.5).

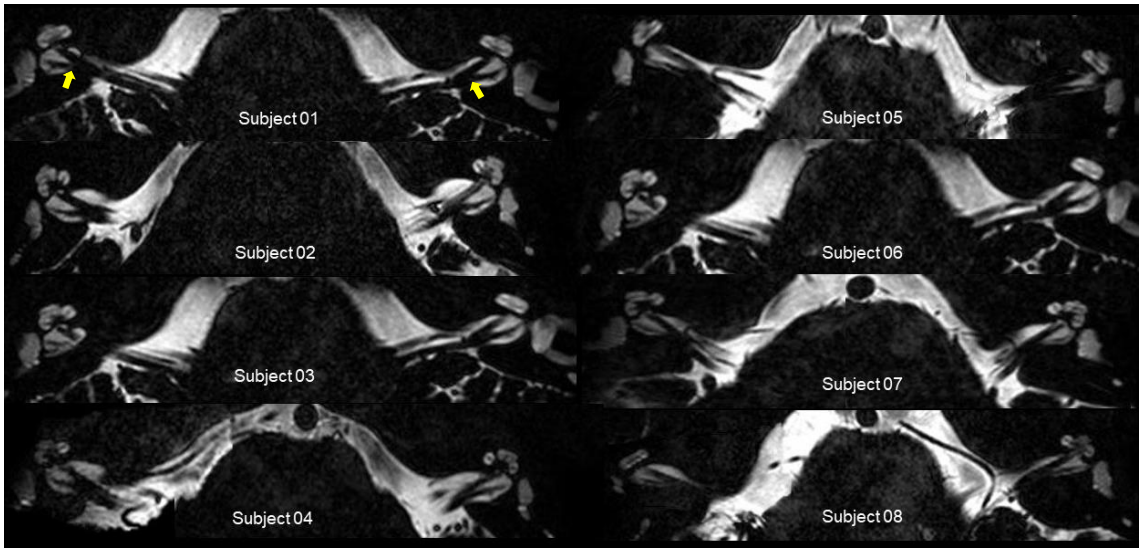


Figure 4.27: The normal anatomy of nerves supply in the auditory canal at 7.0 T MRI (across eight subjects) where the branching of the vestibulocochlear nerve "VCN" can be seen in the axial plane (yellow arrow).

Table 4.4: Cochlear nerve diameter of the eight subject's ears with normal hearing.

	LD (mm)		SD (mm)		CSA (mm^2)	
	Left	Right	Left	Right	Left	Right
Observer 1	1.32±0.07	1.28±0.11	1.08±0.10	1.07±0.13	1.12±0.14	1.08±0.18
Observer 2	1.31±0.06	1.30±0.09	1.05±0.04	1.07±0.09	1.08±0.06	1.09±0.10
Average	1.31±0.1	1.29±0.1	1.06±0.1	1.07±0.1	1.10±0.1	1.1±0.2

Table 4.5: Intra-class correlation coefficient (ICC) showing inter and intra-observer reliability

Nerve diameter		Inter-observer ICC	Intra-observer ICC	
			Observer 1	Observer 2
LD	L	0.744 (0.541-0.943)	0.843 (0.515-0.969)	0.800 (0.609-0.950)
	R	0.694 (0.421-0.943)	0.836 (0.485-0.964)	0.768 (0.541-0.947)
SD	L	0.547 (0.341-0.898)	0.905 (0.527-0.981)	0.866 (0.663-0.973)
	R	0.811 (0.638-0.957)	0.938 (0.690-0.988)	0.848 (0.591-0.981)
CSA	L	0.690 (0.419-0.930)	0.873 (0.564-0.974)	0.869 (0.649-0.930)
	R	0.594 (0.407-0.909)	0.834 (0.473-0.967)	0.777 (0.681-0.954)

Note: 95% confidence interval (lower bound-upper bound)

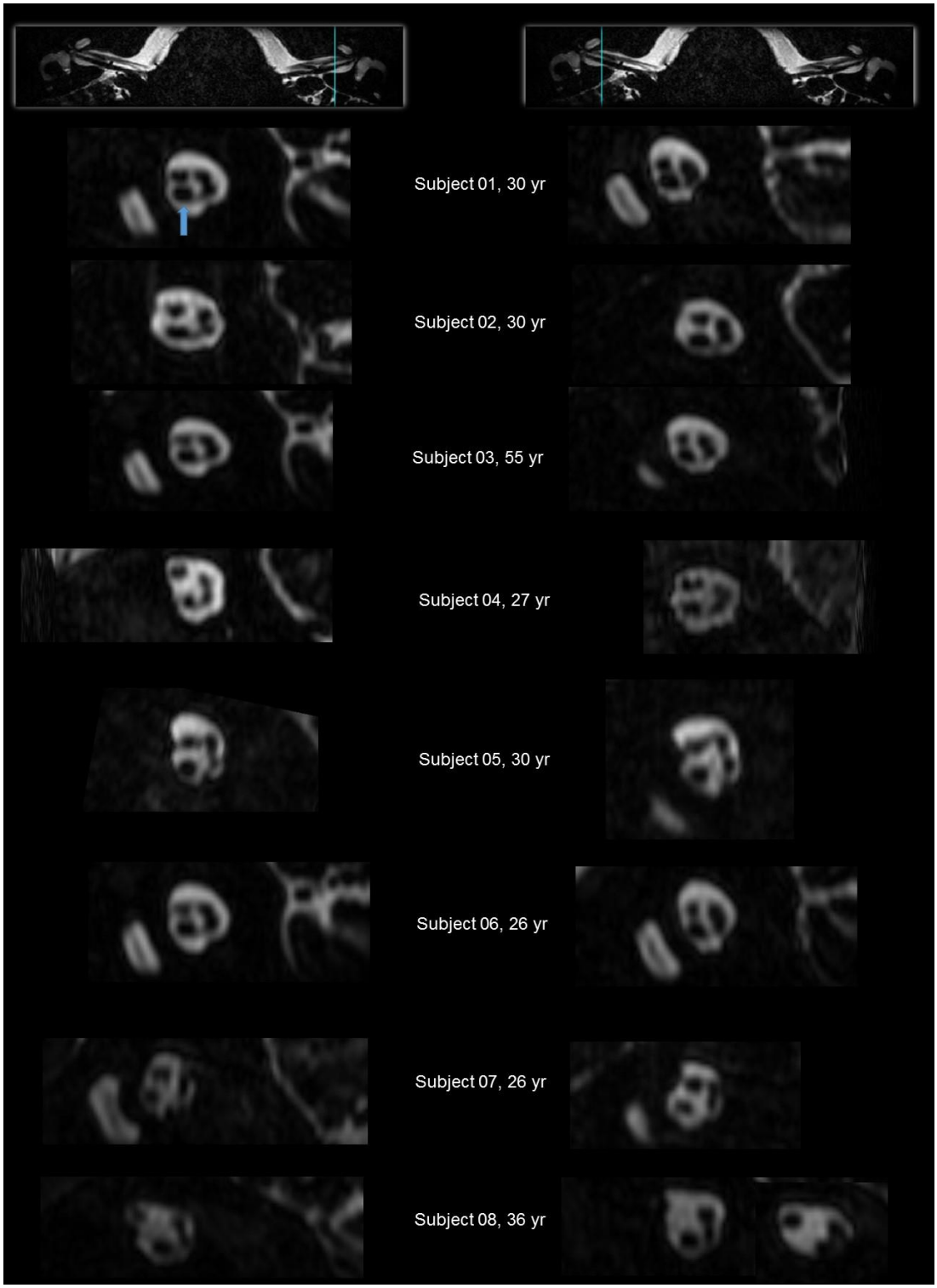


Figure 4.28: The nerve splits into 4 bundles perpendicular to the IAC; cochlear nerve (blue arrow), superior and inferior division of the vestibular nerve and facial nerve separated from each other by the falciform crest and Bill's bar similar to Figure 4.6.

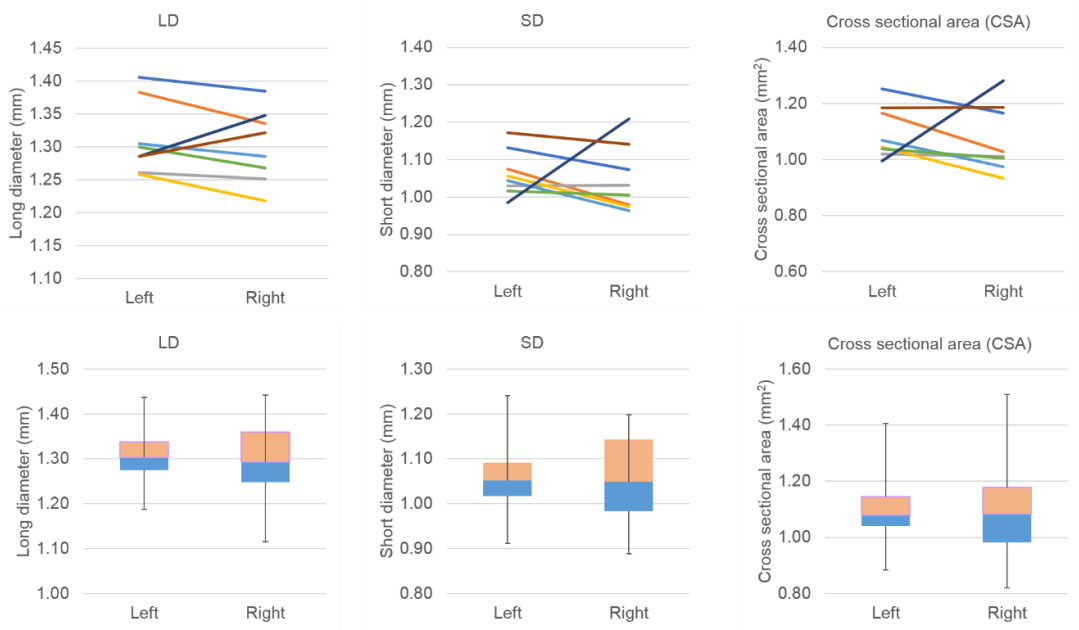


Figure 4.29: Parameters characterizing cochlea nerve diameter in healthy subjects with normal hearing (n=8).

4.3.4 Ultra high resolution imaging of cochlea

Figure 4.30 shows that using isotropic voxels of 0.26 mm^3 improved the visualisation of separated chambers in the cochlea. Figure 4.31 showed three-dimensional volume reconstruction of the cochlea *in vivo* to demonstrate the anatomical relations of the three fluid-filled compartments inside the cochlea. This is the first time these chambers have been seen *in vivo*. On a high resolution scan, branching of the vestibulocochlear nerve are also clearly seen bilaterally. Although there are variations between subjects, evaluation of the nerves in subjects with normal hearing showed the cochlear nerve tended to be larger than the superior or inferior vestibular nerves, and of similar size or larger than the facial nerve. Ultra high resolution imaging provides the detailed structures in the internal auditory canal, however, a few structures cannot visible at 7.0 T MRI including Reissner's membrane and basilar membrane. A further focus on a smaller isotropic voxel of 0.25 mm^3 with sufficient SNR and reasonable scan duration could be usefully explored in practice.

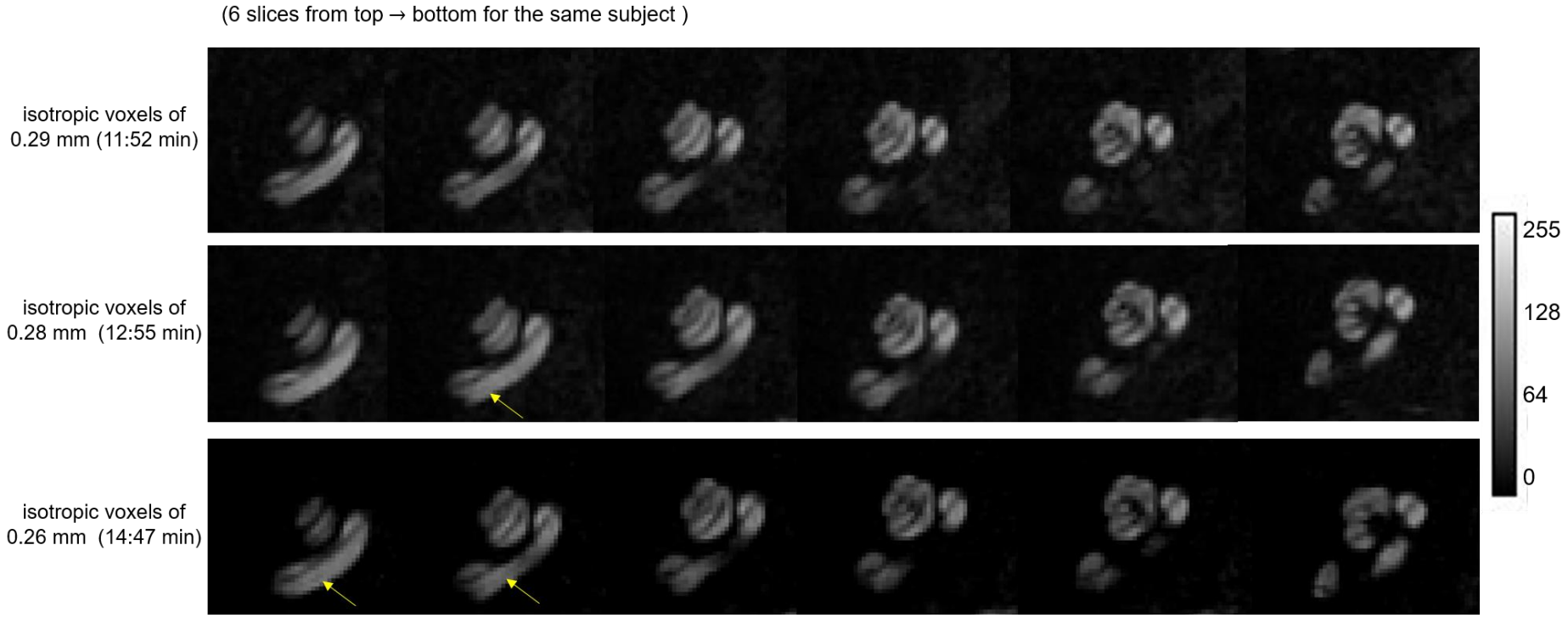


Figure 4.30: 7T MRI which optimize contrast, resolution and scan time for *in vivo* cochlear imaging on 2-channel system using B_1 shimming and the pads with isotropic resolution of 0.29 mm, 0.28 mm and 0.26 mm, respectively. Results compared over six slices in the same subject. Some evidence of the cochlear duct or the third chamber is shown with the thin black line (arrow).

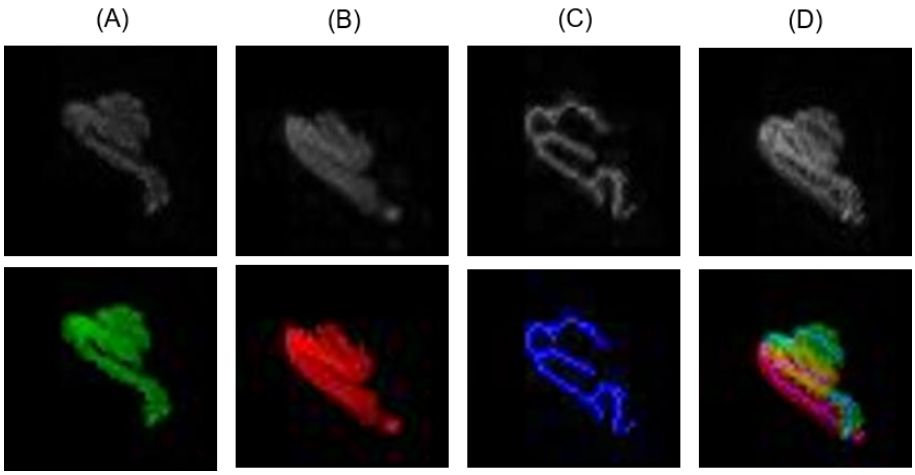


Figure 4.31: Three-dimentional (3D) volume reconstruction of individual fluid space (or scalae) in the human cochlea including the periplymphatic spaces in the scala tympani (A), the periplymphatic spaces in scala vestibuli (B), the endolymphatic space in the scala media (C) and combined all fluid-filled compartments inside the cochlea (D), respectively (from left→right).

4.4 Discussion

This study highlighted that 7.0 T MRI provides the detailed anatomic relationship of the inner ear, internal chamber of cochlea, three semi-circular canals and cranial nerves in a 14.47 minutes scan with an isotropic voxel size of 0.26 mm. Even though 3D bFFE acquisition was faster, banding artefact remained a common problem at 7.0 T where shimming was difficult. The 3D T2W DRIVE sequence provided the best signal-to-noise (SNR) and contrast-to-noise ratio (CNR) *in vivo* imaging of cochlea. A 90° recovery pulse allows magnetization back to equilibrium in a shorter amount of time. Heavy T_2 weighting from the 3D T2W DRIVE sequence was clearly demonstrated in the fine detail of intracochlear structures which matched those observed in previous studies [16, 17]. The increased sensitivity of 7.0 T has been shown to improve visualisation of these structures [25-27].

With increasing field strength, there are several changes in physical properties. B_1 field inhomogeneity leads to substantial variations of flip angle. Low

flip angles across the field of view reduces image contrast and SNR. To improve B_1^+ homogeneity using B_1 shimming, B_1 map needs to be acquired on each channel to select optimal flip angle which extends scan time. Dual refocusing echo acquisition mode (DREAM) has been proposed as a more rapid method of B_1 mapping [28]. Although using multichannel transmission (MTx) can be tailored to achieve uniform B_1 transmit filed, this yields with insufficient image quality to use *in vivo* cochlear imaging. More work on improving the image quality needs to be addressed further.

The 7.0 T MR images were clear and clinically relevant. This will useful for otology surgeons in determining the ideal insertion depth angle of the cochlear implant electrode to avoid intracochlear damage. Interestingly, we demonstrated the observation of the utricular macular and cochlear ducts (scala media) which is not visible at lower field strength [25]. These results confirmed that 7.0 T MRI with dielectric pads and RF shimming resulted in improved visualization of all three chambers of the cochlea. A good separation of internal details of cochlea better than 3.0 T which are similar to those reported by Van Egmond et al. [26, 27].

This study characterized the geometry of the cochlea in normal subjects. Our results concur with similar measurements of dimensions reported previously on high resolution CT images *in vivo* [24]. This will be important in planning cochlea implant surgery which can be complicated by abnormalities of cochlea structure. For future designs of cochlear implantations, high resolution MRI and 3D-printing technologies could be potentially considered. We also recommended that additional imaging planes such as oblique-coronal or oblique-sagittal could be beneficial for detection of pathology inside the internal auditory canal. Additionally, if MRI could detect when ossification happens, we may be in the position to avoid CT scans in young children. MRI would become the method of choice. The locations of the oval and round windows are visible on MRI. These are commonly detected on CT and are useful for surgical planning.

Measurement the cranial nerves at 7.0 T MRI showed the size of facial nerve and vestibulocochlear nerve were nearly the same. Likewise Kim et al [30] found that the relative size of the facial nerve was slightly smaller than cochlear nerve (88% of the 58 cases). It can be assumed that reduced size of cochlear nerve is one of the primary concerns of selecting candidates for cochlear implantation.

Increasing the image SNR on 2-channel system was found when using combined B_1 shimming and dielectric pads, which leads to an improved temporal signal-to-noise ratio (tSNR) at 7.0 T. These results are consistent with data obtained by Triantafyllou et al. [32]. Increased field strength also tends to bring net tSNR benefits at high spatial resolution scan.

The use of dielectric pads over both ears and B_1 shimming shows an improvement in image quality at 7.0 T MRI. These results also showed that image contrast varied between subjects due to different head size and geometry. A person with a small head tends to produce better uniformity with higher SNR in the cochlea than in a big head. However, in particular anatomic location where is near interfaces of substance of different magnetic susceptibilities, stripe-like artefacts still occur near the first turn of cochlea and at the air-fluid interfaces near the round and oval windows.

Better visualization of the vestibular system with respect to the magnetic field will also be important for understanding the origin of vertigo effects in some people exposed to strong magnetic field [29, 31]. High resolution *in vivo* imaging at 7.0 T provided greater anatomy of a crista ampullaris in a semicircular canal (Figure 4.32). This structure contains the vestibular receptors (a group of hair cells) respond to head rotation. The focus remains on the interaction mechanism underlying magnetic field which sense the movement of cupula and otolithic membrane housed in the ampulla.

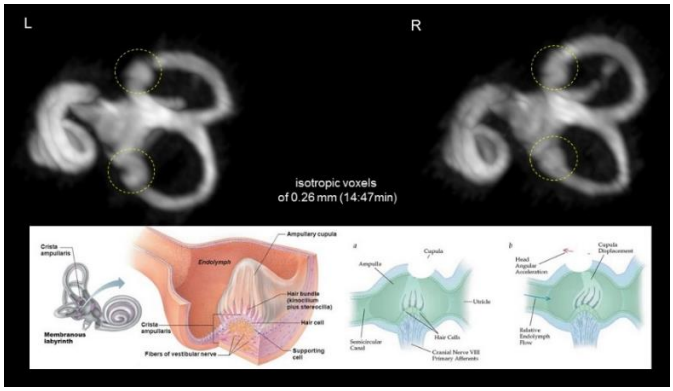


Figure 4.32: Showing observed crista ampullaris in a semicircular canal at high resolution imaging at 7.0 T *in vivo*.

4.5 Conclusion

In conclusion, this study has shown that the use of the 3D T2W DRIVE sequence with 2-channel B_1 shimming and dielectric pads allows very high resolution *in vivo* imaging of internal structure of cochlea and vestibulocochlear nerve at isotropic voxels of 0.26 mm in a 14 minute 47 second scan duration. On the highest resolution scans at 7.0 T, we observed some evidence of the cochlear duct (or scala media). This is the first time anyone has seen the third chambers *in vivo*. The optimised 7.0 T MRI protocols showed better identification anatomic details in the bony cochlea and nerves as compared with 3.0 T MRI. Ultra high field MRI has become attractive to evaluate complex clinical scenarios. A study with more focus on improving B_1 transmit field on 8-channel transmit system needs to be undertaken in future.

Bibliography

[1] L. Monasta, L. Ronfani, F. Marchetti, M. Montico, L. Brumatti, A. Bavcar, D. Grasso, C. Barbiero, and G. Tamburlini, “Burden of disease caused by otitis media: Systematic review and global estimates,” *PLoS ONE*, vol. 7, no. 4. 2012.

[2] S. H. Hayes, D. Ding, R. J. Salvi, and B. L. Allman, “Anatomy and physiology of the external, middle and inner ear,” *Handb. Clin. Neurophysiol.*, vol. 10, pp. 3–23, 2013.

[3] Ö. Özdoğmuş, O. Sezen, U. Kubilay, E. Saka, U. Duman, T. Şan, and S. Çavdar, “Connections between the facial, vestibular and cochlear nerve bundles within the internal auditory canal,” *J. Anat.*, vol. 205, no. 1, pp. 65–75, 2004.

[4] J. Zhang, W. Wei, J. Ding, T. Roland, S. Manolidis, and N. Simaan, “Inroads toward robot-assisted cochlear implant surgery using steerable electrode arrays,” in *Otology and Neurotology*, 2010, vol. 31, no. 8, pp. 1199–1206.

[5] M. H. Hohman and D. D. Backous, “Techniques for cochlear implant electrode placement in the ossified cochlea,” *Oper. Tech. Otolaryngol. - Head Neck Surg.*, vol. 21, no. 4, pp. 239–242, 2010.

[6] B. M. Verbist, “Imaging of sensorineural hearing loss: A pattern-based approach to diseases of the inner ear and cerebellopontine angle,” *Insights into Imaging*, vol. 3, no. 2. pp. 139–153, 2012.

[7] F. Padormo, A. Beqiri, J. V. Hajnal, and S. J. Malik, “Parallel transmission for ultrahigh-field imaging,” *NMR in Biomedicine*, vol. 29, no. 9. pp. 1145–1161, 2016.

[8] J. W. Casselman, R. Kuhweide, M. Deimling, W. Ampe, I. Dehaene, and L. Meeus, “Constructive interference in steady state-3DFT MR imaging of the

inner ear and cerebellopontine angle," *Am. J. Neuroradiol.*, vol. 14, no. 1, pp. 47–57, 1993.

[9] P. Hans, A. J. Grant, R. D. Laitt, R. T. Ramsden, A. Kassner, and A. Jackson, "Comparison of three-dimensional visualization techniques for depicting the scala vestibuli and scala tympani of the cochlea by using high-resolution MR imaging," *Am. J. Neuroradiol.*, vol. 20, no. 7, pp. 1197–1206, 1999.

[10] I. A. Zealley, R. C. Cooper, K. M. A. Clifford, R. S. D. Campbell, A. J. Potterton, I. Zammit-Maempel, C. J. Baudouin, and A. Coulthard, "MRI screening for acoustic neuroma: A comparison of fast spin echo and contrast enhanced imaging in 1233 patients," *Br. J. Radiol.*, vol. 73, no. 867, pp. 242–247, 2000.

[11] R. L. Daniels, C. Swallow, C. Shelton, H. C. Davidson, C. S. Krejci, and H. R. Harnsberger, "Causes of unilateral sensorineural hearing loss screened by high-resolution fast spin echo magnetic resonance imaging: review of 1,070 consecutive cases.," *Am. J. Otol.*, vol. 21, no. 2, pp. 173–80, 2000.

[12] J. Hennig, a Nauerth, and H. Friedburg, "RARE imaging: a fast imaging method for clinical MR.," *Magn. Reson. Med.*, vol. 3, no. 6, pp. 823–833, 1986.

[13] G. E. Valvassori, F. Garcia Morales, E. Palacios, and G. E. Dobben, "MR of the normal and abnormal internal auditory canal.," *AJNR. Am. J. Neuroradiol.*, vol. 9, no. 1, pp. 115–119, 1988.

[14] H. Carr, "Steady-State Free Precession in Nuclear Magnetic Resonance," *Phys. Rev.*, vol. 112, no. 5, pp. 1693–1701, 1958.

[15] G. B. Chavhan, P. S. Babyn, B. G. Jankharia, H.-L. M. Cheng, and M. M. Shroff, "Steady-State MR Imaging Sequences: Physics, Classification, and Clinical Applications," *RadioGraphics*, vol. 28, no. 4, pp. 1147–1160, 2008.

[16] E. Ciftci, Y. Anik, A. Arslan, G. Akansel, T. Sarisoy, and A. Demirci, "Driven equilibrium (drive) MR imaging of the cranial nerves V-VIII: Comparison with

the T2-weighted 3D TSE sequence," *Eur. J. Radiol.*, vol. 51, no. 3, pp. 234–240, 2004.

[17] S. B. Jun, H. J. Kim, J. Y. Yoo, T. K. Sung, P. Jeon, H. K. Keon, S. K. Sam, H. J. Yong, and J. Lee, "MR imaging of the internal auditory canal and inner ear at 3.0 T: Comparison between 3D driven equilibrium and 3D balanced fast field echo sequences," *Korean J. Radiol.*, vol. 9, no. 3, pp. 212–218, 2008.

[18] V. L. Yarnykh, "Actual flip-angle imaging in the pulsed steady state: A method for rapid three-dimensional mapping of the transmitted radiofrequency field," *Magn. Reson. Med.*, vol. 57, no. 1, pp. 192–200, 2007.

[19] K. Setsompop, L. L. Wald, V. Alagappan, B. A. Gagoski, and E. Adalsteinsson, "Magnitude least squares optimization for parallel radio frequency excitation design demonstrated at 7 tesla with eight channels," *Magn. Reson. Med.*, vol. 59, no. 4, pp. 908–915, 2008.

[20] W. M. Teeuwisse, W. M. Brink, and A. G. Webb, "Quantitative assessment of the effects of high-permittivity pads in 7 Tesla MRI of the brain," *Magn. Reson. Med.*, vol. 67, no. 5, pp. 1285–1293, 2012.

[21] W. M. Brink, A. M. A. van der Jagt, M. J. Versluis, B. M. Verbist, and A. G. Webb, "High Permittivity Dielectric Pads Improve High Spatial Resolution Magnetic Resonance Imaging of the Inner Ear at 7 T.," *Invest. Radiol.*, vol. 49, no. 5, pp. 271–277, 2014.

[22] A. G. Webb, "Dielectric Materials in Magnetic Resonance," *Concepts Magn. Reson. Part A*, vol. 38(a), no. 4, pp. 148–184, 2011.

[23] F. Pochini Sobrinho, P. R. Lazarini, H. J. Yoo, L. Abreu Junior, and S. Meira Ade, "A method for measuring the length of the cochlea through magnetic resonance imaging," *Braz J Otorhinolaryngol*, vol. 75, no. 2, pp. 261–267, 2009.

[24] P. Pelliccia, F. Venail, a Bonafé, M. Makeieff, G. Iannetti, M. Bartolomeo,

and M. Mondain, “Cochlea size variability and implications in clinical practice.,” *Acta Otorhinolaryngol. Ital.*, vol. 34, no. 1, pp. 42–9, 2014.

[25] M. A. Van Der Jagt, W. M. Brink, M. J. Versluis, S. C. A. Steens, J. J. Briaire, A. G. Webb, J. H. M. Frijns, and B. M. Verbist, “Visualization of Human Inner Ear Anatomy with High-Resolution MR Imaging at 7.0 T : Initial Clinical Assessment,” *AJNR Am J Neuroradiol*, vol. Feb, no. 36, pp. 378–383, 2015.

[26] S. L. van Egmond, F. Visser, F. a Pameijer, and W. Grolman, “In Vivo Imaging of the Inner Ear at 7.0 T MRI: Image Evaluation and Comparison With 3.0 T.,” *Otol. Neurotol.*, vol. 36, no. 4, pp. 687–693, 2015.

[27] S. L. van Egmond, F. Visser, F. a Pameijer, and W. Grolman, “Ex vivo and in vivo imaging of the inner ear at 7 Tesla MRI.,” *Otol. Neurotol.*, vol. 35, no. 4, pp. 725–9, 2014.

[28] K. Nehrke and P. Börnert, “DREAM - A Novel Approach for Robust, Ultra-Fast, Multi-Slice,” *Imaging*, 2012.

[29] O. S. Mian, Y. Li, A. Antunes, P. M. Glover, and B. L. Day, “Effect of head pitch and roll orientations on magnetically induced vertigo,” *J. Physiol.*, vol. 594, no. 4, pp. 1051–1067, 2016.

[30] H. S. Kim, D. I. Kim, I. H. Chung, W. S. Lee, and K. Y. Kim, “Topographical relationship of the facial and vestibulocochlear nerves in the subarachnoid space and internal auditory canal,” *Am. J. Neuroradiol.*, vol. 19, no. 6, pp. 1155–1161, 1998.

[31] P. M. Glover, I. Cavin, W. Qian, R. Bowtell, and P. A. Gowland, “Magnetic-field-induced vertigo: A theoretical and experimental investigation,” *Bioelectromagnetics*, 2007.

[32] C. Triantafyllou, R. D. Hoge, G. Krueger, C. J. Wiggins, A. Potthast, G. C. Wiggins, and L. L. Wald, “Comparison of physiological noise at 1.5 T, 3 T and 7 T and optimization of fMRI acquisition parameters,” *Neuroimage*, 2005.

Chapter 5 *In vivo* imaging of the Nucleus Basalis of Meynert (NBM) at High Field MRI

5.1 Introduction

The subcommisural basal forebrain region located above and parallel to the optic chiasm, posterior to the amygdala and immediately below the anterior commissure is of strategic importance in health and disease. Within this brain region there are hyperchromic magnocellular cholinergic neurones which project widely to the neocortex [1]. The greatest number of cholinergic neurones are found anteriorly in the subcommisural and subpallidal regions within an area termed the “nucleus basalis of Meynert” (NBM). Due to the complex internal structure and small size of the NBM, analysis of the entire nucleus will not be possible in many histopathological and imaging studies. Therefore, a subdivisonal scheme is required to simplify and standardise future work. Following extensive review of several human brain atlases and NBM publications, separation of the NBM into anterior, intermediate NBM subsectors has been developed [1]. The subdivisions correspond to the original nucleus basalis (Ch4) classification and attempts to separate sections of the NBM based on their cortical projections. The sampling protocol used within this study corresponds to this schema. The NBM is of strategic importance in health and disease as the primary source of acetylcholine to the neocortex, a neurotransmitter required for associative learning, memory formation and attention.

Cholinergic deficits are known to produce memory and attentional deficits. The NBM is particularly susceptible to the pathological deposition of misfolded tau proteins, which results in neuronal cell death, early in the course of Alzheimer's dementia (AD) [2]. There is stepwise reduction in NBM cell number or volume as individuals' progress from cognitively normal to mild cognitive impairment and AD. This cell loss occurs over a long latent period which coincides with the pre-symptomatic and mild cognitive impairment phases of AD and may represent a window where at-risk individuals can be identified and cholinergic ageism (with cholinesterase inhibitors) initiated, which may delay or prevent the onset of dementia [3, 4]. An accurate novel structural imaging biomarker with which the integrity of the basal forebrain cholinergic nuclei can be assessed represents an unmet clinical need. However, the findings of these studies are limited by a number of methodological flaws including the use of probabilistic maps, lack of pathological-anatomical validation and non-uniform sampling of the NBM. Therefore, the aim of this work is to produce improved contrast resolution of the NBM to ultimately provide anatomical localisation for structural imaging studies and deep brain stimulation electrode placement *in vivo*.

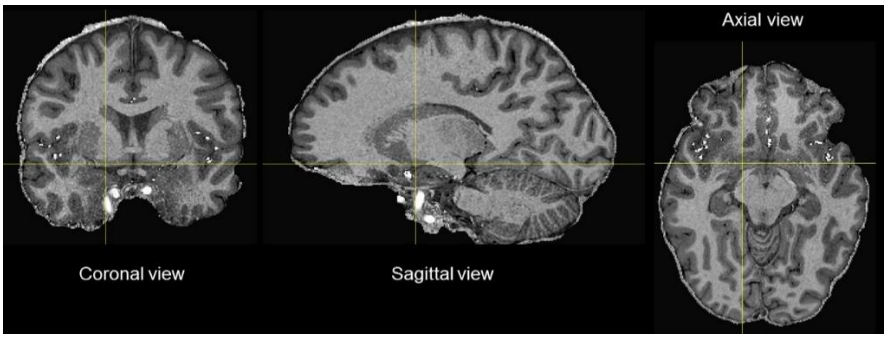


Figure 5.1: Crosshair lines represent the human NBM in three orthogonal views at 7.0 T MRI which appeared as hypointense on T_1 weighted PSIR image.

The NBM has an irregular shape and is not sharply delineated. It is located inferior to the globus pallidus which is below the anterior commissure (Figure 5.1). The nucleus can be traced superiorly and laterally to the anterior portion of the

hypothalamus. Other studies [5-7] consider the NBM to be synonymous with the substantia innominata, or alternatively the region is described as the substantia innominata-nucleus basalis complex. Figure 5.2 shows the NBM contains cholinergic neuron which releases acetylcholine to connect to other parts of the brain.

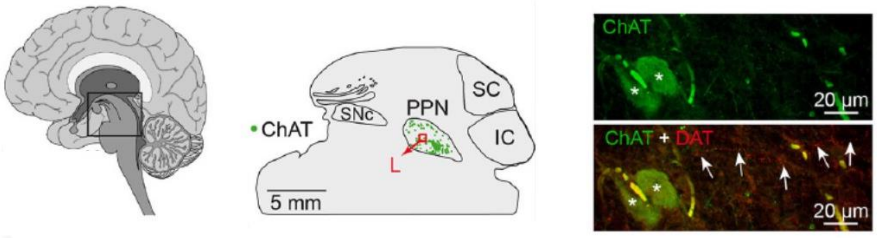


Figure 5.2: The decrease of cholinergic neuron is associated with dysfunction, fibre degeneration, and cell death in AD [8, 9]. In histochemistry, the NBM contained cholinergic cells (Choline acetyltransferase “ChAT”, green) and the dopamine active transport (Dopamine N-acetyltransferase “DAT”, red) involved in communication between brain cells [7].

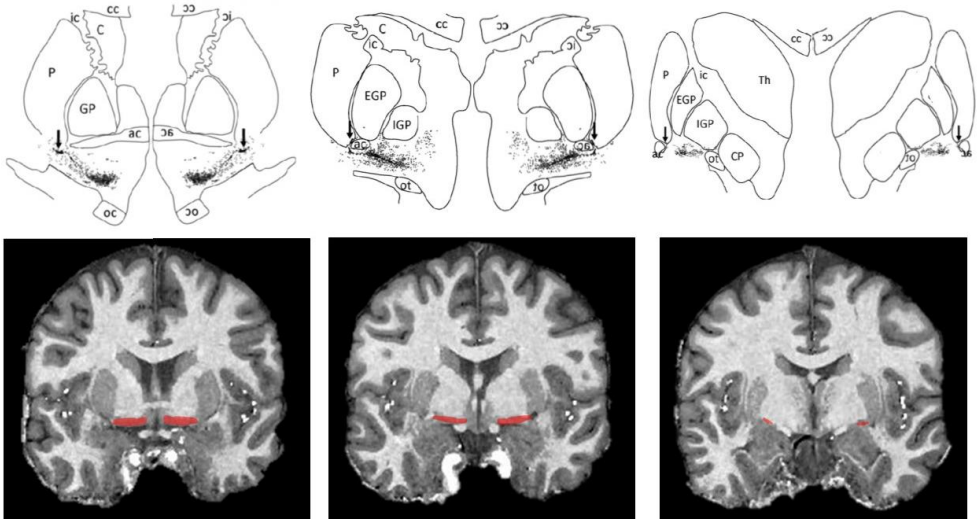


Figure 5.3: Schematic of the nucleus basalis of Meynert in coronal section through the corpus striatum [10] and red shaded area indicates corresponding T_1 weighted MRI of the NBM. The slice shows the anterior, intermediated and posterior segment, respectively.

The reduction of NBM cholinergic neurons or malfunction in the cholinergic system leads to difficulties with memory and attention in people with AD. Accordingly, histological examination showed that the highest concentration of cholinergic neurons in the NBM appeared both beneath and inferior to the medial

part of anterior commissure (Figure 5.3-5.4). Post mortem studies have shown the loss of cholinergic neurons associated with AD [11] due to the reduction of choline acetyltransferase activity related to degree of cognitive decline and progressive course of AD [12].

Around the early 1990s, small-scale research and case studies began to use conventional 1.5 T MRI to define the anatomy of the human NBM and measure morphological change in normal aging and patients with preclinical and clinical advances in AD [13]. Atrophy of the NBM is not specific for AD, but also appears in normal aging, vascular dementia and Parkinson disease with dementia [14]. It was observed that the degree of NBM atrophy was higher in the Parkinson's disease with dementia, while it was less in vascular dementia.

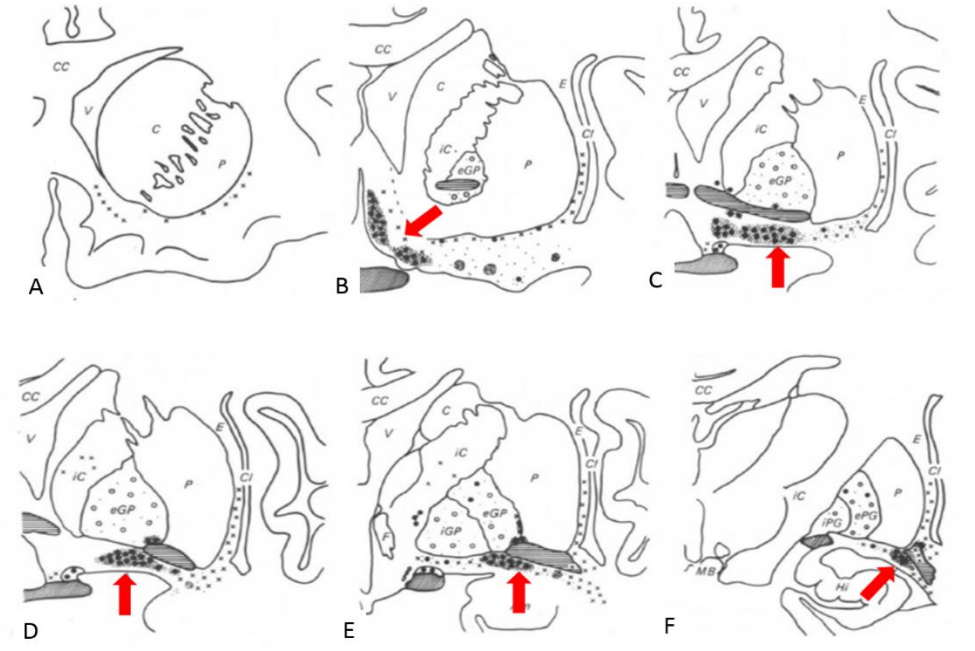


Figure 5.4: (A-F, anterior → posterior). Schematic shows the distribution of Acetylcholinesterase (AChE) staining in the NBM and subcortical structures which makes a cholinergic cell communication in these regions. Red arrows show AChE-stained neuropil and crosses AChE-stained fibres. Horizontal shading represents the anterior commissure and diagonal shading shows the optic tract. Abbreviations used in the figures; Am, amygdala; C, caudate nucleus; CC, corpus callosum; Cl, claustrum; E, external capsule; eGP, external globus pallidus; F, fornix; Hi, anterior hippocampus; iC, internal capsule; iGP, internal globus pallidus; MB, mammillary body; P, putamen; V, ventricle [15].

Damage of cholinergic neurons showed that the degree of atrophy as follows: Parkinson disease with dementia > AD > vascular dementia > normal aging [16, 17].

To address these limitations, including subject variability and limited in spatial resolution, 3.0 T MRI has been used for imaging the NBM *in vivo* to give information about microstructure and functional connectivity. High field MRI was selected to generate new insights into disease involvement associated with subtle changes in the NBM (Figure 5.3). From the measurements of anterior commissure (AC) thickness, Moon et al. [18] found additional clinical clues indicating AD at 3.0 T MRI. The average thicknesses of the bilateral NBM was not significantly difference in AD and non-AD, whereas AC thickness in AD group was significantly lower than healthy older subjects (mean age 68 years). Likewise, the study by Colloby et al. [19] found that volumetric grey matter (GM) changes in the NBM using T_1 weighted image showed significant loss of bilateral grey matter in AD groups relative to normal aging (mean age 77 years). Tracking neuronal shrinkage in the NBM with high field MRI has a great potential to investigate subtle changes and predict future disease trajectory. Although the 7.0 T MRI offers advantages for neuroimaging [20] however, this comes with physical challenges of inhomogeneous transmit fields, higher SAR, increased water-fat shift due to the higher proton Larmor frequency, increased severity of susceptibility effects resulting in larger geometric distortions or signal loss [21, 22]. To date, an optimised 7T MR protocol for the NBM *in vivo* has not yet reported for clinical study.

The purpose of this study was to develop high resolution, high contrast acquisition and analysis protocol for *in vivo* imaging of the NBM with high field MRI. We hypothesized that combining T_1 weighted data with a filtered phase mask filtering and T_2^* weighting would allow improved visualization of the NBM *in vivo*. To test our hypothesis, a small cohort of healthy volunteers was imaged at high field MRI and the resulting images were post processed using SWI and PSIR with a phase mask filtering (SW-PSIR).

5.2 Methods

Data were collected with ethical approval from the University of Nottingham Medical School. Written informed consent was obtained from all participants in the study. After the examinations, all participants were interviewed about adverse effects such as vertigo, dizziness or nausea.

Participants: Eight healthy volunteers (mean age 29 years) were scanned on a Philips 7.0 T Achieva system with T/R 32 channel head coil (Nova Medical). The dielectric pads (size 18x18x0.8 cm^3, containing a suspension of calcium titanate with weights in ratio 2.8:1 in deuterated water) were placed over subject's ears to produce a homogeneous B_1 field [23-25]. MR pulse sequences with appropriate parameters were optimised at 7.0 T in three normal subjects and were retested for reproducibility in five healthy subjects. Subsequently, two subjects from this cohort (mean age 25 years) were scanned at 3.0 T with a comparable PSIR and T_2^* weighted imaging on a Philips MR scanner (Achieva) with a 32-channel head coil. All scans were acquired without contrast media.

Data acquisition: MR protocols consisted of gradient echo (GE) T_2^* weighted sequence and 3D T_1 weighted phase sensitive inversion recovery (PSIR). At 7.0 T dielectric pads were placed over the ears to flatten the B_1^+ field across the brainstem. No parallel imaging (SENSE) was used to maximise contrast to noise ratio at the centre of the field of view, which allowed a relatively narrow RL field of view to be used with RL phase encoding to speed up imaging. T_2^* weighted contrast is effective for imaging structures with higher iron content based on local susceptibility changes, and at 7.0 T sequence parameters were optimized to identify a sequence yielding the highest image quality in a clinically feasible imaging time (Table 5.1). A 3D T_1 weighted PSIR were acquired as previously described in [26] in particular using an inversion pulse tailored to overcome B_1^+ field errors [36]. These timing had previously been optimized for grey/white matter contrast across the

whole brain [26]. Here the resolution and field of view at 7.0 T were optimized for imaging the NBM in a reasonable time with adequate signal to noise ratio. This sequence is the same as the MP2RAGE sequence except the T_1 weighted PSIR image was reconstructed using

$$PSIR = \frac{\pm|SI_1|}{|SI_1|+|SI_2|} \qquad \text{Eq 5.1}$$

where signal SI_1 is the short inversion time (TI_1) and signal SI_2 is the long inversion time (TI_2) as previously described in [26]. Typical SI_1, SI_2 and PSIR images are shown in Figure 5.6. The protocols used for the repeatability cohort and 3.0 T scans are shown in Table 5.1.

Table 5.1: MR sequences and scanning parameters for both scanners and sequences. Parameters that are italicized were optimized with the final optimum values being shown in bold.

Parameters	**7.0 T MRI**		**3.0 T MRI**	
Sequence	PSIR	T_2^*w	PSIR	T_2^*w
Scan mode	3D	2D MS	3D	2D MS
Technique	T_1 FFE	FFE	T_1 FFE	FFE
Voxel size (mm)	0.7x0.7x0.7	0.35x0.35x1.0	1.0x1.0x1.0	0.7x0.7x1.0
Resolution (x,y)	272x224	528x528	220x220	272x272
Slices	100	20	180	20
FOV (AP, RL, FH)	70x191x180	184x184x20	220x220x180	20x190x180
SENSE	1	No	2	No
Orientation/Foldover	Coronal/RL	Coronal/RL	Sagittal/ AP	Coronal/RL
TFE factor/TFE shot	224/100	-	110/108	-
Flip angle (°)	5	***13***,18	9	20
TR (ms)	6.3	235	7.5	442
TE (ms)	2.8	9.4,***11***,20,30	3.5	30
TI_1/TI_2 (ms)	780/2380	-	460/1305	-
Scan time (min)	5:50	4:09	7:12	7:37

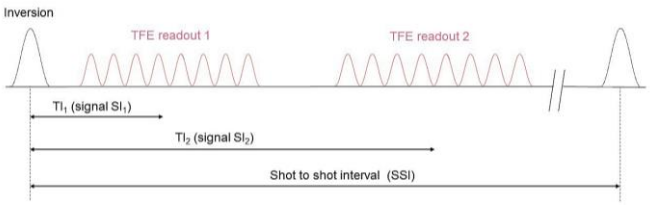


Figure 5.5: Timing diagram of PSIR pulse sequence using dual TFE readouts.

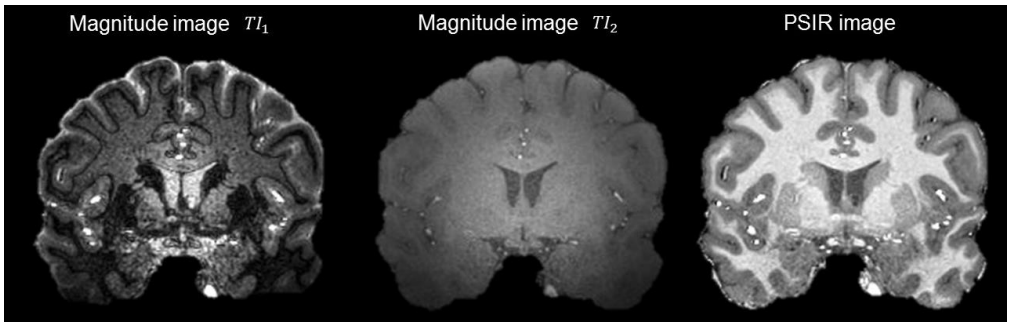


Figure 5.6: Coronal magnitude image from short inversion time $TI_1 = 780$ ms (left), long inversion time $TI_2 = 2380$ ms (middle) and the resulting PSIR image of the NBM *in vivo* (right).

Data processing: The magnitude and phase data images were combined to produce susceptibility weighted images (SWI) [27] according to

$$SWI_i = S_i\,(f_i)^n \qquad \text{for } i = 1 \ldots M \qquad \text{Eq 5.2}$$

$$where$$

$$f_i = \frac{[\pi+\varphi_i]}{\pi}\; for - \pi < \varphi_i < 0 \qquad \text{Eq 5.3}$$

and SWI_i is the signal in the i^{th} voxel of the final SWI image, S_i is the signal in in the i^{th} voxel of the T_2^* weighted magnitude image, φ_i is the signal in the i^{th} voxel of the filtered phase map and M is the number of voxels. The value of n=4 is used in standard SWI reconstructions [27]. We also investigated the use of susceptibility weighting to produce susceptibility weighted PSIR images (SW-PSIR) according to the method previously proposed for susceptibility weighting imaging [27]. The phase mask from the long inversion time (TI_2) image is not affected by the phase shift of inverted magnetization, so this was used to enhance the contrast of the PSIR data:

$$SW - PSIR_i = S_i\,(f_i)^n \qquad \text{for } i = 1 \ldots M \quad \text{Eq 5.4}$$

where SW-PSIR$_i$ is the signal in the i^{th} voxel of the final image, S_i is the signal in the i^{th} voxel of the PSIR image [Eq 5.1], f_i is as defined in Eq 5.3 but considering the signal in the i^{th} voxel of the filtered phase map for the long inversion time (TI_2) image from the PSIR data acquisition. This phase map was used since there was no phase inversion from the inversion pulse in this late inversion time image. The value of n was varied from 3 to 6 to optimize the processing of these inversion recovery images. Each step in the processing for both image types is presented in flowcharts as shown in Figure 5.7-5.8. All data processing was performed in MATLAB (The MathWorks, Natick, Massachusetts, USA, R2012a).

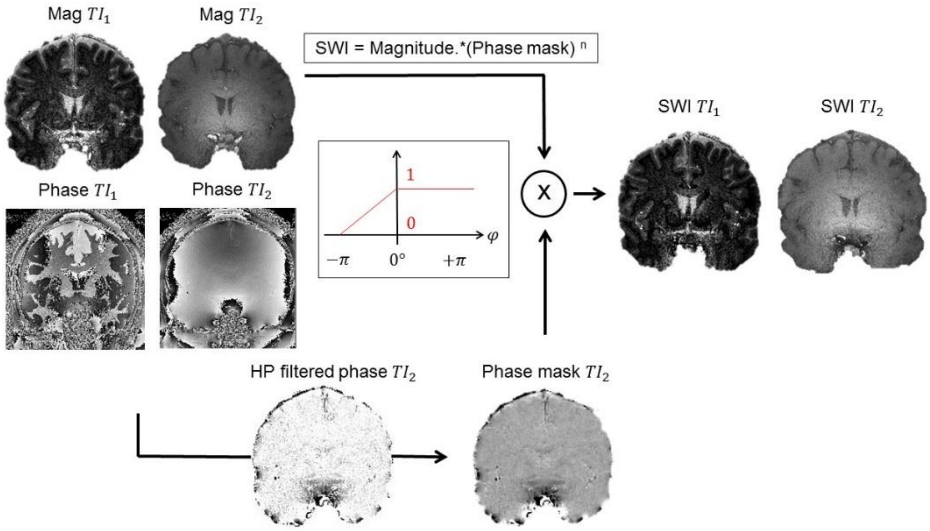


Figure 5.7: Flowcharts of SWI image processing to enhance image contrast.

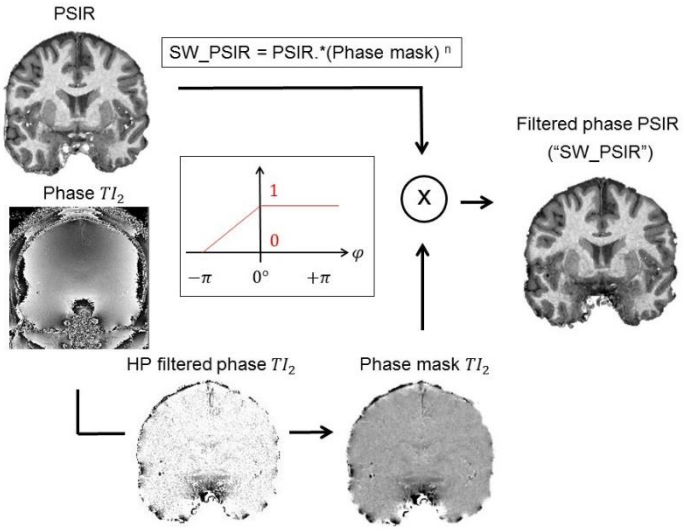


Figure 5.8: Flowcharts of the combination of the original PSIR image and phase data to improve image contrast of the NBM *in vivo*.

Image Analysis:

FSL's Brain Extraction Tool (BET) was used to extract brain tissue for image analysis [28, 29]. A coronal section was used to determine the boundaries of the NBM, starting at the first slice where hemispheric crossing of the anterior commissure was observed and ending at the level of the emergence of the anterior commissure from the temporal lobe. An open source image analysis program, ImageJ [30], was used to draw region of interest (ROIs) and distances for the following quantitative measurements.

The contrast-to-noise ratio (CNR) was assessed between the NBM and surrounding tissue for the different images that were reconstructed:

$$CNR = \frac{|Tissue_{\,1} - Tissue_{\,2}|}{Noise} \qquad \text{Eq 5.5}$$

where $Tissue_{\,1}$ and $Tissue_{\,2}$ are the averaged signal intensities within the NBM (red ROI in Figure 5.9) and the midline anterior commissure (purple ROI in Figure 5.9). $Noise$ was estimated as the standard deviation from a homogeneous region of white matter (green in Figure 5.9) as the data was acquired with standard background filtering so no measurement could be made in the background.

The thickness of the NBM was measured on a coronal image with the anterior commissure in the midline (boundaries: vertical line from inferior most aspect of the ventral pallidum to the base of the brain, corresponding to the anterior division of the NBM) on the PSIR data (Figure 5.9), by two observers making five repeated measurements for each subject. Observer 1 was a radiographer (KA) and observer 2 was a radiologist (KJ) and each observer was blinded to the results assigned by the other observers. In the same way, the total NBM volume (anterior, intermediate and posterior divisions) was determined by manual segmentation of images which allowed the volumetric analysis. All results were reported as mean ± standard deviation (SD) and significance was set at $p<0.05$. Intraclass correlation coefficient (ICC) and 95% confidence intervals were calculated for both intra-

observer and inter-observer reliability. The reliability was classified based on ICC: minimal (ICC ≤ 0.25), low (0.26 ≤ ICC ≤ 0.50), moderate (0.50 ≤ ICC ≤ 0.70), high (0.70 ≤ ICC ≤ 0.90), and excellent (ICC ≥ 0.90) [31, 32].

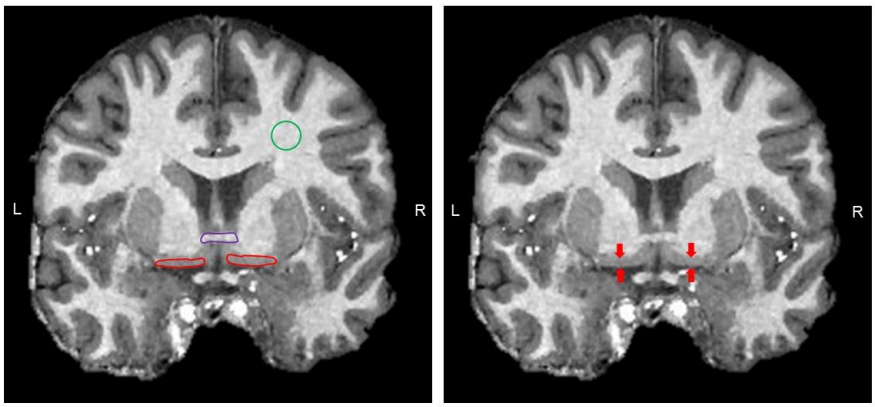


Figure 5.9: Definition of ROIs on PSIR image to evaluate CNR in the NBM. Coronal slices in the anterior segment was chosen. Manual ROIs were drawn in the NBM (red), crossing fibres of the anterior commissure (purple) and a region in white matter (green). The average signal intensities from tissues were calculated. Red arrows show the NBM thickness measurement.

5.3 Results

NBM characteristics:

At 7.0 T MRI, the NBM was well delineated and localised on the standard T_1 weighted PSIR image compared to 3.0 T (Figure 5.10). However, for the T_2^* weighted images the NBM was not well-defined at either field (Figure 5.11). A number of sequence optimisation for effective PSIR protocols at 7.0 T were determined. These results are shown in Figure 5.12. A comparison of 7.0 T and 3.0 T for NBM imaging *in vivo* showed that PSIR images at 7.0 T provided better differentiation between adjacent structures, along with a more complete structural characterization of the NBM at voxel size of 0.7 mm isotropic resolution. We found that using narrow FOV and dielectric pads showed considerable improvement *in vivo* imaging of the NBM contrast. Figure 5.13 shows agreement between MRI and the pathological segmentation proposed by Liu et al. [33]. The NBM is composed of anterior, intermediate and posterior divisions which are defined by the presence of

the decussation of the anterior commissure, the globus pallidus and mammillary bodies, respectively. For the simultaneous identification of NBM structures in the three orthogonal planes, three-dimensional (3D) rendering was made (Figure 5.14).

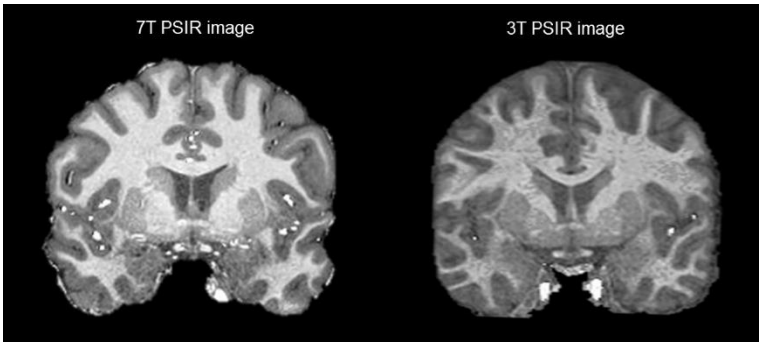


Figure 5.10: High resolution T_1 weighted PSIR images of the NBM in a healthy volunteer at 7.0 T (left) compared with 3.0 T (right).

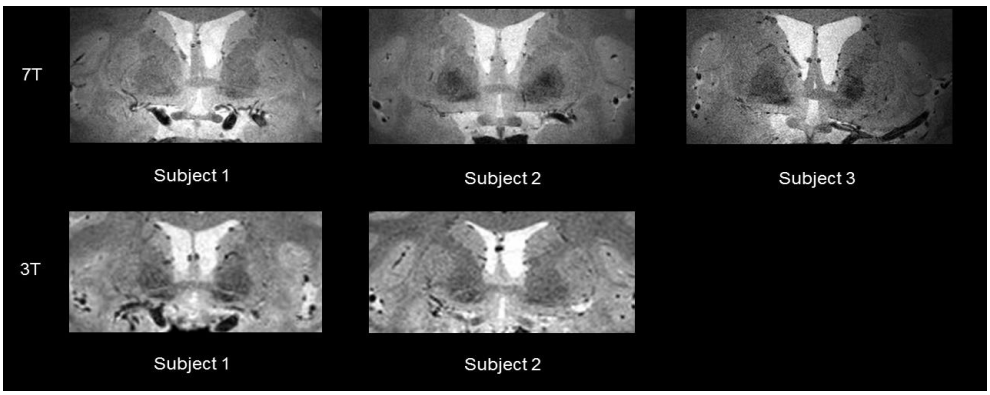


Figure 5.11: GRE T_2^* weighted images of the NBM in young healthy volunteers at 7.0 T MRI (top) compared with 3.0 T MRI (bottom).

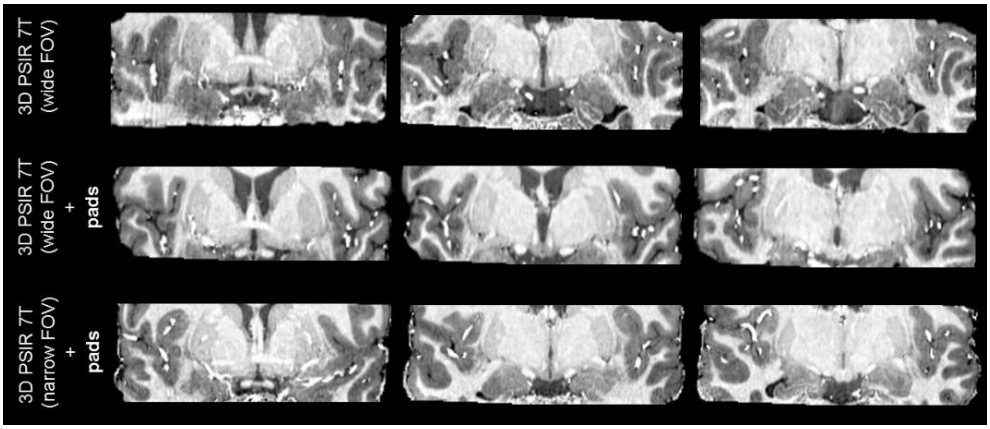


Figure 5.12: Optimised 3D PSIR sequence with appropriate parameters for localisation of the NBM (anterior→posterior) in three healthy volunteers at 7.0 T; (top) 3D PSIR using wide FOV, (middle) 3D PSIR using wide FOV and dielectric pads and (bottom) 3D PSIR using narrow FOV with dielectric pads, respectively.

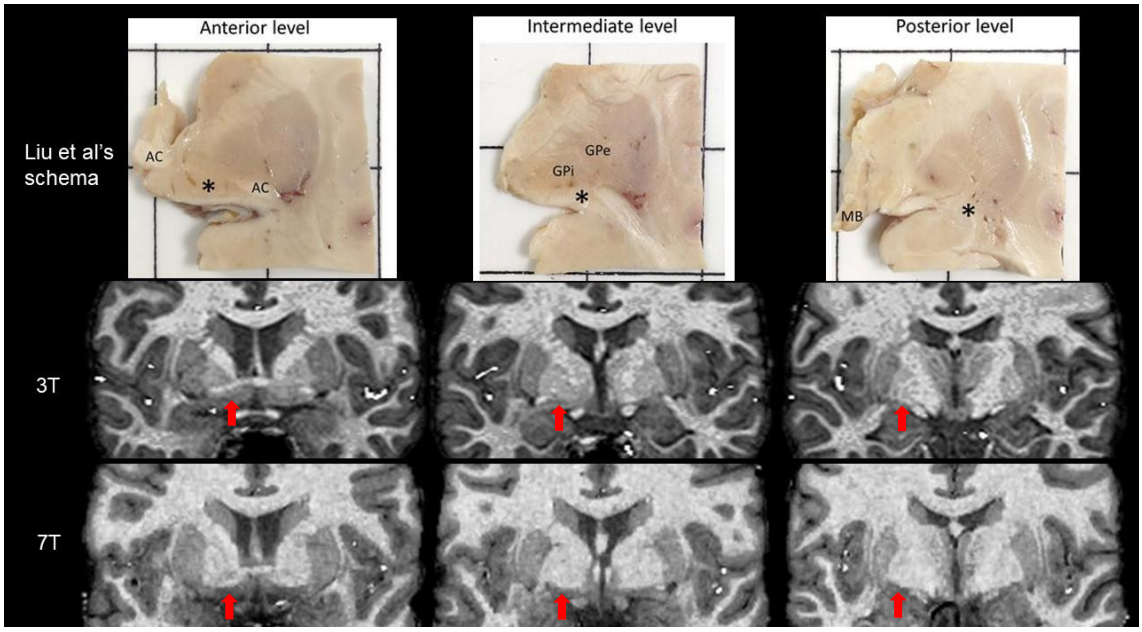


Figure 5.13: Schematic of the NBM in the anterior, intermediate and posterior division of 3D PSIR sequence on coronal planes according to dissection from Liu et al. [33] at high field MRI.

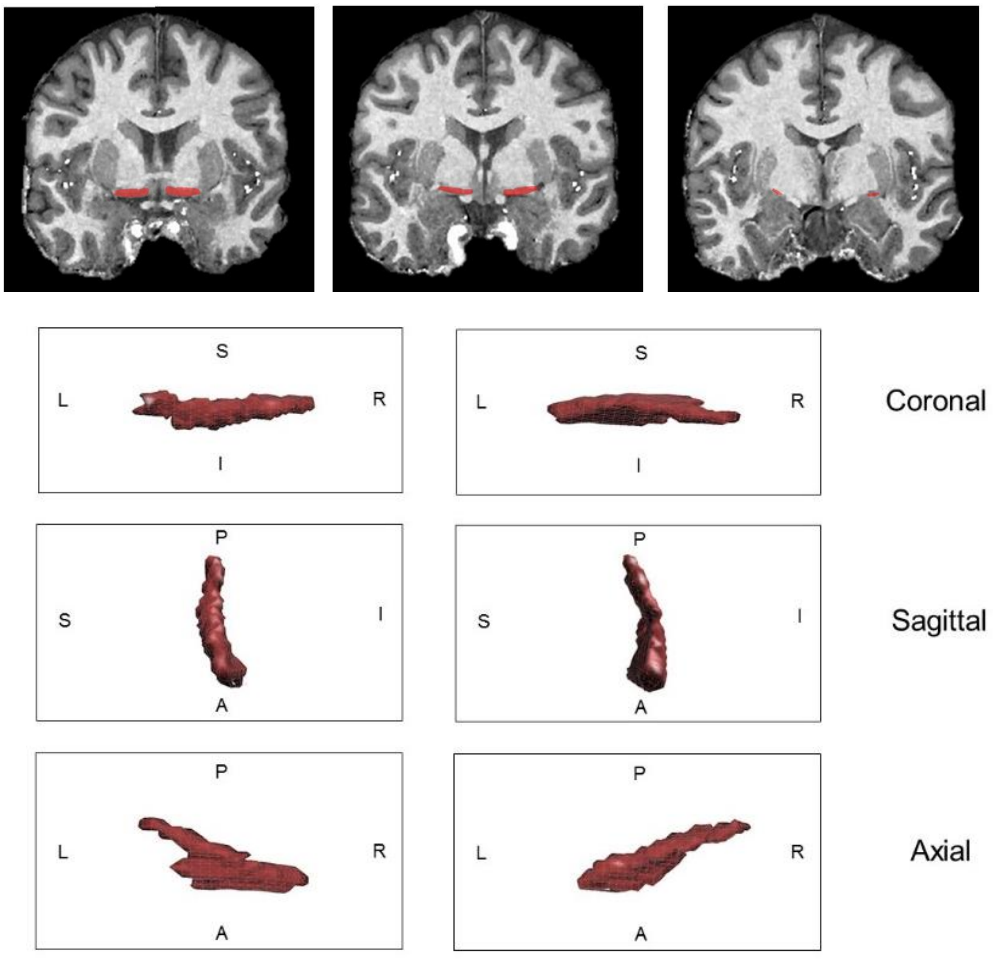


Figure 5.14: 3D rendering of the NBM in three orthogonal planes.

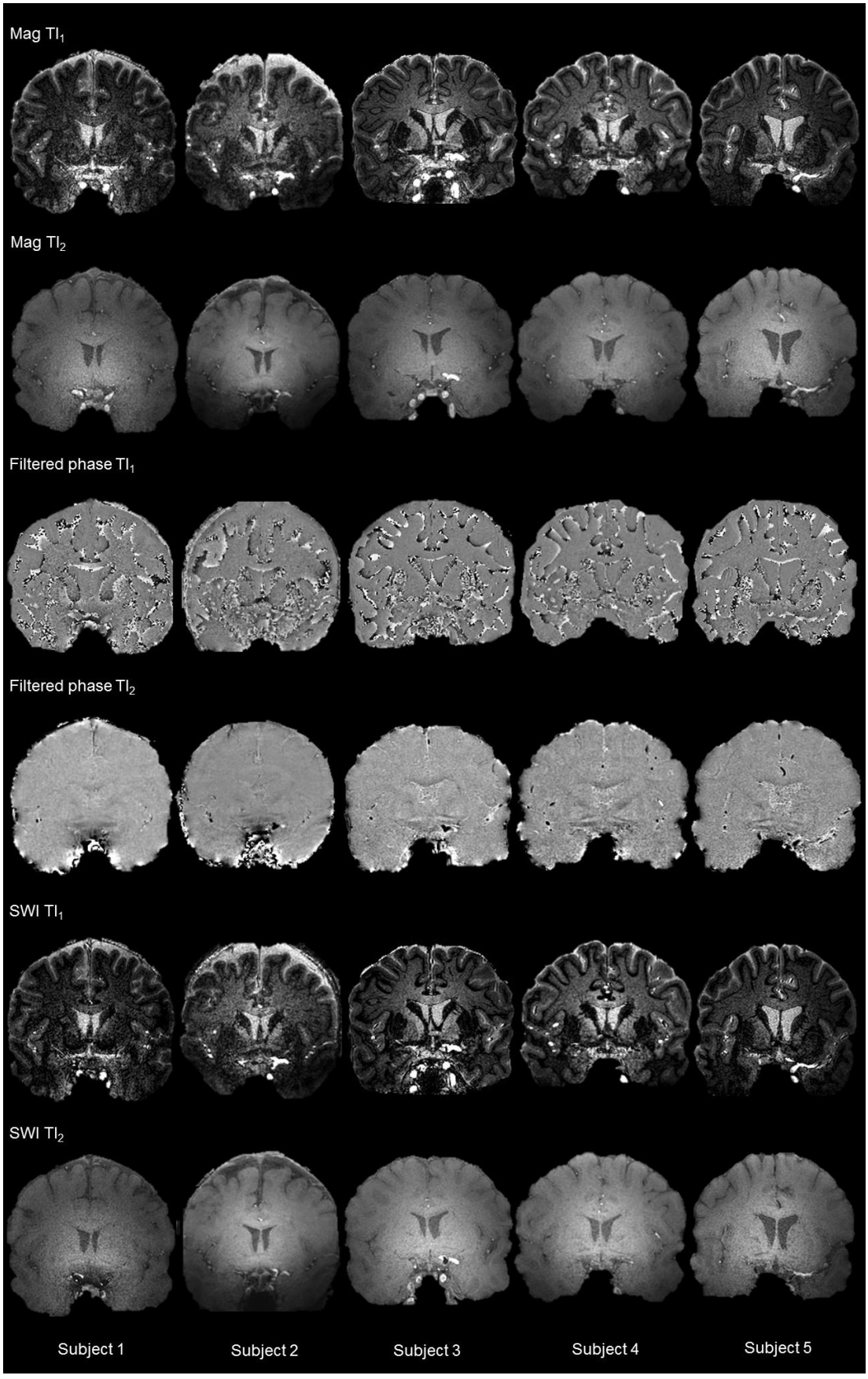


Figure 5.15: Magnitude, phase mask and SWI images from T_1 weighted PSIR images using two inversion times ($TI_1 = 780$ ms and $TI_2 = 2380$ ms) at 7.0 T MRI.

In SWI post processing (Figure 5.15), the visibility of susceptibility differences in these regions showed contrast enhancement compared with original magnitude images. The filtered phase PSIR image (SW-PSIR) provides improved image contrast in the NBM due to the difference in a regional susceptibility are shown on the filtered phase data. The results of repeatability of filtered phase enhanced PSIR T_1 weighting are shown in Figure 5.16-5.20 for each individual healthy volunteer. It can be seen that applying SW-PSIR provided additional contrast specific to NBM which was significantly better than SWI images.

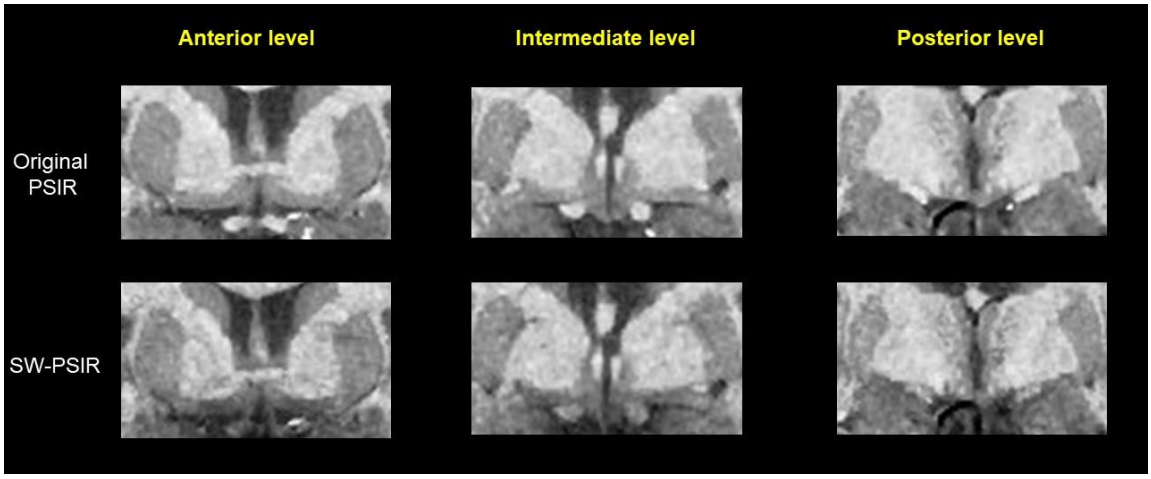


Figure 5.16: Improvement of tissue contrast in the NBM on SW-PSIR images using filtered phase by power of 5th (subject 1).

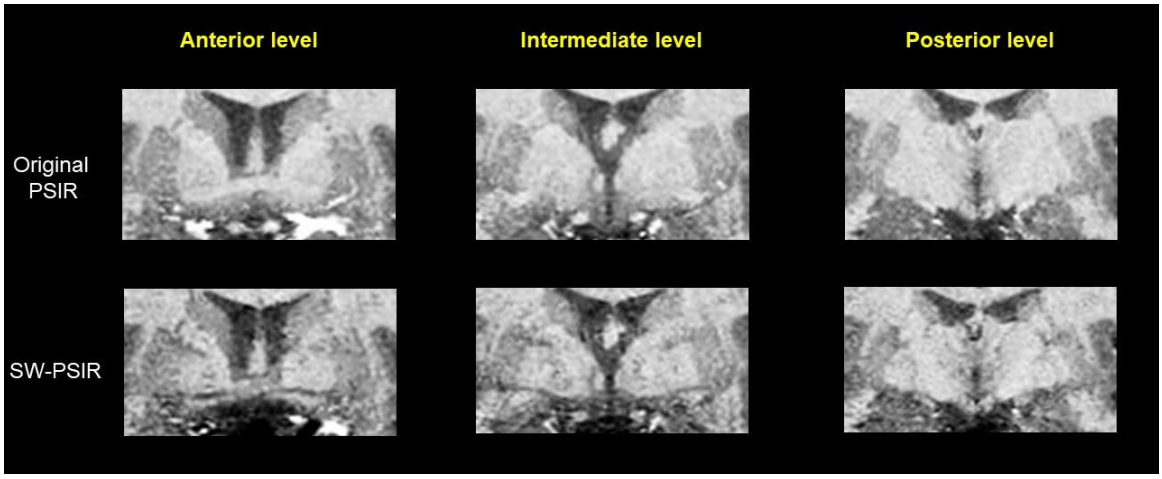


Figure 5.17: Improvement of tissue contrast in the NBM on SW-PSIR images using filtered phase by power of 5th (subject 2).

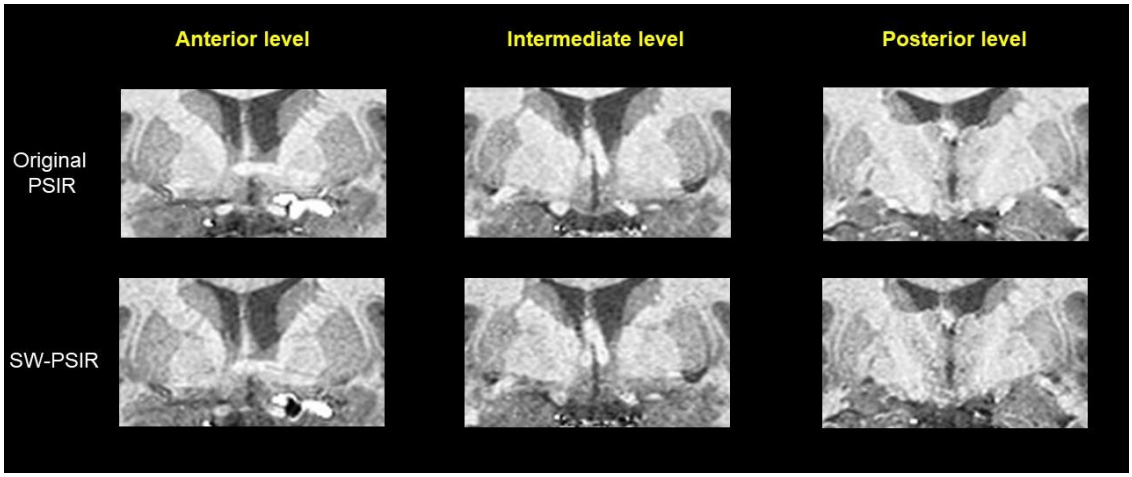


Figure 5.18: Improvement of tissue contrast in the NBM on SW-PSIR images using filtered phase by power of 5th (subject 3).

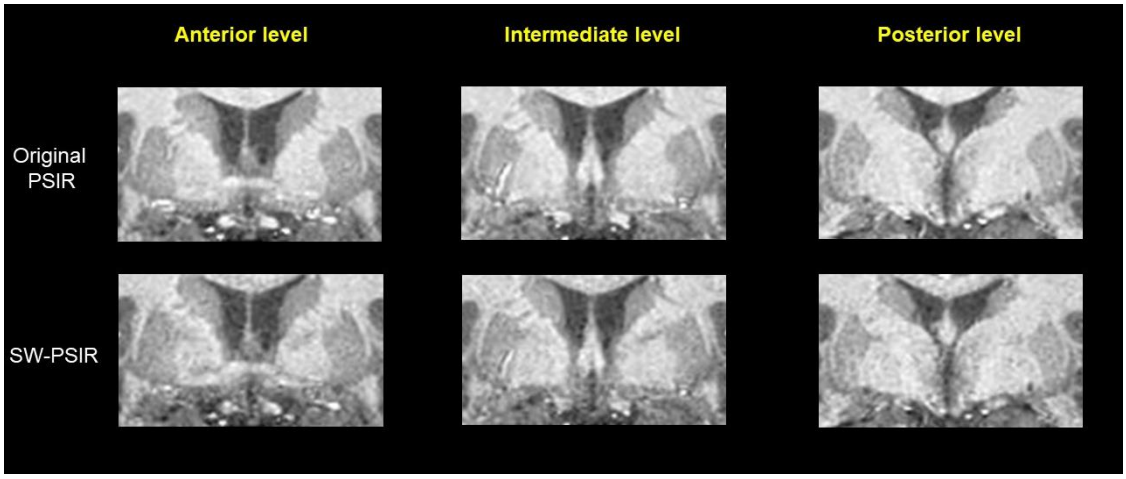


Figure 5.19: Improvement of tissue contrast in the NBM on SW-PSIR images using filtered phase by power of 5th (subject 4).

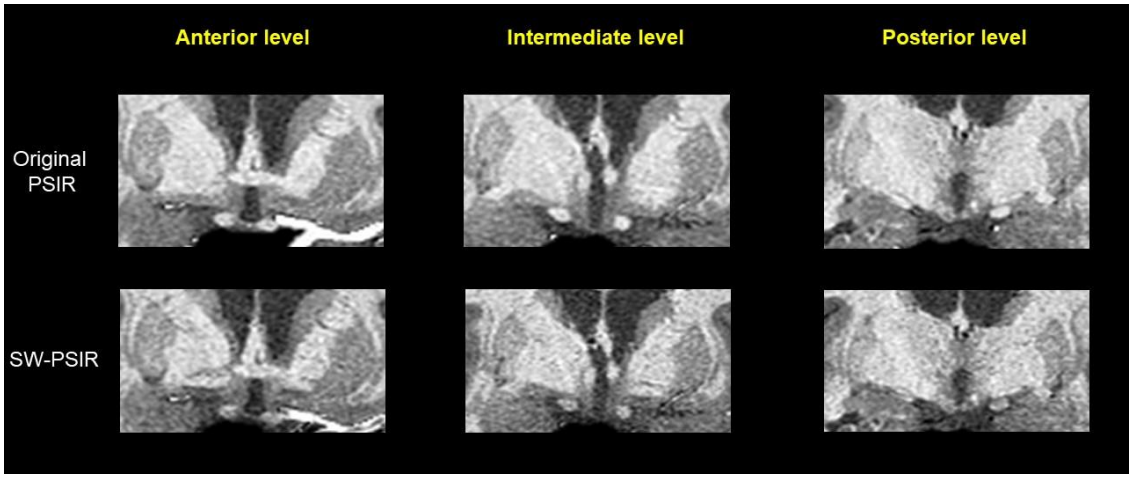


Figure 5.20: Improvement of tissue contrast in the NBM on SW-PSIR images using filtered phase by power of 5th (subject 5).

Contrast-to-noise ratio (CNR) from filtered MRI phase

Figure 5.21 shows the reduction of CNR value in the NBM on SWI images with short inversion time ($TI_1 = 780$ ms) as function of phase mask multiplications compared to original magnitude image in all healthy subjects. In contrast, the distribution of CNR value on SWI images with long inversion time ($TI_2 = 2380$ ms) increases exponentially as a function of phase mask multiplications, compared to original magnitude in all healthy subjects (Figure 5.22).

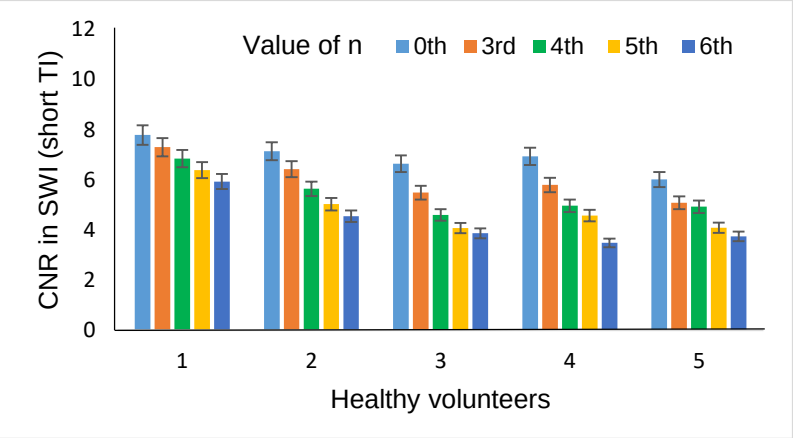


Figure 5.21: CNR in SWI with short inversion time TI_1=780 ms (averaged over both left and right NBM) for phase data raised to power of 3, 4, 5 and 6 (Eq 5.5) compared with original magnitude image (n=0) in all volunteers.

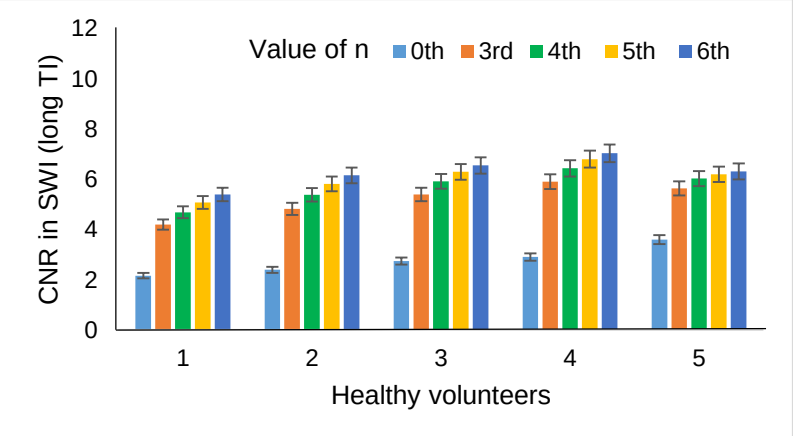


Figure 5.22: CNR in SWI with long inversion time TI_2=2380 ms (averaged over both left and right NBM) for phase data raised to power of 3, 4, 5 and 6 (Eq 5.5) compared with original magnitude image (n=0) in all volunteers.

For filtered phase PSIR images (SW-PSIR), results show much improved CNR in the human NBM sub-regions. The maximum CNR value was obtained by power of 5th phase mask multiplied on T_1 weighted PSIR image (Figure 5.23). This allowed for the anatomical structure of the NBM to be delineated clearly *in vivo* at 7.0 T MRI.

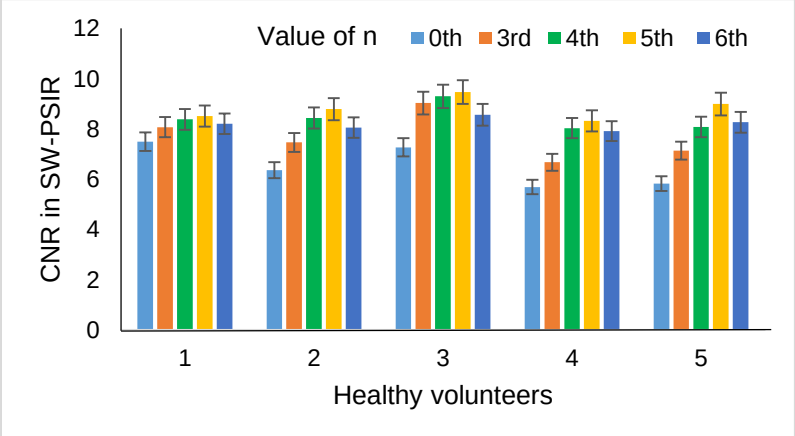


Figure 5.23: CNR in SW-PSIR (averaged over both left and right NBM) for phase data raised to power of 3, 4, 5 and 6 (Eq 5.5) compared with original PSIR (n=0) in all volunteers.

NBM thickness: Table 5.2 shows the average thickness of the left NBM in young healthy volunteers (n=5) measured by first and second observer was 3.5±0.43 mm and 3.8±0.51 mm, respectively, while the average thickness of the right NBM was 3.6±0.52 mmm and 3.7±0.47 mm, respectively. There was no statistically significant differences between left and right NBM thickness for all volunteers. The ICC values for NBM thickness have excellent intra-observer and inter-observer agreement, although intra-observer reliability tended to be lower than inter-observer reliability. The intra-observer ICC of the left NBM was 0.898 for observer 1 and 0.919 for observer 2. The intra-observer ICC of the right NBM was 0.915 for observer 1 and 0.914 for observer 2. The inter-observer ICC of the left NBM was 0.984 and 0.968 for the right NBM (Table 5.3). The Bland-Altman analyses show the average NBM thickness in young healthy subjects (n=5; 1 female and 4 males; mean age 29.2 years) measured by two observers. The limits of agreement are defined as the mean difference ± 1.96 standard deviation (SD) of differences. Results indicate that

95% of mean differences lie within the limit. The NBM thickness measured by 7.0T MRI are considered to be in agreement for all volunteers considered (Figure 5.24).

Table 5.2: Thickness and total NBM volume in young healthy volunteers.

Subject	Sex	Age	NBM thickness (mm)				NBM volume (mm^3)			
			Observer 1		Observer 2		Observer 1		Observer 2	
			L	R	L	R	L	R	L	R
1	F	32	3.43	3.60	3.58	3.52	1255	1212	1335	1279
2	M	29	4.23	4.41	4.70	4.23	854	1090	850	1084
3	M	25	3.03	3.00	3.33	2.99	1023	1093	1070	1178
4	M	25	3.43	3.50	3.66	3.60	827	873	837	872
5	M	35	3.48	3.69	3.82	3.96	1074	1157	1201	1163
Mean ± SD		29.2	3.5 ± 0.43	3.6 ± 0.51	3.8 ± 0.52	3.7 ± 0.47	1007 ± 175	1085 ± 129	1059 ± 218	1155 ± 153

NBM volume: The total volume of the left NBM in young healthy volunteers (n=5), measured by first and second observer was 1007±1.75 mm^3 and 1085±1.29 mm^3, respectively, while the total volume of the right NBM was 1059±2.18 mm^3 and 1155±1.53 mm^3, respectively. No statistically significant differences in volumetric measurement between left and right NBM were observed ($p>0.05$). The ICC values for the volumetric analysis showed excellent intra- and inter-observer agreement (>0.95) in all measurements. Similarly, the statistical Bland-Altman plots for these results indicate that bias and limits of agreement were not influenced (95% CI).

Table 5.3: Intra-class correlation coefficient (ICC) showing inter and intra-observer reliability for measurements of NBM thickness.

Side of brain	Inter-observer ICC	Intra-observer ICC	
		Observer 1	Observer 2
Measurements of NBM thickness			
L	0.984 (0.848-0.998)	0.898 (0.621-0.998)	0.919 (0.700-0.991)
R	0.968 (0.690-0.997)	0.915 (0.683-0.990)	0.914 (0.679-0.990)
Measurements of NBM volume			
L	0.981 (0.822-0.998)	0.987 (0.934-0.999)	0.995 (0.975-0.999)
R	0.977 (0.777-0.998)	0.957 (0.784-0.995)	0.989 (0.942-0.999)

Note: 95% confident interval (lower bound-upper bound)

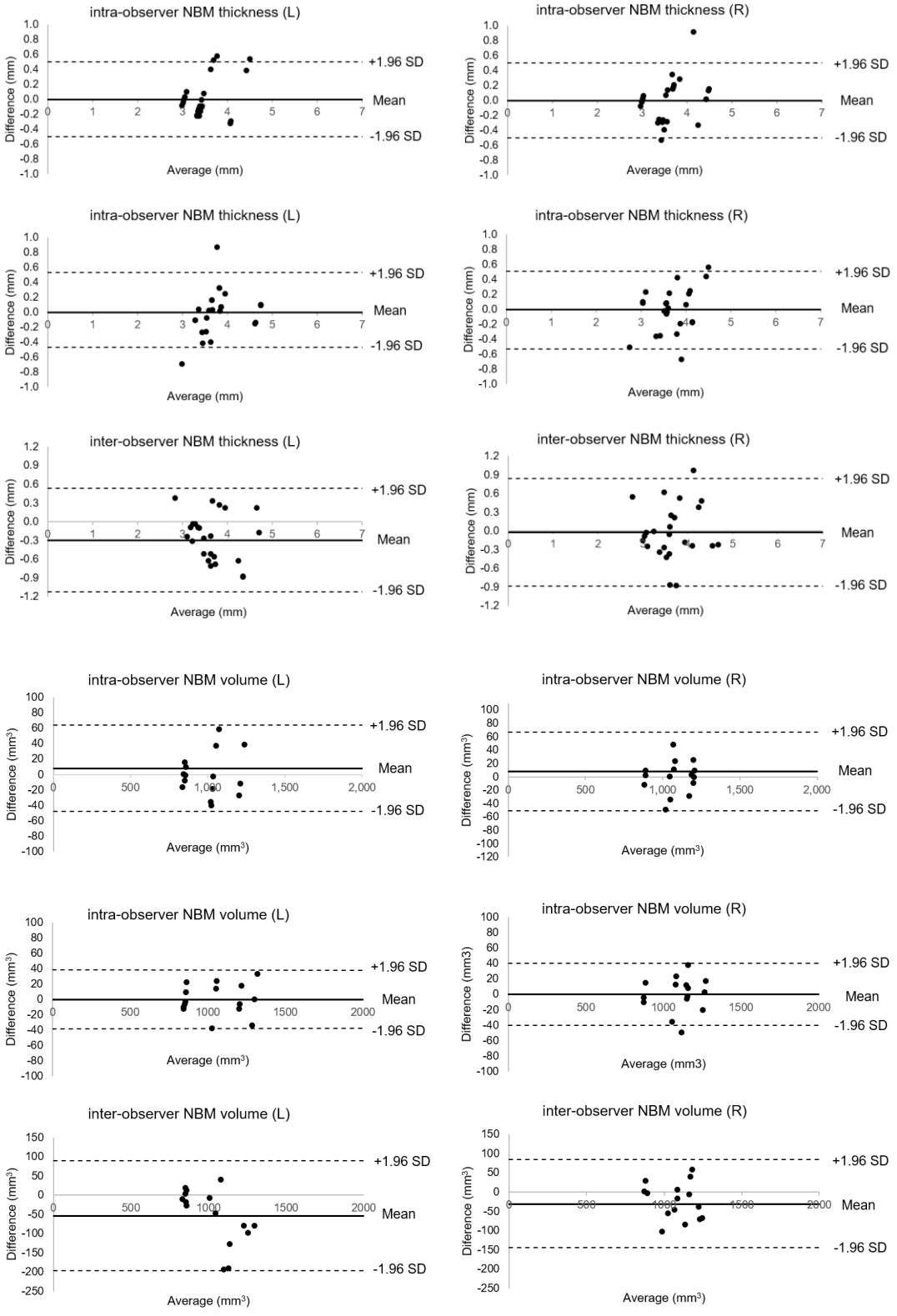


Figure 5.24: Intra-observer and inter-observer reliability of NBM thickness and volume at both sides. The central line corresponds to the mean value of deviation. The dashed lines indicate the interval of standard deviation.

5.4 Discussion

In the study, we developed PSIR sequence for imaging of the NBM *in vivo* at 7.0 T and translated this successfully to clinical application at 3.0 T with high spatial resolution in reasonable imaging time. This sequence allowed reproducible assessment of NBM thickness and volume in young healthy volunteers. We showed that including susceptibility weighting (raising the phase data to a power of 5) improved the CNR between the NBM and the ventral pallidum (different grey matter structures). The contrast can be reduced with respect to grey/white matter or grey matter/CSF border in the SW-PSIR compared to the PSIR images, but the SW-PSIR images are produced with no cost to scan time so both the original PSIR images and SW-PSIR images could be made available for segmentation if required. This is reflected in clearer spatial differentiation and localisation which is promising for predicting disease trajectory, as response to cholinergic augmentation represents an unmet clinical need.

These results could be used to determine changes in the NBM that occur in both health and disease. Although there is no significant difference of NBM thickness in young healthy volunteers, a further study with more focus on different age groups, genders, and diseases changes in the thickness of the NBM is needed to better understanding factors influencing dementia risk. Several studies found that the production of cholinergic neurons decrease in aging and in Alzheimer disease [17], [18], [34]. Similarly, a loss of cholinergic neurons has been reported with MRI in AD [19], [35]. Mapping of areas and cell layers containing cholinergic receptors by measuring NBM thickness is important because these structures undergo significant neuronal depletion in dementia. As hilighted by Hanyu et al. [16, 17] the thickness of NBM in patients with AD, vascular dementia, and Parkinson’s disease with dementia declined more significantly than that in normal aging. Furthermore, Hanyu et al. showed that a reduction of NBM thickness correlated with atrophy in both AD

and non-AD patient [14]. The degree of atrophy in the NBM increased with age in normal healthy subjects which known as age-related neuron loss.

Several limitations exist in this study beginning with the small sample size. Our study was based on young healthy volunteers (n=5) who potentially have higher cholinergic neuron accumulated in the brain compared to older individuals. However, the lack of parallel imaging will make the protocol robust in patient populations. Second, CNR measurements related to the contrast of interest that will be the result of how the signal measure and the noise is defined. In this study, we measured the difference in signal intensity between the NBM region and AC compared to the standard deviation of the signal in a homogeneous region of white matter. Third, B_1 field mapping *in vivo* human brain was not performed in this study. Large B_1 field inhomogeneity can result in proportional variation in flip angle at 7.0 T. Therefore a tailored inversion pulse [36] was used with low sensitivity to B_1 variation and dielectric pads [23-25] was used to reduce these effects. In future it would be useful to acquire a B_1 map in all cases to determine the effect of variation in B_1 on the final results and possibly modify the sequence flip angles at time of data acquisition to limit the consequences of variation in B_1 amplitude [37].

The 7.0 T MRI provided better anatomical localisation of the NBM in a 5 minute 50 second scan duration at 0.7 mm^3 isotropic resolution compared to 3.0 T. Image contrast of the NBM was improved by using 3D PSIR sequence with narrow FOV and dielectric pads. The SW-PSIR with phase mask at 7.0 T MRI offered additional contrast specific to NBM. This allowed for the visualization of the anatomical structure of the NBM and three sub-regions were clearly delineated in young healthy volunteers. Clinical applications for improved NBM visualisation include imaging studies in AD, improved accuracy of deep brain stimulation electrode placement, and morphological assessment across the aging-dementia spectrum. There is ongoing work to translate this imaging sequence to clinical 3.0 T

MRI in the patients with non-AD such as traumatic brain injury (TBI) or healthy aging.

5.5 Conclusion

Improved visualization of the NBM *in vivo* was demonstrated by post processed PSIR with phase mask (SW-PSIR) at 7.0 T MRI. This method allowed for better visualization of anatomical structure of the NBM and provided a clear boundary delineation between the ventral pallidum and chiasmatic cistern in young healthy volunteers. Consideration of the results suggest potential avenues for future work, including the applications of thickness measurement in the assessment of morphological changes within the nucleus basalis in health and disease and more accurate localisation for deep brain stimulation electrode placement.

Bibliography

[1] M. M. Mesulam, “Cholinergic circuitry of the human nucleus basalis and its fate in Alzheimer’s disease,” *Journal of Comparative Neurology*, vol. 521, no. 18. pp. 4124–4144, 2013.

[2] I. Kilimann *et al.*, “Subregional basal forebrain atrophy in Alzheimer’s disease: a multicenter study.,” *J. Alzheimers. Dis.*, 2014.

[3] R. Schliebs and T. Arendt, “The cholinergic system in aging and neuronal degeneration,” *Behavioural Brain Research*. 2011.

[4] T. W. Schmitz, M. Mur, M. Aghourian, M.-A. Bédard, and R. N. Spreng, “Spatial Topography of Alzheimer’s Degeneration Reflects the Cholinergic Projection System,” 2018.

[5] M. Marsel Mesulam, E. J. Mufson, A. I. Levey, and B. H. Wainer, “Cholinergic innervation of cortex by the basal forebrain: Cytochemistry and cortical connections of the septal area, diagonal band nuclei, nucleus basalis (Substantia innominata), and hypothalamus in the rhesus monkey,” *J. Comp. Neurol.*, 1983.

[6] F. Tagliavini and G. Pilleri, “Basal nucleus of meynert. A neuropathological study in Alzheimer’s disease, simple senile dementia, Pick’s disease and Huntington’s chorea,” *J. Neurol. Sci.*, 1983.

[7] D. Ryczko and R. Dubuc, “Dopamine and the brainstem locomotor networks: From lamprey to human,” *Frontiers in Neuroscience*. 2017.

[8] P. Gaspar, B. Berger, A. Lesur, J. P. Borsotti, and A. Febvret, “Somatostatin 28 and neuropeptide Y innervation in the septal area and related cortical and subcortical structures of the human brain. Distribution, relationships and evidence for differential coexistence,” *Neuroscience*, 1987.

[9] A. Lesur, P. Gaspar, C. Alvarez, and B. Berger, “Chemoanatomic compartments in the human bed nucleus of the stria terminalis,” *Neuroscience*, 1989.

[10] M. A. Raghanti, G. Simic, S. Watson, C. D. Stimpson, P. R. Hof, and C. C. Sherwood, “Comparative analysis of the nucleus basalis of Meynert among primates,” *Neuroscience*, 2011.

[11] O. J. M. Vogels, C. A. J. Broere, H. J. Ter Laak, H. J. Ten Donkelaar, R. Nieuwenhuys, and B. P. M. Schulte, “Cell loss and shrinkage in the nucleus basalis Meynert complex in Alzheimer’s disease,” *Neurobiol. Aging*, 1990.

[12] T. Nagai, P. L. McGeer, J. H. Peng, E. G. McGeer, and C. E. Dolman, “Choline acetyltransferase immunohistochemistry in brains of alzheimer’s disease patients and controls,” *Neurosci. Lett.*, 1983.

[13] M. Sasaki *et al.*, “MR anatomy of the substantia innominata and findings in Alzheimer disease: A preliminary report,” *Am. J. Neuroradiol.*, vol. 16, no. 10, pp. 2001–2009, 1995.

[14] H. Hanyu, Y. Tanaka, H. Sakurai, M. Takasaki, and K. Abe, “Atrophy of the substantia innominata on magnetic resonance imaging and response to donepezil treatment in Alzheimer’s disease,” *Neurosci. Lett.*, 2002.

[15] R. H. Perry, J. M. Candy, E. K. Perry, J. Thompson, and A. E. Oakley, “The substantia innominata and adjacent regions in the human brain: Histochemical and biochemical observations,” *J. Anat.*, vol. 138, no. 4, pp. 713–732, 1984.

[16] H. Hanyu, T. Asano, H. Sakurai, Y. Tanaka, M. Takasaki, and K. Abe, “MR analysis of the substantia innominata in normal aging, Alzheimer disease, and other types of dementia,” *Am. J. Neuroradiol.*, 2002.

[17] H. Hanyu, S. Shimizu, Y. Tanaka, K. Hirao, T. Iwamoto, and K. Abe, “MR features of the substantia innominata and therapeutic implications in dementias,” *Neurobiol. Aging*, vol. 28, no. 4, pp. 548–554, 2007.

[18] W. J. Moon, H. J. Kim, H. G. Roh, and S. H. Han, “Atrophy measurement of the anterior commissure and substantia innominata with 3T high-resolution MR imaging: Does the measurement differ for patients with frontotemporal

lobar degeneration and Alzheimer disease and for healthy subjects?," *Am. J. Neuroradiol.*, 2008.

[19] S. J. Colloby, G. J. Elder, R. Rabee, J. T. O'Brien, and J. P. Taylor, "Structural grey matter changes in the substantia innominata in Alzheimer's disease and dementia with Lewy bodies: a DARTEL-VBM study," *Int. J. Geriatr. Psychiatry*, vol. 32, no. 6, pp. 615–623, 2017.

[20] B. U. Forstmann, M. C. Keuken, A. Schafer, P. L. Bazin, A. Alkemade, and R. Turner, "Multi-modal ultra-high resolution structural 7-Tesla MRI data repository," *Sci. Data*, vol. 1, 2014.

[21] A. G. Van Der Kolk, J. Hendrikse, J. J. M. Zwanenburg, F. Visser, and P. R. Luijten, "Clinical applications of 7 T MRI in the brain," *Eur. J. Radiol.*, 2013.

[22] O. Kraff and H. H. Quick, "7T: Physics, safety, and potential clinical applications," *Journal of Magnetic Resonance Imaging*. 2017.

[23] W. M. Brink, A. M. A. van der Jagt, M. J. Versluis, B. M. Verbist, and A. G. Webb, "High Permittivity Dielectric Pads Improve High Spatial Resolution Magnetic Resonance Imaging of the Inner Ear at 7 T.," *Invest. Radiol.*, vol. 49, no. 5, pp. 271–277, 2014.

[24] W. M. Teeuwisse, W. M. Brink, K. N. Haines, and A. G. Webb, "Simulations of high permittivity materials for 7 T neuroimaging and evaluation of a new barium titanate-based dielectric," *Magn. Reson. Med.*, vol. 67, no. 4, pp. 912–918, 2012.

[25] W. M. Teeuwisse, W. M. Brink, and A. G. Webb, "Quantitative assessment of the effects of high-permittivity pads in 7 Tesla MRI of the brain," *Magn. Reson. Med.*, vol. 67, no. 5, pp. 1285–1293, 2012.

[26] O. Mougin, R. Abdel-Fahim, R. Dineen, A. Pitiot, N. Evangelou, and P. Gowland, "Imaging gray matter with concomitant null point imaging from the phase sensitive inversion recovery sequence," *Magn. Reson. Med.*, vol. 76, no. 5, pp. 1512–1516, 2016.

[27] E. M. Haacke, Y. Xu, Y.-C. N. Cheng, and J. R. Reichenbach, “Susceptibility weighted imaging (SWI).,” *Magn. Reson. Med.*, vol. 52, no. 3, pp. 612–618, 2004.

[28] M. Jenkinson, C. F. Beckmann, T. E. J. Behrens, M. W. Woolrich, and S. M. Smith, “FSL,” *Neuroimage*, vol. 62, no. 2, pp. 782–790, 2012.

[29] S. M. Smith, “BET: Brain Extraction Tool,” *Arts Am.*, vol. 39, p. 25, 2006.

[30] C. T. Rueden *et al.*, “ImageJ2: ImageJ for the next generation of scientific image data,” *BMC Bioinformatics*, vol. 18, no. 1, 2017.

[31] P. E. Shrout and J. L. Fleiss, “Intraclass correlations: Uses in assessing rater reliability,” *Psychol. Bull.*, 1979.

[32] S. B. Plichta and E. A. Kelvin, *Statistical Methods for Health Care Research*, Fifth ed. Philadelphia: Lippincott Williams & Wilkins, 2005.

[33] A. K. L. Liu, R. C. C. Chang, R. K. B. Pearce, and S. M. Gentleman, “Nucleus basalis of Meynert revisited: anatomy, history and differential involvement in Alzheimer’s and Parkinson’s disease,” *Acta Neuropathologica*, vol. 129, no. 4. pp. 527–540, 2015.

[34] S. George, E. J. Mufson, S. Leurgans, R. C. Shah, C. Ferrari, and L. DeToledo-Morrell, “MRI-based volumetric measurement of the substantia innominata in amnestic MCI and mild AD,” *Neurobiol. Aging*, vol. 32, no. 10, pp. 1756–1764, 2011.

[35] E. R. Gizewski *et al.*, “High-resolution anatomy of the human brain stem using 7-T MRI: Improved detection of inner structures and nerves?,” *Neuroradiology*, vol. 56, no. 3, pp. 177–186, 2014.

[36] A. C. Hurley, A. Al-Radaideh, L. Bai, U. Aickelin, R. Coxon, P. Glover, and P. A. Gowland, “Tailored RF pulse for magnetization inversion at ultrahigh field,” *Magn. Reson. Med.*, 2010.

[37] K. Nehrke and P. Börnert, “DREAM - A Novel Approach for Robust, Ultra-Fast, Multi-Slice,” *Imaging*, 2012.

Chapter 6 Lesion Evolution of Multiple Sclerosis

6.1 Introduction

Multiple sclerosis (MS) is a neuroinflammatory disease of the central nervous system and can affect a broad range of neurological functions including muscle control, movement, balance and vision. Damage to the insulating myelin sheath of nerve fibres disrupts signals to, from and within the brain, and scar tissue (or sclerosis) begins to build up in the brain and spinal cord. In UK, there are about 100,000 people diagnosed with MS [1] with onset usually occurring between the age of 20 and 40. It is still not known what causes MS and multiple tests such as medical history, neurological exams, and MRI scan are required to manage the condition.

Magnetic resonance imaging (MRI) plays a significant role in the diagnosis of MS due to its excellent soft tissue contrast for detecting MS lesions. Recent studies have summarized the progression of white matter changes for MRI-detectable lesions (Table 6.1) but the MR characteristics of events prior to MS lesion appearance remain speculative. Several studies have attempted to measure early changes in tissues before lesion appearance using longitudinal quantitative MRI studies. However, at lower field MRI (<7.0 T) it is not possible to detect a small pathological lesion or tissue changes at an early stage [2, 3]. Three key changes have been observed in the development of MS lesions including demyelination (axonal loss), inflammation and iron deposition [4] with microglia activation-induced iron deposition at the lesion border observed in histology [5, 6] (Figure 6.1).

Table 6.1: The overview of white matter lesion stages.

	Pre-lesion	Acute lesion	Chronic lesion
Pathology	• Perivenular inflammation • Microgia activation • Fibrinogen	• Perivenular inflammation • Open blood brain barrier (BBB) • Transected axon • Immunopatterns	• Remyelinated • Inactive • Smouldering
MRI	• Subtle permeability • Subtle signal change • Enhancing central vein	• PD, T_2W • T_1weighted, MTR • Variable diffusion, perfusion • Gadolinium enhancement • Mild vasogenic edema • Paramagnetic shift as myelin is cleared	• PD, T_2weighted • T_1weighted, MTR • Essential normal permeability • Smolding paramagnetic rim

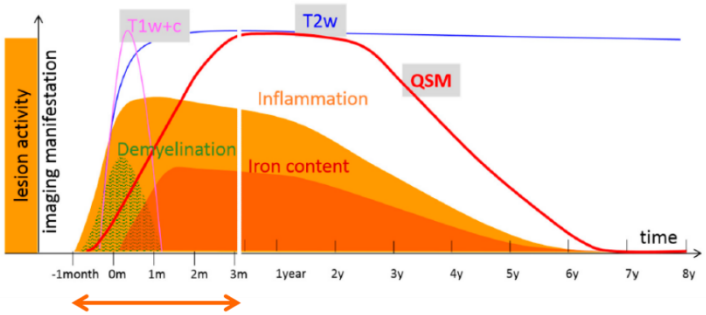


Figure 6.1: Lesion development indicates three key changes including demyelination, inflammation, and iron deposition (adapted from Stuber et al. [4]).

We attempted to investigate the changes occurring prior to lesions being detected. To this end we performed a longitudinal study, repeatedly scanning MS patients, 6 times at 6 week intervals (30 weeks total). We assessed Magnetization transfer (MT) and Nuclear Overhauser Effect (NOE at -3.5 ppm) signals obtained from quantitative analysis of z-spectrum, measured at 7.0 T, as markers of myelination change or other tissue damage. Quantitative susceptibility maps were also acquired using multiple gradient echo to demonstrate pathological changes in

new lesions and surrounding tissue which are related to iron concentration. The susceptibility value of normal myelin is negative with respect to water (diamagnetic) while damaged myelin is more positive (paramagnetic). Moreover, frequency difference mapping (FDM) was calculated from this data to study white matter integrity and tissue microstructure due to the FDM contrast is sensitive to different frequency compartments with different T_2^* and fibre orientation [16]. Finally, susceptibility weighted imaging (SWI) was used to determine whether the visibility of the central vein was affected by new MS lesion.

In this work, we considered the changes in and around lesions at different time points, prior to and after lesion appearance using multiple contrasts including quantitative analysis of z-spectrum (qMT, NOE), susceptibility mapping (QSM), susceptibility weighted imaging (SWI), frequency difference mapping (FDM), T_2^* weighted imaging and compared these with high resolution FLAIR and T_1 weighted PSIR images. The aim of this study was to evaluate longitudinal changes in white matter areas of damaged myelin prior to and after lesion development in MS patients, observable on high resolution scan at 7.0 T MRI.

6.2 Methods

Four patients with chronic MS were scanned 6 times at 6 week interval (30 weeks total) on a Philips 7.0 T Achieva system with T/R 32 channel head coils (Nova Medical). The study was approved by the National Health Service Research ethic committee (12/EM0452). All subjects completed a safety screening questionnaire and gave written informed consent to participate. Multiple scans with different image contrasts were acquired, including FLAIR, PSIR, QSM, SWI, FDM, T_2^* map and z-spectrum data. Parameters for all imaging sequences are provided in Table 6.2.

For data processing, all datasets were co-registered onto the first visit PSIR scan using FSL's $FLIRT$ function (FMRIB's linear image registration tool [10-12]) with the normalized mutual information cost function, six degrees of freedom and sinc resampling. Intra-modal motion correction $(mcflirt)$ in FSL was used for each dataset. Brain mask with Brain Extraction tool (BET) in FSL was used to mask out non-brain region like scalp or skull from the high resolution PSIR image. For each subject visit, the PSIR scan was used to produce a T_1 weighted image with excellent contrast [7] and also to produce an approximate T_1 map via a look up table for use in processing the z-spectrum data. A high contrast-to-noise ratio $(hCNR)$ image was created as reference for image registration onto MT space. B_0, B_1 and T_1 maps were coregistered onto the $hCNR$ image for all further data processing.

Table 6.2: Scanning parameters for multi-contrast at 7.0 T MRI

Contrast	Sequence	Resolution (mm^3)	FOV(AP,RL,FH) (mm)	TR (ms)	TE (ms)	TI (ms)	FA (°)	Duration (min)
FLAIR	IR	0.6x0.6x0.6	192x180x120	4800	258	1650	90	5.28
T_1w, T_1map	IR-TFE with PSIR [7]	0.6x0.6x0.6	200x180x120	13.10	6.04	787	8	11.58
Z-Spectrum	MT-TFE [8], [9]	1.5x1.5x1.5	192x180x60	6.01	2.79		8	11.40
T_2^*, QSM, SWI	FFE (5 echoes)	0.6x0.6x0.6	192x185x70	50	8-28		14	6.77
T_2^*, FDM	FFE (8 echoes)	1.2x1.2x1.2	192x183x60	38	2.5-30.5		14	4.83
B_0	FFE (double echo method)	3.0x3.0x2.0	256x256x150	200	6		25	1.00
B_1	FFE (Dual TR method)	3.2x4.0x4.0	205x180x132	20, 120	5		60	3.05

The z-spectra were acquired using MT-TFE sequence at two nominals B_1 saturation powers (0.33μT, 0.65μT) with saturation pulses applied at 23 offset

frequencies. The z-spectra were corrected for B_0 variations using B_0 maps of the whole brain. For B_0 correction, there were two steps to work out in determining the exact frequency of the saturation. Each voxel in the z-spectrum was interpolated and shifted according to B_0 field offsets. Next, the average minimum of the z-spectrum from all voxels was found to estimate the average of water frequency. Finally, the z-spectra for all voxels were shifted according to the average water frequency, and resamplied at the original offset frequency. The resulting spectra at two different B_1 powers were simultaneously fitted pixel-wise for the amplitude of 3 pools (MT, NOE and APT) relative to water, based on the Bloch-McConnell equations via a look-up table, for all datasets with actual B_1 values estimated from the B_1 maps [9,13]. The look up table (LUT) was simulated from physical parameters proposed by Geades et al. [8] for mapping all quantitative of 3 pools in MS patient with active brain lesions.

High resolution FFE data provided T_2^* weighted images (TE=20 ms) and susceptibility maps. QSM maps were reconstructed using MATLAB in-house software provided in STI Suite v2.2 [14-15]. The magnitude image was used to a create brain mask with Brain Extraction tool in FSL. QSM maps are reconstructed from phase image with correction of field perturbation and tissue field perturbation. The signal phase was processed with the Laplacian-based phase unwrapping, the sophisticated harmonic artefact reduction for phase data (V-SHARP) method with variable-radius kernel at 5 voxels and the improved sparse linear equation and least-square (iLSQR) algorithm to generate susceptibility map for each subject. Moreover, the magnitude and phase data from T_2^* weighted images were combined to produce SWI according to Haacke et al. [33]. For every new lesion, the presence of a central vein was analysed for each time point, appeared as a hypointensity region found at the centre of hyperintense lesion on three orthogonal planes. No calculation of venous diameter was attempted in the study.

The low resolution FFE dataset was used for frequency difference mapping. FDM measures the difference in apparent local frequency calculated from individual phase images in multiple gradient echo sequence. This difference exists because the non-linear accumulation of local MR phase with time in some tissues, especially in white matter. FDM maps were produced by scaling phase data by echo time as previously described in [16]. Two sets of frequency difference data were created. FDMav is the phase accumulated during each echo time which is calculated by summing up the maps over TE-period (8 echoes) and FDM3 is the phase map at the third echo time. With this dataset, another map of relaxation rates ($R_2^* = 1/T_2^*$) was created to help in visualising the changes in WM tissue before and after lesion development.

For ROI processing, lesion masks were drawn by an experienced neurologist on all FLAIR images. Hyperintense FLAIR lesions were marked at every time point separately. Lesions that appeared during the time course of the study were then identified manually. Time courses were referenced to time point of first appearance of the lesion on FLAIR (defined as time=0). Three regions were defined for each lesion: periphery, edge and core on the PSIR images. The core ROI was defined as the lesion mask on the final image (this was always the smallest mask). Masks on which a lesion was observed (from time=0) were then combined using the logical OR operator. The first time point at which the lesion was visible was eroded by one voxel and the difference between the original and eroded ROI was used to define the periphery ROI. The region lying between these two ROIs was defined as edge (Figure 6.2). Control ROIs were drawn in the homogeneous NAWM in both hemispheres, clearly distal to any lesion. The mean and standard deviation of the signals in each ROI were presented.

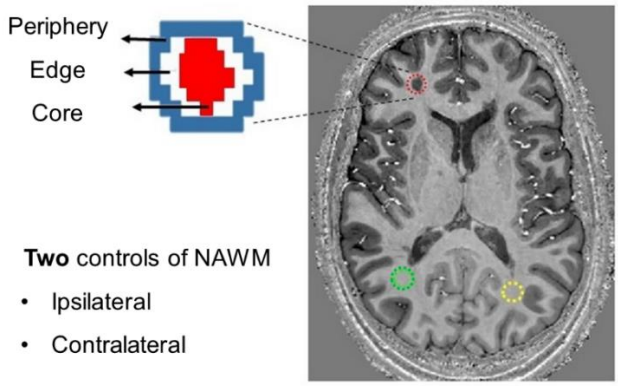


Figure 6.2: The definition of ROIs of MS lesion and NAWM

New MS lesions were divided into two groups: those with and without hyperintense rim visible at the border of the lesion identified on QSM data. There was sometimes a larger rim visible around the lesion on the FLAIR image (Figure 6.9), but this was not considered here. Note that the edge ROI does not necessarily correspond to the rim identified on QSM data.

The signals for the weighted scans including FLAIR, PSIR and T_2^* were normalized to achieve zero mean and unit variance across the whole volume [18-19] to reduce the intensity variation over time. For each subject, for each visit, the images were rescaled by $I_{norm\,i} = (I_i - \mu)/SD$ where I is the signal intensity, i is the observation at the i^{th} pixel, μ is the mean intensity over those values and SD is the standard deviation of whole value. Thus, observed data on weighted scans have the same intensity distribution. For QSM, the average value across four ROIs in the CSF was observed, and then subtracted this value from every value we measured in other ROIs.

6.3 Results

The demographics of the subjects and the numbers of new lesions detected in six months are given in Table 6.3. Based on signal intensity changes and their appearances, there were two types of new MS lesion. The first type (25%) showed a hyperintense rim at the periphery on QSM while other type (75%) were uniformly hyperintense on QSM with no rim (Figure 6.3). If a rim was seen at the first time point, it always visible at later time points. Table 6.3 also shows the number of each type of lesions for each subject. In this study lesions with hyperintense rim were much bigger than lesion with no rim, and lesions were always observed to shrink after their first appearance of lesion on PSIR images (Figure 6.4).

Table 6.3: Demographic characteristics of participants and characterisation of new lesions found at 7.0 T MRI.

Subject	Age	Gender	Lesion with rim on QSM	Lesion without rim on QSM	Average volume of lesion with rim*	Average volume of uniformly lesion with no rim*
1	23	Male	1	6	3944.2	154.9
2	39	Female	0	1	0	8.2
3	35	Female	2	2	630.7	89.4
4	27	Female	2	6	1327.3	398.5
Total			5	15	1475.5	162.8

Note: * at time of first appearance on PSIR scan (mm^3)

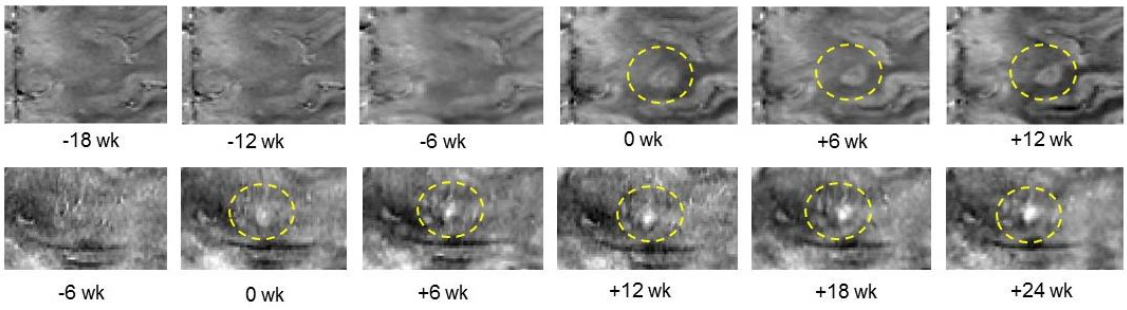


Figure 6.3: The characteristic of demyelinating MS lesions (identified on QSM) showed a different enhancement pattern in MRI (yellow). The first type showed hyperintense rim (top) and other types were uniformly hyperintense with no rim (bottom). The first appearance of the lesion on FLAIR was defined as time=0.

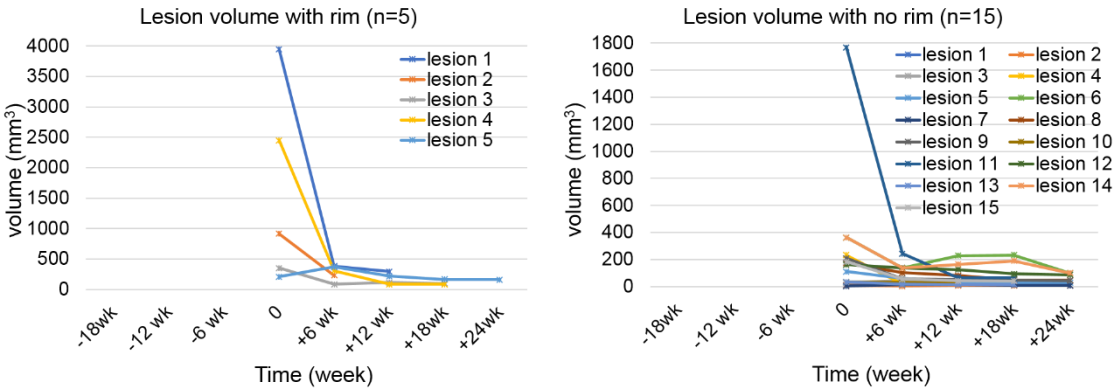


Figure 6.4: Line graphs show progression of volume of twenty new lesions with hyperintense rim (left) and uniformly hyperintense with no rim (right) on PSIR images over the course of study.

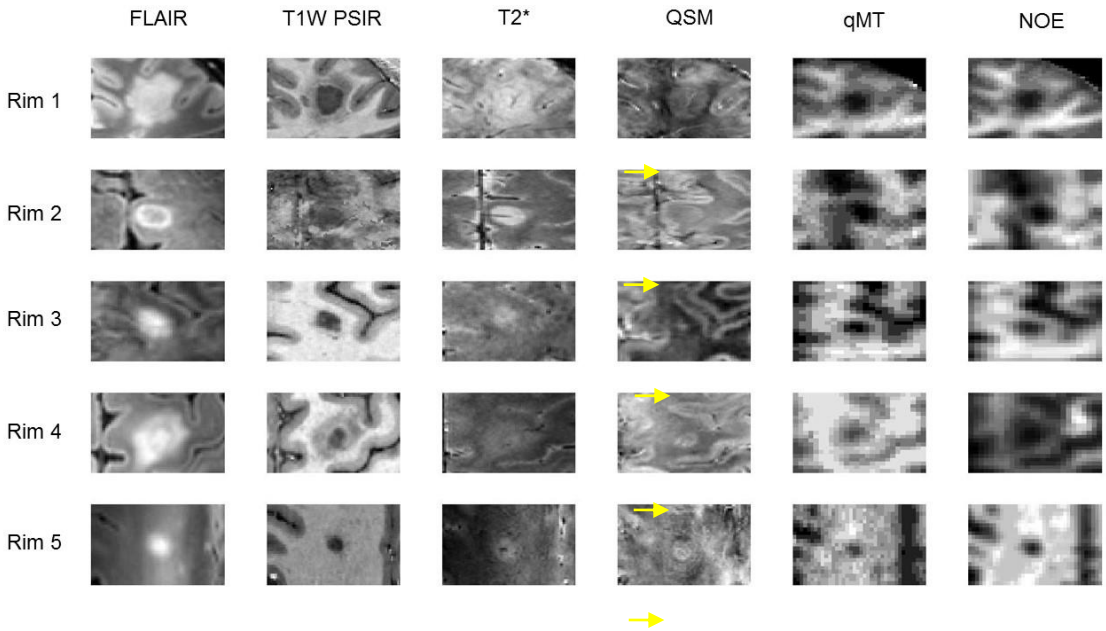


Figure 6.5: Example of multi-contrast MRI in acute MS lesions with hyperintense rim (n=5, identified on QSM) according to the first appearance of lesion (arrow).

Figure 6.5 shows new MS lesion with hyperintense rim in multiple MR contrasts at 7.0 T compared to lesion with no hyperintense rim according to the first appearance of lesion (Figure 6.6). The lesions were generally hyperintense on FLAIR, T_2^* and QSM images, but hypointense on PSIR, qMT and NOE images. For FDM contrast, the white matter lesions always appeared hyperintense relative to normal tissue surrounding, but visualization of changes on FDM maps varied markedly according to the white matter fibre density, morphology, location and

orientation. Interestingly, changes in signal intensity prior to the first appearance of MRI-visible FLAIR lesion was found on QSM, qMT and NOE data. A reduction of qMT and NOE values was found at least 6 weeks prior to lesion formation and susceptibility contrast showed inhomogeneous intensities at lesion site at the same time. However, no changes were found on FLAIR, PSIR and T_2^* images prior to the first appearance of lesion.

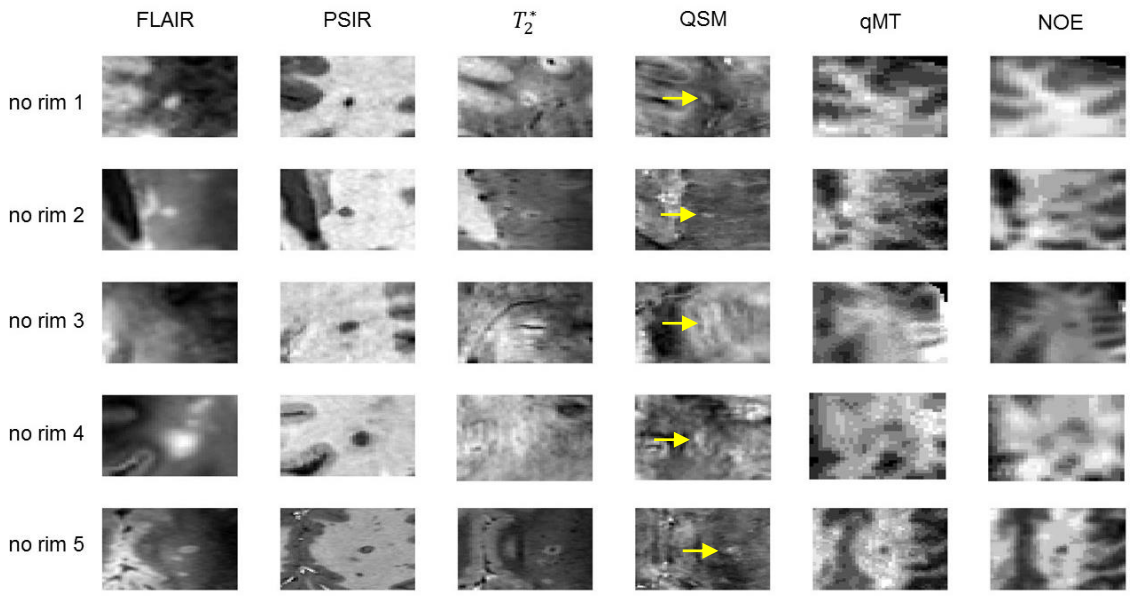


Figure 6.6: Example of multi-contrast MRI in acute MS lesions with no hyperintense rim. In a total of 15 lesions were detected, 5 lesions were selected to compare according to the first appearance of lesion (arrow).

6.3.1 Tracking new MS lesions with hyperintense rim

Figure 6.7-6.11 shows an enhancement pattern of individual MS lesions with hyperintense rim (n=5, identified on QSM) across multiple contrasts MRI at 7.0 T. The areas of damaged myelin appeared as hyperintense on FLAIR, QSM, T_2^*, SWI, FDM3, and FDMav images, but hypointense on PSIR, qMT, NOE and R_2^* maps relative to normal WM tissue surrounding. Taking time = 0 as the first time point in which the lesion appeared on FLAIR.

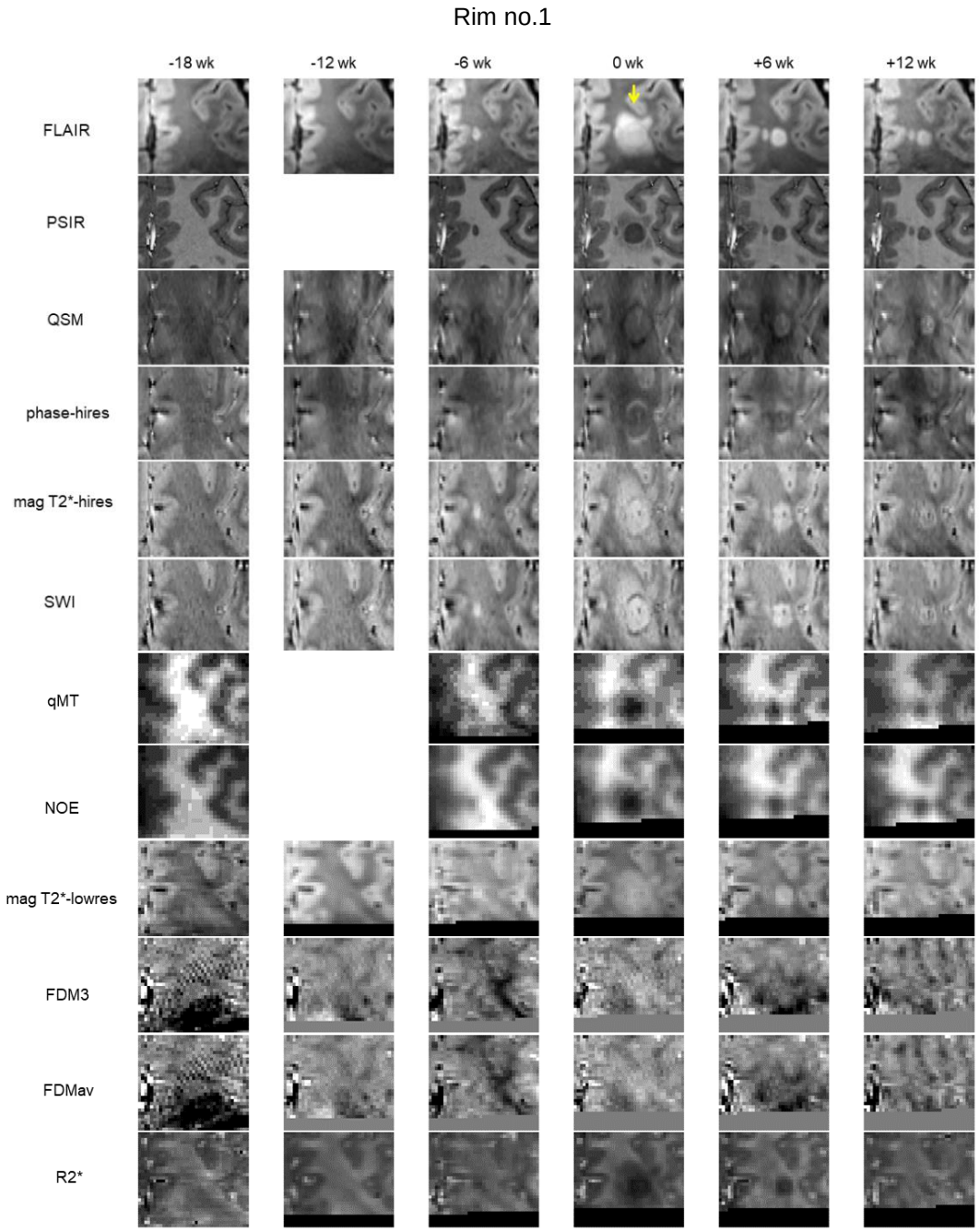


Figure 6.7: Evolution of new MS lesion with hyperintense rim (from patient 1) showed demyelination is “hyperintense” (bright) on FLAIR, QSM, SWI, FDM3, FDMav, and T_2^* images but “hypointense” (dark) on PSIR, qMT, NOE and R_2^* maps. The first appearance of lesion defined as time=0 (yellow arrow).

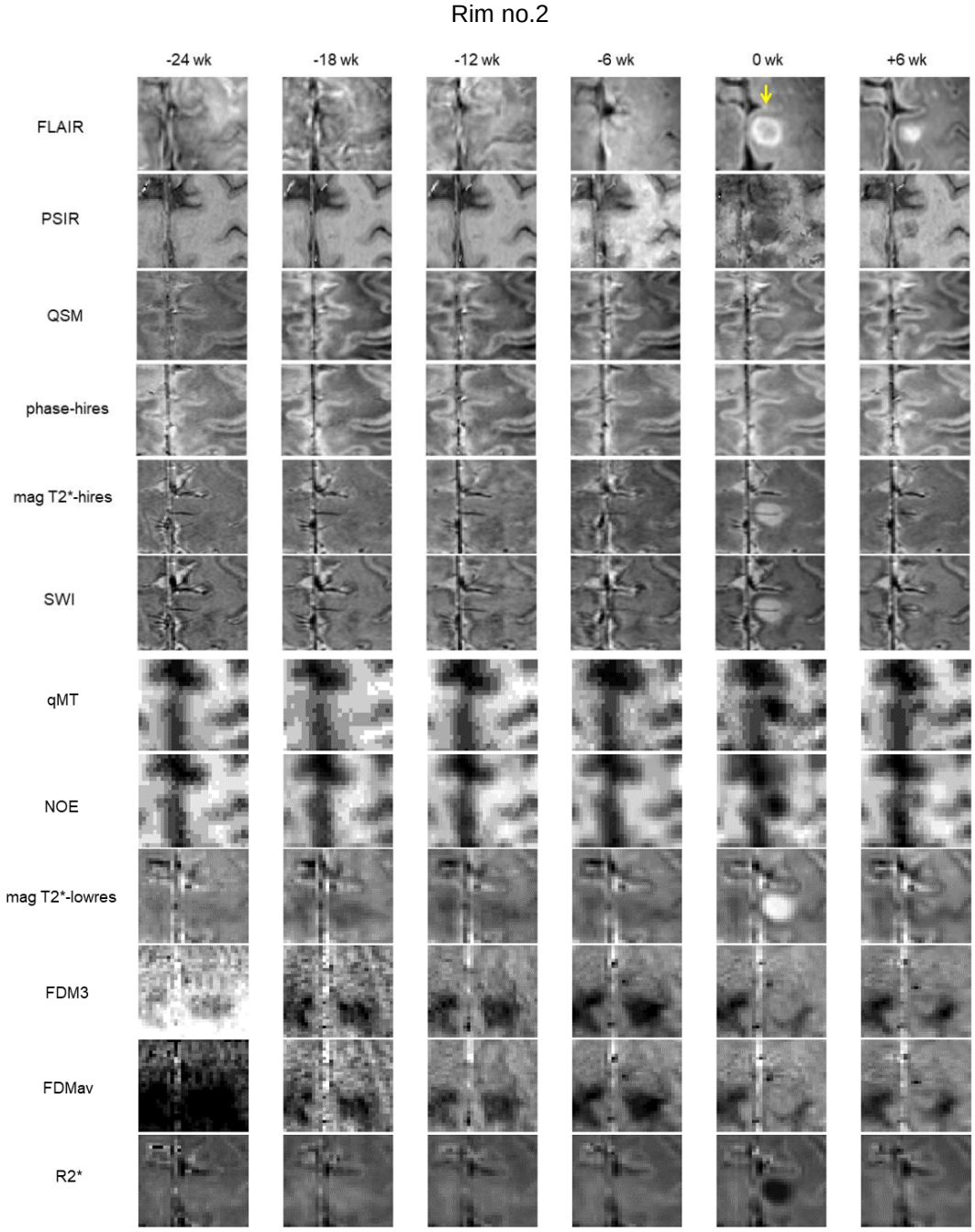


Figure 6.8: Evolution of new MS lesion with hyperintense rim (from patient 3) showed demyelination is "hyperintense" (bright) on FLAIR, QSM, SWI, FDM3, FDMav, and T_2^* images but "hypointense" (dark) on PSIR, qMT, NOE and R_2^* maps. The first appearance of lesion defined as time=0 (yellow arrow).

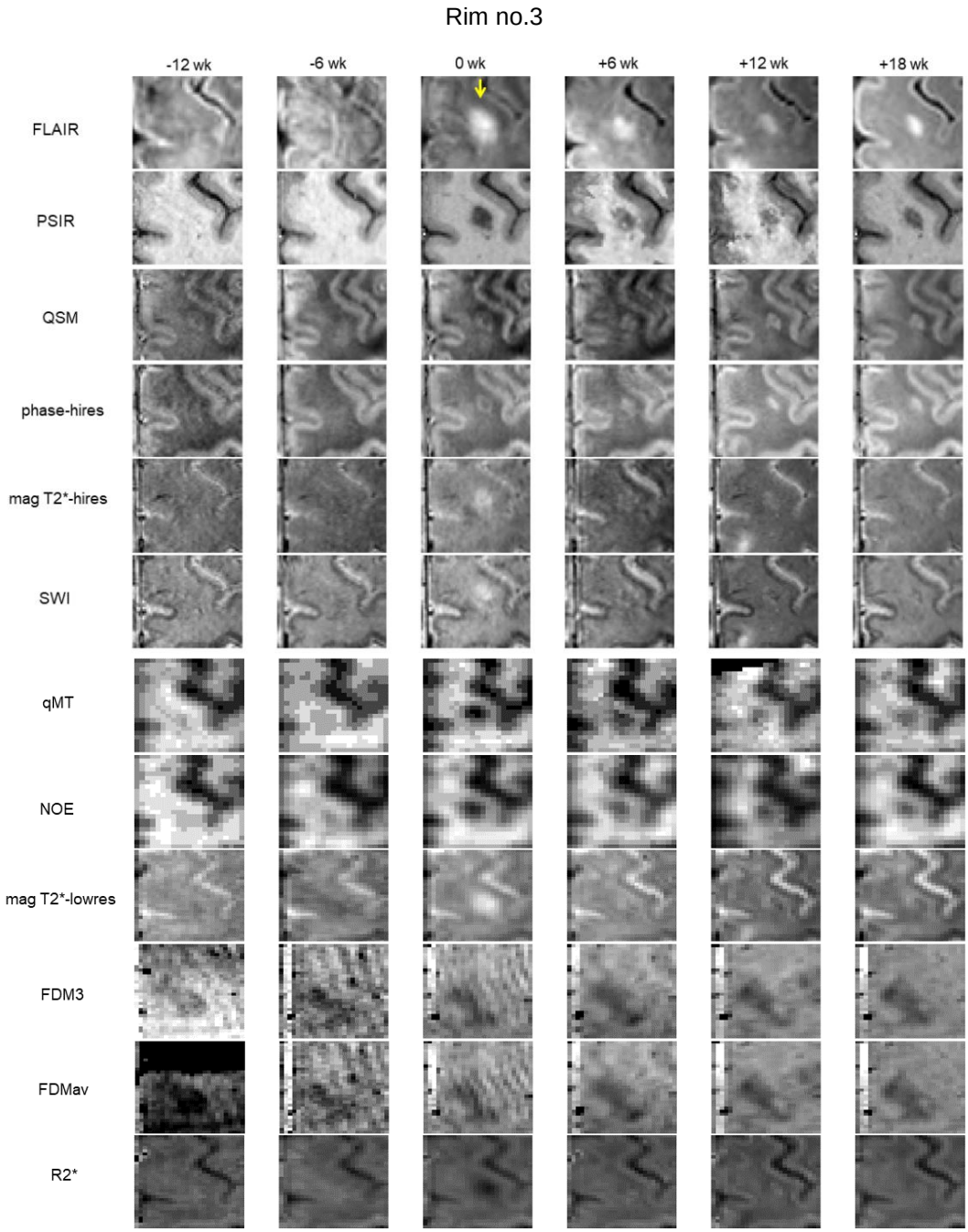


Figure 6.9: Evolution of new MS lesion with hyperintense rim (from patient 3) showed demyelination is “hyperintense” (bright) on FLAIR, QSM, SWI, FDM3, FDMav, and T_2^* images but “hypointense” (dark) on PSIR, qMT, NOE and R_2^* maps. The first appearance of lesion defined as time=0 (yellow arrow).

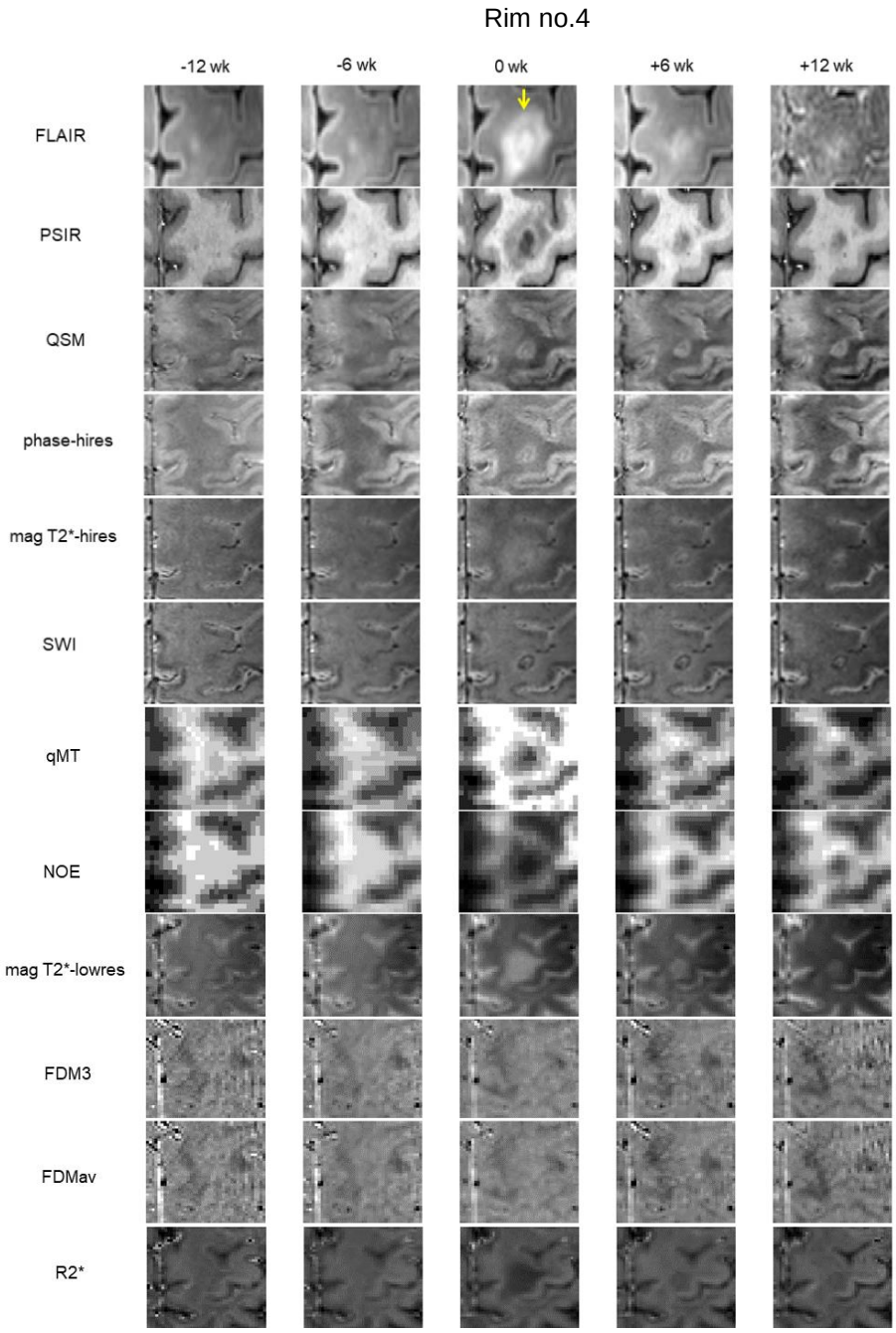


Figure 6.10: Evolution of new MS lesion with hyperintense rim (from patient 4) showed demyelination is “hyperintense” (bright) on FLAIR, QSM, SWI, FDM3, FDMav, and T_2^* images but “hypointense” (dark) on PSIR, qMT, NOE and R_2^* maps. The first appearance of lesion defined as time=0 (yellow arrow).

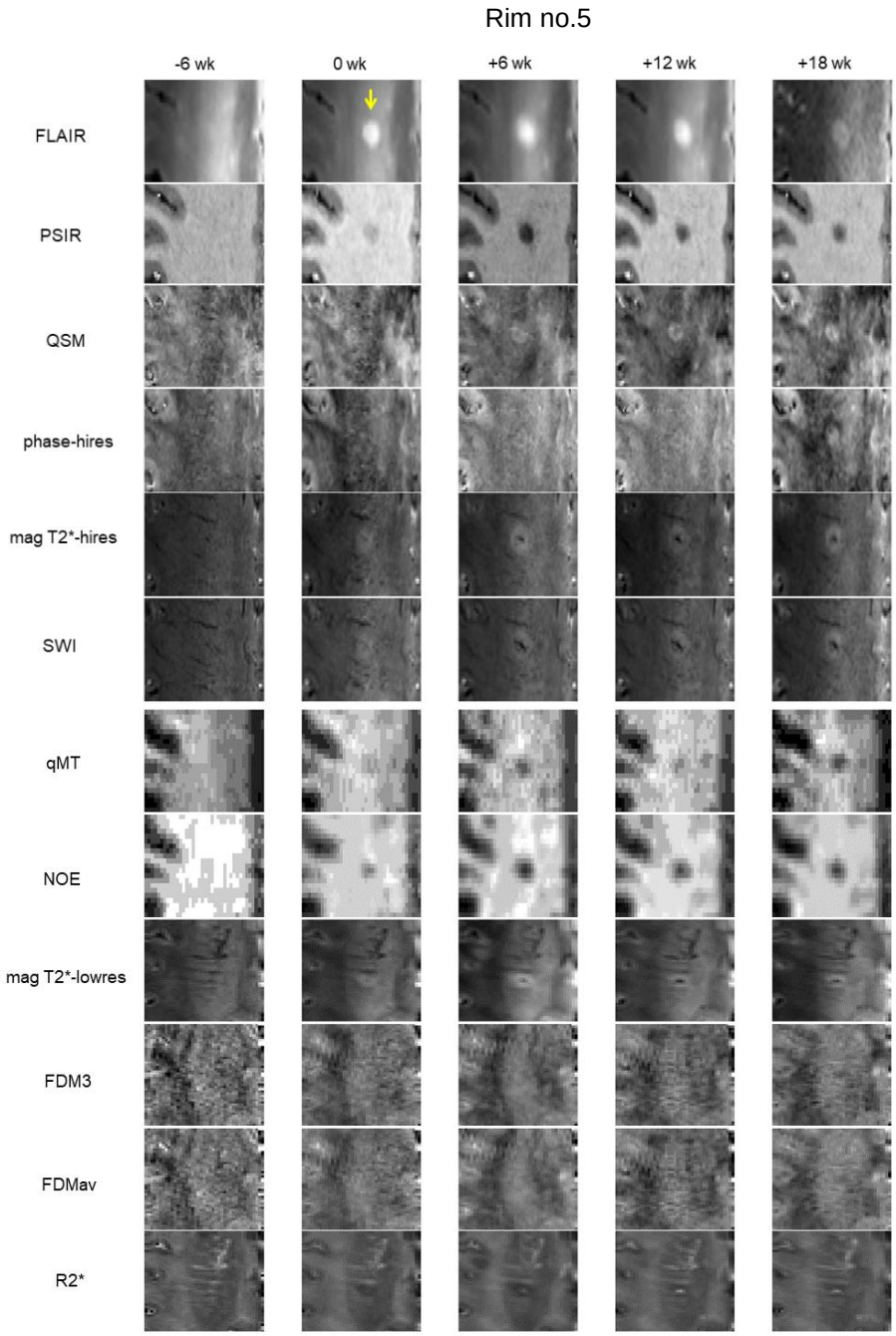


Figure 6.11: Evolution of new MS lesion with hyperintense rim (from patient 4) showed demyelination is “hyperintense” (bright) on FLAIR, QSM, SWI, FDM3, FDMav, and T_2^* images but “hypointense” (dark) on PSIR, qMT, NOE and R_2^* maps. The first appearance of lesion defined as time=0 (yellow arrow).

6.3.2 Signal changes in new MS lesions with hyperintense rim

Figure 6.12 shows the time course of normalized signal changes in different image contrasts such as FLAIR, PSIR, T_2^*, qMT, NOE and QSM, respectively, for the three ROIs of periphery (top), edge (middle) and core (bottom), for individual MS lesions with hyperintense rim (n=5) compared to controls that were detected in contralateral and ipsilateral NAWM.

Prior to the first appearance of lesion on FLAIR images, no significant changes were observed on the T_1 weighted PSIR scan or T_2^* images, but qMT and NOE measurements were reduced at least 6 weeks prior to detection and recovered within 6-12 weeks of lesion formation. The changes in QSM data were more variable. All new lesions with hyperintense rim exhibited heterogeneous signal distribution in susceptibility images 12-18 weeks prior to lesion appearance. Susceptibility values at lesion site tended to increase after lesion development with greater changes being observed in the lesion core compared to the edge and periphery ROIs. In the control group, the NAWM signals showed very little change over the course of the study for all measures. However, evaluation of signal changes in FDM maps does not yield any significant results due to the greater variation in FDM contrast found in this dataset (caused by motion artefacts during FDM acquisition and effect of fibre-orientation).

These results indicate that there was no statistically significant difference on FLAIR, PSIR, and T_2^* images ($p>0.05$) prior to the first appearance of lesion, but statistically significant difference was found in qMT and NOE images at 6 weeks prior to detection ($p<0.05$). QSM data also showed statistically significant difference up to 18 weeks before lesion appearance ($p<0.05$).

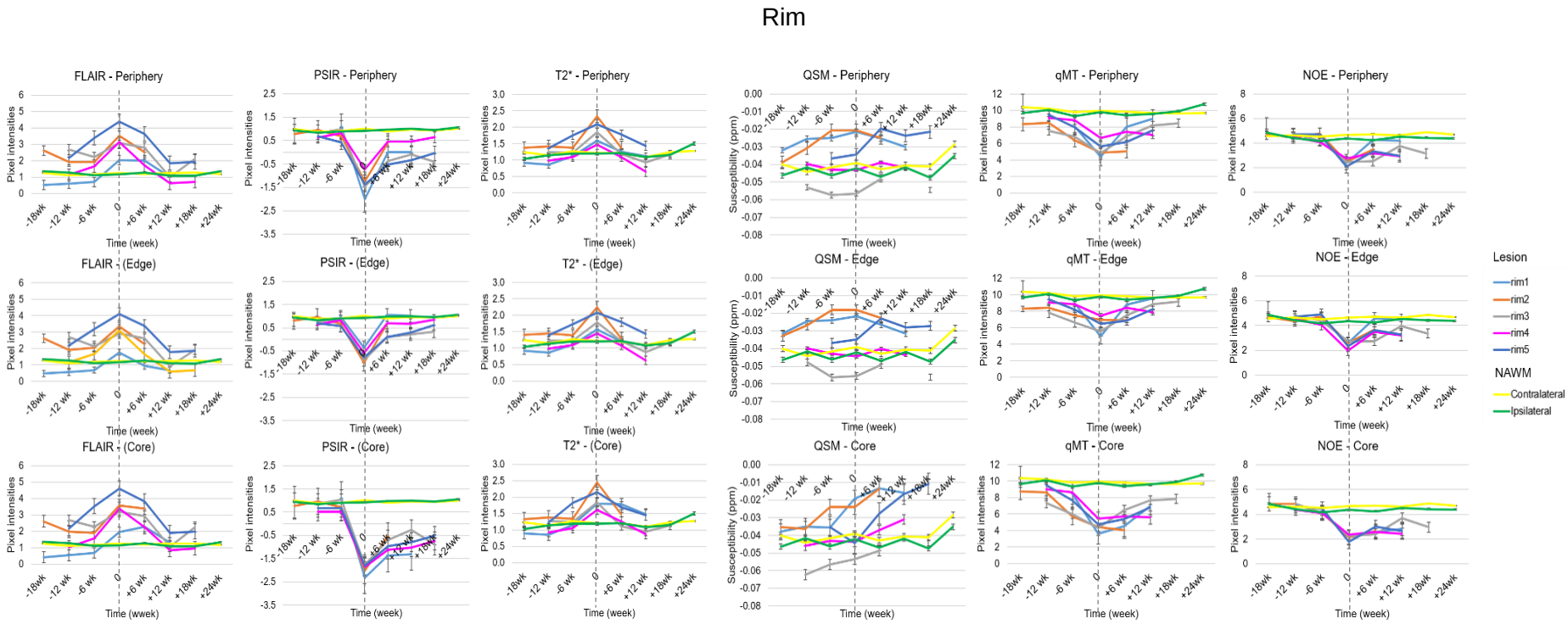


Figure 6.12: Evaluation of pixel intensities of individual new lesions with hyperintense rim (n=5) are presented for each ROIs; periphery (top), edge (middle), and core (bottom), respectively. Lesion ROIs were compared with control ROIs in contralateral (yellow) and ipsilateral NAWM (green) where the first appearance of lesion defined as time=0 (dashed line). Graph on the left to right presents the changes of pixel intensities in FLAIR, PSIR, T_2^*, QSM, qMT, and NOE, respectively.

6.3.3 Tracking new MS lesions with no hyperintense rim (identified on QSM)

Figure 6.13-6.17 shows multi-contrasts MRI of individual lesions with no hyperintense rim (selected 5 lesions from a total of 15 lesions). The behaviour of these lesions was similar. The observed lesion intensity and size were much smaller than lesions with hyperintense rim. However, FDM contrast varied considerably.

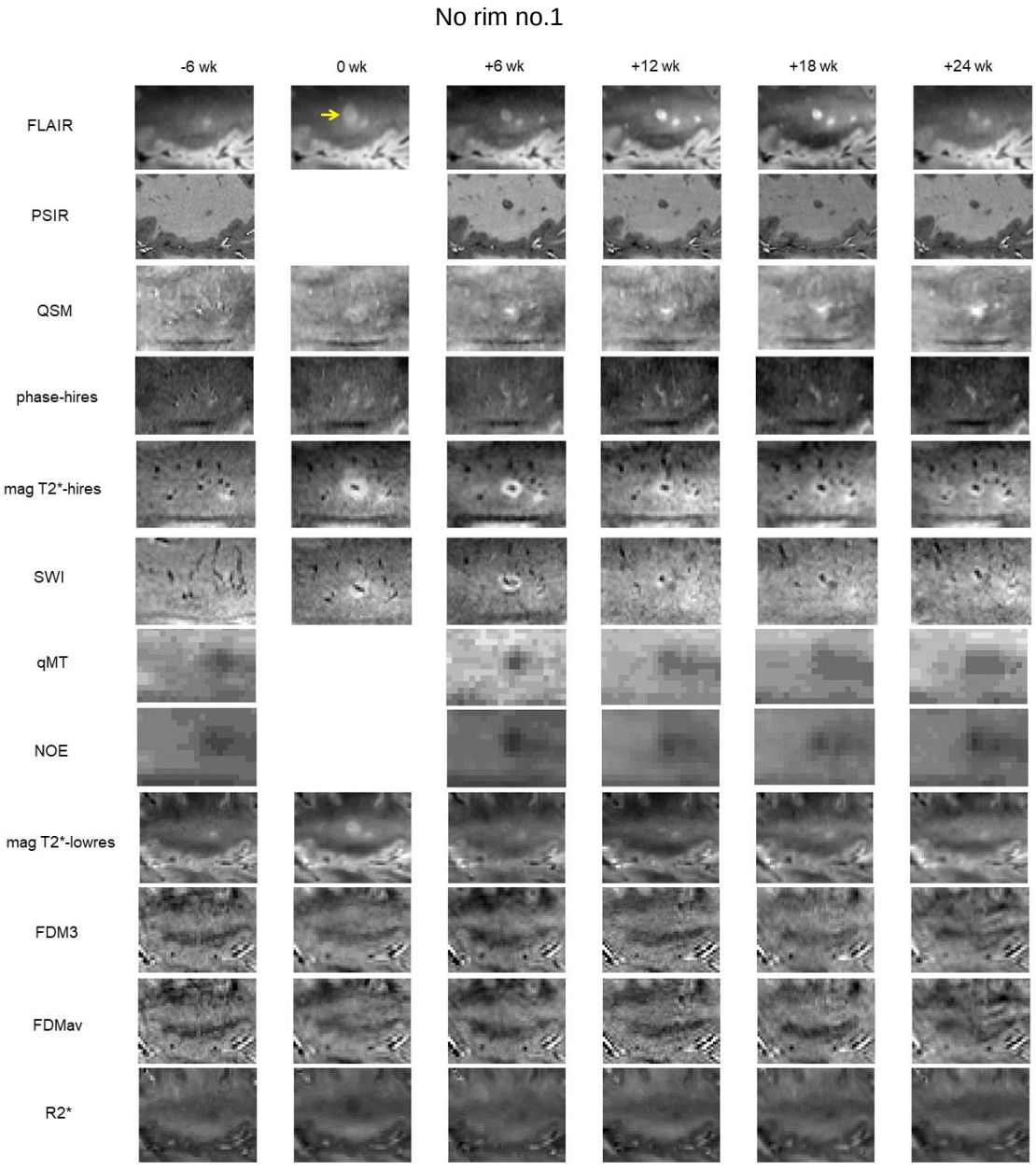


Figure 6.13: Evolution of new MS lesion with no hyperintense rim (from patient 1) showed hyperintense signal (bright) on FLAIR, QSM, SWI, and T_2^* images but hypointense signal (dark) on PSIR, qMT, NOE and R_2^* images. No change was found on FDM maps. The first appearance of lesion defined as time=0 (yellow arrow).

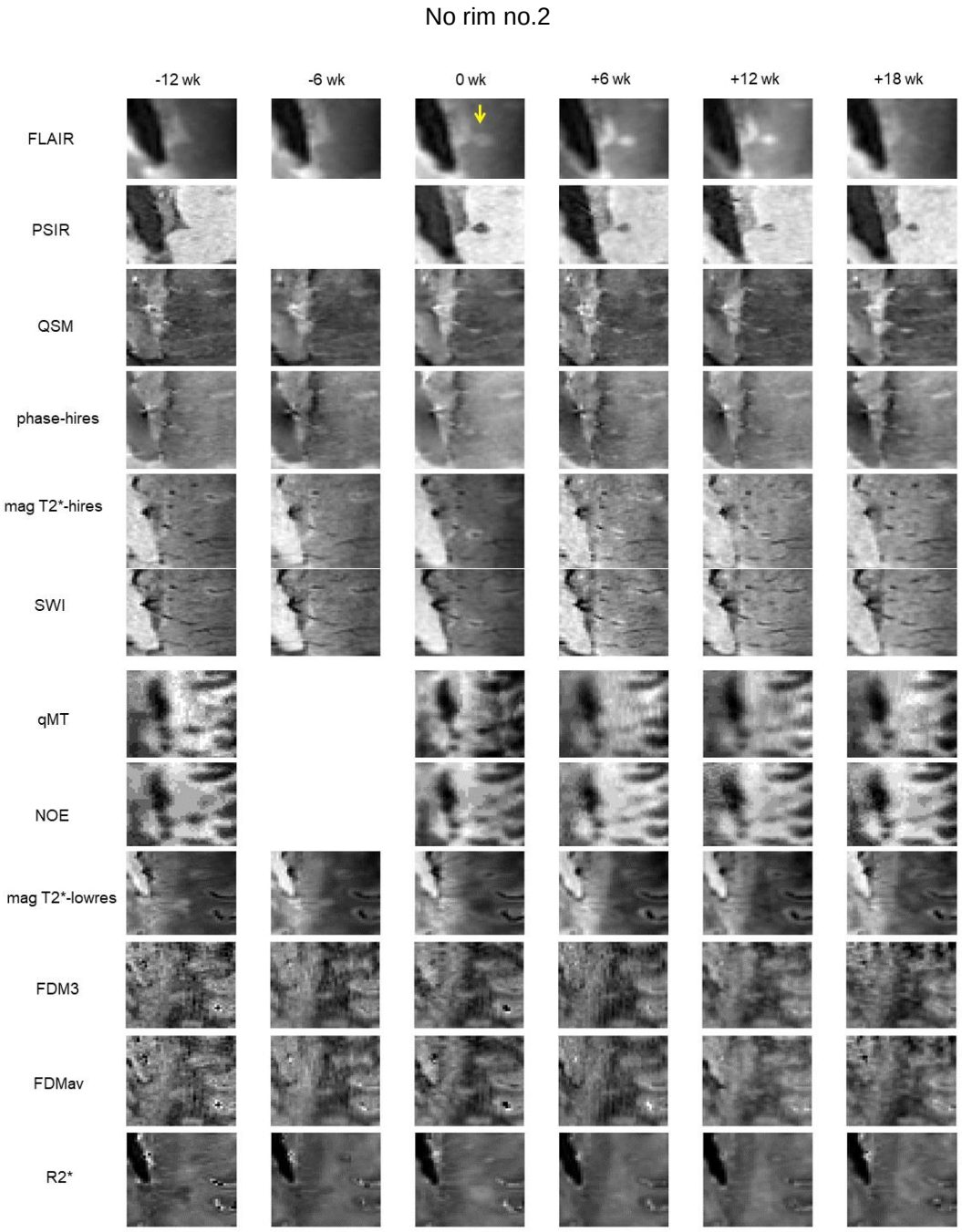


Figure 6.14: Evolution of new MS lesion with no hyperintense rim (from patient 1) showed hyperintense signal (bright) on FLAIR, QSM, SWI, and T_2^* images but hypointense signal (dark) on PSIR, qMT, NOE and R_2^* images. No change was found on FDM maps. The first appearance of lesion defined as time=0 (yellow arrow).

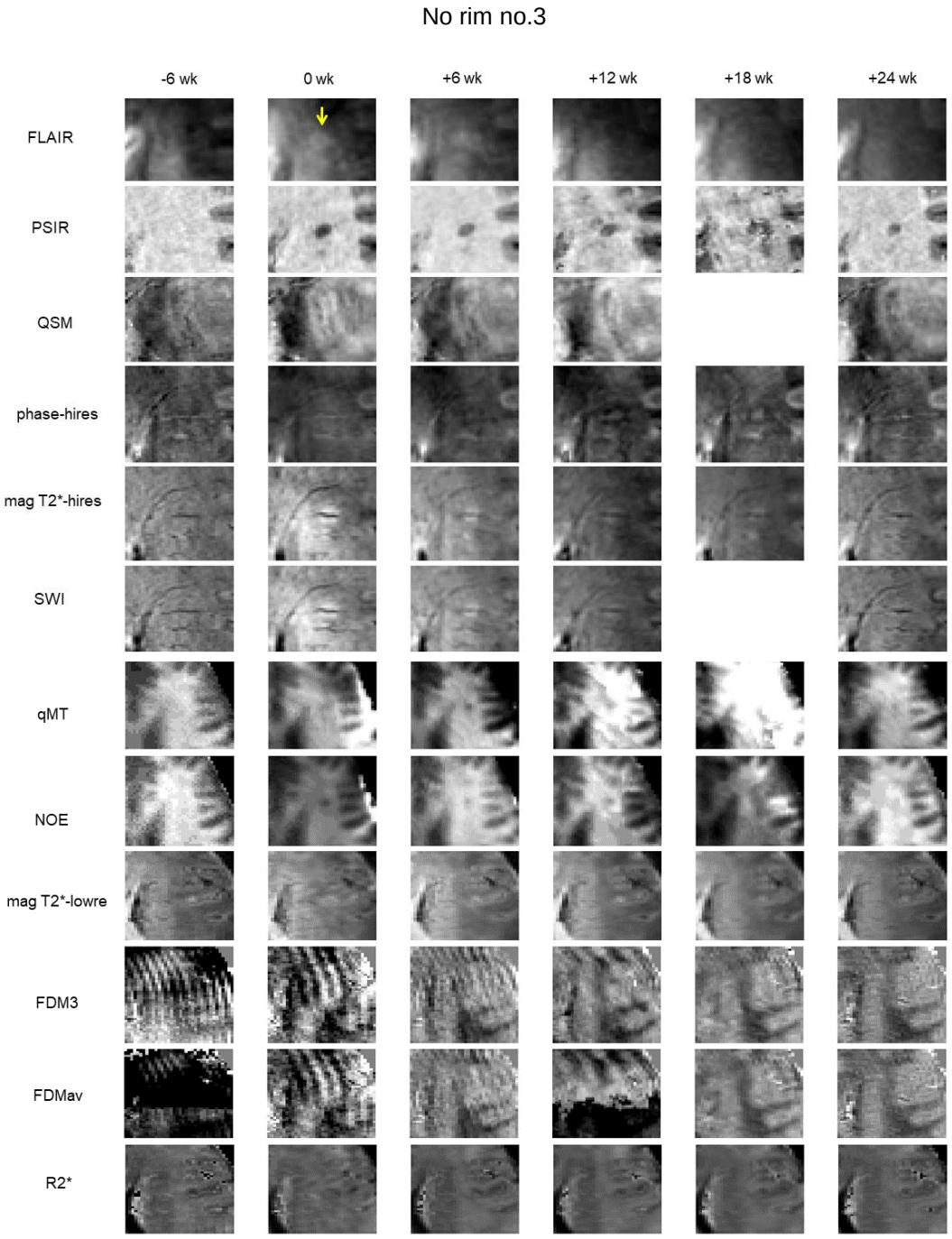


Figure 6.15: Evolution of new MS lesion with no hyperintense rim (from patient 3) showed hyperintense signal (bright) on FLAIR, QSM, SWI, and T_2^* images but hypointense signal (dark) on PSIR, qMT, NOE and R_2^* images. No change was found on FDM maps. Ringing artefact caused by patient motion during image acquisition was found in longitudinal analysis of FDM. The first appearance of lesion defined as time=0 (yellow arrow).

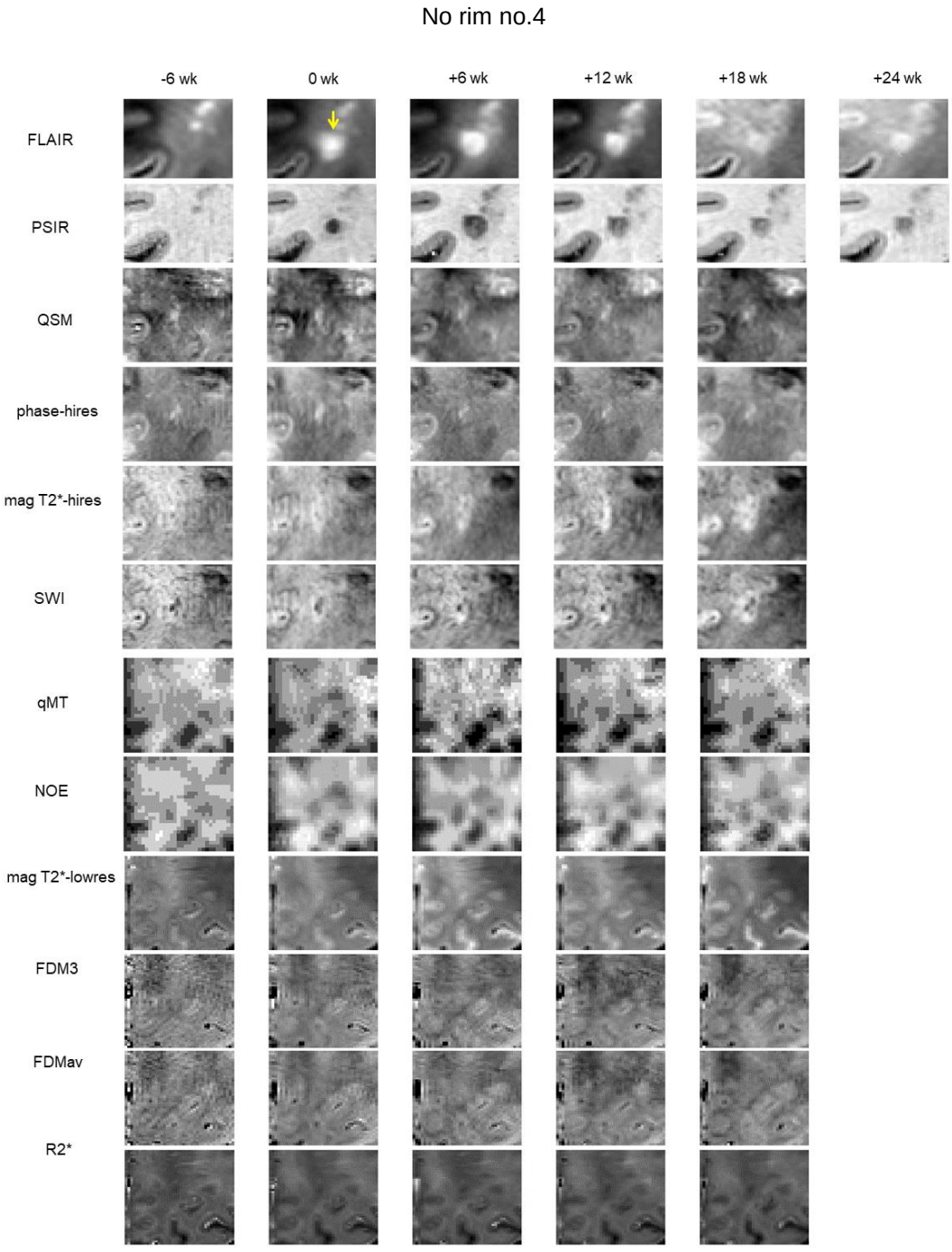


Figure 6.16: Evolution of new MS lesion with no hyperintense rim (from patient 4) showed hyperintense signal (bright) on FLAIR, QSM, SWI, and T_2^* images but hypointense signal (dark) on PSIR, qMT, NOE and R_2^* images. No change was found on FDM maps. The first appearance of lesion defined as time=0 (yellow arrow).

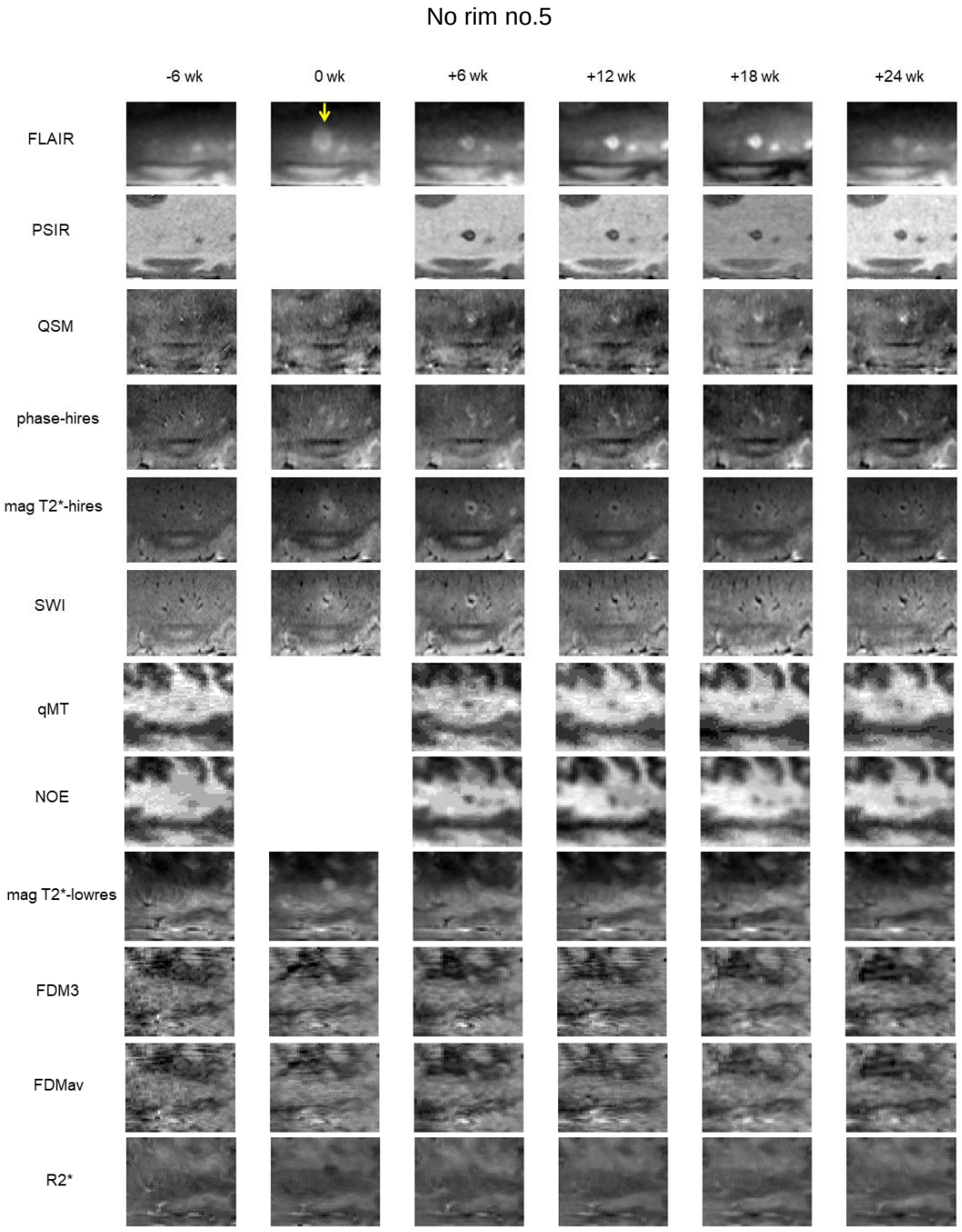


Figure 6.17: Evolution of new MS lesion with no hyperintense rim (from patient 1) showed hyperintense signal (bright) on FLAIR, QSM, SWI, and T_2^* images but hypointense signal (dark) on PSIR, qMT, NOE and R_2^* images. No change was found on FDM maps. The first appearance of lesion defined as time=0 (yellow arrow).

No rim

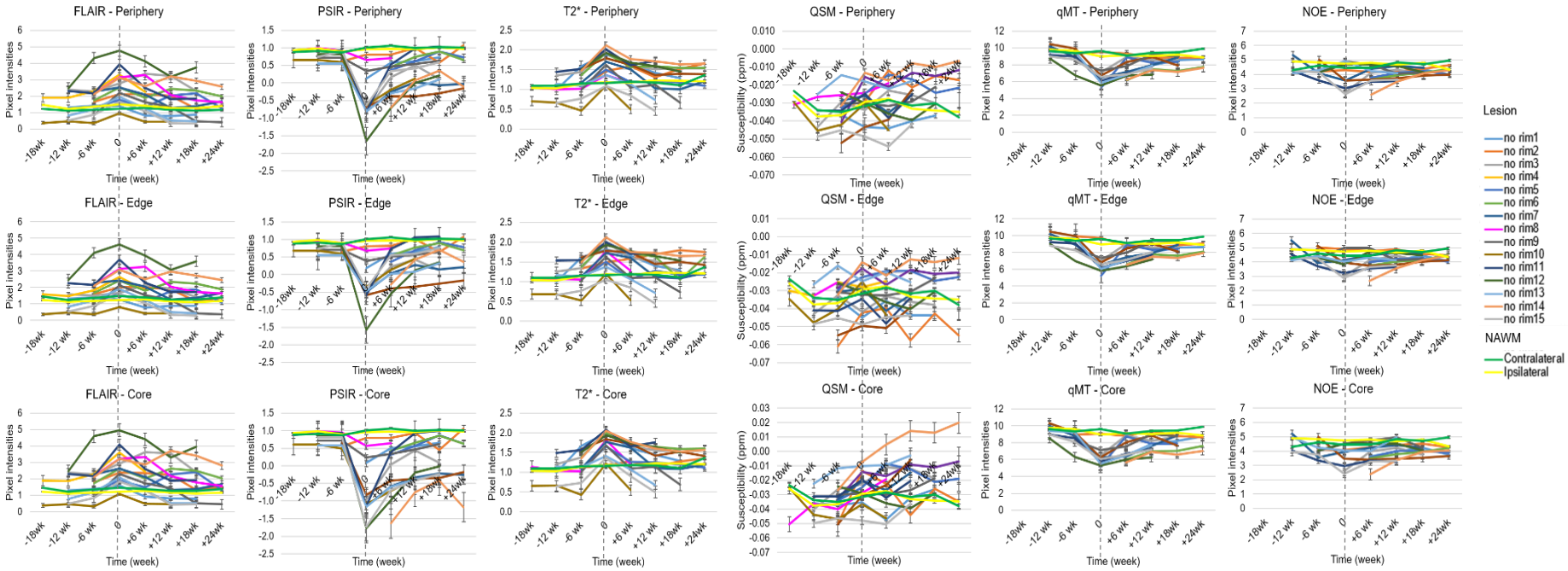


Figure 6.18: Evaluation of pixel intensities of individual new lesions with no rim (n=15) are presented for each ROIs; periphery (top), edge (middle), and core (bottom), respectively. Lesion ROIs were compared with control ROIs in contralateral (yellow) and ipsilateral NAWM (green) where the first appearance of lesion defined as time=0 (dashed line). Graph on the left to right presents the changes of pixel intensities in FLAIR, PSIR, T_2^*, QSM, qMT, and NOE, respectively.

6.3.4 Signal changes in new MS lesions with no hyperintense rim

Figure 6.18 shows the time course of normalized signal changes in different image contrasts such as FLAIR, PSIR, T_2^*, qMT, NOE and QSM, respectively, for the three ROIs of periphery (top), edge (middle) and core (bottom), for individual MS lesions with no hyperintense rim (n=15) compared to controls that were detected in contralateral and ipsilateral NAWM. Smaller changes were detected in new lesions with no hyperintense rim as compared to a rim.

Prior to the first appearance of lesion on FLAIR images, no significant changes were observed on the T_1 weighted PSIR scan or T_2^* images, but qMT and NOE measurements were slightly reduced at least 6 weeks prior to detection and recovered within 6-12 weeks after lesion appearance. The changes in QSM data varied but susceptibility values at lesion site tended to increase after lesion development with greater changes being observed in the lesion core compared to the edge and periphery ROIs. Evaluation of FDM maps showed less contrast due to small lesion size. In NAWM regions, small changes in signals were found over the course of the study for all measures.

These results indicate that there was no statistically significant difference on FLAIR, PSIR, and T_2^* images ($p>0.05$) prior to the first appearance of lesion, but statistically significant difference was found in qMT and NOE images at 6 weeks prior to detection ($p<0.05$). QSM data showed statistically significant difference up to 18 weeks before lesion appearance ($p<0.05$).

6.3.5 Comparison between the changing of qMT and NOE

The decreasing of qMT and NOE are significant at a time point prior to the first appearance of a lesion (time=0). We found an initial reduction of qMT and NOE in demyelinating lesions where qMT data decreased significantly in the core of lesion and slightly lower at the edge than periphery (Figure 6.19). NOE data showed the same trend on a smaller scale. Lesions with hyperintense rim showed a larger change in qMT than lesions with no hyperintense rim.

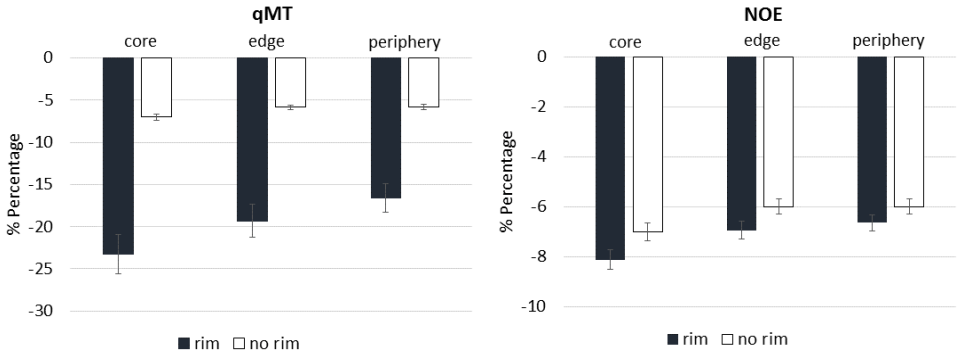
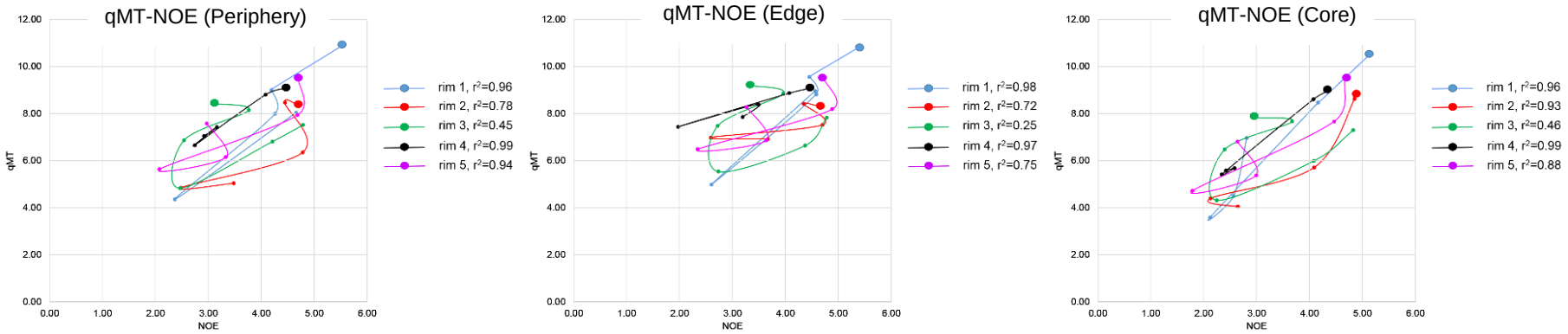


Figure 6.19: The percentage decreased in qMT and NOE, between the first visible lesion on FLAIR images and 6 weeks earlier. Lesion ROIs including core, edge and periphery were compared with respect to hyperintense rim found in QSM data.

6.3.6 Relationship between qMT and NOE

The rim and no rim graphs are on the same scale so in part the differences indicate the changes are more disorderly (decoupled) in the no rim case. With respect to hyperintense rim found in QSM data during the time course of this study, Figure 6.20 suggests that NOE and qMT are positively correlated. The data points are joined to indicate their temporal relationship.

Rim



No rim

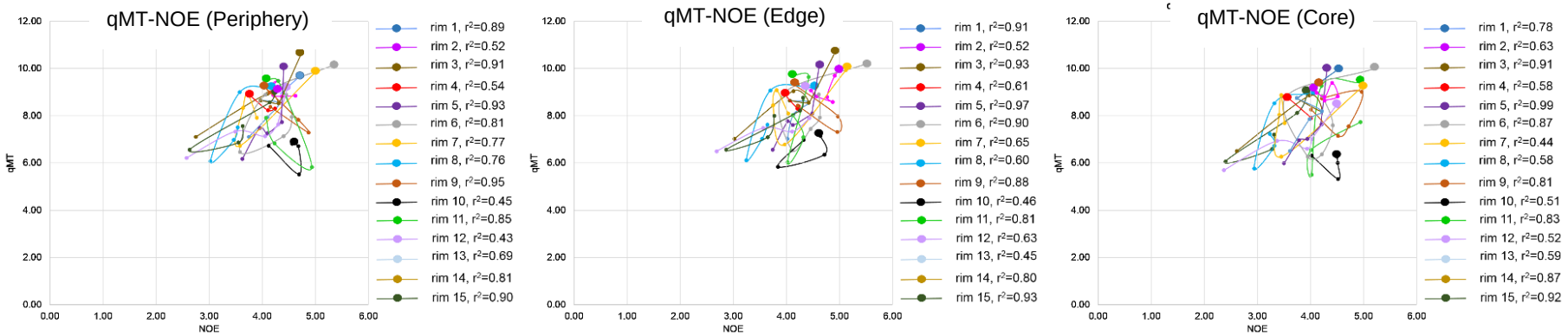
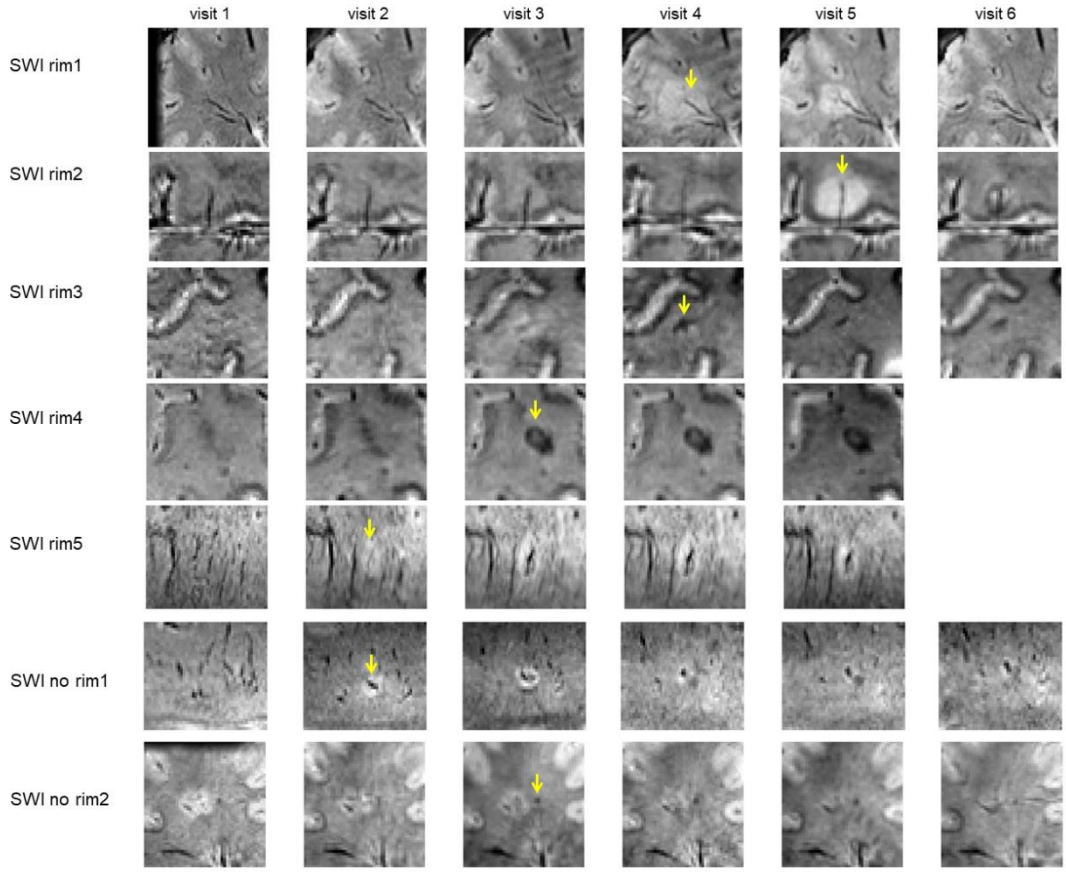


Figure 6.20: The correlation between qMT and NOE signal for the three ROIs, for both types of new lesion separately. Lesion with hyperintense rim is shown on the top and lesion without rim is shown on the bottom. Lesions ROIs of periphery (left), edge (middle) and core (right) were compared with respect to hyperintense rim found in QSM data during the time course of this study.

6.3.7 Intralesional veins on SWI

Paramagnetic properties of deoxygenated haemoglobin in venous blood provides an intrinsic contrast agent that reduces signal intensity and phase in gradient echo T_2^* weighted images. Therefore, the central vein sign appears as a hypointensity region running through hyperintense MS lesions on SWI (Figure 6.21). Central veins were detected for all new lesions considered here. The apparent luminal diameter of veins for every lesion showed differences at each time point compared to the first appearance of lesion on FLAIR image (yellow arrow). Vein narrowing or enlargement was clearly seen on SWI image, but this may be an off-resonance artefacts or phase artefact adjacent to the vessel. No difference between rim and no rim was found on central veins in MS lesions.



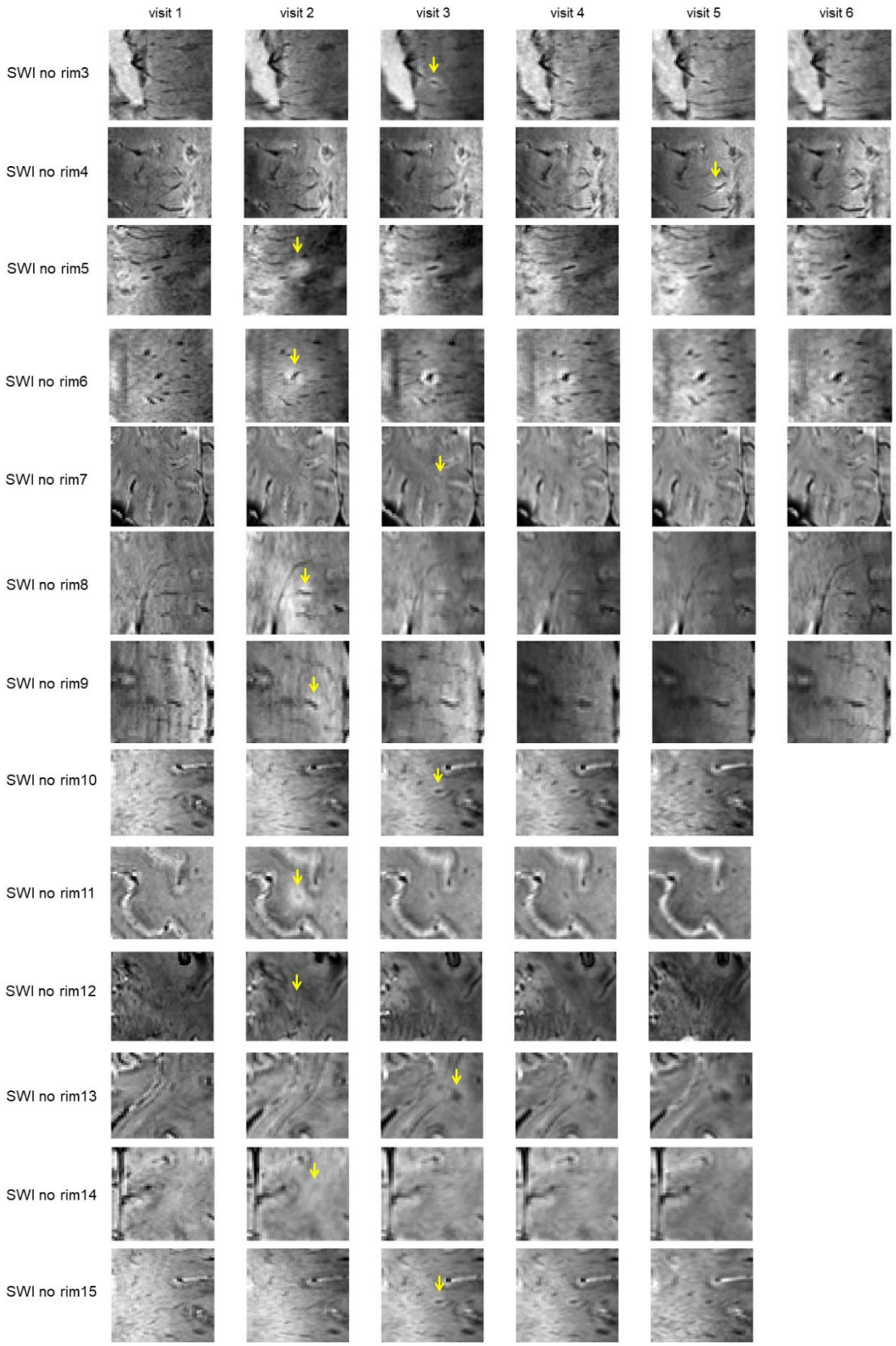


Figure 6.21: Evolution of central vein in all twenty new lesions, a hypointensity region running through the middle of lesion was found on SWI images. An arrow represents the detection of lesion corresponding to the first appearance on FLAIR images.

6.3.8 Dependence on fibre orientation

Figures 6.22-6.24 shows chronic MS lesions located in a dense fibre tract such as corpus callosum or optic radiation which are perpendicular to the B_0 field. In these areas, the fibre orientation dependent apparent frequency which appears as hyperintense signal on FDM maps (both FDM3 and FDMav images). Multi-contrast MRI was used to compare and track the changes.

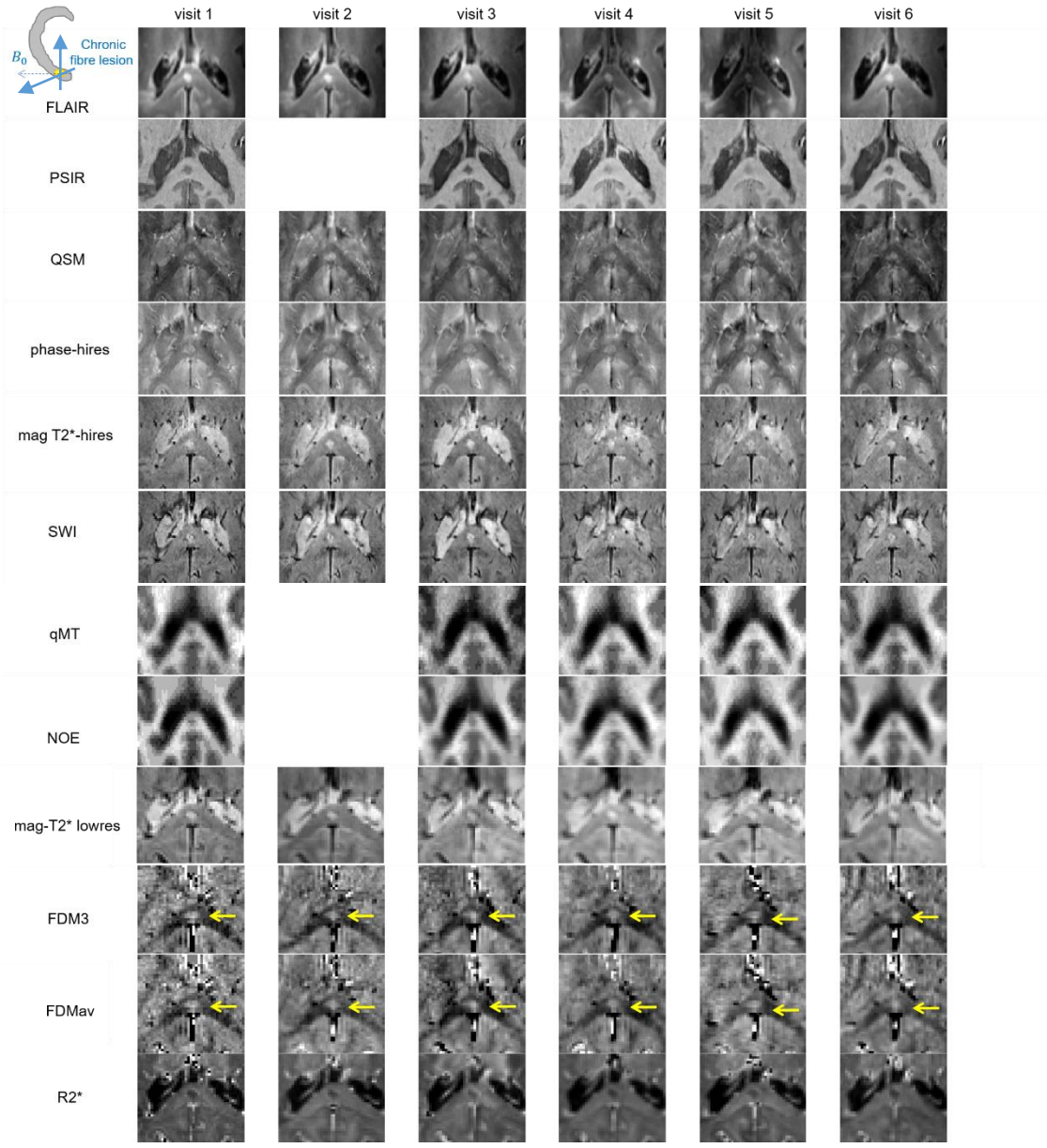


Figure 6.22: Chronic MS lesion in the corpus callosum "splenium region" that connects with the parietal, temporal lobes, and the visual cortex, observed by multi-contrasts MRI. The FDM maps showed a clear contrast in demyelinating lesion compared with normal white matter tissue surrounding (arrow).

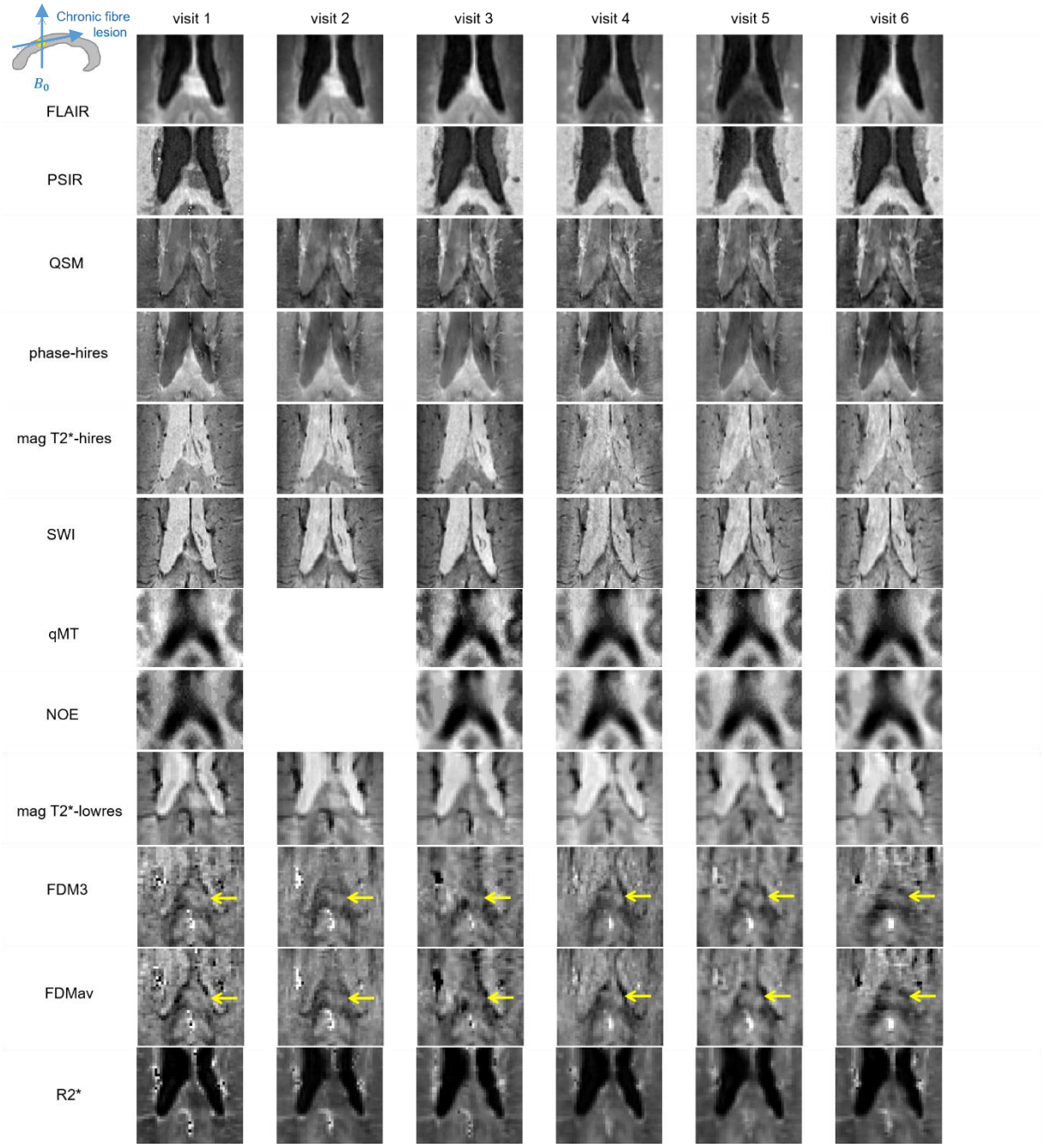


Figure 6.23: Chronic MS lesion in another part of the corpus callosum “isthmus region” that connects with the primary sensory area, observed by multi-contrasts MRI. The FDM maps showed a clear contrast in demyelinating lesion compared with normal white matter tissue surrounding (arrow).

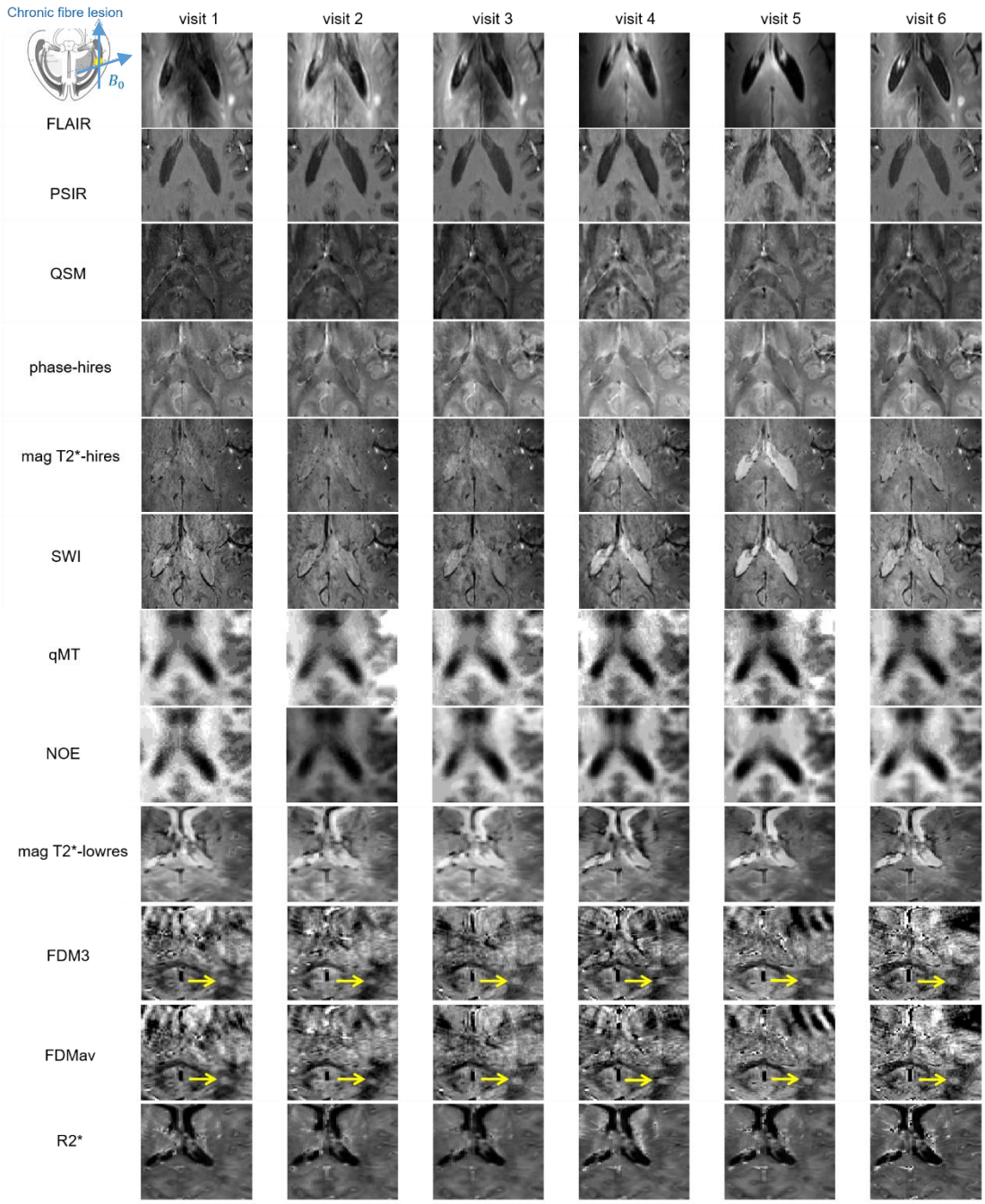


Figure 6.24: Chronic MS lesion in the optic radiation observed by multi-contrasts MRI. The FDM maps also showed a clear contrast in demyelinating lesion located in a dense fibre tract perpendicular to the B_0 field (arrow).

6.4 Discussion

Guidelines for a standardized brain MRI protocol for the diagnosis of MS recommend using four core sequences (3D IR T_1W, 3D FLAIR, 3D T_2W and 2D DWI) with adequate SNR and spatial resolution at a field strength of at least 1.5 T [20]. However using higher field has been shown to improve lesion detection [21]. MS is associated with demyelination, axonal loss, inflammation, and iron deposition in activated microglia. Ultra high field imaging can help in finding more specific features of MS lesions related to inflammation, demyelination, and neurodegeneration which may be valuable in future experimental medicine studies. The 7.0 T MRI protocol proved to be feasible to run in this patient group [22-23].

In a study of four MS patients, we tracked the development of twenty newly forming MS lesions at 6-week intervals. We presented the dynamic pattern of contrast enhancement in damaged tissue rather than reporting presence or absence of lesions. White matter MS lesions were defined as regions of hyperintensity on conventional T_2W FLAIR and T_2^* images during lesion development and hypointensity on T_1W PSIR scans. At the same time, FLAIR provides T_2W contrast with suppression of CSF. Normal myelin is normally dark grey on T_2 weighted image, but in MS lesions appear as hyperintense due to loss of myelin and increase extracellular water with setting of inflammation.

On QSM data, new lesions appeared as hyperintense with a rim and no rim (Figure 6.4 and Figure 6.5). Intensity changes remained fairly flat in the periphery before lesion appearance, and then increased toward the core region after lesion appearance for both types. Lesions also appeared hypointense on qMT and NOE maps. These changes in MT contrasts are consistent with previous report by Rovira et al. [24]. that nonconventional MR contrasts can be used to monitor disease-related changes in newly forming lesions to better understand mechanisms that occur in MS.

Importantly, subtle changes in qMT and NOE could be detected at least 6 weeks prior to the first appearance of lesion on FLAIR and PSIR, and even 18 weeks earlier on QSM. This suggests the pathological changes in myelination and iron accumulation precede and may even contribute to conventional lesion detection with conventional MRI. Here we concentrated on focal lesions but this suggests that monitoring these parameters in normal appearing white matter might open up an earlier window for detection and treatment of relapses. qMT and NOE also showed recovery after lesion formation suggesting remyelination. Figure summarizes the expected course of lesion formation and how the MRI contrasts are expected to follow this. Clearly we did not observe any fluid accumulation that may be related to inflammation prior to the process of iron accumulation or demyelination, and the iron accumulation did not appear to resolve rapidly.

Lesions with hyperintense rim showed a greater decrease in qMT and NOE than lesions without a rim, potentially indicating a different process of disease evolution [27-29]. Although this could also relate to partial volume effects, since these lesions were larger. In some cases the lesions persisted on FDM (Figure 6.13 and Figure 6.15) suggesting disordered myelination, but the lesions were only visible on FDM when tracts were organized perpendicular to the field. Both qMT and NOE signals are sensitive to myelin content in brain [8], [34] and their signals tend to be coupled in the brain, but qMT and NOE apparently behaved somewhat differently between lesions with and without a rim, suggesting that qMT and NOE are sensitive to different changes in tissue microstructure in these two cases (although again this result may be affected by partial volume effects). This needs further examination with more lesions, very careful voxel selection and ideally post mortem validation.

QSM imaging provides a direct marker of tissue iron content [35]. Iron is located in oligodendrocytes and increased brain iron has been found in a variety of neurological disorders including multiple sclerosis. However, loss of myelin is

thought to be linked to a reduction of myelination that will also lead to a signal change in susceptibility contrast. However, comparing qMT and QSM data suggests that iron contributed the QSM signals. Active MS lesions contain microglia or macrophages associated with iron deposition [4, 6, 25, 26]. Lesions with a rim exhibited the changes in susceptibility contrast before the change of qMT and NOE, but smaller changes were detected in lesions without a rim. These results indicated the potential of QSM and qMT to study the correlation of demyelination and iron deposition in MS patients.

FDM maps have potential for identifying changes in WM integrity *in vivo* and sometimes showed a clear contrast which is linked to signal compartmentalization between myelinated and demyelinated nerve fibres [16, 17]. However, clear FDM contrast is only observed in dense fibres running perpendicular to B_0 field such as corpus callosum or optic radiation. The measure is less useful when fibre runs parallel to the B_0 field.

T_2^* weighted imaging was used as a simpler quantitative measure that is sensitive to the absolute content and distribution of both myelin and brain iron. However, at 7.0 T, T_2^* enhanced with SWI processing also provides improved visibility of intralesional veins which appears as a hypointense line running through MS lesions (Figure 6.20). Although central veins were detected for all new lesions, the luminal diameter varied during the time course of the study compared to the first appearance of lesion on FLAIR images. The lack of systematic change may be due to changes in vessel diameter or artefacts for instance related to changes in susceptibility around the vessel. This is comparable to previous studies which showed that smaller diameter of intralesional veins was found in acute MS lesions at the time point of blood-brain barrier breakdown. New lesion growths are closely associated with blood brain barrier permeability changes and disease stages [30-

32]. Therefore, using the combination of SWI, QSM and T_2^* images will help to evaluate local susceptibility changes in newly forming lesion.

Statistical evaluation of these observations is limited by the relatively small number of patients and lesions examined in the study. Additional longitudinal scanning of more subjects is warranted. Moreover, the MR sequences with optimised parameters in this study are limited to a specific MRI machine which may vary from one manufacturer to another.

6.5 Conclusion

This is the first longitudinal study using susceptibility and qMT that we are aware of. We successfully tracked the formation of new MS lesions in small cohort of four MS patients, using multi-contrast 7.0 T MRI. Subtle changes in qMT, NOE and QSM could be detected prior to MRI-visible lesions appearing on FLAIR, PSIR and T_2^* images. qMT and NOE decreased gradually in new lesion followed by a slow increase of signal (compared to NAWM in both hemispheres away from lesion site), indicating demyelination and then remyelination. QSM showed heterogeneous changes contrast with iron accumulation. This reflects degradation of myelin and extracellular accumulation of iron produced by microglia in the diseased area. SWI images improved visibility of intralesional vein. Tracking changes in this way could assist treatment planning in patient with relapsing multiple sclerosis.

Bibliography

[1] I. S. Mackenzie, S. V. Morant, G. A. Bloomfield, T. M. MacDonald, and J. O'Riordan, "Incidence and prevalence of multiple sclerosis in the UK 1990-2010: a descriptive study in the General Practice Research Database," *J. Neurol. Neurosurg. Psychiatry*, vol. 85, no. 1, pp. 76–84, 2014.

[2] I. R. Levesque, P. S. Giacomini, S. Narayanan, L. T. Ribeiro, J. G. Sled, D. L. Arnold, and G. B. Pike, "Quantitative magnetization transfer and myelin water imaging of the evolution of acute multiple sclerosis lesions," *Magn. Reson. Med.*, vol. 63, no. 3, pp. 633–640, 2010.

[3] A. Petzold, "Biomarkers of disease progression," in *Progressive Multiple Sclerosis*, vol. 9781447123, 2013, pp. 115–146.

[4] C. Stüber, D. Pitt, and Y. Wang, "Iron in multiple sclerosis and its noninvasive imaging with quantitative susceptibility mapping," *International Journal of Molecular Sciences*, vol. 17, no. 1. 2016.

[5] D. Pitt, A. Boster, W. Pei, E. Wohleb, A. Jasne, C. R. Zachariah, K. Rammohan, M. V. Knopp, and P. Schmalbrock, "Imaging cortical lesions in multiple sclerosis with ultra-high-field magnetic resonance imaging," *Arch. Neurol.*, vol. 67, no. 7, pp. 812–818, 2010.

[6] V. Mehta, W. Pei, G. Yang, S. Li, E. Swamy, A. Boster, P. Schmalbrock, and D. Pitt, "Iron Is a Sensitive Biomarker for Inflammation in Multiple Sclerosis Lesions," *PLoS One*, vol. 8, no. 3, 2013.

[7] O. Mougin, R. Abdel-Fahim, R. Dineen, A. Pitiot, N. Evangelou, and P. Gowland, "Imaging gray matter with concomitant null point imaging from the phase sensitive inversion recovery sequence," *Magn. Reson. Med.*, vol. 76, no. 5, pp. 1512–1516, 2016.

[8] N. Geades, B. A. E. Hunt, S. M. Shah, A. Peters, O. E. Mougin, and P. A.

Gowland, “Quantitative analysis of the z-spectrum using a numerically simulated look-up table: Application to the healthy human brain at 7.0 T,” *Magn. Reson. Med.*, vol. 78, no. 2, pp. 645–655, 2017.

[9] V. Khlebnikov, N. Geades, D. W. J. Klomp, H. Hoogduin, P. Gowland, and O. Mougin, “Comparison of pulsed three-dimensional CEST acquisition schemes at 7 tesla: steady state versus pseudosteady state,” *Magn. Reson. Med.*, vol. 77, no. 6, pp. 2280–2287, 2017.

[10] M. Jenkinson and S. Smith, “A global optimisation method for robust affine registration of brain images,” *Med. Image Anal.*, vol. 5, no. 2, pp. 143–156, 2001.

[11] M. Jenkinson, P. Bannister, M. Brady, and S. Smith, “Improved optimization for the robust and accurate linear registration and motion correction of brain images,” *Neuroimage*, vol. 17, no. 2, pp. 825–841, 2002.

[12] D. N. Greve and B. Fischl, “Accurate and robust brain image alignment using boundary-based registration,” *Neuroimage*, vol. 48, no. 1, pp. 63–72, 2009.

[13] O. Mougin, M. Clemence, A. Peters, A. Pitiot, and P. Gowland, “High-resolution imaging of magnetisation transfer and nuclear Overhauser effect in the human visual cortex at 7 T,” *NMR Biomed.*, vol. 26, no. 11, pp. 1508–1517, 2013.

[14] W. Li, A. V. Avram, B. Wu, X. Xiao, and C. Liu, “Integrated Laplacian-based phase unwrapping and background phase removal for quantitative susceptibility mapping,” *NMR Biomed.*, vol. 27, no. 2, pp. 219–227, 2014.

[15] W. Li, C. Liu, T. Q. Duong, P. C. M. van Zijl, and X. Li, “Susceptibility tensor imaging (STI) of the brain,” *NMR in Biomedicine*, vol. 30, no. 4. 2017.

[16] S. Wharton and R. Bowtell, “Fiber orientation-dependent white matter contrast in gradient echo MRI,” *Proc. Natl. Acad. Sci.*, vol. 109, no. 45, pp. 18559–18564, 2012.

[17] M. J. Cronin, S. Wharton, A. Al-Radaideh, C. Constantinescu, N. Evangelou,

R. Bowtell, and P. A. Gowland, “A comparison of phase imaging and quantitative susceptibility mapping in the imaging of multiple sclerosis lesions at ultrahigh field,” *Magn. Reson. Mater. Physics, Biol. Med.*, vol. 29, no. 3, pp. 543–557, 2016.

[18] M. Shah, Y. Xiao, N. Subbanna, S. Francis, D. L. Arnold, D. L. Collins, and T. Arbel, “Evaluating intensity normalization on MRIs of human brain with multiple sclerosis,” *Med. Image Anal.*, vol. 15, no. 2, pp. 267–282, 2011.

[19] A. Madabhushi and J. K. Udupa, “New methods of MR image intensity standardization via generalized scale,” *Med. Phys.*, vol. 33, no. 9, pp. 3426–3434, 2006.

[20] A. Traboulsee, J. H. Simon, L. Stone, E. Fisher, D. E. Jones, A. Malhotra, S. D. Newsome, J. Oh, D. S. Reich, N. Richert, K. Rammohan, O. Khan, E. W. Radue, C. Ford, J. Halper, and D. Li, “Revised recommendations of the consortium of MS centers task force for a standardized MRI protocol and clinical guidelines for the diagnosis and follow-up of multiple sclerosis,” *American Journal of Neuroradiology*, vol. 37, no. 3. pp. 394–401, 2016.

[21] M. P. Wattjes and F. Barkhof, “High field MRI in the diagnosis of multiple sclerosis: High field-high yield?,” *Neuroradiology*, vol. 51, no. 5. pp. 279–292, 2009.

[22] F. Visser, J. J. M. Zwanenburg, J. M. Hoogduin, and P. R. Luijten, “High-resolution magnetization-prepared 3D-FLAIR imaging at 7.0 tesla,” *Magn. Reson. Med.*, vol. 64, no. 1, pp. 194–202, 2010.

[23] W. L. De Graaf, J. J. M. Zwanenburg, F. Visser, M. P. Wattjes, P. J. W. Pouwels, J. J. G. Geurts, C. H. Polman, F. Barkhof, P. R. Luijten, and J. A. Castelijns, “Lesion detection at seven Tesla in multiple sclerosis using magnetisation prepared 3D-FLAIR and 3D-DIR,” *Eur. Radiol.*, vol. 22, no. 1, pp. 221–231, 2012.

[24] A. Rovira, C. Auger, and J. Alonso, “Magnetic resonance monitoring of lesion

evolution in multiple sclerosis," *Ther. Adv. Neurol. Disord.*, vol. 6, no. 5, pp. 298–310, 2013.

[25] X. Li, D. M. Harrison, H. Liu, C. K. Jones, J. Oh, P. a. Calabresi, and P. C. M. van Zijl, "Magnetic susceptibility contrast variations in multiple sclerosis lesions.," *J. Magn. Reson. Imaging*, p. n/a-n/a, 2015.

[26] F. Bagnato, S. Hametner, B. Yao, P. Van Gelderen, H. Merkle, F. K. Cantor, H. Lassmann, and J. H. Duyn, "Tracking iron in multiple sclerosis: A combined imaging and histopathological study at 7 Tesla," in *Brain*, 2011, vol. 134, no. 12, pp. 3599–3612.

[27] K. Mehindate, D. J. Sahlas, D. Frankel, Y. Mawal, A. Liberman, J. Corcos, S. Dion, and H. M. Schipper, "Proinflammatory cytokines promote glial heme oxygenase-1 expression and mitochondrial iron deposition: implications for multiple sclerosis.," *J. Neurochem.*, vol. 77, no. 5, pp. 1386–95, Jun. 2001.

[28] J. R. Connor and S. L. Menzies, "Altered cellular distribution of iron in the central nervous system of myelin deficient rats," *Neuroscience*, vol. 34, no. 1, pp. 265–271, Jan. 1990.

[29] H. M. Schipper, "Heme oxygenase-1: transducer of pathological brain iron sequestration under oxidative stress.," *Ann. N. Y. Acad. Sci.*, vol. 1012, pp. 84–93, Mar. 2004.

[30] J. E. Dixon, A. Simpson, N. Mistry, N. Evangelou, and P. G. Morris, "Optimisation of T2*-weighted MRI for the detection of small veins in multiple sclerosis at 3 T and 7 T," *Eur. J. Radiol.*, vol. 82, no. 5, pp. 719–727, 2013.

[31] P. Eisele, K. Szabo, A. Ebert, W. Brueck, M. Platten, and A. Gass, "Spatiotemporal evolution of venous narrowing in acute MS lesions.," *Neurol. Neuroimmunol. neuroinflammation*, vol. 5, no. 2, p. e440, Mar. 2018.

[32] M. I. Gaitán, M. P. de Alwis, P. Sati, G. Nair, and D. S. Reich, "Multiple sclerosis shrinks intralesional, and enlarges extralesional, brain parenchymal veins.," *Neurology*, vol. 80, no. 2, pp. 145–51, Jan. 2013.

[33] E. M. Haacke, Y. Xu, Y.-C. N. Cheng, and J. R. Reichenbach, “Susceptibility weighted imaging (SWI).,” *Magn. Reson. Med.*, vol. 52, no. 3, pp. 612–618, 2004.

[34] D. Liu, J. Zhou, R. Xue, Z. Zuo, J. An, and D. J. J. Wang, “Quantitative characterization of nuclear overhauser enhancement and amide proton transfer effects in the human brain at 7 Tesla,” *Magn. Reson. Med.*, 2013.

[35] A. K. Lotfipour *et al.*, “High resolution magnetic susceptibility mapping of the substantia nigra in Parkinson’s disease,” *J. Magn. Reson. Imaging*, 2012.

Chapter 7 Conclusion

7.1 Summary

This thesis presents methods for neuroimaging *in vivo* using high field MRI. Structural imaging, quantitative measurement with multi-contrast analysis were used to study microstructure and macromolecules in both health and disease. The primary focus of the work was to develop high resolution, high contrast acquisition and analysis protocols for imaging the human brain at 7.0 T.

Ultra high field MRI is hindered by B_1^+ inhomogeneity. This problem can be addressed by several methods which are presented in Chapter 3. In this study, two simple methods (B_1 shimming technique and dielectric pads) on a 2-channel system were used to improve B_1 transmit field for non-invasive *in vivo* neuroimaging. Multi-channel transmission technology on an 8-channel system was also employed in order to obtain uniform B_1^+ transmit fields inside a human head.

Chapter 4 presents the MR protocol which optimizes contrast, resolution and scan time for *in vivo* imaging of adult cochlea and auditory nerves at high field. The use of the 3D T2W DRIVE sequence provided better contrast resolution and the optimised 7.0 T MRI protocols showed better identification of anatomic details in the bony cochlea including utricular macular, interscalar septum and scala media when compared with 3.0 T MRI. Using 3D T2W DRIVE sequence with 2-channel B_1 shimming and dielectric pads allowed for better visualization detailed of bony cochlea and vestibulocochlear nerve in a reasonable scanning time for subjects with normal hearing. However, using 3D T2W DRIVE with 8-channel B_1^+ shimming is limited by insufficient image quality; additional investigation is still required. On the highest resolution scan in a subject with normal hearing at 7.0 T (a 0.26 mm^3 isotropic resolution), we observed evidence of the cochlear duct (or scala media)

associated with the sensory hair cells responsible for hearing, for the first time *in vivo*. These results showed that ultra high resolution imaging has the potential to be used to evaluate complex clinical scenarios such as vestibular schwannoma, congenital internal auditory canal (IAC) malformations, or IAC lipoma. For future work, a study of auditory arteries and blood flow in the inner ear at 7.0 T would be worthwhile in order to further detect changes in disease.

Chapter 5 presents the development of a novel MRI acquisition and analysis protocol for reliable delineation of normal anatomy of the nucleus basalis of Meynert (NBM) and then quantification of its thickness and volume *in vivo*. A novel susceptibility T_1 weighted sequence (SW-PSIR) at 7.0 T provided good visualization of the NBM with a 0.7 mm^3 isotropic resolution in a 5 minute and 50 second scan duration. SWI processing offered additional contrast specific to the NBM in the T_1 weighted PSIR scans. Applying phase mask multiplications (n=5) showed the highest CNR which allowed for clear boundary delineation of the NBM between the ventral pallidum and chiasmatic cistern enabling robust morphometry *in vivo*. Consideration of these results suggest potential avenues for future work, including the improved assessments of morphological NBM changes in health and disease, and more accurate localisation for emerging deep brain stimulation electrode placement.

Chapter 6 presents the evaluation of longitudinal changes in white matter tissue contrast prior to, and after, lesion appearance in four patients with chronic MS by acquiring multiple image contrasts at 7.0 T MRI. Twenty new lesions appeared over six months. All lesions tended to shrink in subsequent time points. Based on contrast enhancement pattern, 25% showed a hyperintense rim and 75% showed no rim in QSM data. At least 6 weeks prior to the first lesion appearance, no statistically significant difference was found on FLAIR, PSIR, and T_2^* images ($p>0.05$), but there was statistically significant difference in qMT, NOE and QSM

($p<0.05$). qMT and NOE decreased significantly in new lesions below the normal myelin (compared to both hemispheres away from lesion site) and then recovered within 6-12 weeks of lesion formation. QSM images showed a diverse range of heterogeneous susceptibility contrast at lesion site up to 18 week earlier, reflecting degradation of myelin induced extracellular accumulation of iron produced by microglia in the diseased area. Although the changes in QSM data were more variable, susceptibility values at the lesion site tended to increase before and after lesion development with greater changes being observed in the lesion core compared to the edge and periphery ROIs. On average, lesions with hyperintense rim on QSM showed a greater decrease in qMT and NOE than lesions with no rim, potentially indicating a different process of lesion evolution. At 7.0 T MRI, the visualization of a central vein within MS lesion is clearly seen on SWI. The changes of apparent luminal diameter of central veins were found at different time points supporting the notion that inflammatory MS lesions are associated with venous vasculature.

When looking the future of ultra high field MRI in neuroimaging, there are several trends to follow. First, the use of 7.0 T MRI provides insight into brain structure-function relationships for improved diagnostics and personalized disease management. High resolution anatomical imaging at 7.0 T allows us to identify some functional areas *in vivo* without the use of contrast agents (invasive technique). Superior intrinsic contrasts at 7.0 T also provide additional information about microstructure and tissue composition changes which may address unmet clinical need. Second, UHF-MRI can be used to validate the interpretation of MRI findings *in vivo* relative to histology (postmortem imaging). Postmortem MRI is useful to investigate complex anatomy and microscopic tissue structure. A third trend with the advance technology of ultra high field MRI can bridge the gap between imaging and intervention. This may help cut down unnecessary

interventions and reduce the risk of complications in patients with brain tumor or epilepsy. On one hand, the surgeon will remove the tumour to minimize the risk of recurrence, one the other hand, the location of vital functions like motor control and language should spared. Using UHF-MRI allows more accurate detection, improved localization and staging of disease. The area outside the brain (e.g. heart, breast, or abdomen) is being developed on Multix methods described here. Finally, with the capabilities provided by UHF-MRI, integration of these systems with PET or LINAC may provide more accurate information and I look forward to seeing new applications of multi-modal UHF-MRI in the future.

In conclusion, this thesis presents methods for neuroimaging at 7.0 T MRI. The methodology has been successful in providing high resolution imaging and high contrast in a reasonable scanning time. Consideration of the results presented suggest potential avenues for clinical research and clinical practice.

7.2 Future work

Future work with UHF-MRI includes looking at repeatability of high resolution in vivo 3D imaging of adult cochlea, investigating blood supply to the cochlea, and finding potential markers that can help people with hearing loss improve their ability to communicate. As people get older, the auditory nerves and sensory cells slightly die. For future NBM experiments, we will determine the volumetric change in individual AD patients that can help to improve accuracy and precision of anatomical targeting during deep brain stimulation. Moreover, we will investigate morphometric brain changes over time in ageing and patients with traumatic brain injury. Finally, lesion evolution of multiple sclerosis has remained an active field due to the early lesion changes are still not fully understood in the literatures. Possible future directions for this project should repeat in a larger sample size. Additional data will facilitate more sensitive characterisation of the specific WM

tissue changes that precede the earliest signs of lesion development in MS. This data could be useful in patients with relapses and delaying MS progression.